Constraints on the impact of active galactic nuclei on star formation in galaxies

JAN SCHOLTZ

Constraints on the impact of active galactic nuclei on star formation in galaxies

Jan Scholtz

Abstract

Super massive black holes (SMBH) are known to reside at the centre of massive galaxies, and are visible during their growth phases as active galactic nuclei (AGN). Current theoretical models of galaxy evolution require AGN feedback processes to reproduce many of the fundamental properties of galaxies and the intergalactic medium. In an effort to constrain the effect of AGN feedback on star formation in AGN host galaxies, this thesis uses observations to test predictions from the cosmological simulations. I present ALMA and integral field unit (IFU) observations of AGN host galaxies to trace obscured and unobscured star formation as well as ionised gas kinematics. Using deep ALMA continuum observations and multi-wavelength photometry I estimate specific star formation rate distributions of 81 X-ray AGN at z=1.5–3.2 with AGN luminosities of 10^{43}–10^{45} ergs s^{-1}. Comparison of the observations with predictions from the EAGLE cosmological simulations shows that AGN feedback is responsible for broadening the sSFR distribution of both active and inactive galaxies by suppressing their star formation. In the second scientific experiment, I present IFU and ALMA observations of eight X-ray AGN at z=1.4–2.6 with AGN luminosities of 10^{42}–10^{45} ergs s^{-1} to investigate the connection between AGN driven ionised outflows and star formation. Using these observations, I conclude that star formation in AGN host galaxies is not instantly suppressed by AGN driven outflows, consistent with the global conclusions from my earlier study. I reach this conclusion whenever I use obscured or unobscured star formation tracer. Furthermore, I conclude that it is necessary to use Hα emission with caution when using it to trace star formation in AGN host galaxies. In the last scientific experiment, I investigate star formation in three quasars at z$\sim$2.5 that were previously presented in the literature as having evidence for suppressed star-formation at the location of ionised outflows. Using new ALMA band

7 continuum observations and re-analysing the existing archival Hα observations, I do not observe any suppression of star formation in these quasars. Based on the evidence from all of my studies, I conclude that AGN feedback does not instantly suppress star formation on a global scale, but rather the feedback may have an impact seen on smaller spatial scales (< 4 kpc), or on longer timescales than a single AGN episode.

Constraints on the subtle impact of active galactic nuclei on star formation in galaxies

Jan Scholtz

A thesis presented in accordance with the regulations for admittance to the degree of Doctor of Philosophy

Centre for Extragalactic Astronomy
Department of Physics
University of Durham
United Kingdom

September 2019

Dedicated to

Mum, Dad & Jakub

Declaration

The work described in this thesis was undertaken between October 2015 and September 2019 while the author was a research student under the supervision of D.M. Alexander, C.M. Harrison, D. Rosario, A.M. Swinbank and V. Mainieri in the Department of Physics at the University of Durham. No part of this thesis has been submitted for any other degree at the University of Durham or any other university.

Portions of this work have appeared or been submitted in the following papers:

- *Chapter 3*: "**Identifying the subtle signatures of feedback from distant AGN using ALMA observations and the EAGLE hydrodynamical simulations**"

  J. Scholtz, D. M. Alexander, C. M. Harrison, D. J. Rosario, S. McAlpine, J.R Mullaney, F. Stanley, J. Simpson, T. Theuns, R. G. Bower, R. C. Hickox, P. Santini, and A. M. Swinbank., MNRAS 475 1288S (2018)

- *Chapter 4*: "**KASHz: No evidence for ionised outflows instantaneously suppressing star-formation in moderate luminosity z=1–2.5 AGNs**" C.M. Harrison, D.J. Rosario, D.M. Alexander, C-C. Chen, D. Kakkad, V. Mainieri, A.L. Tiley, O. Turner, M. Cirasuolo,R.M Sharples S. Stach, Submitted to MNRAS

The work described in Chapter 3 and 4 was performed in collaboration with the co-authors mentioned above. The work described in Chapter 5 was performed in collaboration with Harrison, C. M., Alexander, D. M., Rosario, D. J. Chapter 3 is based on the results of observing proposals led by J. R. Mullaney and D. M. Alexander. The data-reduction of the ALMA observations of Chapter 3 was done by J. M. Simpson. The SED fitting in Chapter 3 was performed by F. Stanley and D.J. Rosario and SED fitting in Chapters 4 was performed by D.J. Rosario. The IFU data reduction in Chapter 4 & 5 was done by C.M. Harrison, C-C. Chen and A.L. Tiley. Chapter 5 is based on the results of observing proposal led by C.M. Harrison. All of the text has been written by the author.

In addition to the work presented in this thesis, the author has also been involved in the following work during the period of their PhD:

"A contribution of star-forming clumps and accreting satellites to the mass assembly of z$\sim$2 galaxies"
A. Zanella, E. Le Floc'h, C. Harrison, E. Daddi, E. Bernhard, R. Gobat, V. Strazzullo, F. Valentino, A. Cibine, J. Sanchez Almeida, M. Kohandel, J. Fensch, M. Behrendt, A. Burkert, M. Onodera, F. Bournaud, J. Scholtz, MNRAS in print

"The East Asian Observatory SCUBA-2 Survey of the COSMOS Field: Unveiling 1147 Bright Sub-millimeter Sources across 2.6 Square Degrees"
Simpson, J. M.; Smail, Ian; Swinbank, A. M.; Chapman, S. C.; Chen, Chian-Chou; Geach, J. E.; Matsuda, Y.; Wang, R.; Wang, Wei-Hao; Yang, Y.; Ao, Y.; Asquith, R.; Bourne, N.; Coogan, R. T.; Coppin, K.; Gullberg, B.; Hine, N. K.; Ho, L. C.; Hwang, H. S.; Ivison, R. J. Kato, Y.; Lacaille, K.; Lewis, A. J. R.; Liu, D.; Michałowski, M. J.; Oteo, I.; Sawicki, M.; Scholtz, J.; Smith, D.; Thomson, A. P.; Wardlow, J. L., 2019ApJ 880 43S

"Cosmic dance at z = 3: Detecting the host galaxies of the dual AGN system LBQS 0302-0019 and Jil with HAWK-I+GRAAL"
Husemann, B., Bielby, R., Jahnke, K., Arrigoni-Battaia, F., Worseck, G., Shanks, T., Wardlow, J., Scholtz, J., A&A 614, L2

"Deep ALMA photometry of distant X-ray AGN: improvements in star formation rate constraints, and AGN identification"
Stanley, F., Harrison, C. M., Alexander, D. M., Simpson, J., Knudsen, K. K., Mullaney, J R., Rosario, D. J., Scholtz, J., MNRAS 478 3721S

Acknowledgements

There are so many people I would like to thank for helping me during my PhD. I am extremely lucky to have Dave Alexander, Chris Harrison, David Rosario, Mark Swinbank and Vincenzo Mainieiri as my supervisors who taught me and helped me in every aspect of my degree. I would especially like to thank them for all the time they spend helping me in the last few weeks. Without them, I would never be able to hand in my thesis on time. I would like to also thank Chris for proposing the idea of applying for the ESO studentship over a beer.

Throughout my PhD I had amazing friends that helped me to get through this in both Durham and Garching. All that time spent with Flora, Andrew, Stuart, Lizelke, Piotr, Stefan, and Steve were, one way or the other, unforgettable. I would like to also thank Carlo, Tereza, Aleks, Nelly and Pablo for showing me the joy of climbing. My time at ESO would also be significantly more dull without Chiara, Johanna, Dinko, Calum, Thabs, Christian and Theresa. I was part of great teams during my time in Durham: Hatfield Rowing Club, Hatfield Frisbee team and Durham Frisbee team. You guys were great. Finally, the day-to-day work routine was significantly improved by my hilarious office mates: George, Will, Steph, Ruari, Calvin, Behzad, Lizelke and Andrew. Cheese Wednesdays will never be forgotten.

Finally, I would like to thank my whole family, who were encouraging, inspiring and supporting me in pursuing science and engineering from my early childhood, as well as helping me conquer my chronic laziness. I would never be able to get here without my amazing parents and wonderful brother. Among the amazing experiences I had during my degree, nothing rivals my girlfriend Clari. She has shown an incredible amount of patience with me. Her unbelievable wit, sense of humour and support was the most wonderful companion during my PhD.

Contents

List of Tables

List of Figures

CHAPTER 1

Introduction

"Astronomy's much more fun when you're not an astronomer. "
–Brian May, Musician

1.1 Overview

It is now widely accepted that all massive galaxies host a super massive black hole (SMBH) in their centres, and while they grow, they become visible as active galactic nuclei (AGN; Soltan, 1982; Merloni et al., 2004). During the SMBH growth, the AGN releases a large amount of energy, making them the brightest objects in the Universe. This released energy has the potential to substantially alter galaxies in two ways: either by heating the gas necessary to form stars or ejecting it from the galaxy via outflows. This influence is referred to as AGN feedback and has been hypothesised to regulate star formation in the host galaxy. The majority of the leading theoretical models of galaxy evolution require AGN feedback to reproduce basic properties of the Universe such as galaxy luminosity functions, galaxy sizes, metal enrichment of circum-galactic gas, and re-ionisation of the Universe (e.g., Silk & Rees, 1998; Di Matteo et al., 2005; Alexander & Hickox, 2012; Vogelsberger et al., 2014; Hirschmann et al., 2014; Crain et al., 2015; Segers et al., 2016; Beckmann et al., 2017; Harrison, 2017; Choi et al., 2018). Despite these predictions from simulations, observational astronomers have not found clear evidence ("smoking gun") of the impact of AGN feedback on star formation in galaxies (e.g., Harrison, 2017; Cresci & Maiolino, 2018).

The aim of this introductory chapter is to provide a brief introduction and motivation to the research presented in this thesis. Throughout this thesis, I use the following definitions

for the different wavelength ranges: X-ray (0.2–10 keV), UV (ultraviolet; 0.01-–0.4μm), optical (0.4-–0.8μm), IR (infrared; 8—1000μm), NIR (near-infrared; 0.8-–5μm), MIR (mid-infrared; 5—40μm), FIR (far-infrared; 40— 500μm), and Sub-mm (sub-millimeter; 500-–1200μm) wavebands. Also, the term "AGN" is used to indicate both an Active Galactic Nucleus and a plural form of Active Galactic Nuclei.

1.2 Discovery of galaxies and Active Galactic Nuclei

To understand the relationship between AGN and galaxy evolution, I will first give a brief historical background about the discovery of both.

1.2.1 Discovery of Galaxies

Despite the first observation of galaxies having taken place nearly 250 years ago, the discipline of extra-galactic astronomy, the study of galaxies other than our own, is barely 100 years old. Galaxies were first detected by Messier in 1781 and by Herschel in 1786 (Messier, 1781; Herschel, 1786). Because they were both mostly interested in comets, these galaxies were catalogued as other "nebulous" or "fuzzy" objects that are not comets. In the 18th century, Thomas Wright speculated that some of these objects might be groups of stars outside our own galaxy, the Milky Way.

Only at the beginning of the 20th century, scientists confirmed that they do not lie in our galaxy. The first use of spectroscopy showed that spiral nebulae (spiral galaxies) are composed of stars (e.g. Huggins & Miller, 1864; Scheiner, 1899). Their large radial velocities were not seen in any other galactic objects (Slipher, 1915, 1917a). The discovery of the tight relation between the luminosity and pulsation period of the Cepheid stars by Henrietta Leavitt (Leavitt, 1908) allowed astronomers to accurately measure the distances to these objects, proving that they are truly extra-galactic (Hubble, 1926, 1929). Very soon afterwards, astronomers realised that galaxies are very common in the Universe and diverse in shapes and sizes (Hubble, 1926).

With the launch of the Hubble Space Telescope (*HST*) in 1990 and the start of the Sloan Digital Sky Survey (SDSS, Alam et al. 2015) in 2000, we realised that the Universe contains around 10^{12} galaxies. Despite all this, we still do not have a full picture of

galaxy formation and evolution. In this introduction, I will describe two crucial processes for galaxy evolution: the growth of SMBHs and star formation.

1.2.2 Discovery of Active Galactic Nuclei

The first active galactic nucleus (AGN) was studied in 1908 by Edward A. Fath, who observed spectra of stellar clusters and "spiral nebulae" (spiral galaxies, described above) using the Lick Observatory in California (Fath, 1909). He noticed that the spectrum of NGC 1068 showed very strong emission lines. Eight years later, in 1917, Vesto Slipher noticed that its spectrum contained broadened high-excitation emission lines (Slipher, 1917b). In his seminal work, published in 1943, Carl Seyfert studied twelve spectra, six of which exhibited the same basic features as the NGC 1068 (Seyfert, 1943). These objects are now commonly known as "Seyfert galaxies". After several decades of study astronomers realised the Seyfert galaxies could be split into two main categories: (a) "Type 1" AGN, which show extremely broad permitted emission lines compared to forbidden lines and (b) "Type 2" AGN, which show both forbidden and permitted lines with the same narrow width (Weedman, 1970; Khachikian & Weedman, 1971). To date, at least a million AGN have been identified since their discovery in 1943. Further studies have revealed that many of these objects contain a very compact and extremely luminous nucleus, emitting variable UV to optical continuum in addition to bright and broad emission lines (see the review given by Weedman, 1977). These suggest that an AGN hosts a very compact powerful energy source.

AGN were also independently discovered through the work of radio astronomy, a field of astronomy created from the development of radio technologies during World War II. In the 1950s, radio astronomers discovered a new class of bright compact radio sources, which were the counterparts of optical point sources (e.g. Matthews & Sandage, 1963). Since these objects were point sources and therefore looked like stars, they got the name "quasi-stellar radio sources" or quasars (QSOs). Further studies showed that QSOs preferentially reside at high redshifts ($z > 0.1$) and are therefore extremely luminous (e.g. Schmidt, 1963; Greenstein, 1963). After considerable debate and research, it has become apparent that the most likely origin of these extreme sources is mass accretion onto a massive compact object such as SMBH (with a mass of $10^6 - 10^9 M_\odot$ Salpeter, 1964; Zel-

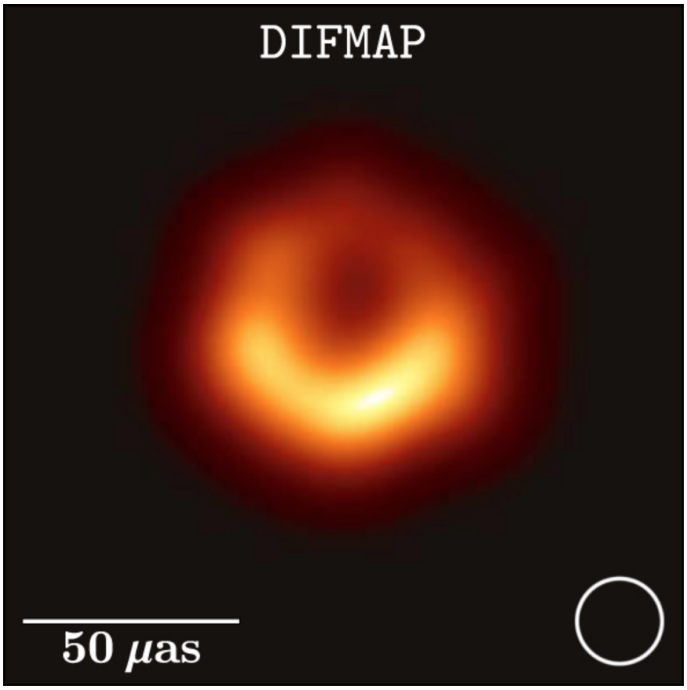

Figure 1.1: Image of the SMBH in M87 from Event Horizon Telescope Collaboration et al. (2019). The observations were performed at λ= 1.3 mm. The ring is the hot material, and the dark region in the middle is the SMBH.

dovich & Novikov, 1964; Lynden-Bell, 1969; Rees, 1984). These QSOs are now known to be the most luminous end of the AGN population.

Despite a significant amount of effort devoted to understanding SMBHs and AGN, the first SMBH has only been directly observed recently. On 10th April 2019, scientists from the Event Horizon Telescope (EHT) collaboration announced that they had observed a SMBH in our Milky Way and in M87. The Event Horizon telescope is a major technological achievement of linking telescopes at millimetre wavelengths across the entire world – from Hawaii to Chile, continental USA, Mexico, Europe and the South Pole to achieve spectacular spatial resolution - up to 25 mas (milli arcseconds), corresponding to the physical scale of 0.035 pc in M87. Figure 1.1, the first image of the SMBH in M87, was a direct confirmation that AGN host a SMBH at their centre.

Before I progress, it is also worth mentioning that our own galaxy, the Milky Way, also hosts a SMBH (Genzel et al., 2010). It is called Sagittarius A* and it has a mass of $2.6 \pm 0.2 \times 10^6$ solar masses, quite small for a galaxy of its size (see §1.5.1). It has also been imaged using the EHT. From a first look, it must be exciting for an astronomer studying AGN to have a SMBH so close to home. Unfortunately, Sagittarius A* is a small

and inactive black hole, and therefore it does not provide much information about AGN. On the other hand, an active SMBH would look like a second sun in our sky and be a major source of X-ray (and potentially gamma-ray) emission, so we should find solace in that!

1.3 AGN - SMBH growth

As described above, an Active Galactic Nuclei (AGN) is the observed manifestation of a super massive black hole (SMBH) growing via mass accretion. The accretion comes from material (mostly cold gas) being funnelled to the centre of the galaxy where the SMBH resides. However, for the gas to fall under the direct influence of the gravitational potential of a SMBH, it must lose more than 99.99 % of its angular momentum. The exact mechanism of funnelling cold gas into the gravitational potential of SMBH is currently still under debate and is beyond the scope of this thesis. Regardless, as this material falls into the gravitational potential of the SMBH, it creates a disk to conserve its angular momentum, surrounding the inner $\sim$ 1 pc around the SMBH (Jogee, 2006). The material heats up via viscous friction within the disk and emits high-energy photons. The accretion luminosity is given by:

$$L_{\rm acc} = \mu \dot{M} c^2 \tag{1.3.1}$$

Assuming that the accretion disk is composed of ionised hydrogen we arrive at a theoretical upper limit to $\dot{M}$. We then can derive a theoretical upper limit on AGN luminosity called the Eddington luminosity ($L_{\rm Edd}$). We can express $L_{\rm Edd}$ as:

$$L_{\rm Edd} = \frac{4\pi G M_{\rm SMBH} m_p c}{\sigma_{\rm T}} \approx 1.3 \times 10^{38} (M_{\rm SMBH}/M_{\odot}) {\rm ergs}^{-1} \tag{1.3.2}$$

where $M_{\rm SMBH}$ is the mass of the SMBH, m_p is a mass of a proton (mass of ionised hydrogen ion), G is the gravitational constant and $\sigma_{\rm T}$ is the Thomson cross-section for an electron. However, since the accretion is happening in a disk rather than in a sphere as assumed above, it is possible for AGN to have luminosities above the Eddington limit (as observed in Ultra Luminous X-ray sources; see review by Roberts et al., 2016). It is worth pointing out that this equation is valid for any accretion of ionised material onto a

compact object (such as a neutron star), and not just a SMBH.

The ratio between the AGN luminosity and the theoretical Eddington luminosity is called the Eddington ratio ($\lambda_{\rm Edd}$) and it is a useful normalisation of accretion rates over a wide range of SMBH masses:

$$\lambda_{\rm Edd} = \frac{L_{\rm AGN}}{L_{\rm Edd}} \propto \frac{\dot{M}}{M_{\rm SMBH}} \tag{1.3.3}$$

1.3.1 AGN standard model and AGN emission

In order to study AGN activity, we first have to understand the physical origin of the AGN emission. In this section I describe the proposed physical structure of an AGN and the resulting continuum emission and emission lines.

To explain the light emitted by the AGN, I will use the standard AGN model (Urry & Padovani, 1995) as a starting point to explain where each of the components of AGN emission originates. While this model does not explain all of the observed characteristics of an AGN (e.g, Nenkova et al., 2008; Bianchi et al., 2012; Elvis, 2012; Netzer, 2015) the basics of this model is still accepted and is sufficient to demonstrate the key emission properties of AGN. The standard AGN model (see Figure 1.2) explains different components of the AGN spectral energy distribution (SED) shown in Figure 1.3. It is worth mentioning that each component can dominate the overall SED for different types of AGN. In this thesis, I primarily focus on the high-accretion AGN, sometimes called radiatively efficient (or in "radiative mode", $\lambda > 10^{-3}$, Heckman & Best, 2014).

Continuum emission from AGN

The SMBH is surrounded by a rotationally dominated and geometrically thin accretion disk which is optically thick (Shakura & Sunyaev, 1973). This accretion disk has a sub-pc size and it is characterised by black-body emission in the optical and UV wavebands (blue curve in Figure 1.3). This emission is the result of the accretion disk having a temperature of T$\sim 2 \times 10^5$K and it peaks in UV (10-400 nm).

Around the accretion disk is an optically thin hot corona. In this corona, the UV photons produced from the accretion disk are boosted to X-ray energies through inverse Compton scattering (cyan line in Figure 1.3). The X-ray photons can also reflect off the

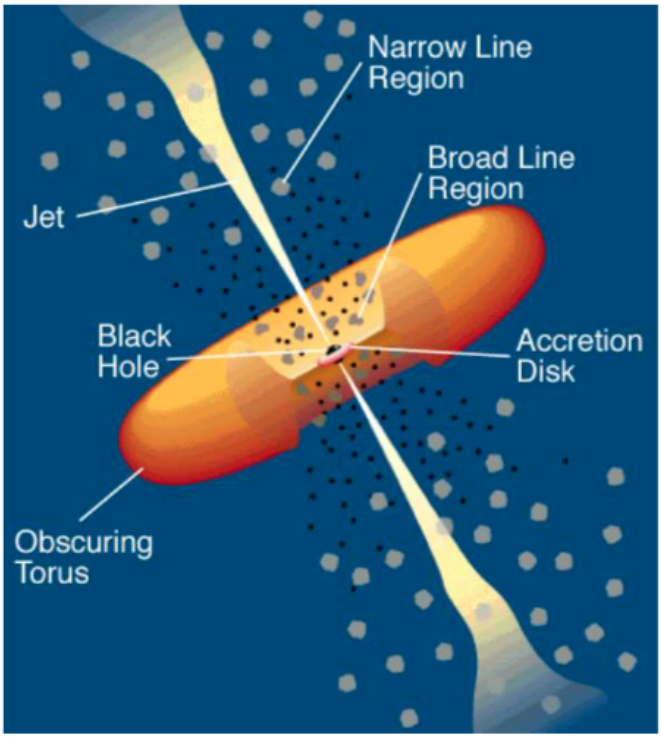

Figure 1.2: The schematic diagram of the standard AGN model (adapted from Urry & Padovani 1995). The SMBH is surrounded by the accretion disk, which is itself surrounded by the dusty torus. There are two distinctive emission line regions: (1) the broad-line region (BLR) which is under the gravitational influence of the SMBH and (2) narrow line region (NLR), extended up to kpc scales. Radio jets may also be launched from close to the accretion disk. The standard model of AGN implies that, along certain lines of sight, obscuration by the dusty torus will prevent the optical emission from the accretion disk and BLR from being observable. In contrast, observing emission from the NLR, torus and radio jets is less dependent on the line of sight.

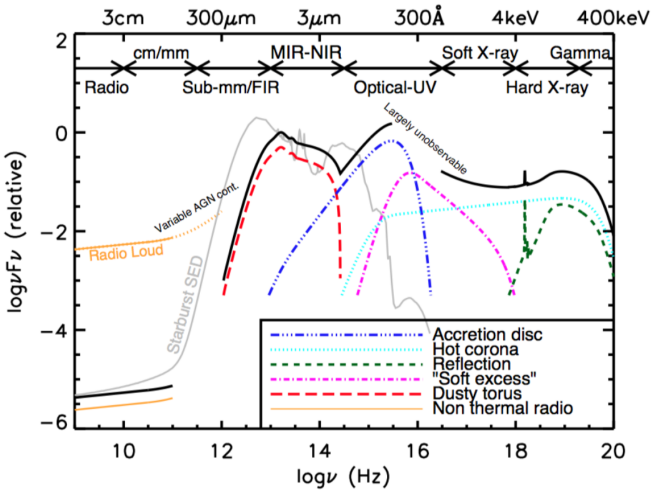

Figure 1.3: A schematic of a SED of an AGN. The shapes of the individual components are loosely based on observations of radio quiet quasars (e.g., Elvis et al., 1994; Richards et al., 2006). The black solid curve shows the total SED and the individual coloured curves (with an arbitrary offset) represent the individual components. The SED of an AGN in the sub-mm region are uncertain although it is believed that AGN have minimal contribution to the galaxy SED compared to obscured star formation, except for the most powerful radio-loud AGN. The AGN emission peaks in the UV and optical wavebands. The grey line shows the radio-UV SED of the star forming galaxy M82 (from the GRASIL library; Silva et al. 1998). Image credit: C. M. Harrison.

torus and/or the accretion disk to produce an additional reflection component in the X-ray region (e.g. George & Fabian, 1991, green curve in Figure 1.3). There is an additional component of the X-ray emission called the “soft-excess”, emission at the soft X-ray energies (0.2–2 keV) that exceeds what is expected by the simple accretion disk model, and the origin of which is still debated (see Done et al., 2012, and references there-in).

Surrounding the accretion disk at a distance of 0.1-10 pc is the so-called ”dusty torus”, an optically and geometrically thick dusty structure. This torus is most likely clumpy (Hönig et al., 2006; Nenkova et al., 2008), rather than the solid structure depicted in Figure 1.2. The optical/UV emission from the accretion disk is absorbed by the torus’s dust, heating up the torus in the process to T$\sim$ 150 K. This energy is then re-radiated at IR wavelengths (red curve in Figure 1.3 Pier & Krolik, 1992; Rowan-Robinson, 1995). While the exact shape of the dusty torus SED can vary from AGN to AGN, the usual peak of this emission is at $\lambda \approx 20-50\,\mu$m and has a steep drop-off at longer wavelengths (Elvis et al., 1994; Netzer et al., 2007; Mullaney et al., 2011). In the sub-mm/FIR wavebands, it is generally thought that the majority of AGN do not significantly contribute to the overall

SED of the galaxy and is often dominated by the dust heated by the star formation in the host galaxy.

AGN also emit in the radio arising from synchrotron emission, which may take the form of relativistic jets from the SMBH. AGN have a large range of AGN luminosities, which resulted in classification of radio-loud and radio-quiet AGN. Historically, radio-loud AGN have been defined as sources with a ratio of 5 GHz radio (L_λ[5 GHz]) to B-band luminosity (optical band; L_λ[B]) higher than 10 (Kellermann et al., 1989). These sources are also sometimes called Radio AGN, since their radio emission is significantly higher than what would be expected from star formation. Furthermore, AGN with luminosity at 1.4 GHz (L_λ[1.4 GHz]) higher than 10^{25} W Hz^{-1} are also described as radio-loud AGN, since at these luminosities, the radio emission is certainly dominated by the AGN [1]. However, it is worth noting that there is much discussion about this in the literature.

The radio SEDs of AGN are very diverse, with both large ranges in luminosity and spectral slopes, when we consider radio-quiet and radio-loud AGN (e.g. Kellermann et al., 1989; Elvis et al., 1994, ; see Figure 1.3). In radio-loud AGN, this emission originates from relativistic jets, beams of ionised particles launched from around the accretion disk. The exact physics responsible for launching these particles to close to the speed of light is not yet fully understood, but it is believed that SMBH spin and magnetic fields are a key quantities. These jets can be extended at up to tens of kpc, eventually dispersing in the CGM creating large radio structures called radio-lobes.

On the other hand, the radio emission from radio-quiet AGN is more compact and the processes that produce the radio emission is uncertain. The possible sources of this emission are supernovae, compact small scale radio jets, corona around the accretion disk and ISM shocked by AGN-driven outflows (see e.g. Smith et al., 1998; Polletta et al., 2000; Laor & Behar, 2008; Mullaney et al., 2013; Zakamska & Greene, 2014, and references therein).

The individual emission components mentioned above are obscured by the dust by a different amount and therefore the final AGN emission is sensitive to the amount of dust surrounding the AGN. An obscured AGN, i.e. an AGN with a significant amount of dust,

[1] Star formation can also produce radio emission. The neutron stars inside supernovae remnants emit in radio wavebands. (Kennicutt & Evans, 2012; Calzetti, 2013)

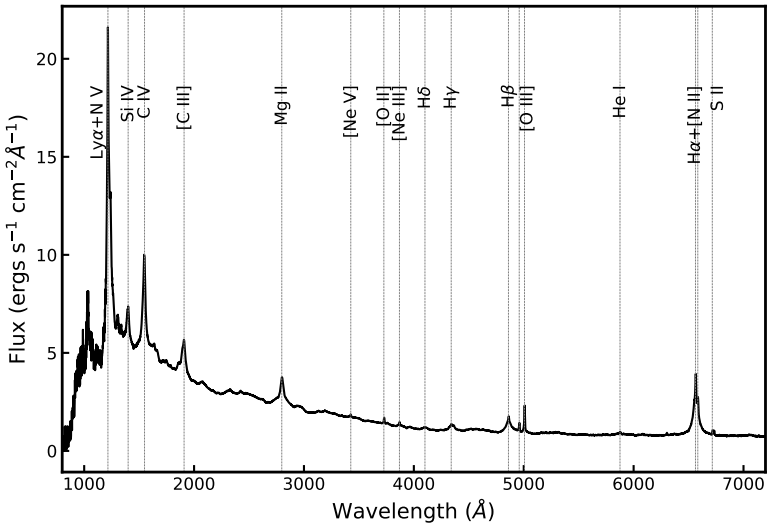

Figure 1.4: UV-optical quasar spectrum (AGN) showing typical optical and UV emission lines from Vanden Berk et al. (2001). The steep UV continuum comes from the accretion disk. The permitted lines such as Hα, Hβ, Mg II and C IV show broad features coming from the BLR, while forbidden lines such as [O III], [N II] and [O II] show narrow features.

have the UV and optical continuum suppressed. Also, in obscured AGN, the soft X-ray emission (0.2–2 keV) is more suppressed compared to hard X-ray emission (2–10 or 2–70 keV). Since star formation does not produce large amounts of hard X-ray emission (see §1.4), hard X-ray observations are an ideal waveband to find AGN (see Hickox & Alexander 2018 and Chapter 3).

Emission lines produced by AGN

The previous subsection described the origin of the continuum emission from AGN (Figure 1.3). However, AGN also emit significant amounts of energy in emission lines, and here I will briefly discuss where they originate. Figure 1.4 shows an example of a UV/optical spectrum for a quasar.

Surrounding the SMBH in its direct gravitational influence are dense hydrogen clouds (with electron densities $n_e > 10^8$ cm^{-3}; Osterbrock & Ferland 2006; see Figure 1.2). The UV photons from the accretion disk excite these dense hydrogen clouds creating extremely broad permitted emission lines with line FWHMs $\approx 10^3$ – 10^4 km s^{-1}. The region where these broad lines are produced is called the broad-line region (BLR; see

Figure 1.2), which has a size of a few light days. The forbidden lines are not emitted from this region since the density of the gas is too high and the ions are collisionally de-excited before they can de-excite via photon emission. The absence or presence of broad permitted lines in the AGN spectrum leads to a Type 2 or Type 1 classification (see §1.2.2). The absence of broad lines in the spectra of Type 2 AGN are believed to be the result of the dusty torus blocking the view of the BLR.

Furthermore, the ionising photons can escape the central region surrounding the SMBH and ionise the low-density gas well beyond the BLR (with electron densities $n_e < 10^6$ cm^{-3}; Osterbrock & Ferland 2006; see Figure 1.2). These emission lines have narrower line widths (i.e. FWHM = 250–2000 kms^{-1}) and we refer to this region as the narrow-line region (NLR). Since the density in the NLR is significantly lower than in the BLR, both permitted and forbidden emission lines are produced. The scale of the NLR is more diverse; from 100 pc to 10 kpc (e.g. Walker, 1968; Wampler et al., 1975; Wilson & Heckman, 1985; Boroson et al., 1985; Stockton & MacKenty, 1987; Osterbrock, 1989; Tadhunter & Tsvetanov, 1989; Bennert et al., 2002; Greene et al., 2011). The NLR is beyond the torus and it is visible in both Type 1 and 2 AGN.

1.3.2 AGN-driven outflows

A significant fraction of AGN research concentrates on whether AGN drive energetic outflows. However, AGN are not the only phenomenon that is capable of driving outflows. Star formation can also drive galaxy wide outflows powered by supernovae or stellar winds (e.g. Heckman et al., 1990; Lehnert & Heckman, 1996; Swinbank et al., 2009; Genzel et al., 2011; Newman et al., 2012; Bradshaw et al., 2013; Genzel et al., 2014; Förster Schreiber et al., 2018b; Swinbank et al., 2019, and review by Veilleux et al. 2005). These outflows can have a significant impact on galaxy evolution (e.g. Dalla Vecchia & Schaye, 2008; Hopkins et al., 2013a). However, star formation is not capable of driving the most powerful outflows which are necessary to disrupt galaxies in high-mass halos (e.g. Benson et al., 2003; McCarthy et al., 2011; Hopkins et al., 2013b; Zubovas & King, 2014; Bower et al., 2017).

The AGN-driven outflows are launched from the dusty torus or the accretion disk surrounding the SMBH, either as a radiatively-driven wind (by the photon/radiation pres-

sure) or radio jets. These jets and winds are believed to eventually impact on the ISM, shocking and sweeping up the gas on kpc scales (e.g., Springel et al., 2005; King, 2005; Di Matteo et al., 2005; Hopkins & Hernquist, 2006; Faucher-Giguère & Quataert, 2012; Debuhr et al., 2012). From observational evidence, we know that AGN-driven winds are prevalent in luminous AGN at both low and high redshift. Using the X-ray and UV absorption line spectroscopy, it is now agreed that these winds have velocities up to 0.1c (e.g, Reeves et al., 2003; Blustin et al., 2003; Trump et al., 2006; Gibson et al., 2009; Tombesi et al., 2010; Gofford et al., 2011; Page et al., 2011) and are a common property of luminous AGN (Ganguly & Brotherton, 2008). However, these fast velocity winds are likely to be only located near the accretion disk ($<$ 1 pc scale; e.g., Crenshaw et al. 2003; Tombesi et al. 2012). In order for these winds to have a significant effect on the galaxy evolution, their energy must couple to the ISM on 1–10 kpc, scales of the host galaxy. Therefore, it is necessary to study the outflows on kpc scales.

In recent years, spatially resolved spectroscopy such as single-slit and integral field spectroscopy (see Chapter 2) has been an essential tool in searching and characterising the kpc-scale wide outflows. Such observations have now found that kpc scale outflows are also a common property of luminous AGN (e.g. Holt et al., 2008; Rupke & Veilleux, 2011; Alatalo et al., 2011; Westmoquette et al., 2012; Veilleux et al., 2013; Rupke & Veilleux, 2013; Liu et al., 2013; Harrison et al., 2014; Genzel et al., 2014; Harrison et al., 2016b; Carniani et al., 2016; Förster Schreiber et al., 2018b). I discuss the observations of AGN outflows with integral field spectroscopy in §1.5.3 and their impact on star formation in AGN galaxies in §1.5.4.

1.4 Star formation

One of the key processes in galaxy evolution is the formation of stars. We measure this process with a quantity called the star formation rate (SFR), typically given in units of solar masses per year ($M_\odot$ yr^{-1}). Star formation occurs in cold molecular gas (H_2) clouds called Giant Molecular Clouds (GMC). The star formation process involves these parts of the gas clouds collapsing under their own gravity. During the collapse, the GMC fractures into multiple proto-stars, regions which ultimately collapse to form stars. Once the

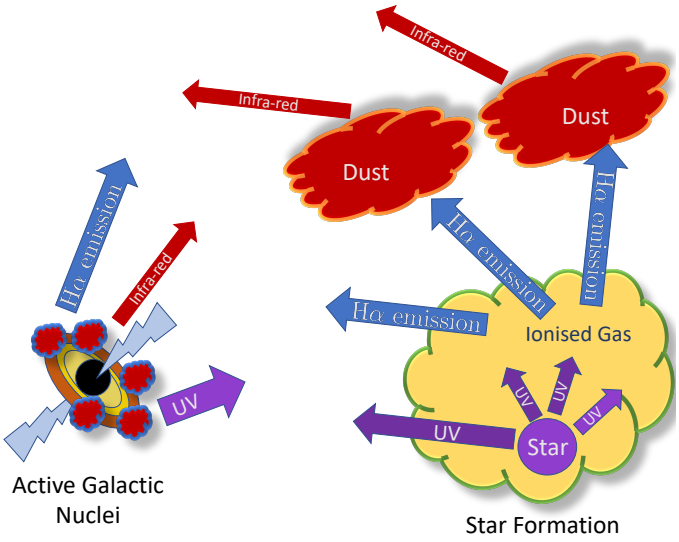

Figure 1.5: Schematic of a star formation region and the emission used to trace the star formation. The young stars emit UV and optical continuum ionising the gas clouds surrounding them. The ionised gas then emits this energy through emission lines such as Hα. The UV continuum from the stars and the emission from ionised gas is absorbed by dust surrounding the star formation regions. The dust then thermally re-radiates the energy at IR wavelengths. AGN also emit at similar wavelengths to these star formation tracers (see §1.3.1), making it sometimes difficult to decompose light emitted from star formation and from an AGN.

pressure and temperature reach sufficient levels to overcome the Coulomb force between the protons in the core of a proto-star, the nuclear fusion starts and a star is born. In order for the GMC to start collapsing, the gravitational force has to exceed the gas pressure (in the case of stable gas; the Jeans instability) and the shear force (in cases where the gas is in a differentially rotating disk; Toomre's criterion). As the cloud collapses, it converts its potential energy to kinetic energy which has to be radiated away. As a result, the collapse of the cloud is limited by the ability of the cloud to radiate its energy away.

Star formation can be triggered when the equilibrium between the internal gas pressure and the gravitational force is disrupted by outside events. In this case, molecular clouds can collide with one another or a cloud can be compressed by a nearby supernova explosion, stellar wind or an outflow. Similarly, an outside event can potentially disrupt the star formation process, heating up the molecular gas cloud or destroying it altogether.

1.4.1 Star formation tracers

When measuring and mapping star formation in galaxies, we can use a number of different tracers, each with their own advantages and disadvantages. Overall, in this thesis I split the tracers into two separate groups: direct and indirect tracers. Figure 1.5 shows a schematic diagram of the different star formation tracers. The direct star formation tracers trace the light emitted from the young, recently formed stars, while indirect star formation tracers trace the re-emitted light from the material heated by young stars. The direct star formation tracers are the UV and optical continuum emission; by tracing young, hot and massive OB stars can measure the SFR on the timescales of 0-100 million years (Myr; with higher frequency UV light tracing shorter timescales; e.g., Hao et al., 2011; Murphy et al., 2011). The X-ray emission (photons of energy 0.1–10 keV), traces supernovae and their remnants, and high mass X-ray binaries all of which are a measure of the recent star formation in galaxies (0-100 Myr; Ranalli et al., 2003).

The indirect star formation tracers do not directly trace young stars, but rather material heated by them (see Figure 1.5; infra-red and Hα emission). The UV emission ionizes the surrounding gas (mostly hydrogen). This ionised gas then radiates the energy at different permitted and forbidden emission lines, such as Hα, Hβ, [O III], [O II] and Lyα. It is worth noting that most cooling of ionised gas does not happen through the optical Hydrogen lines, but rather FIR lines like [C II]. In this thesis, I primarily use the Hα emission line (6562 Å), measuring the SFR on the timescales of 0–10 Myrs. However, the UV and optical continuum, as well as emission lines, are at relatively short wavelengths (100–700 nm), and therefore they are more sensitive to dust obscuration. The dust surrounding the star formation regions absorbs the light emitted from the young stars and the surrounding ionised gas. This heats up the dust to 30–60 K. Fortunately this light is then thermally re-emitted at infra-red (IR) wavelengths. Due to the nature of the process, the IR continuum emission is tracing the obscured star formation regions that would not be otherwise detected by direct star formation tracers. However, the IR tracer provides SFR measurements on the time-averaged scale of 10–100 Myrs (see reviews by Kennicutt & Evans, 2012; Calzetti, 2013). As the early Universe (high redshift galaxies) contained significant amounts of gas and dust, most of the star formation in galaxies is obscured and traced in the IR wavebands, greatly contributing to the cosmic IR background (see review by Lutz,

2014, and Chapter 2). The significant advantage of FIR emission as a star formation tracer is that it is not strongly absorbed by dust. To quantify the contribution between obscured and unobscured star formation, a study by Burgarella et al. (2013) have investigated the relative ratios of the UV and IR luminosity densities (calculated by integrating over the luminosity functions). They found that in the local universe the IR luminosity density is a factor of $\sim$4 above the UV luminosity density, and by z$\sim$ 1.2 the IR luminosity density is more than an order of magnitude larger than that of the UV. Consequently, to successfully trace the majority of star formation at high redshifts requires predominantly sensitive IR observations, in addition to UV observations (see Chapter 4).

1.5 Connections between star formation and AGN

AGN are incredibly efficient sources of energy inside galaxies. During the growth of a SMBH with mass up to f 10^8 $M_\odot$ via mass accretion, the SMBH releases energy equivalent to 10^{61} ergs (i.e., assuming a mass-to-energy conversion of 10%; see §1.3), which is three orders of magnitudes higher than the binding energy of the galaxies that these SMBH typically reside in (10^{58} ergs). Therefore, even if the AGN manages to couple only 1% of the energy to the galaxy and CGM on 0.1–100 kpc scales, then the SMBH could have a substantial impact on the evolution of the galaxy, and since AGN requires cold gas for its own feeding, the AGN can regulate themselves as well.

Figure 1.6 provides a basic illustration of the relationships between AGN, star formation and the cold gas supply. Given that both AGN and star formation are two processes that strongly rely on a supply of cold gas and that both can influence this supply, we would expect at least a broad connection between these two processes. However, AGN only depend on the supply of gas in and around the accretion disk on sub-pc scales, while the star formation is a galaxy wide process on kpc scales. This vast difference in size scales has led to suggestions that any tight connection between AGN –star formation must be due to one process regulating the other.

This regulation could come from the AGN and/or the galaxy. The AGN is able to heat up the cold gas reservoir through radiation and/or eject it via galaxy scale outflows launched in the vicinity of the accretion disk and radio jets (most easily identified in

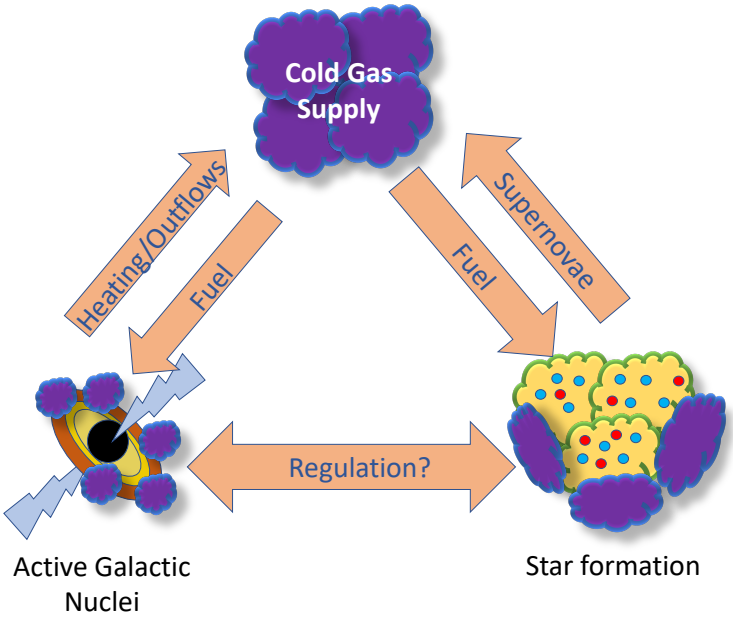

Figure 1.6: Schematic diagram to illustrate how AGN and star formation can influence each other and the supply of the cold gas in the galaxy. Both AGN and star formation inject energy and momentum to their surrounding material (through radiation and outflows) influencing the future star formation or SMBH growth. The study of how SMBHs can influence star formation in their host galaxy is a key question in this thesis.

the radio waveband). Similarly, star formation can affect the cold gas reservoir through supernovae and stellar winds. As a result AGN and star formation can both regulate themselves (see Alexander & Hickox, 2012; Fabian, 2012; Kormendy & Ho, 2013) as well as regulate each other. In this thesis, I will focus on the process of AGN regulating star formation, which is often referred to under the generic term of ”AGN feedback”.

1.5.1 Archaeological evidence

The most cited evidence for a connection between star formation and AGN feedback is the observed tight correlations between the mass of the SMBH and various galaxy spheroid properties such as mass (see Figure 1.7), velocity dispersion, and luminosity for galaxies in the local Universe (Kormendy & Ho, 2013; Magorrian et al., 1998). In this context, the term “spheroid“ is referring to both elliptical galaxies and bulges in disk galaxies (see Kormendy & Ho, 2013). However, despite the common use of these correlations in the literature as evidence of AGN feedback, this could also just suggest a common fuelling of the AGN and galaxy. It is worth noting that in the local Universe, the masses of SMBHs

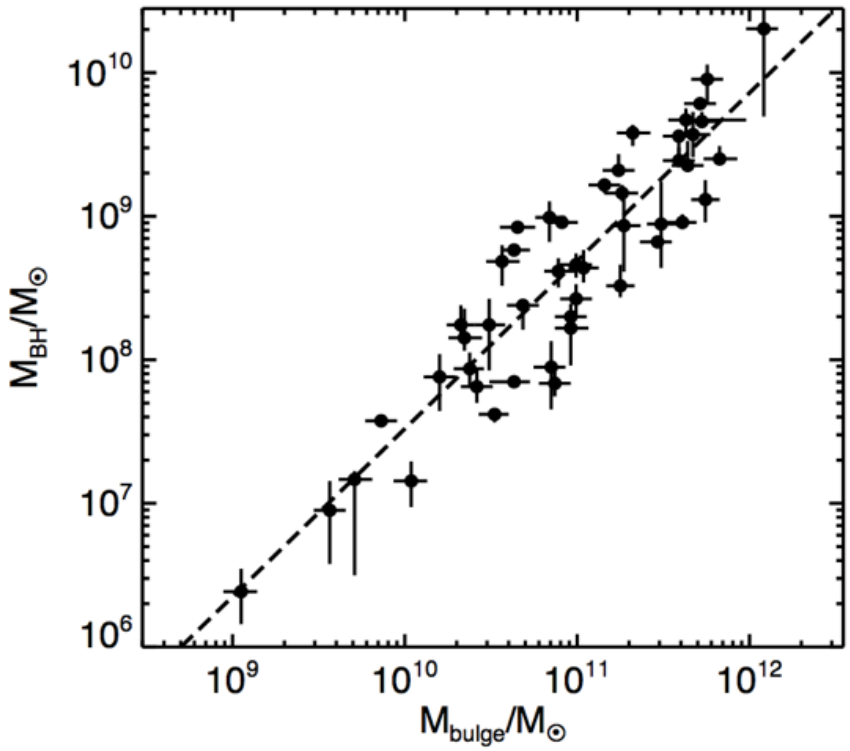

Figure 1.7: Figure from Kormendy & Ho (2013). Relationship between SMBH mass and bulge mass. There is a tight correlation between these two quantities, suggesting a common fuelling of these two processes and potentially indirect evidence for AGN feedback.

do not correlate with galaxy disks or pseudo-bulges (e.g. Greene et al., 2008, 2010; Ho, 2008; Kormendy et al., 2011; Kormendy & Ho, 2013, ; see Kormendy & Ho (2013) for comprehensive review).

Further evidence for a connection between star formation and AGN activity comes from the similar shapes of the volume average SMBH accretion density and SFR density which track one another out to z$\sim$2–3 with a $\sim$3–4 orders of magnitude offset (see Figure 1.8 and Aird et al., 2010, 2015). However, this does not provide direct support for AGN feedback, as it again could be caused by the common fuelling of these two processes.

1.5.2 Role of AGN feedback in galaxy evolution

With the emergence of sophisticated cosmological simulations of galaxy formation, it has become apparent that AGN feedback is likely to be a driver of galaxy evolution (Di Matteo et al., 2005; Hopkins et al., 2005; Debuhr et al., 2012; Schaye et al., 2015; Lacey

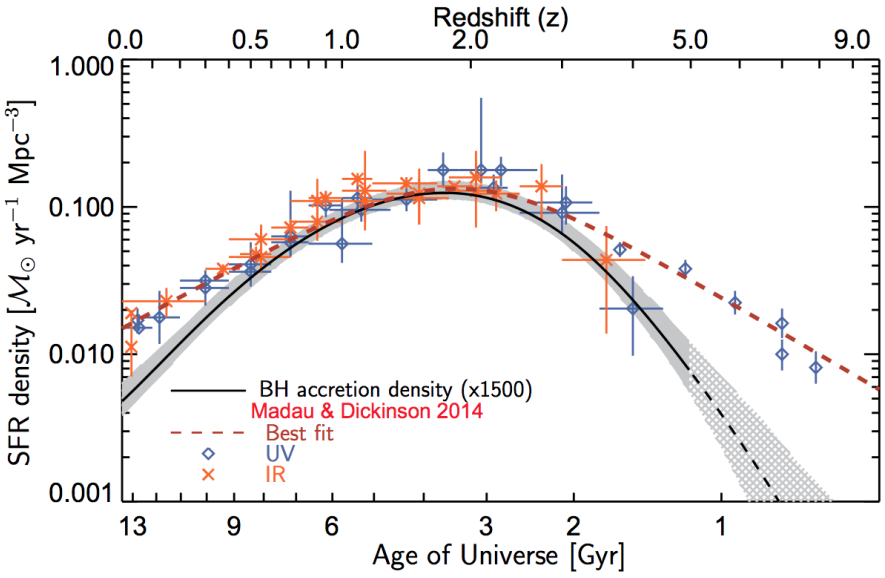

Figure 1.8: Total star-formation rate (SFR) density compared to our estimate of the total SMBH accretion density from Aird et al. (2015). The blue diamonds and orange crosses show SFR density from the recent review by Madau & Dickinson (2014) using UV and FIR data, respectively. The estimate of the SMBH accretion density (solid black line) is scaled up by an arbitrary factor of 1500. Shaded regions indicate the 99 % confidence interval.

et al., 2016). In these simulations, AGN inject significant amounts of energy into the ISM, either inhibiting the star formation by ejecting the gas out of the galaxy or simply heating the gas and preventing it from cooling. Figure 1.9 shows the average stellar mass/halo mass ratio as a function of the host halo mass from a set of simulations by Somerville et al. (2008). This ratio peaks at halo mass of $\sim 10^{12}$ M$_\odot$ for a fiducial model of galaxy evolution. An inherent advantage of simulations over observations is that it is possible to switch off individual processes in the simulations to investigate what impact they have on the properties of the simulated galaxies. These flavours of simulations have shown us that while the stellar feedback suppresses galaxy growth in low mass halos ($< 10^{12}$ M$_\odot$), AGN feedback is responsible for decreasing the stellar mass of galaxies in high mass halos ($> 10^{12}$ M$_\odot$; Bower et al. 2006; Croton et al. 2006; Somerville et al. 2008)

However, despite the strong predictions from these cosmological simulations, we still lack the direct observational evidence of the impact of AGN feedback on star formation. With the launch of the *Herschel* Space Observatory in 2009, it was possible to investigate the mean star formation rates of distant AGN (z $>$ 1), providing insight into the global trends between AGN activity and star formation. With the new sensitive infra-red data, an

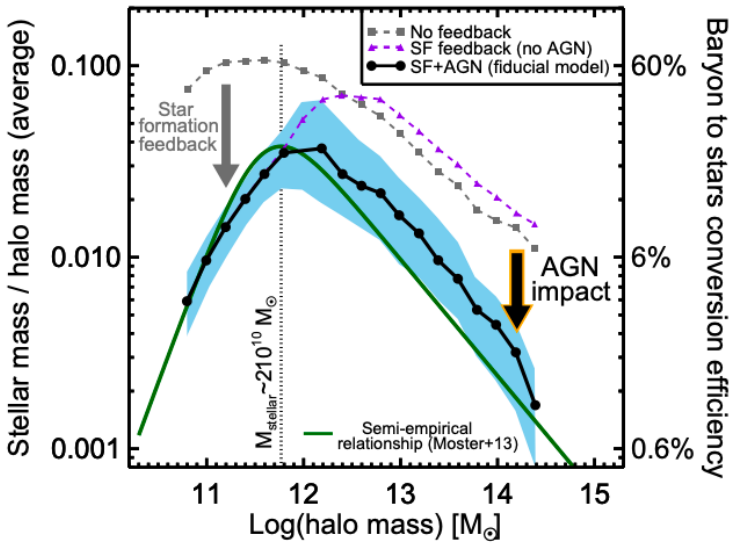

Figure 1.9: The ratio of stellar to halo mass as a function of halo mass from simulations by Somerville et al. (2008). The right y-axis indicates the efficiency of turning baryons into stars. The shaded regions describe the 16th to 84th percentiles of the fiducial model that includes both star formation and AGN feedback. The most efficient galaxy growth occurs around 10^{12} $M_\odot$. At lower halo masses, stellar feedback is believed to regulate the galaxy growth, while at large halo masses, AGN feedback is thought to be responsible for regulating the galaxy growth. Credit: Harrison (2017)

accepted view emerged that moderate luminosity AGN ($L_{Bol} = 10^{43} - 10^{46}$ ergs s^{-1}) have mean SFR and sSFR (i.e. SFR/stellar mass) consistent with those of typical star forming galaxies when binned by bolometric luminosity (e.g. Lutz et al., 2010; Shao et al., 2010; Harrison et al., 2012b; Mullaney et al., 2012a; Santini et al., 2012; Rosario et al., 2013; Azadi et al., 2015; Stanley et al., 2015; Cowley et al., 2016; Ramasawmy et al., 2019) [2]. Overall, studies investigating mean SFR typically show very weak correlation with L_{Bol} (see Figure 1.10), but this is consistent with the modest increase of stellar mass with the increasing AGN luminosity. Stanley et al. (2017) extended the SFR–L_{Bol} plane to quasars with $L_{Bol} > 10^{46}$ ergs s^{-1}, further showing a flat trend when the mass of the host systems is taken into account. Conversely, studies that calculate average AGN luminosity as a function of SFR or galaxy mass (i.e., AGN luminosity is calculated in bins of SFR of galaxy mass), find a strong positive correlation between AGN luminosity and SFR (e.g. Mullaney et al., 2012b; Chen et al., 2013; Azadi et al., 2015; Lanzuisi et al., 2017).

[2]Sometimes referred to as the star forming main sequence (SFMS; e.g. Noeske et al., 2007; Elbaz et al., 2011; Speagle et al., 2014; Whitaker et al., 2014; Schreiber et al., 2015).

The difference in the correlation between these two quantities can be explained by the different time scales at which we measure SFR and AGN activity. The positive correlation between AGN activity and SFR can be explained by the fact that star forming galaxies have more cold gas and hence are more likely to host an AGN. Hickox et al. (2014) showed that even if AGN activity is instantaneously suppressing the SFR, it would not result in a positive correlation between SFR and AGN activity. This might be counter-intuitive, as more luminous AGN release more energy into the galaxy, disrupting the ISM even further. However, this can be explained by considering the timescales over which each process is measured. While AGN activity can vary on time scales of 1 Myr (see section 1.3), the SFR varies on the scales of up to 100 Myr. Therefore, over SFR time scale, the AGN have multiple episodes, wiping any potential correlation between these two quantities (Stanley et al., 2015; Harrison, 2017). This is further confirmed by the cosmological simulations, where AGN activity plays a crucial role in reproducing key galaxy properties (McAlpine et al., 2017).

However, the limitations of the *Herschel* sensitivity (see Chapter 2) typically resulted in $\sim$10% detection rate at z$>$1. As a result, the studies were forced to calculate the average (linear mean) SFR. However, average quantities are a crude parameter to describe the actual distribution of SFR values; for example, two very different distributions could have the same linear mean. Therefore, it is possible that any trend in SFR with AGN luminosity are too subtle to be traced by the linear mean. With the commissioning of the Atacama Large Millimetre Array (ALMA; see Chapter 2) in 2011, it was possible to constrain SFRs of high redshift galaxies an order of magnitude lower than the previous *Herschel* studies (Stanley et al., 2018). Using ALMA data, Mullaney et al. (2015) showed that the majority of X-ray AGN (i.e., as defined by the mode of the distribution) have SFRs lower than the star formation main sequence by 0.3 dex and a broader distribution than the SFR distribution of star formation main sequence, even though the linear means of these distributions both agree (see also Bernhard et al., 2019). In Chapter 3, I extend the Mullaney et al. (2015) work, with the largest sample of X-ray AGN (114 sources) with sensitive ALMA dust continuum observations to constrain the SFR distributions as a function of X-ray luminosity and stellar mass.

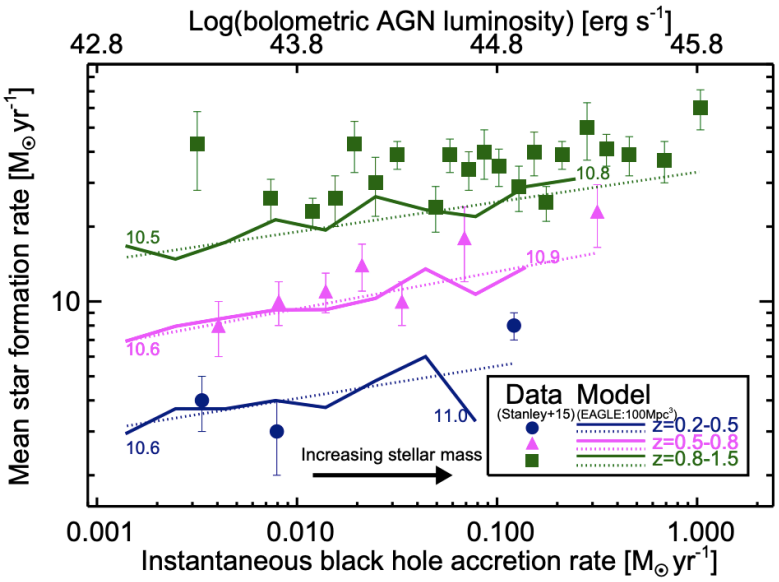

Figure 1.10: Figure from Harrison (2017). Mean star formation of AGN host galaxies rates vs the accretion rates of the AGN. The data (the points Stanley et al., 2015) agree with the simulations (dashed and solid lines). The marginal increase of mean SFR is explained by the increase of average stellar mass of the AGN host galaxies. Although the simulations require AGN feedback to suppress star formation, we do not see any evidence that more powerful AGN instantaneously suppressing star formation on this plane.

1.5.3 Observing AGN outflows

As discussed above, AGN are required in cosmological simulations of galaxy formation to heat the ISM or eject the gas out of the galaxy via AGN-driven outflows. Therefore, to study AGN feedback and its effect on the evolution of galaxies, it is necessary to study galaxy wide AGN-driven outflows.

The most common diagnostic used to identify outflowing material over large scales is the identification of broad (emission line width larger than expected from galaxy kinematics), asymmetric and high-velocity profiles of the [OIII]λ5007 emission-line. Since the [OIII]λ5007 emission line is a forbidden line, it can only be produced in a low-density material, making it a tracer for the kinematics of the NLR, that is not contaminated by the gas in the BLR (see §1.3.1).

The [OIII]λ5007 emission line has been used extensively in the past to identify galaxy wide outflows in small samples of local and low-redshift AGN (e.g., Weedman, 1970; Stockton, 1976; Veron, 1981; Heckman et al., 1981, 1984; Feldman et al., 1982; Vrtilek, 1985; Whittle, 1985; Whittle et al., 1988; Veilleux, 1991; Veilleux et al., 1995; Boroson &

Green, 1992; Nelson & Whittle, 1996); however, the small sample sizes made it difficult to know how common these outflows are. The dawn of large spectroscopic surveys such as the SDSS (York et al., 2000) made it possible to study the NLR kinematics of large samples of AGN (e.g., Boroson, 2005; Komossa et al., 2008; Zhang et al., 2011; Wang et al., 2011; Mullaney et al., 2013). Using these observations, it has been possible to study both the prevalence of ionised outflows and constrain their properties as a function of various AGN properties (such as obscuration, bolometric luminosity). Unfortunately, due to the one-dimensional nature of the SDSS spectra, it is not possible to study the spatial extent of these outflows.

With the arrival of long-slit and integral-field spectroscopy, it was possible to study the spatially resolved properties of AGN-driven outflows. At low redshifts ($z < 0.4$) observations showed high velocity outflows on kpc scales (e.g., McCarthy et al., 1996; Colina et al., 1999; Villar-Martín et al., 1999; Tadhunter et al., 2001; Holt et al., 2008; Lipari et al., 2009; Lípari et al., 2009; Fu & Stockton, 2009; Humphrey et al., 2010; Greene et al., 2011; Rupke & Veilleux, 2011, 2013; Westmoquette et al., 2012; Harrison et al., 2012a; Husemann et al., 2013; Liu et al., 2013; Harrison et al., 2014). These studies have showed that the outflows are carrying a significant amount of mass and their velocities are higher than that of the host galaxy escape velocity. These results suggest that, in agreement with theoretical models, AGN outflows are able to remove gas from the host galaxy.

With the emergence of new NIR integral field unit (IFU) instruments, there have been significant advances in tracing the ionised gas kinematics at high redshift. Many studies have identified galaxy-wide AGN-driven outflows in small samples selected in a variety of different ways (Nesvadba et al., 2006, 2008; Alexander et al., 2010; Harrison et al., 2012a; Förster Schreiber et al., 2014; Brusa et al., 2015; Cresci et al., 2015a; Carniani et al., 2015; Collet et al., 2015), with the largest sample of 14 AGN in Genzel et al. (2014). Commissioning of the KMOS (KMOS Multi-Object Spectrograph, 2013, see Chapter 2 for more information) on the VLT made observing a large sample of AGN and building a statistically significant and unbiased sample possible. I will describe KMOS in detail in Chapter 2.

The KMOS AGNs at High-z survey (KASHz; Harrison et al., 2016b) was designed

to overcome the problems of low number statistics and is exploited in this thesis. The KASHz survey observed 256 AGN at z=0.6-2.5 with L_X= 10^{42}–10^{45} ergs s^{-1} in the deep fields such as CDFS (The Chandra Deep Field South), COSMOS, UDS (Ultra Deep Survey) and SSA22. The survey is designed to explore the properties of the ionised outflows in AGN, without any pre-selection on potential outflow property, or [OIII] luminosity. The KASHz survey has shown, that AGN host galaxies are more likely to host an outflow compared the star forming galaxies, and that AGN outflows are more prevalent in targets with higher AGN luminosities (Harrison et al., 2016b, and Harrison et al in prep). KMOS3D, another KMOS GTO programme, focuses primarily on star forming galaxies at z=1.5–2.5, but it also investigated the outflows in AGN host galaxies. Förster Schreiber et al. (2018a) showed that more massive galaxies are more likely to host AGN-driven outflows than low mass galaxies.

Another on-going IFU survey at high redshift focused on the AGN is the SUPER survey (The SINFONI Survey for Unveiling the Physics and Effect of Radiative feedback; Circosta et al., 2018). This SINFONI VLT large programme focuses on observing both AGN-driven outflows and unobscured star-formation to investigate the effect of AGN feedback on star formation. Although the SUPER survey has a sample size that is a factor of 10 smaller than the KASHz survey, it utilises SINFONI's adaptive optics. As a result, their observations are diffraction-limited, rather than seeing limited, improving the spatial resolution by a factor of 3 when compared to the KMOS surveys.

1.5.4 AGN outflows suppressing star formation

Despite significant efforts dedicated to research for the impact of AGN-driven outflows on star formation, there is surprisingly little direct observational evidence that AGN-driven outflows have any significant effect on star formation.

There are three main statistical studies that have focused on constraining the effect of AGN-driven outflows on star formation at z$<$1; while Wylezalek & Zakamska (2016) showed a decrease of sSFR (SFR/stellar mass) with the velocity of the AGN outflow, Woo et al. (2016) found that AGN with outflows have larger sSFRs when compared to AGN without outflows, while Balmaverde et al. (2016) show a flat trend of SFR with [O III] velocity. Interestingly, two of these apparently contradictory conclusions were interpreted

as a signature of negative AGN feedback. Wylezalek & Zakamska (2016) interpreted their negative correlation as outflows suppressing AGN, while Woo et al. (2016) argued that their results are evidence of delayed AGN feedback, as it takes a few dynamical times to suppress star formation by the outflows. Despite the importance of constraining the impact of AGN outflows on SF, we lack a similar statistical study at z>1 and this will be a subject within the discussion of future work in Chapter 6.

Another approach to study the impact of AGN-driven outflows is to use spatially-resolved observations to map both the outflows and the star formation. For example, using long-slit and integral-field spectroscopy, star formation has been detected *inside* outflows in local AGN host galaxies, which may be a form of 'positive' feedback (i.e., AGN outflows enhancing star formation; Maiolino et al., 2017; Gallagher et al., 2019). Recently, Shin et al. (2019) observed both positive and negative feedback in NGC 5728, a nearby Seyfert-like galaxy. The MUSE and ALMA/CO observations showed enhanced star formation on the edges of the outflow in the very core of the galaxy, as well as a lack of molecular gas in the outflow in the outskirts of the galaxy.

There are currently four claimed objects that show AGN-driven outflows with signatures of suppressed star formation (Cano-Díaz et al., 2012; Cresci et al., 2015a; Carniani et al., 2016) in the literature at z>1. All four objects are luminous QSO with fast outflows (>800 km s^{-1}) and high [OIII] luminosities, representing rare and powerful AGN. In all four QSOs, these studies identified a spatial anti-correlation between the AGN-driven outflows and the narrow Hα emission and/or cavity in the Hα emission (lack of Hα emission) in the location of the outflows, argued to be a tracer of unobscured star formation. These studies have interpreted these observations as evidence that AGN-driven outflows are suppressing star formation in their host galaxies. However, there are several caveats worth pursuing. The narrow Hα primarily traces the unobscured star formation and any cavity in the Hα can be caused by dust extinguishing the Hα emission (see section 1.4.1 for more information about star formation tracers). Furthermore, the narrow Hα emission is easily contaminated by emission from the NLR due to photo-ionisation from the AGN (see section 1.3.1) and it is no longer a reliable tracer of the star forming regions. Similarly, to provide a reliable map of the Hα emission it is necessary to remove the contamination from the BLR. This makes the morphology of the narrow Hα dependant on

the technique used to subtract the broad Hα emission. These objects, potential star formation tracers, and the techniques used to create the star formation maps are a key topic in Chapters 4 and 5.

1.6 Thesis overview

The overall aim of this thesis is to constrain the impact of AGN activity on star formation in galaxies. This is achieved through two main approaches: (1) Comparing the star formation properties of AGN host galaxies to a set of simulations with and without a prescription for AGN feedback; (2) investigating the locations and extent of AGN-driven outflows with respect to the star formation in AGN host galaxies. Here, I briefly outline the content of each of the Chapter:

- **Chapter 2:** In this chapter, I give a summary of the observational methods used in this thesis. First I discuss the rest-frame FIR observatories used in this thesis, focusing on the technique of interferometry and the ALMA observatory in Chile which is utilised in all science chapters. I also give a description of integral field spectroscopy, the method to obtain spatially resolved spectra of galaxies, extensively used in Chapters 4 & 5.

- **Chapter 3:** In this chapter, I describe the observations and construction of the largest sample of distant X-ray selected AGN observed with ALMA at the time of this thesis. I used these observations to create a sample of 86 X-ray selected AGN with X-ray luminosity of 10^{43} –10^{45} erg s^{-1} at z=1.5-3.2. Using multi-wavelength photometry and the ALMA band 7 continuum observations (centred on 870μm) I constrain the specific star formation rate (SFR/stellar mass) distributions of the AGN host galaxies. Furthermore, I compare my observational results to the EAGLE cosmological simulations with and without a prescription of AGN feedback.

- **Chapter 4:** In this chapter, I investigate the effect of AGN-driven outflows on star formation in moderate luminosity AGN. Using IFU observations of [OIII] and Hα from the KASHz survey as well as ALMA continuum observations (rest-frame 200–400 μm), I assess whether it is possible to rely on a single star formation tracer

such as Hα or rest-frame FIR observations, or whether it is necessary to use both tracers. I then compare the location of star formation mapped by ALMA and Hα with observations of AGN-driven outflows to investigate the effect of AGN-driven outflows on star formation.

- **Chapter 5:** In this chapter, I re-analysed the IFU data of the three famous QSO showing signatures of AGN-driven outflows suppressing star formation. I combine these data sets with deep ALMA continuum observations to trace both the obscured and unobscured star formation to provide a more comprehensive assessment of the impact of outflow on star formation.

- **Chapter 6:** In this Chapter, I summarise the work done in this thesis and I outline three future projects to address key outstanding questions that have resulted from this thesis.

- **Appendices:** List of abbreviations used in this thesis.

CHAPTER 2

Observational Techniques

"It is never simple with IFU data."

–Dave Alexander, Astronomer

The aim of this thesis is to place empirical constraints on the impact of AGN feedback on the star formation in galaxies. As such, it is necessary to use observations to trace the two key processes involved: star formation and AGN activity. In this thesis, I use integral field spectroscopy to trace the unobscured star formation and to identify and characterise AGN driven outflows, and ALMA to trace the obscured star formation. Therefore, in this chapter, I give a brief introduction to ALMA and interferometry observations (see §2.1) and integral field spectroscopy (see §2.2).

2.1 Interferometry observations and ALMA

Throughout this thesis, I observe rest-frame FIR emission (observed at sub-mm wavelengths) from the dust to estimate the obscured star formation rate (Chapter 3) or to map the morphology of the dust obscured star formation in AGN host galaxies (Chapter 4 & 5). In this section, I give a brief historical background to FIR and sub-mm astronomy, the limitations of single dish observations and provide an introduction to interferometry.

2.1.1 FIR and Sub-mm astronomy before ALMA

The cosmic FIR background was discovered in 1996 at wavelengths of $> 200\mu$m (Puget et al., 1996) with the Cosmic Background Explorer (COBE) and later extended over the wavelengths of 70–850 μm (e.g. Lagache et al., 1999; Dole et al., 2006; Berta et al., 2011;

Magnelli et al., 2013). This Cosmic FIR background (CIB) can be described by a modified black-body (e.g. Fixsen et al., 1998) with peak at $\sim$ 150-–200μm. The CIB is dominated by the emission from high redshift galaxies. In these galaxies, most of the UV and optical emission is absorbed by dust and re-emitted at FIR and sub-mm wavelengths. Studies showed that 50 % of the emission from global star formation that has ever occurred is emitted at the FIR wavelengths (e.g. Dole et al., 2006; Madau & Dickinson, 2014; Lutz, 2014, and see Chapter 1). FIR and sub-mm observations have been performed by many observatories such as JCMT, IRAM, *ISO*, *IRAS*, *AKARI*, *Herschel*, APEX, and SOFIA. In this introduction, I primarily focus on JCMT and *Herschel*, to illustrate the challenges of observing at FIR and sub-mm wavebands.

In 1987, the James Clerk Maxwell Telescope (JCMT) was commissioned with its 15 m mirror, designed for sub-mm observations. In 1997 the SCUBA instrument (and subsequently SCUBA-2 in 2011) was commissioned on the JCMT. Both instruments were designed to observe FIR continuum emission at 450 and 850 μm. In the late 1990s, deep blank fields observed with this instrument directly detected, for the first time, a population of high redshift, sub-mm bright galaxies (Hughes et al., 1998). However, these observations are challenging since the water vapour in the atmosphere is a significant absorber of FIR and sub-mm emission. In Figure 2.1 shows the transmission of the atmosphere as a function of wavelength. The atmosphere is mostly opaque at FIR and sub-mm wavelengths with very few atmospheric windows, i.e., small wavelength ranges with better atmospheric transmission. And even though JCMT is at an altitude of 4200 m above sea level [1] and in one of the driest locations on Earth, atmospheric absorption is still a major obstacle. Therefore the ground based FIR and sub-mm observations are limited to very few wavelengths.

The Herschel Space Observatory (*Herschel*; Pilbratt et al 2010) was launched in 2009 and was operational until June 2013. Since the telescope is in space, there is no issue with atmospheric absorption, and therefore it had excellent sensitivity. With its onboard instruments, astronomers were able to observe at the wavelength that corresponds to the peak of the FIR emission of star-forming galaxies. Onboard *Herschel*, there were two

[1] At 4200 m, the pressure is 0.5 atmospheric pressure, and $\sim$40 % air of the molecules are below this altitude.

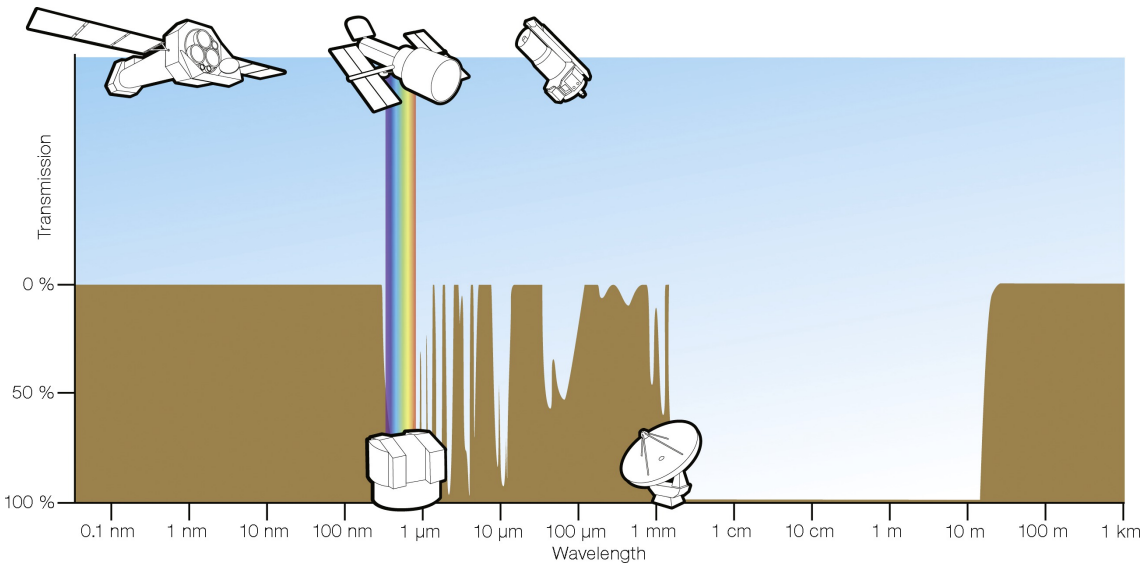

Figure 2.1: Illustration of the atmospheric transmission across the electromagnetic spectrum. The atmosphere is very opaque at FIR and sub-mm wavebands. Therefore, it is necessary to put FIR and sub-mm observatories in high altitude or space to improve the quality of the observations. Image Credit: ESA/Hubble (F. Granato)

instruments: the Photoconductor Array Camera and Spectrometer (PACS; Poglitsch et al. 2010) with filters centred at 70, 100, and 160 μm, and the Spectroscopic and Photometric Imaging Receiver (SPIRE; Griffin et al., 2010) with bands centred at 250, 350 and 500 μm. The excellent wavelength coverage provided by *Herschel* allowed many discoveries in both galaxy AGN evolution (see review by Lutz 2014 and Chapter 1 for discoveries of star forming properties of AGN with *Herschel*). It is worth noting that *Herschel* also has a spectroscopic instrument called HIFI, however, FIR spectroscopy is not a part of this thesis and hence I will not get into more detail.

However, despite the excellent sensitivity of *Herschel*, and having the largest mirror ever launched (3.6 m; and will stay largest until the launch of *JWST*), *Herschel* still suffered from issues with its limited spatial resolution. Indeed, since the diffraction limited spatial resolution of a telescope is:

$$\sigma = 1.22\frac{\lambda}{D} \tag{2.1.1}$$

where σ is the spatial resolution in radians, λ is the observed wavelength and D is the diameter of the primary mirror. For the *Herschel* and JCMT observatories with mirrors of the diameter of 3.6 and 18 m, the final resolution corresponds to $\sim$ 7–36 arcseconds

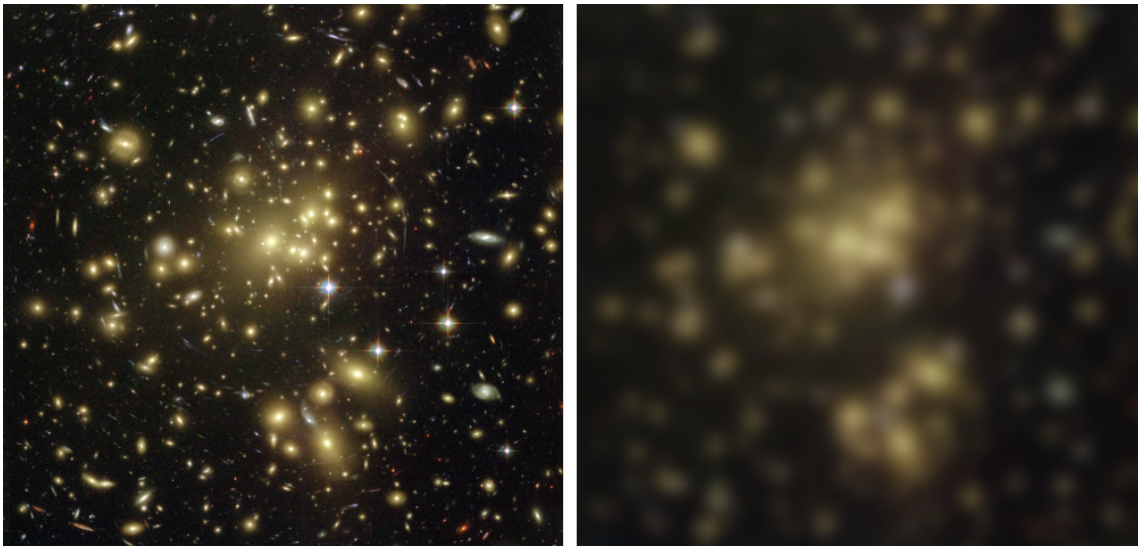

Figure 2.2: Illustration of poor resolution of *Herschel* observatory. Left: Original image of galaxy cluster Abell 1689 by HST. The high resolution imaging of HST resolves individual galaxies in the cluster. Right: Image of the galaxy cluster smoothed by a Gaussian PSF, effectively reducing the spatial resolution, simulating observations by *Herschel* or JCMT. The galaxies are smoothed together and the light is dominated by the brightest galaxies. Original image credit: NASA, ESA, L.Bradley (JHU), R. Bouwens (UCSC), H. Ford (JHU), and G Illingworth (UCSC)

for λ=250-850 μm. With this spatial resolution, it is not possible to resolve individual galaxies.

Furthermore, the limited spatial resolution means that the observations are limited by the source confusion, rather than the instrumental noise. The noise of the observations is dominated by the unresolved background emission after a short integration time and this noise does not decrease with integration time. The large beam of these observatories includes a large portion of the sky and hence large amount of background noise. Due to their large beams, the observations blend multiple sources together (as illustrated in Figure 2.2). These limitations can be partially overcome by the image deblending technique; i.e. fitting the telescope beams (PSF) for sources detected in higher resolution observations (such as MIPS/*Spitzer* for *Herschel* deblending) to estimate the flux of fainter objects. However, despite the best efforts from the literature (Swinbank et al., 2014), this results in individual detection rates of galaxies at z$>$1.5 with *Herschel* of no more than 10% (Stanley et al., 2018).

The next section describes the interferometry and ALMA telescope which addresses the spatial resolution limitations of single dish telescopes like JCMT and *Herschel*.

2.1.2 Interferometry

This section describes interferometry, a technique which combines multiple telescopes and can achieve angular resolution equivalent to the largest distance between the telescopes. In particular, I will discuss and its application to the Atacama Large Millimetre Array in Chile. For example, in order to reach sub arcsecond resolution at 870 μm, a single dish telescope would have to be at least 220 m in diameter, too impractical to build. However, through interferometry, the signals from multiple antennas/telescopes are effectively combined into a single virtual telescope. As a result of this technique, the resolution of this new virtual telescopes is:

$$\sigma = 1.22\frac{\lambda}{D_{\text{baseline}}} \tag{2.1.2}$$

where D_{baseline} is the largest distance between the telescopes in the array and σ and λ as in equation 2.1.1.

Figure 2.3 shows a schematic diagram of a telescope interferometer. The basic principle of an interferometer is similar to the Double slit experiment. The radiation from an object on the sky travels to each of the antennas, but since they are in slightly different locations, the radiation has to take paths of different length and hence the light is out of phase. The final data set from an interferometer is a set of interference patterns from each of the pair of antennas called visibilities. This method of combining signals from multiple antennas is called aperture synthesis.

A single dish telescope can be described as an interferometer with an infinite number of antennas (and baselines) and therefore samples the objects true visibilities perfectly. However, in an interferometer there are limited number of antennas pairs and hence we do not sample the object's visibilities (also called as uv coverage) completely. This can be partially solved by observing over a period of time. As the Earth rotates, the orientation of the array with respect to the source of light changes, essentially observing it with additional baselines. The final image from an interferometer is a model that best describes the observed visibilities.

The limited sampling of the visibilities provides a complication during the setup of the interferometry observations. Each baseline is only sensitive to the emission on the

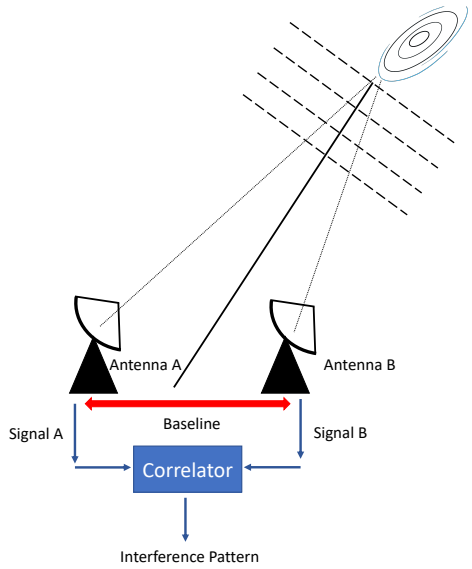

Figure 2.3: A schematic diagram of a basic two antennas interferometry array. The light from a point source has slightly different path lengths, making the signals out of phase. The signals from each antenna go to the Correlator - a supercomputer that combines the signals and creates the interference pattern just like in the Double slit experiment.

sky on scales smaller than $\sim \frac{1}{D_{\text{baseline}}}$. In Fourier space small sky-scales are equivalent to large Fourier scales and vice versa. As a result, any spatial structures larger than $\sim \frac{1}{D_{\text{baseline}}}$ will be resolved out, or in Fourier-space, any Fourier components that are smaller than the smallest baseline will be missed. Therefore, if the observations does not include sufficient small baselines, it is no longer possible to sample emission on large scales. Furthermore, since the individual small spatial components, we require longer integrations to successfully detect all the flux. It is possible to partially correct for this during imaging (see below). During creation of the dirty image, we can exclude long baseline, reducing the resolution of the final image.

The most common algorithm to image the data from the visibilities and remove the confusion from the strong side-lobes caused by the complex beam is the CLEAN algorithm described in Högbom (1974). Briefly, they first create a ”dirty image”, by performing inverse Fourier transforms of the visibilities. The algorithms describe the sources as a set of delta functions (perfect point sources), with no emission coming from the sky. The algorithms then convolve these ”clean-components” with the dirty beam (derived from the spatial distribution of the antennas in the array) and subtract them from the dirty image. This is repeated until there are no remaining sources in the field above a user-specified

level (usually 3 $\times$ the noise; 3σ). The final image is created by convolving the modelled emission with a clean beam, a Gaussian fit to the central lobe (region) of the dirty beam. The accuracy of a cleaned image can be improved by putting constraints on the algorithm. It is possible to put clean boxes around visible targets on the dirty images. The CLEAN algorithm will then only search for sources of emission within the map regions specified by the clean boxes. This reduces the risk of a spurious noise peak being identified as a source and included in the source model, where it could be mistaken for a real source. [2]

The technique of interferometry at FIR, sub-mm and millimetre wavelength is used in observatories such as ALMA, SMA and PdBI (now NOEMA). Throughout this thesis, I extensively use data from the Atacama Large Millimetre Array to observe the dust emission coming from AGN host galaxies. In the next section, I introduce this observatory.

2.1.3 ALMA

The Atacama Large Millimetre Array is an array of antennas in the Atacama desert in Chile at an altitude of 5000 m above sea level. The first scientific observations started in September 2011, with twelve 12 m telescopes in the array. At the time of this thesis, Cycle 6 observations are finishing with $\sim$ fifty 12-m antennas and an additional twelve 7 m antennas. ALMA can perform observations between 350 μm to 3 mm in 7 bands (bands 3–10). ALMA antennas were designed to be moved with two heavy haulers. Because of this, the shape and size of the array can be adjusted, changing the baselines between 150m and 16 km. These baselines give spatial resolution up to 0.02 arcsecond at 450 μm. Since each antenna has a heterodyne receiver, it is possible to sample light at high spectral resolution (below 50 km/s) and therefore detect and map emission and absorption lines, an analogous way to the integral field spectroscopy, described in the next section, but at FIR-mm wavelengths

[2] However, the final image can be very sensitive to the clean procedures used, especially when looking for faint sources. The legend around astronomy goes that you can use the clean boxes in such way that the image ends up looking like a smiley face. Despite my best efforts I was not able to track the smiley face down. This algorithm is implemented into the Common Astronomy Software Applications (CASA), which is used for the analyses of ALMA and JVLA observations. This algorithm is represented in CASA as `tclean` and `clean` functions.

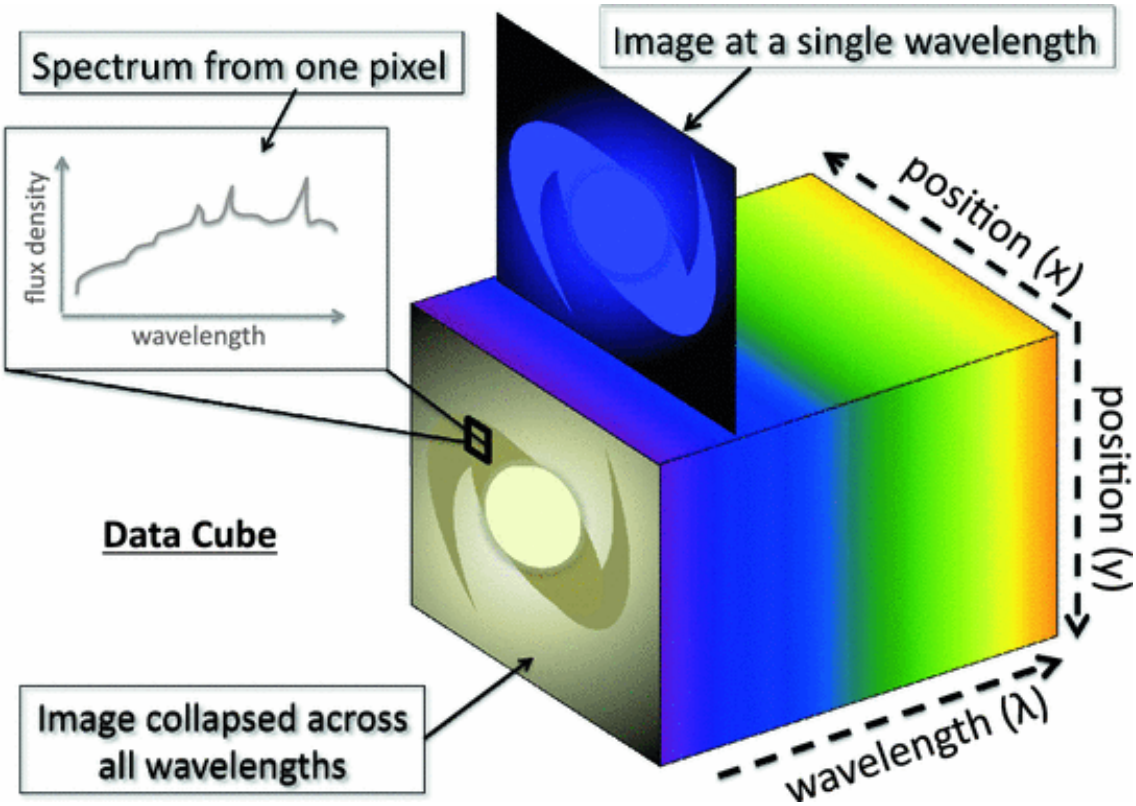

Figure 2.4: Schematic diagram of a data cube from integral field spectroscopy. The data cube consists of three dimensions - two spatial axes (x,y or RA, Dec) and a wavelength direction (λ or velocity). Each spatial pixel (spaxel) contains a spectrum of the object at a specific spatial position in the data cube. Collapsing the data cube along a wavelength range can create a narrowband image. Credit: CM Harrison

2.2 Integral Field Spectroscopy

In Chapters 4 & 5, I extensively use Integral Field Spectroscopy to map the [OIII] and Hα emission in the host galaxies of AGN and quasars at z=1.2–2.5. In this section I describe the basic concept of this spectroscopic technique.

2.2.1 Introduction to IFS

Integral field spectroscopy (IFS) is an observational technique in astronomy to obtain spatially resolved spectra of an object. These spectrographs generate 3-dimensional data and output it in the form of a data cube: there are two spatial dimensions (x,y on the spectrograph or RA and Dec on the sky) and a third wavelength dimension (λ) or velocity.

Figure 2.4 shows a schematic diagram of the IFS data cube. With IFS, it is possible to provide an image of objects at a range of wavelengths (narrowband – broadband), while

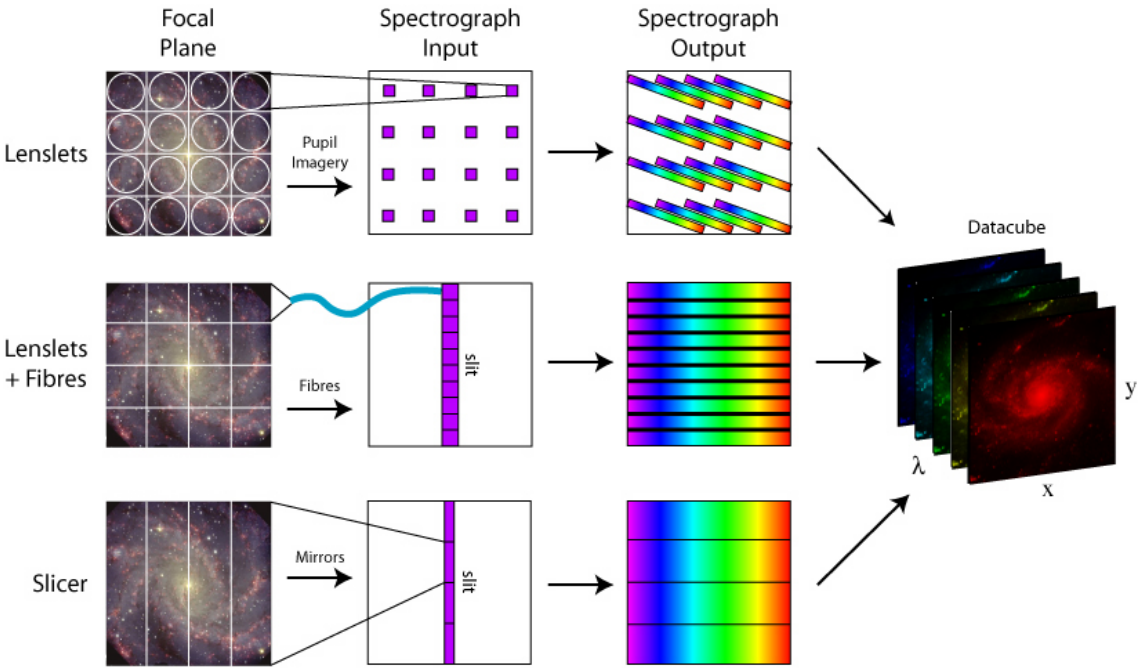

Figure 2.5: Schematic diagram of different techniques used in integral field spectroscopy (Westmoquette 2007). IFUs are capable of sampling the light from the focal plane into the separate region using a range of techniques. The light is then dispersed over a grating or a prism to create a spectrum before the data is reformatted into a data cube.

obtaining spectrum at each individual spatial pixel (spaxel). With the current technologies, it is possible to construct IFS instruments in the optical and infrared wavebands. There are two components of IFS instrument, the integral field unit (IFU) which samples the field into the separate spatial components and a spectrograph which disperses the light. IFUs split the field of view into separate samples using fibres, lenslets, or slicers (slicing mirrors). In Figure 2.5, we summarise the main technological concepts used in an IFU, which we also describe below:

- Lenslets: Using lenslets within the array, the IFU can focus the light from the individual spaxels onto the spectrograph to be dispersed. Instruments such as SAURON on the William Herschel Telescope and the SPHERE IFS on the VLT use this technique.

- Fibres: These can be used on their own or in combination with the lenslets. In this design, a bundle of optical fibres is used to sample the image directly, or alternatively, they are used behind a lenslet array. The light from the fibres is then sent to the pseudoslit that passes the light onto the spectrographs. This technique is used on

the Sydney-AAO Multi-object Integral-field (SAMI) at the Australian Astronomical Observatory, and Mapping Nearby Galaxies at APO (MaNGA) which is an IFU survey with SDSS.

- Slicers: These image slicers consist of tilted segmented mirrors that slice the image into individual strips. These strips are then reflected in slightly different directions on to another set of mirrors, formatting these slices on top of each other into a "pseudoslit" that is then passed to the spectrograph. The KMOS and SINFONI IFS instruments on the Very Large Telescope (VLT) utilise image slicers.

Whichever method is used to split the field into the individual spaxels, the light is then collimated on to the spectrograph, which uses a prism or a grating to disperse the light on to a detector, a CCD chip. The final output of the IFS is multiple spectra, each corresponding to a position on the sky. The data reduction software is then required to calibrate and format the data into a data cube.

2.2.2 Instruments used in this Thesis

In this thesis, two different IFS instruments are used, each mounted on a telescope unit on the VLT. The two instruments are: (1) KMOS - K-band multi-object spectrograph; (2) SINFONI - The Spectrograph for INtegral Field Observations in the Near Infrared. In this subsection, I will give a brief overview of each of the instruments.

- **KMOS** - K-band Multi-Object Spectrograph
  This instrument is mounted on the telescope two (UT2) of the Very Large Telescope at Paranal in Chile. This instrument has 24 arms each with a field of view of 2.4x2.4 arcsecond with spatial pixel scale of 0.2 arcseconds. Each of the arms has an IFU at the end and can be deployed within a 7.2 arc minute patrol field to observe 24 targets at once, greatly enhancing the efficiency of the observations compared to single object IFU like SINFONI. The instrument operates between 0.8–2.5 μm (IZ-K band) with spectral resolution R between 1800–4200.

- **SINFONI** - The Spectrograph for INtegral Field Observations in the Near Infrared
  This instrument was until recently located on the VLT at Paranal, on telescope

number 4 (UT4); however, it has been recently taken down to be integrated into new ERIS instrument. SINFONI is a near infra-red instrument operating at 1.1–2.45 μm (J–K Band) with a spectral resolution R between 1500–4000. The spatial pixel scale varies from 0.25, 0.1 to 0.025 arcsecond per image slice, depending on the field of views of 8×8, 3×3 and 0.8×0.8 arcseconds, respectively. This instrument is capable of making use of Adaptive Optics (AO), however, this mode is not used in this thesis.

Using these IFU instruments, it is possible to perform the following science goals:

- Mapping the spatial properties of the emission lines and absorption lines.
- Mapping the velocity structure across the object using the emission and absorption lines.

The astronomical community has used IFS of galaxies and AGN for experiments such as (1) measuring the dynamical structures of gas and stars; (2) spatially resolving stellar populations; (3) measuring the spatial distribution of on-going star formation; (4) searching for and characterising outflowing or inflowing gas. In this thesis, I use the IFS to map Hα and [O III] emission, as well as constrain the kinematics of the [O III] emission line.

CHAPTER 3

Identifying the subtle signatures of feedback from distant AGN using ALMA observations and the EAGLE hydrodynamical simulations

"The Bible tells us how to go to Heaven, not how the heavens go."

–Galileo Galilei, Astronomer, Physicist and Engineer

Abstract

We present sensitive 870 μm continuum measurements from our ALMA programmes of 114 X-ray selected AGN in the CDF-S and COSMOS fields. We use these observations, in combination with data from *Spitzer* and *Herschel*, to construct broad-band spectral energy distributions in the infrared band (8 – 1000 μm) and constrain star-formation rates (SFRs) uncontaminated by the AGN. Using a hierarchical Bayesian method we fit the SFR and specific SFR (sSFR) distributions (taking account of upper limits) for the subset of X-ray AGN at $z = 1.5 - 3.2$ with stellar mass $> 2 \times 10^{10}\ M_{\odot}$. We explore these distributions as a function of both X-ray luminosity and stellar mass. We compare our measurements to two versions of the EAGLE hydrodynamical simulations: the reference model with AGN feedback and the model without AGN. We found good agreement between the observations and that predicted by the EAGLE reference model for the modes and widths of the sSFR distributions as a function of both X-ray luminosity and stellar mass; however, we found that the EAGLE model without AGN feedback predicted a significantly narrower width when compared to the data. Overall, from the combination of the observations with the model predictions, we conclude that (1) even with AGN feedback, we expect

no strong relationship between the sSFR distribution parameters and instantaneous AGN luminosity and (2) a signature of AGN feedback is a broad distribution of sSFRs for all galaxies (not just those hosting an AGN) with stellar mass above $\approx 10^{10}\mathrm{M}_{\odot}$.

3.1 Introduction

The most successful models of galaxy formation require AGN activity (via "AGN feedback") to explain many of the puzzling properties of local massive galaxies and the intergalactic medium (IGM); e.g. the red colours, the steep luminosity functions, the black hole–spheroid relationships and the metal enrichment of the intergalactic medium (see Alexander & Hickox, 2012; Fabian, 2012; Harrison, 2017, for reviews). The key attribute of the AGN in these models is the injection of significant energy into the interstellar medium (ISM), which inhibits or suppresses star formation by either heating the ISM or ejecting the gas out of the host galaxy through outflows (Sturm et al., 2011; Fabian, 2012; Cicone et al., 2014). In recent years it has been shown that low-redshift ($z < 1$), low-accretion rate AGN are responsible for regulating the inflow of cool gas in massive galaxy clusters through heating (see McNamara & Nulsen, 2012, for review). However, despite spectroscopic observations that have shown that energetic outflows are a common property of luminous AGN (e.g. Veilleux et al., 2005; Ganguly & Brotherton, 2008; Mullaney et al., 2013; Cicone et al., 2014; Harrison et al., 2014; Balmaverde & Capetti, 2015; Harrison et al., 2016b; Leung et al., 2017) , we lack direct observational support that they dramatically impact on star formation in the distant Universe ($z > 1.5$), which is a fundamental requirement for the majority of the galaxy formation and evolution models (e.g. Bower et al., 2006; Croton et al., 2006; Springel et al., 2005).

With high sensitivity at infrared (IR) wavelengths, *Herschel* has provided new insight into the star forming properties of distant AGN ($z > 1$).[1] The broadly accepted view is that the mean star-formation rates (SFRs) and specific SFRs (sSFRs; i.e., SFR/stellar mass) of moderate-luminosity AGN ($L_{\mathrm{X}} \approx 10^{43}$–$10^{44}$ erg s^{-1}) are consistent with those

[1]The majority of studies have used X-ray observations to identify AGN since they provide an efficient and near obscuration-independent selection (see §2 at Brandt & Alexander, 2015, for an overview of the advantages of X-ray observations in identifying AGN).

of the coeval star-forming galaxy population (e.g. see also Shao et al. 2010; Harrison et al. 2012b; Mullaney et al. 2012a; Santini et al. 2012; Rosario et al. 2013; Azadi et al. 2015; Stanley et al. 2015; Cowley et al. 2016) . The definition of the star-forming galaxy population in this context is that of the "main sequence"; i.e., the redshift and stellar-mass dependent evolution of sSFRs of star-forming galaxies (e.g., Noeske et al., 2007; Elbaz et al., 2011; Speagle et al., 2014; Whitaker et al., 2014; Schreiber et al., 2015). To first order these results suggest a connection between AGN activity and star formation without providing clear evidence that moderate-luminosity AGN impact on star formation. By contrast, the current picture is more mixed for luminous AGN ($L_{\rm X} > 10^{44}$ erg s^{-1}), with different studies arguing that AGN either suppress, enhance, or have no influence on star formation when compared to moderate-luminosity AGN (e.g. Harrison et al., 2012b; Page et al., 2012; Rosario et al., 2012; Rovilos et al., 2012; Azadi et al., 2015; Stanley et al., 2015).

The majority of the current *Herschel* studies suffer from at least one of the following limitations, which hinder significant further progress: 1) SFRs are often calculated from single-band photometry, which doesn't account for the factor $\approx$ 2–3 difference in the derived SFR between star forming galaxy templates (depending on wavelength; see Stanley, 2016), 2) a modest fraction of X-ray AGN are detected by *Herschel* (often $< 10\%$ for X-ray AGN at $z > 1.5$), which drives the majority of studies to explore the stacked average SFR rate, which can be strongly affected by bright outliers (e.g., see Mullaney et al. 2015 for solutions to this problem), 3) the contribution to the IR emission from the AGN is often not directly constrained which can be significant even for moderate-luminosity AGN (e.g. Mullaney et al., 2011; Del Moro et al., 2013), and 4) upper limits on SFRs are often ignored, which will bias reported SFRs towards high values, potentially missing key signatures of suppressed star formation. Furthermore, since mass accretion onto black holes is a stochastic process with a timescale shorter than that of star formation (e.g. Hickox et al., 2014; King & Nixon, 2015; Schawinski et al., 2015; McAlpine et al., 2017), we must be cautious about what can inferred from AGN feedback using the observed relationships between SFRs and AGN luminosities (e.g., see Harrison, 2017). To more completely constrain the impact that AGN have on star formation we need to measure *SFR distributions* as a function of key properties (e.g., X-ray luminosity, stellar mass),

which will provide more stringent tests of the current models of galaxy formation and evolution (e.g. Vogelsberger et al., 2014; Schaye et al., 2015; Lacey et al., 2016).

As described above, previous studies exploring the topic of star formation in AGN typically used linear means to estimate the SFR and sSFR of the AGN population; a single parameter description of the population. However, by using ALMA data, to go deeper than is possible with Herschel data alone, we already have shown in our pilot study (Mullaney et al., 2015) that the linear mean is consistently higher than the mode (the most common value). A linear mean of two samples can be consistent, while their distributions can be inconsistent. In that study we showed that X-ray AGN have consistent mean sSFRs but inconsistent distributions compared to main sequence galaxies. Therefore in order to adequately describe the unique star-forming properties of a population, we must constrain the parameters (the mode and the width) of the distributions of SFR or sSFR. These values are much more powerful, than a simple linear mean, to compare between different samples and to rigorously test model predictions, see §3.4.2.

The aim of this paper is to use sensitive ALMA observations of X-ray AGN at $z > 1.5$, in conjunction with *Spitzer–Herschel* photometry, to address the challenges outlined above and answer the question: what impact do luminous AGN have on star formation? The significantly improved sensitivity and spatial resolution that ALMA provides over *Herschel* allows for the detection of star forming emission from galaxies at $z > 1.5$ up to an order of magnitude below the equivalent sensitivity of *Herschel* (see Mullaney et al. 2015; Stanley et al, in prep). In an earlier study (Mullaney et al., 2015), we presented the first ALMA constraints on the SFRs of X-ray AGNs at $z > 1.5$ and showed that, while the mean SFRs were consistent with those of co-eval star-forming galaxies, the SFR distributions had a significantly lower mode and a broader spread of values. In this paper we expand on the Mullaney et al. (2015) study with additional ALMA observations of X-ray AGN to increase the overall source statistics, particularly at the high luminosity end (i.e., $L_X > 10^{44}$ erg s^{-1}). We also make a quantitative comparison of our results to those from a leading set of hydrodynamical cosmological simulations (EAGLE; Evolution and Assembly of GaLaxies and their Environments; Schaye et al., 2015).

In §2 we describe the data and the basic analyses used in our study, in §3 we present our main results, including a comparison to EAGLE, in §4 we discuss our results within

the broader context of the impact of AGN on the star forming properties of galaxies, and in §5 we draw our conclusions. We also provide in the appendix the ALMA 870μm photometry for all of the X-ray sources that were either targetted in our ALMA programmes or serendipitously lay within the ALMA field of view. In all of our analyses we adopt the cosmological parameters of $H_0 = 71$ km s^{-1}, $\Omega_M = 0.27$, $\Omega_\Lambda = 0.73$ and assume a Chabrier (2003) initial mass function (IMF).

3.2 Data and basic analyses

In this section we describe the main sample of X-ray AGN used in our analyses, along with the calculation of the key properties (stellar masses, SFR and sSFR) and associated errors (see §3.2.1), our approach in measuring the properties of the (s)SFR distributions (see §3.2.2), and the EAGLE hydrodynamical cosmological simulations used to help interpret our results (see §3.2.3).

3.2.1 Main sample: definition and properties

The prime objective of our study is to constrain the star forming properties of X-ray AGN to search for the signature of AGN feedback. To achieve this we 1) need to select AGN over the redshift and luminosity ranges where AGN feedback is thought to be important and 2) require sensitive star formation and stellar-mass measurements. On the basis of the first requirement our main sample is defined with the following criteria:

1. rest-frame 2–10 keV luminosity of $L_X = 10^{43} - 10^{45}$ erg s^{-1},
2. redshift of $z = 1.5 - 3.2$, and
3. stellar mass of $M_* > 2 \times 10^{10}$ M$_\odot$.

The redshift and X-ray luminosity ranges ensure that we include AGN that 1) are most likely to drive energetic outflows (Harrison et al., 2016b), and consequently have direct impact on the star formation in the host galaxies and 2) contribute to the majority of the cosmic black-hole and galaxy growth (Madau & Dickinson, 2014; Brandt & Alexander, 2015). The stellar-mass cut is required since probing the star forming properties below

the main sequence for individual systems with $M_* < 2 \times 10^{10}$ M$_\odot$ requires deeper IR data than is currently available. Furthermore, the cosmological simulations predict that the impact of AGN feedback is most significant in more massive galaxies (e.g. Bower et al., 2017; McAlpine et al., 2017).

Given these criteria, we selected X-ray AGN from the *Chandra* Deep Field-South (CDF-S) and the central regions of Cosmic Evolution Survey (COSMOS), which have the deepest multi-wavelength ancillary data available in the well-observed CANDELS (Cosmic Assembly Near-infrared Deep Extragalactic Legacy Survey) sub regions (Grogin et al., 2011; Koekemoer et al., 2011). For the CDF-S field we selected X-ray AGN at $z = 1.5$–3.2 with $L_{\rm X} = 10^{43} - 10^{44}$ erg s^{-1} from the 4 Ms *Chandra* catalogues of Xue et al. (2011) and Hsu et al. (2014). For the COSMOS field we primarily selected X-ray AGN with $L_{\rm X} = 10^{44} - 10^{45}$ erg s^{-1} from the central $12'.5$-radius region using the *Chandra* catalogues of Civano et al. (2016) and Marchesi et al. (2016); however, to ensure a sufficient number of AGN at $z = 1.5$–3.2 with $L_{\rm X} = (0.3-1) \times 10^{45}$ erg s^{-1} we expanded the selection of the most luminous AGN to the central $25'$-radius region of COSMOS. Stellar mass and star formation measurements (augmented by our sensitive ALMA observations; see appendix) were obtained for all of the X-ray AGN that met these criteria and the systems with $M_* < 2 \times 10^{10}$ M$_\odot$ were removed; see §3.2.1 and §5.4.1 for details of the stellar-mass and star-formation measurement procedures.

Overall our main sample includes 81 X-ray AGN. In Figure 4.1 we plot the X-ray luminosity versus redshift of the overall X-ray source population in the CDF-S and COSMOS fields and highlight the z–$L_{\rm X}$ parameter space explored by our main sample. The properties of the individual X-ray AGN in the main sample are presented in Tables 3.1 and 3.2. Of the 81 X-ray AGN, 63 ($\approx 78\%$) have SFR measurements or upper limits augmented by ALMA observations. To search for trends in the star forming properties of X-ray AGN as a function of key properties, we also defined subsamples based on X-ray luminosity and stellar mass: low $L_{\rm X}$ ($10^{43} - 10^{44}$ erg s^{-1}; 39 X-ray AGN), high $L_{\rm X}$ ($10^{44} - 10^{45}$ erg s^{-1}; 42 X-ray AGN), low mass ($2 \times 10^{10} - 8 \times 10^{10}$ M$_\odot$; 41 X-ray AGN), and high mass ($8 \times 10^{10} - 1 \times 10^{12}$ M$_\odot$; 40 X-ray AGN). We note that the mean and median redshifts of the $L_{\rm X}$ and stellar mass subsamples are well matched: $\delta z = 0.1$ for the $L_{\rm X}$ subsamples and $\delta z = 0.05$ for the stellar mass subsamples.

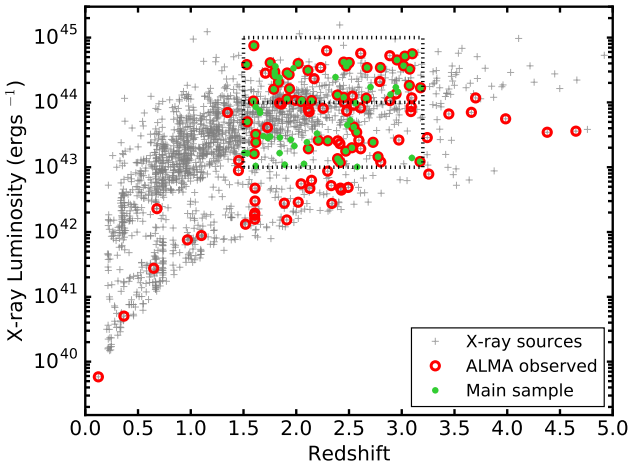

Figure 3.1: X-ray luminosity (2-10 keV: rest frame) versus redshift for the X-ray sources in the CDF-S and COSMOS fields. The X-ray sources that lie within our ALMA observations are indicated as red circles (see appendix). The X-ray AGN used in our star formation analyses, which comprise our main sample, are further highlighted with green filled circles (see §2.1); the dotted square indicates the region of the X-ray luminosity–redshift plane used in our main analyses. Not all of the objects in the dotted square are selected for our main sample since many lie below our stellar mass threshold.

Stellar mass measurements

The stellar masses of the X-ray AGN were calculated by performing SED fitting on the broad-band UV-MIR photometry (0.1–24 μm) from archival catalogs in the CDF-S and COSMOS fields. For the sources in the CDF-S field, we used the multi-wavelength catalogue of Guo et al. (2013), which covers the CANDELS GOODS-S Deep+Wide+ERS area. A fraction ($\approx 33\%$) of our targets lie outside the CANDELS footprint; for these, we included photometry from the MUSYC ECDFS catalog of Cardamone et al. (2010). For the sources in the COSMOS field, we used the multi-wavelength catalogue of Laigle et al. (2016). Catalogue-specific procedures were used to convert tabulated aperture photometry to zero-point corrected total photometry. In both fields, we used *Spitzer* MIPS 24 μm photometry from Le Floc'h et al. (2009) and the PEP survey (Lutz et al., 2011) to extend the SEDs into the observed MIR.

We modelled the broad-band SEDs of the X-ray AGN using the CIGALE package (v0.8.1, Burgarella et al., 2005; Ciesla et al., 2015). The SEDs were fitted using combinations of stellar and AGN emission templates. The population synthesis models of Bruzual & Charlot (2003) represented the stellar emission, to which dust extinction was applied

following the power-law prescription of Charlot & Fall (2000). The AGN emission was modelled on the library of Fritz et al. (2006), which takes a fixed shape power-law SED representing an accretion disc, and geometry-dependent dust emission from a smooth AGN torus. After an examination of the entire Fritz et al. (2006) library, we adopted a subset of the AGN templates (described below) that reproduce empirical AGN IR SEDs (e.g.; Mullaney et al., 2011; Mor & Netzer, 2012). We fixed the power-law indices that describe the radial and polar dust density distribution in the torus to 0.0 and 6.0, implying a uniform density torus that has a sharp gradient with elevation. We assumed a single value of 150.0 for the ratio between the outer radius and inner (sublimation) radius of the torus, and allowed for three values of the 9.7 μm Si optical depth (0.1, 1.0, 3.0). We allowed for the full range in torus inclination angles with respect to the line of sight and set the normalisation of the torus models to run through the MIPS 24 μm photometric point.

From the posterior distributions of stellar mass for each galaxy computed using CIGALE, we calculated the median stellar mass and the 16^{th} and 84^{th} percentile values as a measure of the uncertainty on the stellar mass; see Tables 1 & 2.

Star-formation measurements

The star forming properties of the X-ray AGN were calculated from *Spitzer*-IRAC 8μm, *Spitzer*-IRS 16μm, *Spitzer*-MIPS 24μm, deblended *Herschel*-PACS (70, 100, 160 μm), deblended *Herschel*-SPIRE (250, 350, 500 μm) and our ALMA photometry (870μm, see appendix for more details). The *Spitzer* and *Herschel* photometry were taken from the same catalogues as for our earlier Stanley et al. (2015) study: the *Spitzer* IRAC and IRS data is from Sanders et al. (2007), Damen et al. (2011) and Teplitz et al. (2011) for the CDF-S, COSMOS, and GOODS-S fields, respectively. The deblended photometry consists of the MIPS 24μm and the PACS bands from Magnelli et al. (2013)[2] and SPIRE photometry from Swinbank et al. (2014). For the objects that were undetected in the *Spitzer* and *Herschel* maps, we calculated 3σ upper limits.

We used SED decomposition techniques to separate the AGN and star-forming com-

[2]Magnelli et al. (2013) published the PACS catalogues for GOODS-S. The catalogue for the COSMOS field was created using the same method and is available to download at http://www.mpe.mpg.de/ir/Research/PEP/DR1.

ponents from the total IR SED. The full SED fitting procedure is presented in Stanley et al. (2018); however, we provide brief details here and note that we used a slightly modified approach to obtain the final SFR values and errors for application in our sSFR distribution fitting (see §3.2.2). The SED fitting procedure is based on Stanley et al. (2015), which fitted AGN and star forming templates to *Spitzer* and *Herschel* photometry but is updated to include ALMA continuum measurements. The AGN and 5 of the 6 star forming templates are from Mullaney et al. (2011) but extrapolated to $3-1000\mu$m by Del Moro et al. (2013), while a 6^{th} star forming template is the Arp220 galaxy template from Silva et al. (1998), which represents an extremely dusty star forming galaxy. The photometric measurements, uncertainties, and upper limits were taken into account when fitting the IR SEDs. Two sets of best-fitting SED solutions were calculated for each X-ray AGN, giving 12 best-fitting SED solutions overall: one set using each of the 6 star forming templates and the other set using the 6 star forming templates plus the AGN template. To determine whether the fit requires an AGN component or not, we used the Bayesian Information Criteria (BIC; Schwarz, 1978) [3] which allows for an objective comparison between non-nested models with a fixed data set. To establish if the fit of the source requires an AGN component, the SED with the AGN component has to have a smaller BIC than that of the SED with no AGN component with a difference of ΔBIC>2 (for more information and examples see §3 of Stanley et al. 2018). This way we obtain 6 SED solutions. I present the final SED in the Appendix of this chapter.

We integrated each star forming template from each of the 6 SED solutions to estimate the total IR luminosities due to star formation for that SED solution ($L_{IR,SF,Sol}$). Using this procedure we obtained 6 different values of $L_{IR,SF,Sol}$ and their errors from the fitting routine. The final value of the IR luminosity due to star formation ($L_{IR,SF}$) and its error is calculated using the Bootstrap method. To each value of $L_{IR,SF,Sol}$ we assigned a probability P(χ^2) (in the shape of the χ^2 distribution) that it is the true value of $L_{IR,SF}$. Then we picked a $L_{IR,SF,Sol}$ based on its P(χ^2) and drew a value of $L_{IR,SF}$ from a normal distribution

[3]The Bayesian Information Criterion (Schwarz, 1978) is a criterion used to choose a model from a finite number of models. It uses $\Delta\chi^2$ but also takes into the account the number of free parameters, by penalising the fit for more free parameters. BIC is defined as BIC=$\Delta\chi^2 + k\log(N)$, where N is the number of data points and k is the number of free parameters. Unlike χ^2, the BIC can more reliably distinguish between models with different number of free parameters.

with the mean and width as the best value and error returned from $L_{IR,SF,Sol}$. We repeated this procedure 10^5 times to build a distribution of all possible values of $L_{IR,SF}$. The created distribution was dominated by the template with the least χ^2 value, but it also took into consideration other template solutions. For the upper limit calculations, we selected an SED solution with the highest value of $L_{IR,SF,Sol}$.

We converted $L_{IR,SF}$ to SFR using Equation 4 from Kennicutt (1998) corrected to the Chabrier (2003) IMF. In order to calculate the sSFR we also created a distribution of stellar masses for each object by drawing 10^5 times from the normal distribution with the mean and width as the best value and error returned from CIGALE (see §3.2.1). We then calculated the sSFR by dividing draws of SFR by the draws of stellar mass. We calculated the final (and adopted) values of the SFR and sSFR and their errors as the median and standard deviation of the 10^5 SFR and sSFR values, respectively; see Tables 1 & 2.

3.2.2 Measuring the star-formation distributions

The majority of previous studies have explored the mean SFRs and sSFRs of X-ray AGN. However, the mean is sensitive to bright outliers and can hide subtle trends in the data. A more comprehensive approach to characterising the star forming properties of X-ray AGN, is the measurement of the *distributions* of SFRs and sSFRs. In our analyses here we fitted the SFR and sSFR distributions of the X-ray AGN assuming a log-normal function:

$$N(x) \propto \exp\left(-\frac{\log_{10}\left(\frac{x}{\mu}\right)^2}{2w^2}\right), \tag{3.2.1}$$

where x is the SFR or sSFR, μ is the mode, and w is the width of the distribution. The motivation for fitting a log-normal function is: 1) the SFR and sSFR values for main-sequence galaxies broadly follow this distribution (e.g. Schreiber et al., 2015), and 2) the SFR and sSFR distributions of the AGN in the EAGLE simulations are consistent with a log-normal function, as we demonstrate in §3.3.1. Also, our source statistics are not high enough to fit a more complex model with more parameters. However, even if the log-normal distribution is not absolutely correct, it allows us to broadly characterise the typical values and range in values to search for trends and compare to the different models

Table 3.1: X-ray selected AGN in the main sample from the CDF-S field. The columns show the X-ray ID, optical position, redshift (2 and 3 decimal places indicate photometric and spectroscopic redshifts, respectively), X-ray luminosity (rest-frame 2-10 keV) (all from Hsu et al., 2014), the estimated SFR from our IR SED fitting (see §5.4.1, the estimated stellar mass from our UV–MIR SED fitting (see §3.2.1), and a flag to indicate whether the X-ray AGN was observed with ALMA (see Table A1).

X-ray ID	RA (J2000)	Dec (J2000)	Redshift	$\log_{10}$ ($L_{2-10keV}$/erg s^{-1})	$\log_{10}$ ($SFR/M_{\odot}yr^{-1}$)	$\log_{10}$ ($M_*/M_{\odot}$)	Observed with ALMA?
88	53.01025	−27.76681	1.616	43.5	2.30 ± 0.04	10.99 ± 0.19	yes
93	53.01271	−27.74731	2.573	43.5	< 1.81	10.97 ± 0.21	yes
111	53.02229	−27.77890	2.51	43.7	1.83 ± 0.04	11.28 ± 0.23	no
117	53.02548	−27.82436	1.69	43.5	1.83 ± 0.16	10.97 ± 0.15	no
142	53.03637	−27.66547	1.54	43.2	1.69 ± 0.18	10.84 ± 0.21	no
166	53.04548	−27.73749	1.615	43.9	2.27 ± 0.02	10.46 ± 0.17	no
176	53.04905	−27.77449	1.51	43.2	2.03 ± 0.04	10.35 ± 0.15	no
188	53.05392	−27.87690	2.562	44.0	< 1.81	10.49 ± 0.21	no
199	53.05791	−27.83357	2.42	43.1	< 2.25	11.40 ± 0.16	yes
211	53.06195	−27.85111	1.60	43.2	1.71 ± 0.17	10.71 ± 0.15	yes
213	53.06240	−27.70691	1.891	43.0	< 2.20	11.79 ± 0.16	no
215	53.06331	−27.69971	2.402	43.1	< 1.68	10.86 ± 0.23	yes
222	53.06595	−27.70185	2.07	43.1	< 1.69	11.10 ± 0.23	no
240	53.07128	−27.69358	2.20	43.5	< 2.21	10.81 ± 0.22	no
257	53.07645	−27.84873	1.536	43.7	< 2.07	11.17 ± 0.23	yes
277	53.08318	−27.71205	2.21	43.4	< 2.20	10.45 ± 0.23	yes
290	53.08738	−27.92962	2.54	43.6	< 1.49	11.04 ± 0.24	yes
301	53.09235	−27.80322	2.47	43.2	< 2.41	10.92 ± 0.22	yes
310	53.09408	−27.80419	2.39	43.1	< 1.64	10.68 ± 0.23	yes
344	53.10491	−27.70528	1.617	43.4	< 1.76	11.22 ± 0.15	yes
359	53.10816	−27.75405	2.728	43.4	1.84 ± 0.07	10.56 ± 0.18	yes
369	53.11110	−27.67038	1.658	43.8	1.65 ± 0.08	10.49 ± 0.22	no
410	53.12414	−27.89127	2.53	43.3	2.24 ± 0.12	11.13 ± 0.17	yes
440	53.13244	−27.95390	2.10	43.4	< 2.10	10.68 ± 0.20	no
443	53.13366	−27.69865	1.982	43.3	< 1.85	10.83 ± 0.20	no
450	53.13639	−27.86421	1.95	43.4	< 1.92	11.24 ± 0.17	no
456	53.13805	−27.86831	3.17	43.1	< 1.84	10.68 ± 0.23	yes
466	53.14169	−27.81662	2.78	43.2	< 1.87	10.73 ± 0.19	yes
486	53.14670	−27.88834	1.84	43.5	2.19 ± 0.03	10.41 ± 0.21	no
490	53.14883	−27.82112	2.578	43.0	< 1.77	11.24 ± 0.24	no
522	53.15850	−27.77403	2.12	43.3	< 1.83	10.38 ± 0.24	yes
524	53.15959	−27.93142	3.10	43.1	2.69 ± 0.04	11.49 ± 0.21	no
549	53.16557	−27.76979	1.754	43.5	< 2.54	10.81 ± 0.22	no
575	53.17935	−27.81251	1.730	43.4	< 2.03	10.75 ± 0.18	no
620	53.19608	−27.89264	2.48	43.7	< 1.72	10.86 ± 0.20	no
625	53.19886	−27.84391	1.615	43.0	< 2.20	11.06 ± 0.18	no
633	53.20492	−27.91801	2.30	43.4	2.15 ± 0.02	10.59 ± 0.20	yes
663	53.22878	−27.75165	1.84	43.2	< 1.85	11.21 ± 0.24	no
683	53.24718	−27.81631	1.65	43.9	< 2.13	11.35 ± 0.18	no

Table 3.2: X-ray selected AGN in our main sample from the COSMOS field. The columns show the X-ray ID, optical position, redshift (2 and 3 decimal places indicate photometric and spectroscopic redshifts, respectively), X-ray luminosity (rest-frame 2-10 keV) (all from Marchesi et al., 2016), SFR from our IR SED fitting (see §5.4.1), stellar mass from our UV–MIR SED fitting (see §3.2.1), and a flag to indicate whether the X-ray AGN was observed with ALMA (see Table A2).

X-ray ID	RA (J2000)	Dec (J2000)	Redshift	$\log_{10}$ ($L_{2-10keV}$/erg s^{-1})	$\log_{10}$ (SFR/$M_\odot$yr^{-1})	$\log_{10}$ ($M_*/M_\odot$)	Observed with ALMA?
cid 434	149.72072	2.34901	1.530	44.6	< 1.63	11.70 ± 0.18	yes
cid 580	149.85469	2.60694	2.11	44.5	< 1.81	11.13 ± 0.22	yes
cid 558	149.88252	2.50513	3.10	44.8	1.53 ± 0.18	11.42 ± 0.21	yes
cid 330	149.95583	2.02806	1.753	44.6	< 1.65	10.72 ± 0.26	yes
cid 2177	149.96660	2.43247	2.89	44.1	1.63 ± 0.07	11.20 ± 0.23	no
cid 529	149.98158	2.31501	3.017	44.6	< 1.80	11.43 ± 0.20	yes
cid 474	149.99390	2.30146	1.796	44.5	1.11 ± 0.27	10.38 ± 0.20	yes
cid 451	150.00253	2.25863	2.450	44.6	1.14 ± 0.19	11.19 ± 0.19	yes
cid 1127	150.01057	2.26939	2.390	44.1	< 1.49	11.02 ± 0.19	yes
cid 532	150.01985	2.34914	1.796	44.4	< 1.82	11.49 ± 0.23	yes
cid 1216	150.02008	2.35365	2.663	44.1	< 1.86	10.69 ± 0.20	yes
cid 659	150.03290	2.45859	2.045	44.0	1.29 ± 0.12	10.89 ± 0.19	yes
cid 1214	150.03677	2.35852	1.59	44.0	< 1.62	10.97 ± 0.21	yes
cid 351	150.04262	2.06329	2.018	44.6	< 1.62	11.15 ± 0.15	yes
cid 443	150.04597	2.20114	2.704	44.2	< 1.81	10.95 ± 0.18	no
cid 458	150.05524	2.14317	1.974	44.5	1.27 ± 0.18	10.83 ± 0.25	no
cid 352	150.05891	2.01518	2.498	44.6	1.41 ± 0.04	10.83 ± 0.23	yes
cid 1215	150.06454	2.32905	2.450	44.1	< 1.46	11.00 ± 0.24	yes
cid 72	150.09154	2.39908	2.475	44.6	< 1.85	10.99 ± 0.22	yes
cid 466	150.10094	2.16782	2.055	44.0	< 1.44	10.75 ± 0.17	no
cid 149	150.10371	2.66577	2.955	44.7	< 1.83	11.06 ± 0.27	yes
cid 1144	150.10477	2.24364	1.912	44.1	< 1.64	10.86 ± 0.24	yes
cid 86	150.11958	2.29591	1.831	44.3	< 1.46	11.40 ± 0.18	yes
cid 87	150.13304	2.30328	1.598	44.9	1.53 ± 0.18	11.52 ± 0.22	yes
cid 965	150.15218	2.30785	3.178	44.2	1.41 ± 0.19	10.83 ± 0.17	yes
cid 914	150.18001	2.23128	2.146	44.0	1.60 ± 0.18	10.90 ± 0.17	yes
cid 124	150.20532	2.50293	3.07	44.3	< 1.80	10.79 ± 0.16	yes
cid 83	150.21416	2.47502	3.075	44.5	< 1.83	11.21 ± 0.20	yes
cid 21	150.21466	2.20428	1.841	44.4	1.50 ± 0.22	10.41 ± 0.30	no
cid 23	150.22403	2.27080	2.944	44.2	1.26 ± 0.24	11.88 ± 0.19	no
cid 127	150.22702	2.53761	1.801	44.4	2.08 ± 0.08	11.12 ± 0.23	no
cid 954	150.23180	2.36401	1.936	44.2	< 1.83	10.64 ± 0.30	yes
cid 970	150.23550	2.36176	2.501	44.6	< 2.20	11.30 ± 0.17	yes
cid 75	150.24779	2.44215	3.029	44.7	2.73 ± 0.05	10.87 ± 0.20	yes
cid 725	150.27097	2.36507	2.962	44.2	< 2.42	10.73 ± 0.16	no
cid 89	150.28117	2.41590	2.372	44.4	2.69 ± 0.05	10.69 ± 0.22	no
cid 90	150.28482	2.39505	1.932	44.4	< 2.11	11.29 ± 0.25	yes
cid 365	150.28563	2.01459	2.671	44.5	< 2.55	10.62 ± 0.20	yes
cid 94	150.30956	2.39915	1.802	44.6	< 2.26	11.01 ± 0.18	no
cid 58	150.32689	2.09415	2.798	44.5	< 2.41	11.89 ± 0.23	yes
cid 53	150.34372	2.14067	1.787	44.2	2.48 ± 0.06	11.09 ± 0.20	yes
cid 62	150.37364	2.11203	1.914	44.5	< 2.48	10.51 ± 0.30	yes

(see §3.4.2).

The majority (≈ 65 %) of the X-ray AGN in our main sample are undetected by both *Herschel* and ALMA and therefore only have a SFR upper limit. The SFR and sSFR distributions cannot be obtained trivially without the appropriate consideration of these limits. Following Mullaney et al. (2015), we use a hierarchical Bayesian method to find the best fitting parameters to sample the probability distribution (PD) of our parameters μ and w, using Gibbs sampling and Metropolis–Hastings Markov Chain [4] Monte Carlo (MCMC) algorithms. There are several advantages of this method: 1) the uncertainties and upper limits can be taken into account, and 2) the PD produced in this way can be used to estimate errors on μ and w. The fitting routine treats upper limits and detections differently, but in a statistically consistent way. For a detection, we assumed that the likelihood function of the errors has a log-normal shape, while for the upper limits we assumed that the likelihood function is in the form of a log-error function. The final values and errors of the mode μ and width w are taken to be the median values of the PD and the 68% confidence interval, respectively. As was done in Mullaney et al. (2015), we assume uniform, uninformative priors on μ and w which do not influence the final PDs. We quote the final values of our fits to the sSFR distributions for the main sample (see §3.3.1) in Table 3.3.

In Figure 3.2 we demonstrate our model fitting approach by showing the fits to the SFR distributions of X-ray AGN at $z = 1.5$–2.5. We selected this example to test whether our method gives results that are consistent with our earlier work (Stanley et al., 2015), which used the same SED fitting procedure as that adopted here but was based on linear means; however, since this paper selected X-ray AGN at $z = 1.5 - 2.5$ without a stellar mass cut, for this test we added back into the sample X-ray AGN with $M_* < 2 \times 10^{10}$ $M_\odot$. To make

[4]The Metropolis–Hastings algorithm works by generating a series of values that, if long enough, starts to closely approximates the desired distribution, in our case, the posterior distribution of the fitting values. The series of values is produced using an iterative method, at each iteration the algorithm picks a new values based on the value of the current sample value. Given the probability calculated from prior distribution, the new value is either accepted into the series or rejected and the current value is reused instead. The Gibbs sampling is modification of the Metropolis-Hastings algorithm that allows easier sampling of multi-dimensional distribution.

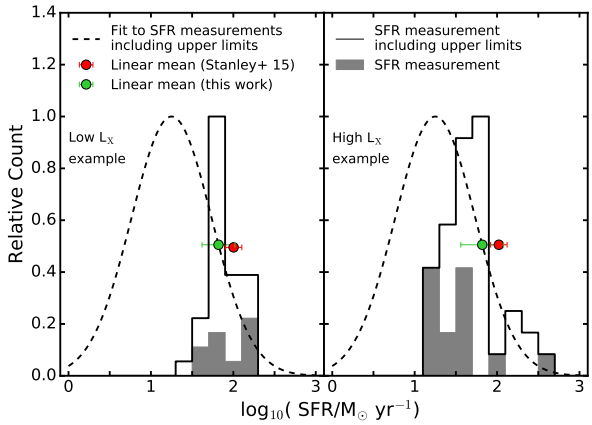

Figure 3.2: Example SFR distributions to demonstrate our model-fitting approach; see §2.2. The X-ray AGN lie at $z = 1.5$–2.5 and have $L_X = 10^{43} - 10^{44}$ erg s^{-1} (left panel) and $L_X = 10^{44} - 10^{45}$ erg s^{-1} (right panel). The filled grey histogram indicates the distribution of SFR measurements and the unfilled histogram indicates the distribution of SFR measurements including upper limits. The dashed curve indicates the best-fitting log-normal distribution to the measured SFRs including upper limits (see §3.2.2) and the filled green circle indicates the mean SFR calculated from the best-fitting distribution. The filled red circle indicates the mean SFR from Stanley et al. (2015) for a larger sample of X-ray AGN at z =1.5–2.5 in the same L_X range but with SFR constraints from *Spitzer* and *Herschel* data. The error bars represent the 68% confidence interval for each of the measurements.

the comparison, we calculated the linear mean ($\langle x \rangle$) of our log-normal distribution as:

$$\langle x \rangle = 10^{(\mu + 1.15w^2)}, \tag{3.2.2}$$

where μ is the mode and w is the width of the distribution as in Equation 3.2.1. The linear mean was calculated from the PD of μ and w from our MCMC analysis, from which the median and 68% confidence interval were derived.

The $\log_{10}(\langle \mathrm{SFR} \rangle \ / \ \mathrm{M_{\odot}yr^{-1}})$ of our low and high L_{X} subsamples were $1.94^{+0.33}_{-0.20}$ and $1.8^{+0.22}_{-0.15}$, respectively, as compared to 2.00 ± 0.10 and 2.02 ± 0.10 from Stanley et al. (2015). As such, our estimates are in good agreement with those of Stanley et al. (2015) and confirms that our new method is consistent with previous work. In comparison, the $\log_{10}(\mu / \ \mathrm{M_{\odot}yr^{-1}})$ of the SFR distribution for low and high L_{X} subsamples are $1.27^{+0.31}_{-0.22}$ and $1.12^{+0.15}_{-0.19}$, respectively. The linear mean of the SFR is always higher (depending on the width of the distribution) than the mode of the distribution, making the mode of the distribution a more reliable tracer of the typical values of the population.

3.2.3 EAGLE hydrodynamical simulation and source properties

Cosmological simulations of galaxy formation have provided some evidence that AGN feedback has a significant effect on star formation in the galaxy population. To aid in the interpretation of our data we have therefore compared the sSFR distributions of the X-ray AGN in our main sample to those computed from the EAGLE cosmological hydrodynamical simulation (Crain et al., 2015; Schaye et al., 2015). A key advantage of our approach is that we can compare our results to models from the cosmological simulations both with and without AGN feedback included, to allow us to identify the signature of AGN feedback on the star forming properties of galaxies (also see e.g. Beckmann et al., 2017; Harrison, 2017).

EAGLE is a suite of cosmological hydrodynamical simulations, which uses an enhanced version of the GADGET-3 code (Springel, 2005) which consists of a modified hydrodynamics solver, time-step limiter, and employs a subgrid treatment of baryonic physics. The subgrid physics takes into account of the stellar-mass loss, element-by-element radiative cooling, star formation, black-hole accretion (i.e., AGN activity), and

Table 3.3: Best fitting log-normal fit parameters for the sSFR distributions of our main sample and sample from EAGLE simulations binned by X-ray luminosity and stellar mass. The quoted μ and w and their errors are the median of the their posterior probability distributions (PDs) and 68% confidence intervals. The linear mean is calculated from μ and w using equation 3.2.2.

Sample	Mode (μ) $\log_{10}(\mu/\mathrm{Gyr}^{-1})$	Width(w) (dex)	linear mean $\log_{10}(\langle \mathrm{sSFR} \rangle/\mathrm{Gyr}^{-1})$
Main Sample (Observed AGN):			
Low L_x AGN	$0.03^{+0.14}_{-0.17}$	$0.52^{+0.13}_{-0.10}$	$0.34^{+0.18}_{-0.15}$
High L_x AGN	$-0.32^{+0.15}_{-0.17}$	$0.65^{+0.15}_{-0.11}$	$0.17^{+0.26}_{-0.19}$
Low Mass AGN	$-0.01^{+0.13}_{-0.15}$	$0.53^{+0.13}_{-0.08}$	$0.31^{+0.16}_{-0.14}$
High Mass AGN	$-0.48^{+0.17}_{-0.20}$	$0.67^{+0.18}_{-0.12}$	$0.05^{+0.29}_{-0.22}$
EAGLE ref model:			
Low L_x AGN	$-0.08^{+0.05}_{-0.04}$	$0.45^{+0.06}_{-0.06}$	$0.14^{+0.08}_{-0.1}$
High L_x AGN	$0.14^{+0.05}_{-0.04}$	$0.45^{+0.05}_{-0.04}$	$0.38^{+0.08}_{-0.07}$
Low Mass AGN	$0.04^{+0.02}_{-0.02}$	$0.47^{+0.02}_{-0.02}$	$0.23^{+0.03}_{-0.03}$
High Mass AGN	$-0.23^{+0.07}_{-0.07}$	$0.42^{+0.05}_{-0.05}$	$-0.03^{+0.09}_{-0.07}$
Low Mass galaxy	$-0.14^{+0.02}_{-0.02}$	$0.48^{+0.02}_{-0.02}$	$0.22^{+0.02}_{-0.02}$
High Mass galaxy	$-0.31^{+0.02}_{-0.02}$	$0.45^{+0.02}_{-0.02}$	$-0.15^{+0.02}_{-0.02}$
EAGLE no AGN model:			
Low Mass galaxy	$0.13^{+0.01}_{-0.01}$	$0.23^{+0.01}_{-0.01}$	$0.20^{+0.02}_{-0.02}$
High Mass galaxy	$-0.10^{+0.01}_{-0.01}$	$0.28^{+0.01}_{-0.01}$	$0.0^{+0.02}_{-0.02}$

star formation and AGN feedback. The free parameters of the subgrid physics were calibrated on the stellar mass function, galaxy size, and the black-hole–spheroid relationships at $z \approx 0.1$ (Crain et al., 2015; Schaye et al., 2015). The simulation is able to reproduce a wide range of observations of low and high redshift galaxies (e.g., fraction of passive galaxies, Tully-Fisher relation, evolving galaxy stellar mass function, galaxy colours and the relationship between black hole accretion rates and SFRs; see e.g. Furlong et al., 2015; Schaye et al., 2015; McAlpine et al., 2017; Trayford et al., 2017). We stress that since the EAGLE model was not directly calibrated on the SFR or sSFR of galaxies, our comparison will be an independent test of the EAGLE model.

In the context of this work, it is necessary to further describe the part of subgrid physics that is dealing with SMBH growth and its feedback to the host galaxy. SMBH seeding in EAGLE follows the prescription described in Springel et al. (2005), where the SMBH are dropped as collisionless sink particle in the centre of dark matter halo with mass $> 1.475 \times 10^{10} M_{\odot}$, which do not already contain one. These seeds then growth via mass accretion modified Bondi-Hoyle formalism introduced in Rosas-Guevara et al. (2015), capped at the Eddington limit or SMBH merger during a galaxy merger. AGN feedback is implemented as a single mode, where the energy from the mass accretion is thermally and stochastically injected into the ISM of the galaxy as described in Booth & Schaye (2009). Feedback is performed assuming a single efficiency, independent of halo mass and accretion rate.

In our analyses we have used two models from EAGLE: the reference model (hereafter EAGLE ref), designed to reproduce a variety of key observational properties (see above), and a model with no AGN feedback (hereafter EAGLE noAGN). The EAGLE noAGN model is identical to the EAGLE ref model in all aspects except black holes are not seeded, which effectively turns off the AGN feedback. A comparison of the results between these two models therefore allows for the identification of the signature of AGN feedback on the star forming properties of the simulated galaxies. The EAGLE ref model was run at volumes of 25^3, 50^3, and 100^3 cubic comoving megaparsecs (cMpc^3) with time steps of $\sim 40 - 60$Myr. We present here the results from the largest volume which contains the largest number of rare high-mass systems; however, we note that we performed our analysis on all volumes and found no significant differences in the overall results. The

Table 3.4: Basic properties of the EAGLE models used in the paper. From left to right: the model name used in the text, the reference name in the EAGLE database, the comoving volume (cMpc^3), the initial mass m_g of the baryonic particles, and a flag to indicate whether AGN feedback was adopted in the model. See Schaye et al. (2015) for more information.

Model name in text	Database Reference	Volume (cMpc^3)	m_g ($M_\odot$)	AGN feedback?
EAGLE ref	RefL0100N1504	100^3	1.81×10^6	Yes
EAGLE no AGN	NoAGNL0050N0752	50^3	1.81×10^6	No

EAGLE noAGN model was only performed at a volume of 50^3 cubic comoving megaparsecs. A summary of the two different EAGLE models used in our analyses are given in Table 3.4.

To construct the AGN and galaxy catalogues from the EAGLE models we queried the public database [5] (McAlpine et al., 2016) for any dark matter halo with a galaxy of stellar mass of $M_* > 2 \times 10^{10}$ $M_\odot$, for redshift snapshots over $z = 1.4$–3.6; the slightly broader redshift range than that adopted for our main sample ensures that the AGN and galaxy samples from EAGLE have the same mean and median redshift as our main sample. We then applied the same stellar mass and AGN luminosity cuts to the EAGLE sample as we used to select our main sample. To calculate the properties of the simulated AGN and galaxies, to allow for a systematic comparison to our main sample, we also: 1) converted the black-hole accretion rates from the EAGLE ref model to L_X by converting them first to AGN bolometric luminosities (assuming a nominal radiative efficiency of $\epsilon = 10\%$) and then converting to L_X by multiplying it by a bolometric correction factor of 0.1 (McAlpine et al., 2017) and 2) scaled up the SFRs calculated in both EAGLE models by 0.2 dex to account for the offset found by Furlong et al. (2015) (see also §2.4 of McAlpine et al. 2017) from comparing the global SFR density of the EAGLE ref model to the observed global SFR density of galaxies. In total we found 472 AGN and 2333 galaxies in the EAGLE ref model and 682 galaxies in the EAGLE noAGN model with the same properties as in our main sample.

During the selection of the galaxies and AGN from the EAGLE simulation we used

[5] Available at http://icc.dur.ac.uk/Eagle/database.php

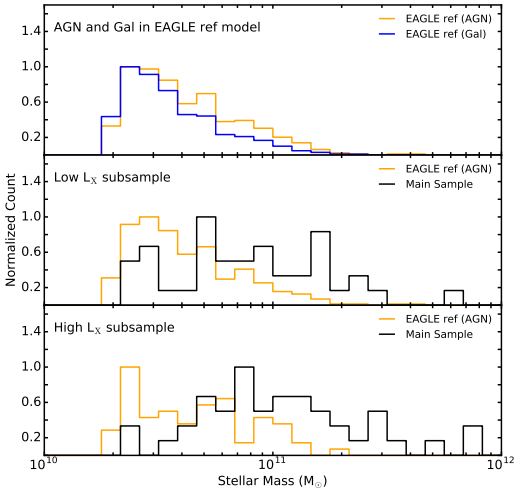

Figure 3.3: Comparison of the normalized stellar mass distributions from our different samples. Top panel: Comparison of the stellar mass distributions of the AGN in the EAGLE ref model (blue line) and galaxies in the EAGLE ref model (orange line). Middle Panel: Comparison of the stellar mass distribution of the low L_X AGN in the EAGLE ref model (orange line) and the low L_X AGN of the observed main sample (black line). Bottom panel: Comparison of the stellar mass distribution of the high L_X AGN in the EAGLE ref model (orange line) with the high L_X AGN of the main sample (black line). We take the differences in stellar mass distributions into consideration in §3.3.2.

7 snapshots between the $z = 1.4$–3.6. As a result, we might select the same galaxy at different snapshots. For the AGN, this not a problem, since the AGN varies on scale of 1–10 Myr, and therefore the probability of the same galaxy hosting an AGN at 7 random snapshots is low. For selecting the inactive galaxies, the snapshots are sufficiently apart that they can be treated as independent galaxies (Furlong et al., 2015; McAlpine et al., 2016).

We split the AGN in the EAGLE ref model into low and high L_X subsamples using the same luminosity threshold as for our main sample (see §3.2.1); the EAGLE ref low and high L_X subsamples contain 403 and 69 AGN, respectively. In Figure 3.3 we compare the stellar mass distributions of the simulated AGN and galaxies to the AGN in our main sample. The stellar mass distributions for the AGN in the EAGLE ref model and the main sample are different in both L_X subsamples. The median stellar masses of the low and high L_X AGN in the EAGLE ref model are both $10^{10.6}$ $M_\odot$. By comparison the median stellar masses of the observed low and high L_X subsamples in our main sample are $10^{10.7}$ and $10^{11.0}$ $M_\odot$, respectively. This difference in median stellar masses is caused

by the different volumes probed to select the samples. While the EAGLE ref model has a volume of 10^6 cMpc^3, the low and high L_X subsamples of our main sample were selected from larger volumes of $10^{6.4}$ cMpc^3 and 10^7 cMpc^3, respectively.

The differences in the stellar mass distributions between the AGN in the main sample and EAGLE will also cause the differences in the sSFR distributions (i.e. since the sSFR distributions also depend on stellar mass; see §3.3.1). We therefore have to take account of the different stellar mass distributions to fully compare the observed and simulated AGN. We do this using the mass matching methods described in §3.3.2.

3.3 Results

In this section we present our results on the sSFR distributions of the distant X-ray AGN in our main sample. We measure the sSFR distributions of our main sample and search for trends in the star forming properties as a function of L_X and stellar mass (see §3.3.1). To aid in the interpretation of our results we make comparisons to the EAGLE ref model (see §3.3.2).

3.3.1 sSFR trends with X-ray luminosity and stellar mass

To search for trends in the sSFR properties of the X-ray AGN, we measured the properties (i.e., the mode and the width) of the sSFR distributions as a function of L_X and stellar mass. The mode of the sSFR distribution provides a more reliable measurement of the typical sSFR than the linear mean (see Figure 3.2 and §3.2.2). The width of the sSFR distribution provides a basic measure of the range in sSFRs: a narrow width indicates that most systems have similar sSFRs while a broad width indicates a large range of sSFRs. We fitted log-normal distributions to the L_X and stellar mass subsamples within our main sample (see §3.2.1) using the method described in §3.2.2. Table 3.3 presents the overall results.

In Figure 3.4, we plot the sSFR properties (individual measurements and measurements of the distributions) of the main sample as a function of L_X. The modes ($\log_{10}(\mu/\mathrm{Gyr}^{-1})$) of the sSFR distributions of the low L_X and high L_X subsamples are $0.03^{+0.14}_{-0.17}$ and $-0.32^{+0.15}_{-0.17}$, respectively. The mode of the sSFR decreases with L_X, but the drop is modest (1.5σ), rul-

ing out a simple AGN-feedback model where high-luminosity AGN instantaneously shut down SF. We also note that the same qualitative result is obtained if we consider the mean sSFR rather than the mode; however, the mean values are $\approx$ 0.3–0.5 dex higher than the mode (see Table 3.3). The widths of the sSFR distributions for the low $L_{\rm X}$ and high $L_{\rm X}$ subsamples are also consistent, with values of $0.52^{+0.13}_{-0.10}$ and $0.65^{+0.15}_{-0.11}$, respectively.

In Figure 3.5, we plot the sSFR properties (individual measurements and measurements of the distributions) of the main sample as a function of stellar mass. Quantitatively similar results are obtained to those shown in Figure 3.4 for the sSFRs as a function of $L_{\rm X}$, with no clear evidence for a strong change in the sSFR properties towards high stellar mass: the mode ($\log_{10}(\mu/{\rm Gyr}^{-1})$) and width of the sSFR distribution for the low stellar mass subsample is $-0.01^{+0.13}_{-0.15}$ and $0.53^{+0.13}_{-0.08}$ respectively, while the mode ($\log_{10}(\mu/{\rm Gyr}^{-1})$) and width of the sSFR distribution for the high stellar mass subsample is $-0.48^{+0.17}_{-0.20}$ and $0.67^{+0.18}_{-0.12}$ respectively. However, the difference in the mode of the sSFR distributions between the two stellar mass subsamples is marginally more significant (2.0σ) than between the two $L_{\rm X}$ subsamples. Again, the mean sSFRs are also $\approx$ 0.3–0.5 dex higher than the modes (see Table 3.3).

3.3.2 Comparison to the EAGLE simulations

The EAGLE ref model (see Table 3.4) reproduces the global properties of the galaxy population (see §3.2.3). To help interpret our results from §3.3.1, we investigate whether the simulated AGN in this model show the same sSFR relationships as we have found among the main sample. The properties of the sSFR distributions are calculated for the EAGLE AGN in the same $L_{\rm X}$ and stellar-mass bins as for our main sample, following §3.2.2; see Table 3.3. To further aid in the comparison, we also calculated the running mode of the sSFR in $L_{\rm X}$ and stellar-mass bins of 50 objects, following §3.2.2.

In Figures 3.4 and 3.5, we compare the sSFR distributions of the EAGLE AGN to our main sample as a function of $L_{\rm X}$ and stellar mass, respectively. From these figures and Table 3.3, we note that EAGLE can generally reproduce the widths of the observed sSFR distributions of AGN. At low $L_{\rm X}$ and stellar mass, the modes of the sSFR distributions for the EAGLE AGN are also in good agreement with those of the main sample, but they deviate marginally at high stellar mass, and strongly at high $L_{\rm X}$.

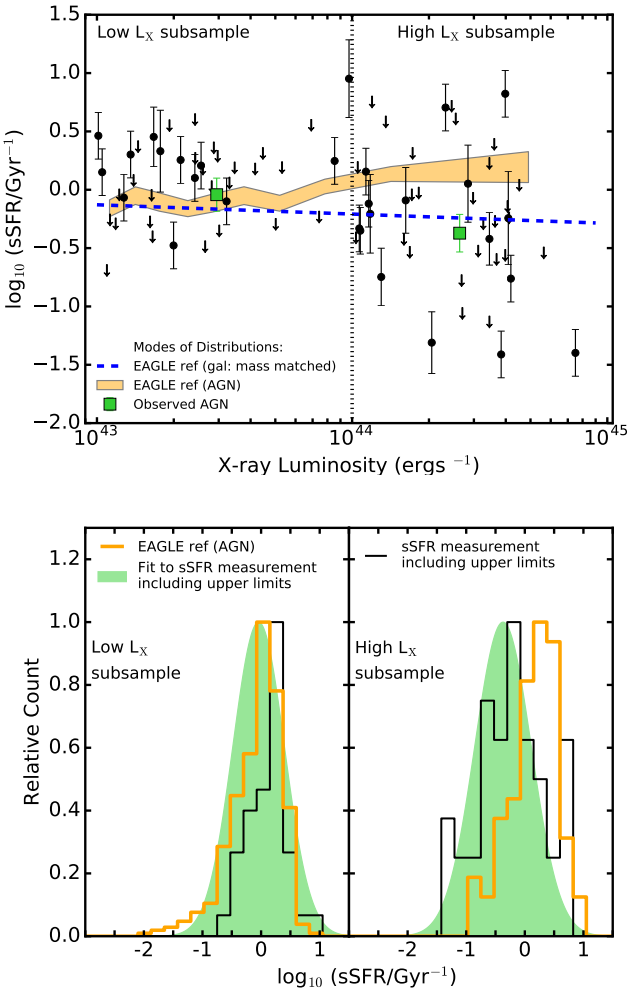

Figure 3.4: Top panel: sSFR versus X-ray luminosity (2–10 keV: rest frame) for the X-ray AGN in our main sample. The black filled circles indicate individual X-ray AGN, the filled green squares indicate the modes of the sSFR distributions for the low and high X-ray luminosity subsamples (see Table 3.3); error bars represent the 68% confidence interval. The dotted vertical line indicates the division in X-ray luminosity between the low and high X-ray luminosity subsamples. The orange shaded region indicates the X-ray luminosity dependence on the sSFR distribution for AGN from the EAGLE ref model (the width corresponds to the 68% confidence interval around the mode of the distribution) and the blue dashed line indicates the predicted sSFR–X-ray luminosity relationship from the EAGLE ref model for galaxies with masses matched to those found from our observed X-ray AGN (see §3.3.2). Bottom panel: sSFR distributions for our data (black histogram), the AGN from the EAGLE ref model (orange open histogram), and the best-fitting log-normal distribution (green filled histogram; see §3.2.2). The sSFR distributions are shown separately for the low (left) and high (right) X-ray luminosity subsamples.

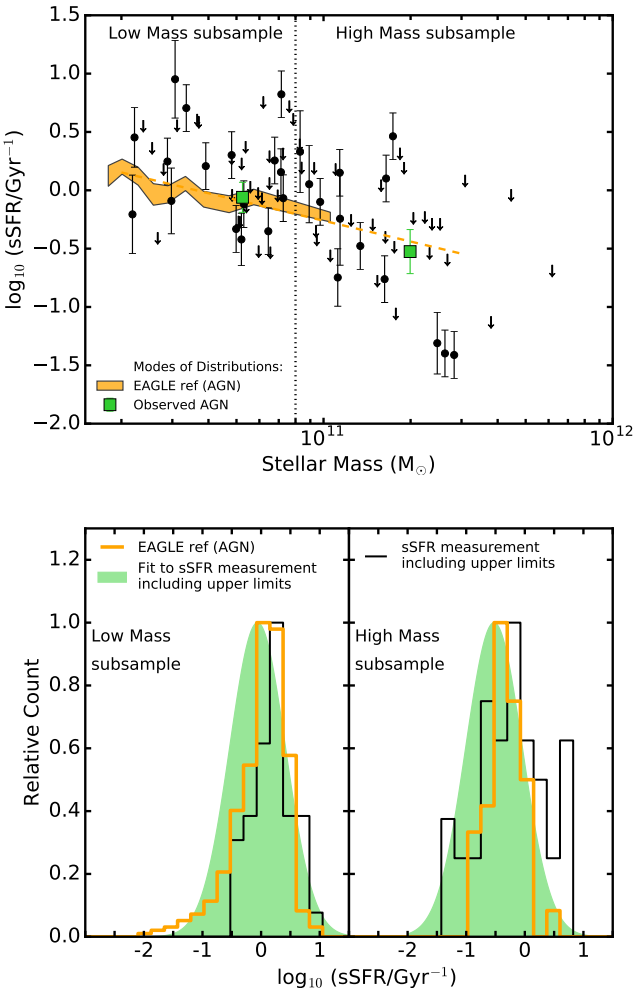

Figure 3.5: Top panel: sSFR versus stellar mass for the X-ray AGN in our main sample. The black filled circles indicate individual X-ray AGN, the filled green squares indicate the modes of the sSFR distributions for the low and high mass subsamples (see table 3.3); the error bars represent the 68% confidence interval. The dotted vertical line indicates the division in mass between the low and high stellar mass subsamples. The orange shaded region indicates the stellar mass dependence on the sSFR distribution for AGN from the EAGLE ref model (the width corresponds to the 68% confidence interval around the mode of the distribution) and the orange dashed line is the linear extrapolation of the mode to higher stellar masses (see §3.3.1). Bottom panel: sSFR distributions for our data (black histogram), the AGN from the EAGLE ref model (open orange histogram), and the best-fitting log-normal distribution (green filled histogram; see §3.2.2). The sSFR distributions are shown separately for the low (left) and high (right) stellar mass subsamples.

We can qualitatively understand the marginal difference in the sSFR modes with stellar mass (see Figure 3.5) as due to the different stellar mass distributions between the simulated AGN in EAGLE and the observed AGN in the main sample. There are more massive AGN hosts in the main sample than in the EAGLE ref model, which is a consequence of the different volumes probed by the EAGLE simulation and our observational survey (see §3.2.3 and Figure 3.3). Since sSFR is a decreasing function of stellar mass, the more massive AGN in the main sample will have lower sSFRs than the less massive AGN. Indeed, if we extrapolate the running mode of the sSFR from the EAGLE ref model towards high stellar masses (the dashed line in Figure 3.5), we can fully reproduce the mode of the sSFR among the observed high mass AGN hosts.

Figure 3.3 shows that the stellar masses of the observed AGN and the simulated AGN from the EAGLE ref model differ substantially in the two L_X bins. This difference in stellar mass could also be the driver of the significant differences in the sSFR mode as a function of L_X seen between EAGLE and the main sample (see Figure 3.4)? We explore this idea by considering how the mode of the sSFR changes for subsamples with different stellar mass distributions using the EAGLE ref model. Unfortunately, in the limited volume of the EAGLE simulation there are no AGN hosts with masses $> 2 \times 10^{11}$ $M_\odot$. Therefore, we turn to the more numerous galaxy population in the EAGLE ref model. So long as the sSFRs of these simulated galaxies decrease with stellar mass in the same functional form as the AGN, we can use them as analogues to understand the role of differing stellar mass distributions in the interpretation of the sSFR differences between the simulated and observed AGN. In Figure 3.6 we compare the mode of the sSFR distribution versus the stellar mass for both the AGN and galaxies in the EAGLE ref model and demonstrate that they follow the same trend but with a ≈ 0.1 dex offset (which we further explore in §4.1).

To quantify the impact of different stellar mass distributions on our results we constructed four subsets of galaxies from the EAGLE ref model that are matched in their mass distributions to 1) simulated AGN from the EAGLE ref model in the low L_X bin, 2) simulated AGN from the EAGLE ref model in the high L_X bin, 3) observed AGN from the main sample in the low L_X bin, and 4) observed AGN from the main sample in the high L_X bin. For each of these four subsets, we determined the mode of the sSFR dis-

tribution following the method in §3.2.2. If differences in stellar mass are the principal driver for the different trends shown by the observed and simulated AGN in Figure 3.4, we would expect offsets in the sSFR modes of the mass-matched subsets corresponding to the simulated and observed AGN in each respective L_X bin, particularly at high L_X where the stellar mass differences are most pronounced (see Figure 3.3). This is indeed what we find.

The mode of the sSFR for the two mass-matched EAGLE galaxy subsets corresponding to the low L_X bin differ by only a small amount (< 0.1 dex), as expected given the similar stellar mass distributions (see Figure 3.3) and in agreement with the results for this L_X bin given in Table 3.3. On the other hand, the mode of the sSFRs for the two mass-matched EAGLE galaxy subsets corresponding to the high L_X bin differ by ≈ 0.4 dex. From this we conclude that the high masses of the high L_X AGN in the main sample leads to a measured sSFR that is lower than that of equivalently X-ray luminous simulated AGN from the EAGLE ref model. If we correct the sSFR trend with L_X for the EAGLE AGN to reflect the different stellar mass distributions of the observed AGN, using the offsets determined above, we obtain the blue dashed line in Figure 3.4, which is a remarkably good match to our observations.

From these results it is clear that stellar mass is a strong driver of the properties of the sSFR distributions. Consequently, the stellar-mass distribution needs to be taken into account when interpreting the sSFR results from samples of AGN and galaxies.

3.4 Discussion

On the basis of our results on the fitted sSFR distributions of X-ray AGN at $z = 1.5 - 3.2$ we found that, once the effects of different volumes and survey selections are taken into account (in particular with respect to stellar mass distributions), the EAGLE ref model provides a good description of the sSFR properties of the AGN in our main sample. The good agreement between the observations and EAGLE means that we can employ further comparisons to explore the connection between galaxies and AGN and the role of AGN feedback in producing the SF properties of the galaxy population.

3.4.1 AGN among the galaxy population at $z \approx$ 1.5-3.2

In our study so far we have considered the star forming properties of distant AGN but we have not put these results within the context of the overall galaxy population. In Figure 3.6 we compare the mode of the sSFR versus stellar mass for our main sample to that of the main sequence for coeval star-forming galaxies.[6] Although there is some uncertainty in the sSFR of the main sequence at this redshift, the AGN clearly lie substantially ($\approx$ 0.2–0.8 dex) below it particularly at higher stellar mass (see dotted and dashed tracks in Figure 3.6). This result is in good agreement with earlier studies (Santini et al., 2012; Rosario et al., 2013; Vito et al., 2014; Mullaney et al., 2015) and demonstrates that a large fraction of the AGN population do not lie in "star-forming galaxies".

Given the good agreement between our observational results and the EAGLE ref model (see §3.3.2), we can use EAGLE to provide additional insight on the connection between distant galaxies and AGN. In Figure 3.6 (top panel) we show that the sSFR properties of the AGN in EAGLE are $\approx$ 0.1 dex higher than the galaxies in EAGLE, at a given stellar mass. This indicates that, although AGN do not typically reside in strong star-forming galaxies, their SFRs are elevated when compared to the overall galaxy population. In Figure 3.6 (bottom panel) we show the fraction of galaxies that host an AGN with $L_{\rm X} > 10^{43}$ erg s^{-1} in the EAGLE ref model across the sSFR–stellar mass plane. The fraction of galaxies hosting an AGN increases as a function of both sSFR and stellar mass (i.e., effectively as a function of SFR), from an AGN fraction of $< 10\%$ at low values to $> 50\%$ at high SFR values (SFR > 50 M$_{\odot}$yr^{-1}). Overall the highest AGN fractions are found for galaxies with the highest SFRs, suggesting a connection between the cold-gas supply required to fuel intense star formation and the gas required to drive significant AGN activity. By selecting AGN with $L_{\rm X} > 10^{43}$ erg s^{-1} we are therefore biased towards galaxies with elevated SFRs when compared to the overall galaxy population. This bias is responsible for the $\approx$ 0.1 -0.2 dex difference in the sSFR properties between galaxies and AGN in the EAGLE ref model (see Figure 3.6).

[6] We used the parameters from Table 1 of Mullaney et al. (2015) to convert between the linear mean and the mode of the sSFR distribution of the star-forming galaxy main sequence.

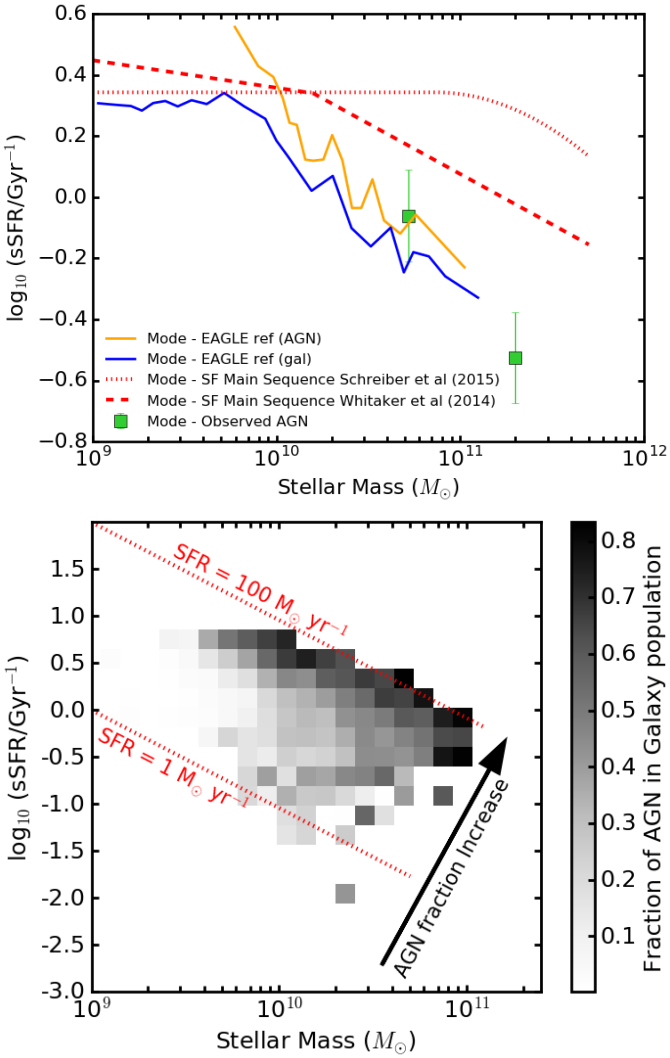

Figure 3.6: Top Panel: sSFR versus stellar mass for the X-ray AGN in our main sample and AGN and galaxies in the EAGLE ref model. The green filled squares indicate the mode of the sSFR distributions for the observed X-ray AGN with error bars representing the 68% confidence interval (see Table 3.3) and are compared to the modes of the AGN (orange curve) and galaxies (blue curve) from the EAGLE ref model, coeval ($z \approx 2.2$) main sequence galaxies from Schreiber et al. (2015) (red dotted line) and Whitaker et al. (2014) (red dashed line). The mode of the sSFR for AGN is higher than the overall galaxy population but lower than galaxies on the star-forming main sequence. Bottom Panel: The grey shaded regions indicate the fraction of galaxies in a given sSFR–stellar mass bin that host AGN activity (with $L_X > 10^{43}$ erg s^{-1}) in the EAGLE ref model; the AGN fraction values are indicated by the greyscale bar to the right of the figure. The dotted red lines indicate constant values of SFR. The fraction of galaxies hosting AGN activity in the EAGLE ref model is a function of the SFR (illustrated by the black arrow).

3.4.2 Identifying the signature of AGN feedback on the star forming properties of galaxies

Our analyses of the EAGLE simulation in §3.4.1 suggested that AGN have elevated sSFRs when compared to the overall galaxy population. Furthermore, both the data and the model do not reveal a negative trend between sSFR and AGN luminosity (see Figure 3.4). These results may appear counter intuitive for a model in which AGN feedback quenches star formation in galaxies. Therefore, what is the signature of AGN feedback on the star-forming properties of galaxies? This question can be explored from a comparison of the sSFR properties of galaxies and AGN for two different EAGLE models: the EAGLE ref model with AGN feedback and the EAGLE noAGN model, which is identical to that of the EAGLE ref model except that black holes are not seeded in this model and consequently there is no AGN activity and no AGN feedback (see §3.2.3).

We calculated the running mode and width of the sSFR distributions for the galaxies in both the EAGLE ref model and the EAGLE noAGN model in stellar-mass bins of 50 objects, following §3.2.2. In Figure 3.7 we compare the mode and width of the sSFR distributions of the galaxies between these two models. There are several clear differences between the sSFR properties of the galaxies with $> 10^{10}$ $M_{\odot}$ in the EAGLE ref and the EAGLE noAGN models: 1) the sSFR distribution is a factor ≈ 2 broader in the EAGLE ref model, 2) the mode of the sSFR is ≈ 0.2 dex lower in the EAGLE ref model, and 3) the slope of the mode of sSFR distribution as a function of mass is steeper in the EAGLE ref model; -0.52 ± 0.02 and -0.35 ± 0.02 for the EAGLE ref and EAGLE noAGN model, respectively when we fitted a linear model to the data in logarithmic space. Of these three potential signatures of AGN feedback, we consider the broadening of the sSFR distribution to be the most reliable quantity for comparison with observations since it is less sensitive to calibration differences in stellar mass and SFR calculations between the observations and simulations. In Figure 3.7 we compare the sSFR properties of the AGN in the EAGLE ref model to the galaxies in the same model. These signatures of AGN feedback are seen in both the AGN and galaxy population, implying that the impact of AGN feedback is slow and occurs on a timescale that is longer than the episodes of AGN activity (see McAlpine et al., 2017). This slow impact of AGN feedback on the star

forming properties helps to explain why AGN luminosity (L_X) is not observed in the data for the EAGLE reference model to be a strong driver of the sSFR properties (see Figure 4); i.e., although the luminosity of the AGN may dictate the overall impact of the feedback on star formation, the observational signature of that impact on the star formation across the galaxy is not instantaneous. However, we note that since the measurements of star formation in our study are for the entire galaxy, these results do not rule out AGN having significant impact on the star formation in localised regions within the galaxy.

In Figure 3.7 we show how the measured sSFR properties of the AGN in our main sample compare to systems in the EAGLE ref and noAGN models. From this comparison it is clear that the broad width of the sSFR distribution for our main sample is in better agreement with the EAGLE ref model than the EAGLE noAGN model, providing indirect observational support for AGN feedback. The broad width of the sSFR distribution indicates a wide range in sSFRs. This is seen in Figure 3.8, where we compare the sSFR versus stellar mass for the galaxies in the EAGLE ref and the EAGLE noAGN models. The clearest differences between the two models across the sSFR–stellar mass plane are the broader range of sSFRs for the galaxies in the EAGLE ref model and the presence of a population of galaxies with low sSFRs (less than $\log_{10}(\mathrm{sSFR/Gyr^{-1}})$=$-0.5$ $\mathrm{Gyr^{-1}}$) not seen in the EAGLE noAGN model. Since the only difference between the two EAGLE models is the presence/absence of AGN feedback, we conclude that AGN feedback is directly responsible for creating this low sSFR ("quenched") part of the galaxy population in the EAGLE ref model (Trayford et al., 2016).

3.5 Conclusions

We observed 114 X-ray selected AGN with ALMA at 870μm across a broad range in luminosity ($L_X = 5\times10^{39} - 10^{45}$ erg s^{-1}) and redshift ($z = 0.1 - 4.6$). Utilising the ALMA data in combination with archival *Herschel* and *Spitzer* data, we fitted the broad-band SEDs to obtain SFR and stellar-mass measurements uncontaminated by AGN emission. In the current paper we focused our analyses on a main sample of 81 X-ray selected AGN (irrespective of ALMA coverage) at $z = 1.5 - 3.2$ with $L_X = 10^{43} - 10^{45}$ erg s^{-1} and stellar mass of $> 2\times10^{10}$ M$_\odot$. We used the SFR and stellar-mass measurements to

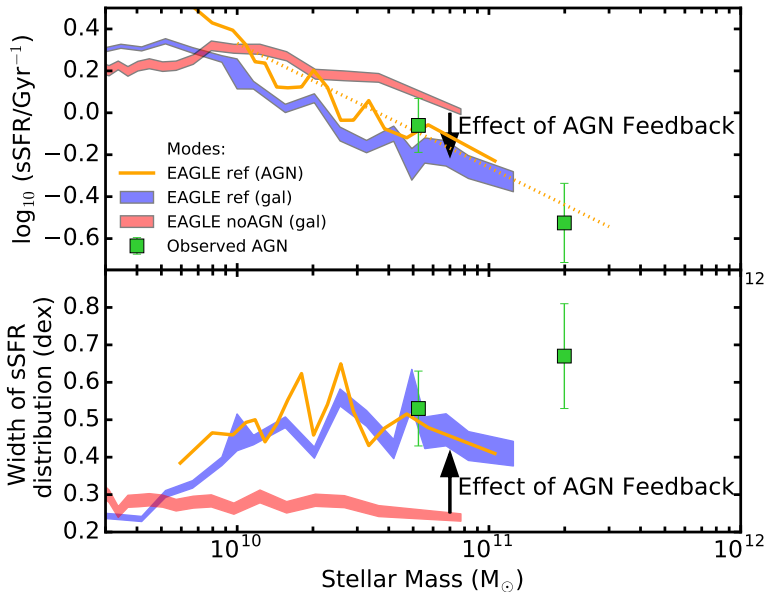

Figure 3.7: Mode of the sSFR (top panel) and width of the sSFR (bottom panel) versus stellar mass for the X-ray AGN in our main sample and two different EAGLE models. The solid green squares indicate the measurements from the X-ray AGN in our main sample; the error bars indicate the 68% confidence interval (see Table 3.3). The blue and red shaded regions indicate the modes and widths of the sSFR for galaxies in the EAGLE ref model and the EAGLE model without AGN, respectively. The orange solid line indicates the modes and widths of the sSFR for AGN in the EAGLE ref model and the orange dashed line in the top panel indicates the linear extrapolation to higher stellar masses.

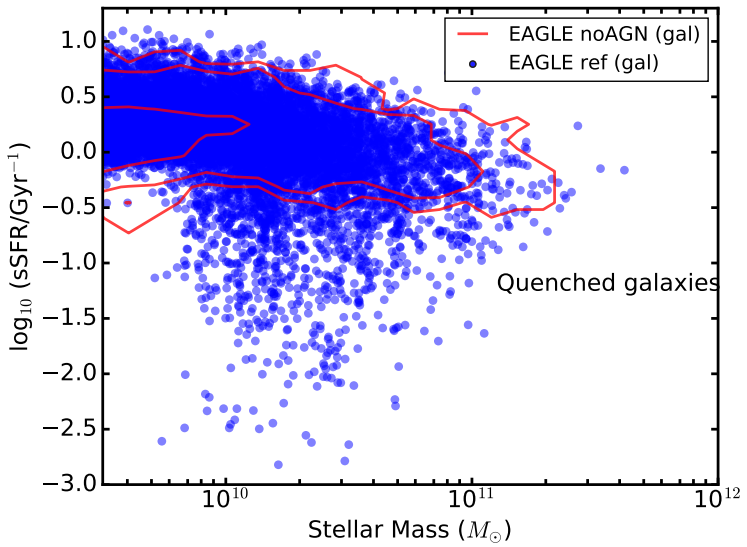

Figure 3.8: Individual galaxies from the EAGLE ref (blue points) and 1, 2 and 3 σ contours (red lines) of the galaxies in the EAGLE noAGN model on the sSFR–stellar mass plane. In the EAGLE noAGN model, there are no galaxies with $\log_{10}$(sSFR/Gyr^{-1})$<$ -0.5 Gyr^{-1}. The sSFR distributions in the EAGLE ref model is a factor ≈ 2 broader than in the EAGLE noAGN model.

parameterise the sSFR distributions as a function of X-ray luminosity and stellar mass, taking into account of both detections and upper limits using Bayesian techniques. To assist in the interpretation of our results, we made comparisons to the predictions from two different models from the EAGLE hydrodynamical cosmological simulation: the reference model (EAGLE ref model), which includes AGN feedback, and a model without black holes which, consequently, does not include AGN feedback (EAGLE noAGN). On the basis of our analyses we obtained the following results:

1. We found no strong (> 3 σ) observational evidence for differences in the mode or width of the sSFR distribution for the AGN in our main sample as a function of either L_X or stellar mass. The lack of a dependence on the sSFR properties with L_X rules out a simple AGN-feedback model where high-luminosity AGN instantaneously shut down star formation. However, we do find good agreement between the properties of the sSFR distributions of our main sample and the EAGLE ref model as a function of both L_X and stellar mass, although only when the samples are matched in mass. This result indicates the importance of taking account of stellar mass in sSFR comparisons. See §3.3.1 and §3.3.2.

2. From a comparison of the properties of the sSFR distributions of the galaxies in the EAGLE ref model to the galaxies in the EAGLE noAGN model we identified a clear signature of AGN feedback on the star forming properties of galaxies. We found that the sSFR distribution is significantly broader (by a factor of ≈ 2) for the galaxies in the EAGLE ref model due to the presence of a significant population of "quenched" galaxies with low sSFRs. The broad width of the sSFR distribution of the observed population is in better agreement with the EAGLE ref model than the EAGLE nonAGN model, providing indirect evidence for AGN feedback. See §3.4.1 and §3.4.2.

Overall, from the combination of the observations with the model predictions, we conclude that (1) even with AGN feedback, there is no strong relationship between the sSFR distribution parameters and instantaneous AGN luminosity, indicating that the impact of AGN feedback on star formation is slow and (2) a signature of AGN feedback is a broad distribution of sSFRs for all galaxies (not just those hosting an AGN) with $M_* > 10^{10} M_\odot$, which implies the presence of a population of "quenched" galaxies with low sSFRs. With future larger samples of AGN and galaxies with sensitive sSFR measurements (e.g., from deeper ALMA observations and other SFR tracers) we aim to measure the sSFR distribution parameters to greater accuracy to further constrain the role of AGN in models of galaxy formation.

3.6 APPENDIX: ALMA observations and catalogues

In this appendix we describe the band 7 (870 μm) ALMA observations and the construction of the ALMA catalogues for the X-ray AGN observed from our Cycle 1 (project 2012.1.00869.S; PI: J. Mullaney) and Cycle 2 (project 2013.1.00884.S; PI: D. Alexander) programmes. A subset of the ALMA-observed X-ray AGN are used in our main analyses, as described in §2, and SFR constraints for all of the ALMA-observed X-ray AGN at $z > 1$ are presented in Stanley et al. (in prep); we note here that the SFRs in Stanley et al. (in prep) can differ by up-to 0.1 dex from those presented here due to a slightly different method adopted to select the best-fitting SED solution (see §5.4.1).

Here we provide an overview of the ALMA target selection (see §3.6.1), the details

of the ALMA observations (see §3.6.2), the reduction of the ALMA data (see §3.6.3), the detection of ALMA sources and the matching of ALMA-detected sources to X-ray AGN, including ALMA upper limits for the X-ray AGN that are undetected by ALMA (see §3.6.4).

3.6.1 ALMA target selection

All of the ALMA-selected targets from our Cycle 1 and Cycle 2 programmes are X-ray AGN that are detected in either the 4 Ms *Chandra* Deep Field South (CDF-S; Xue et al. 2011) or the *Chandra* Cosmic Evolution Survey (COSMOS) surveys (Civano et al. 2009; Elvis et al. 2009). The overall target selection criteria were X-ray AGN at $z > 1.5$ with $L_{\rm X} > 10^{42}$ erg s^{-1}, for the reasons outlined in §3.2.1; however, we also note that the lower limit on the redshift selection was also required to make the most efficient use of ALMA for SFR constraints since the sensitivity of *Herschel* for measuring SFRs is comparable to, or better than, ALMA at 870μm for sources at $z < 1.5$ (see Casey et al. 2014 for a general review).

For the X-ray AGN in CDF-S we selected sources across the whole of the *Chandra*-observed region while for COSMOS we selected sources from the central 12.5′-radius region for X-ray AGN with $L_{\rm X} = (1-3) \times 10^{44}$ erg s^{-1} and from the central 25′-radius region for X-ray AGN with $L_{\rm X} = (0.3-1) \times 10^{45}$ erg s^{-1}; the larger region for the AGN with $L_{\rm X} = (0.3-1) \times 10^{45}$ erg s^{-1} was required to allow for a comparable number of AGN as that in the $L_{\rm X} = (1-3) \times 10^{44}$ erg s^{-1} bin. IR-based star forming luminosity constraints were obtained for all of the X-ray AGN in CDF-S and COSMOS that met these criteria from fitting the *Spitzer–Herschel* IR SEDs with AGN and star forming templates, following Stanley et al. (2015). These star formation luminosity constraints were used to select X-ray AGN to observe with ALMA, with the majority of the selected targets having star formation luminosity upper limits.

Overall we selected 30 X-ray AGN in CDF-S to observe in Cycle 1 and 86 X-ray AGN in CDF-S and COSMOS to observe in Cycle 2 for 116 targets overall. The X-ray AGN selected for the Cycle 1 observations had redshifts of $z = 1.5$–4.0 and the majority had X-ray luminosities of $L_{\rm X} \approx 10^{42} - 10^{44}$ erg s^{-1}, with a minority at $L_{\rm X} > 10^{44}$ erg s^{-1}. The X-ray AGN selected for the Cycle 2 observations were typically more luminous than

in Cycle 1 ($L_X \approx 10^{43} - 10^{45}$ erg s^{-1}) and covered the narrower redshift range of $z = 1.5$–3.2.[7]

3.6.2 ALMA observations

From the 116 X-ray AGN that we proposed for ALMA observations in Cycle 1 and Cycle 2 (see §3.6.1), 107 were observed; the 9 X-ray AGN not observed were Cycle 2 targets in the CDF-S at $z = 1.5$–2.0. The 107 X-ray AGN were observed by ALMA in band 7 using a fixed continuum correlated setup with 7.5 GHz of bandwidth centered at 344 GHz (870 μm) and four 128-channel dual-polarisation basebands. The ALMA pointings were centered on the optical counterpart positions of the X-ray sources. The Cycle 1 data for project 2012.1.00869.S were taken on 2013 November 2 and 2013 November 16–17 using thirty-two 12 m antennas and nine 7 m antennas in the compact array (see also Mullaney et al. 2015 for details). The Cycle 2 data for project 2013.1.00884.S were taken on 2014 September 2, 2014 December 31, and 2015 January 1–2 using thirty-four 12 m antennas and nine 7 m antennas in the compact array.

The requested spatial resolution for both programmes was $\approx 1''$ to ensure that the measured 870 μm continuum emission was from the entire galaxy (physical scales of $\approx$ 7.0–8.5 kpc over the redshift range of $z = 1.5$–4.0 for our assumed cosmology) to remove the need to apply aperture-correction factors to match the lower-resolution *Spitzer* and *Herschel* infrared data. However, the ALMA observations were taken with a variety of baselines across both programmes (91–393 m), which leads to some variation in the spatial resolution ($0''.18$-$0''.85$); see Tables 3.5 & 3.6 for the measured median baseline for each target.

The requested sensitivity for each target was broadly based on that required to detect star-formation emission from systems that lie on or below the star-forming galaxy main sequence (e.g. Schreiber et al., 2015; Whitaker et al., 2014). For the Cycle 1 programme the sensitivity limits were determined taking account of both the stellar mass and red-

[7]We note that in selecting X-ray AGN targets and planning for the ALMA observations we used the redshifts, X-ray luminosities, and optical positions from Xue et al. (2011) and Civano et al. (2009). However, for our analyses in this paper we have adopted the updated redshifts, X-ray luminosities, and optical positions from Hsu et al. (2014) and Marchesi et al. (2016).

shift of each X-ray AGN (see Mullaney et al., 2015, for more details) for more while for the Cycle 2 programme only the redshift was taken into account. On the basis of these parameters, the proposed root mean squared (RMS) sensitivities varied over 0.075–0.24 mJy. However, the final sensitivities often deviated from the proposed sensitivities due to either non-optimal conditions or baseline configurations (i.e., a more extended array configuration than proposed). The final RMS sensitivities were re-measured from the tapered images (see §3.6.3); the final RMS sensitivities measured for each target are given in Tables 3.5 & 3.6.

3.6.3 ALMA data reduction

Our data reduction and source detection approach follows that described in Simpson et al. (2015). Here we provide a brief description of the procedures.

The data were imaged using the Common Astronomy Software Application (CASA version 4.4.0). The uv-visibilities were Fourier transformed to create "dirty" images. These dirty images were consequently "cleaned" using a similar technique to that described by Hodge et al. (2013); cleaning is a common technique applied to interferometric data to reduce the strength of the side lobes from bright sources to allow for the detection of faint sources. We used an iterative approach to cleaning the images. We estimated the RMS in the dirty maps and we cleaned the maps to 3 σ (i.e., until peaks down to 3 σ become identifiable). We then estimated the RMS in the cleaned maps and identified any objects at $\geqslant 5$ σ. If a source was detected at $\geqslant 5$ σ then the cleaning process was repeated on the cleaned map in a tight region around the detected source. If a source was not detected at $\geqslant 5$ σ then the cleaned map was adopted as the final map.

To ensure that the 870 μm emission is measured over a common physical size scale for all of the targets, we "tapered" all of the images to give a synthesized beam of $0''.8$; this size scale was chosen to provide 870 μm constraints from the entire galaxy to allow for consistent comparisons with the lower-resolution *Spitzer–Herschel* data. We applied a Gaussian taper which lowers the weighting given to the long baselines to increase the size of the synthesised beam. However, this procedure also increases the noise of the maps by up-to a factor of ≈ 6 for the highest-resolution data. All final maps and all measured 870 μm properties have the same spatial resolution of $0''.8$.

3.6.4 ALMA source detection and source properties

The final maps described in §3.6.3 were used to detect ALMA sources. To construct a catalogue of ALMA-detected sources we require a clear detection threshold to reliably distinguish between spurious sources and real detections. To provide an assessment of the rate of spurious sources as a function of detection threshold, we created inverted maps by multiplying the final maps by -1. These inverted maps have the same noise properties as the original maps but they do not contain any positive peaks due to real sources (all real sources will have negative peaks).

To estimate the number of spurious sources in our final maps we compared the ratio of sources "detected" in both the final maps and inverse maps as a function of the detection threshold. To achieve this we extracted all positive peaks of at least 2.5 σ from the cleaned maps corrected for the primary beam, and the inverted maps using *Source Extractor* (Bertin & Arnouts, 1996). Since we are only interested here in the ALMA properties of X-ray sources, rather than performing a blind search for ALMA sources, our total source-detection region size is substantially smaller than the combined area for all of the ALMA images. Consequently, we can detect sources down to lower significance levels than would be possible from a blind source-detection approach. We therefore split the number of detected peaks in the final and inverse ALMA maps into three different σ bins: $2.5-3$ (low-significance peaks), $3-4$ (medium-significance peaks) and >4 (high-significance peaks). Adopting a search radius of $0.5''$, we calculate a total of 2.41, 0.89 and 0.052 spurious objects for the σ bins of 2.5–3, 3–4, and >4.0, respectively. Since the spurious fraction for the high-significance bin was so small, we increased the search radius of this bin to $1''$, which still gives a low 0.20 spurious sources.

We note that the our detection limit of 2.5 σ is below the threshold for cleaning the sidelobes of bright sources (3 σ). However, these sources would only be affected by cleaning if there is a bright source in the vicinity. The visual checks of the maps show no bright sources in the vicinity of our 2.5–3.0 σ detections, indicating that the discrepancy between our cleaning and detection threshold is not an issue.

In matching ALMA sources to X-ray sources we therefore adopted a $0''.5$ radius for low and medium significance ALMA sources and a $1''$ radius for high-significance ALMA sources. With this source-matching approach we identified ALMA counterparts with a

$\sigma \geqslant 2.5$ ALMA detection for 20 X-ray sources in CDF-S and 20 X-ray sources in COSMOS.[8] Example *HST* and ALMA images of the X-ray sources are shown in Fig. 3.9 to demonstrate the quality of the optical and ALMA data. The ALMA detection rate is comparable between X-ray sources with photometric and spectroscopic redshifts, suggesting that inaccurate redshifts are not a major reason for the non-detections. Although our matching radii were $0.5''$ and $1''$, $\sim 80\%$ of the ALMA counterparts lie within $0.3''$ or less from the optical position of the X-ray sources, including all of the 7 low-significance ALMA sources giving us confidence that the majority are real sources.

The positions, redshifts and ALMA 870μm fluxes are summarised in Tables 3.5 & 3.6. In addition to the 107 primary targets, there were a further 7 X-ray sources that serendipitously lay within the field-of-view of the primary beam of some of our ALMA maps. As a result we have ALMA coverage for 60 and 54 X-ray sources in the CDF-S and COSMOS fields respectively, covering a $L_{\rm X}$ range of $5 \times 10^{39} - 10^{45}$ erg s^{-1} and a redshift range of $z = 0.1$–4.6; see Fig. 4.1 for the z–$L_{\rm X}$ coverage. For the X-ray sources without an ALMA counterpart, we calculated 3σ upper limits directly from the map. In Fig. 3.10 we show the ALMA 870 μm flux density versus redshift for the 114 X-ray sources with ALMA coverage.

3.6.5 MIR to submm SEDs for our AGN

[8]During the inspection of the optical and ALMA images, we noticed a systematic offset between the ALMA and optical-based astrometry in the central GOODS-S region of CDFS ($+0.19''$ in RA and $-0.23''$ in declination), which was not present between the VLA radio data and ALMA. As noted in other papers (e.g., Miller et al. 2008; Xue et al. 2011; Hsu et al. 2014), the optical reference frame is probably shifted with respect to the radio calibrator reference frame used for ALMA astrometric calibration. We therefore corrected the optical positions in the GOOD-S region) by this offset.

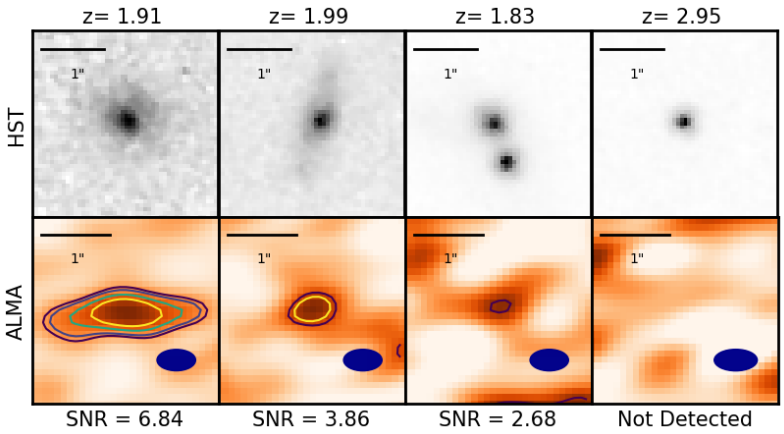

Figure 3.9: Example HST (H-band: 1.6μm; top) and ALMA (870μm; bottom) images of X-ray AGN to indicate the range in σ (SNR) from our ALMA data. All images are $3'' \times 3''$ in size; the solid bar indicates $1''$, which corresponds to $\approx$ 8 kpc over the redshift range for our main sample. The plotted contours indicate the 2.5, 3.0, 4.0, and 5.0 σ levels for the ALMA data. The dark blue area indicates the size of the ALMA beam.

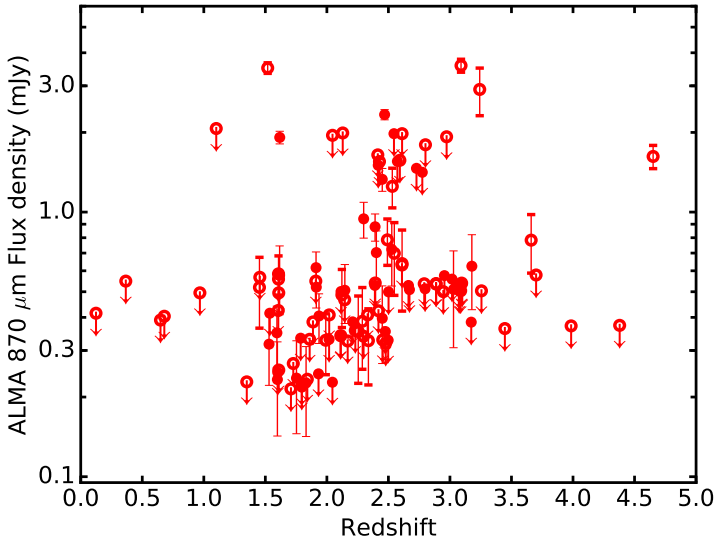

Figure 3.10: ALMA 870 μm flux density versus redshift for the X-ray detected that lie within our ALMA observations. The error bars represent the 1σ error on the flux density.

Table 3.5: X-ray selected sources observed with ALMA at 870μm in CDF-S field. The columns show X-ray ID (from Hsu et al., 2014), optical positions, ALMA positions, redshift (2 and 3 decimal places indicate photometric and spectroscopic redshifts, respectively), X-ray luminosity (rest-frame 2-10 keV), primary beam corrected ALMA fluxes, median baseline of the ALMA configuration, the RMS of the map containing the X-ray AGN and the observing ID.

X-ray ID	RA Optical (J2000)	Dec Optical (J2000)	RA ALMA (J2000)	Dec ALMA (J2000)	redshift	$\log_{10}$ ($L_{2-10keV}$/erg s^{-1})	$F_{870\mu m}$ (mJy)	Median baseline (m)	RMS (mJy)	Observing ID
88	53.01019	−27.76674	53.01025	−27.76677	1.616	43.5	0.58 ± 0.17	220	0.168	2012.1.00869.S
93	53.01265	−27.74724			2.573	43.5	< 1.87	393	0.622	2013.1.00884.S
123	53.02794	−27.74866			2.33	42.7	< 0.49	220	0.163	2012.1.00869.S
129	53.02961	−27.87481			3.45	43.8	< 0.44	91	0.145	2013.1.00884.S
137	53.03333	−27.78258			2.610	43.9	< 0.76	220	0.252	2012.1.00869.S
155	53.04094	−27.83607			2.02	< 42.5	< 0.49	220	0.163	2012.1.00869.S
156	53.04098	−27.83766	53.04108	−27.83774	4.65	43.6	1.62 ± 0.16	220	0.163	2012.1.00869.S
158	53.04264	−27.86558			2.05	42.7	< 2.34	393	0.780	2013.1.00884.S
163	53.04495	−27.77439			1.607	< 42.3	< 0.67	220	0.223	2012.1.00869.S
167	53.04567	−27.81557			1.46	43.1	< 0.68	220	0.227	2012.1.00869.S
184	53.05220	−27.77477			1.605	42.3	< 0.51	220	0.170	2012.1.00869.S
185	53.05233	−27.82728	53.05237	−27.82737	2.34	< 42.4	0.33 ± 0.10	220	0.104	2012.1.00869.S
195	53.05584	−27.81555	53.05584	−27.81566	1.45	42.9	0.52 ± 0.16	91	0.155	2013.1.00884.S
199	53.05786	−27.83350			2.42	43.1	< 1.80	393	0.601	2013.1.00884.S
211	53.06190	−27.85105			1.60	43.2	< 0.30	220	0.099	2012.1.00869.S
215	53.06326	−27.69964	53.06326	−27.69971	2.402	43.1	0.70 ± 0.15	91	0.146	2013.1.00884.S
221	53.06567	−27.87887			1.89	42.4	< 0.46	220	0.154	2012.1.00869.S
230	53.06774	−27.92342	53.06781	−27.92361	3.98	43.7	0.43 ± 0.15	91	0.149	2013.1.00884.S
249	53.07446	−27.84980			0.124	< 39.8	< 0.50	220	0.166	2012.1.00869.S
254	53.07600	−27.87816			2.801	43.1	< 2.16	393	0.719	2013.1.00884.S
257	53.07640	−27.84866			1.536	43.7	< 0.50	220	0.166	2012.1.00869.S
262	53.07846	−27.85986	53.07840	−27.86004	3.660	43.8	0.78 ± 0.20	220	0.195	2012.1.00869.S
276	53.08270	−27.86657	53.08275	−27.86657	1.52	42.1	3.50 ± 0.16	220	0.161	2012.1.00869.S
277	53.08313	−27.71198			2.21	43.4	< 0.46	91	0.154	2013.1.00884.S
290	53.08732	−27.92955			2.55	43.6	< 2.37	393	0.791	2013.1.00884.S
294	53.08918	−27.93047			2.611	43.3	< 2.37	393	0.791	2013.1.00884.S
301	53.09229	−27.80316	53.09234	−27.80322	2.47	43.2	2.34 ± 0.10	220	0.104	2012.1.00869.S
305	53.09379	−27.80131			2.42	42.7	< 0.51	220	0.169	2012.1.00869.S
308	53.09392	−27.76772			1.727	43.6	< 0.32	220	0.107	2012.1.00869.S
310	53.09403	−27.80413	53.09404	−27.80419	2.39	43.1	0.88 ± 0.10	220	0.104	2012.1.00869.S
318	53.09636	−27.74506	53.09639	−27.74505	1.607	< 42.2	0.58 ± 0.10	220	0.099	2012.1.00869.S
320	53.09765	−27.71528	53.09771	−27.71537	2.145	42.8	0.56 ± 0.19	220	0.186	2012.1.00869.S
326	53.10081	−27.71599			2.298	42.9	< 0.41	91	0.136	2013.1.00884.S
344	53.10486	−27.70522	53.10487	−27.70532	1.617	43.4	1.92 ± 0.11	220	0.105	2012.1.00869.S
351	53.10702	−27.71823	53.10709	−27.71834	2.532	44.1	1.25 ± 0.21	220	0.214	2012.1.00869.S
359	53.10811	−27.75398			2.728	43.4	< 1.76	393	0.585	2013.1.00884.S
371	53.11156	−27.76777	53.11157	−27.76782	3.24	43.5	2.91 ± 0.59	393	0.594	2013.1.00884.S
386	53.11783	−27.73430	53.11797	−27.73438	3.256	< 42.9	0.55 ± 0.20	220	0.202	2012.1.00869.S
388	53.11858	−27.88480			2.13	42.7	< 2.39	393	0.796	2013.1.00884.S
405	53.12283	−27.72280			1.609	42.7	< 0.30	220	0.101	2012.1.00869.S
410	53.12409	−27.89120	53.12405	−27.89123	2.53	43.3	0.72 ± 0.20	220	0.197	2012.1.00869.S
412	53.12436	−27.85163			3.700	44.1	< 0.69	220	0.231	2012.1.00869.S
422	53.12557	−27.88646	53.12560	−27.88651	2.49	< 42.7	0.79 ± 0.16	220	0.156	2012.1.00869.S
423	53.12558	−27.88497			0.648	< 41.4	< 0.47	220	0.156	2012.1.00869.S
444	53.13403	−27.78096			2.39	43.4	< 0.65	220	0.216	2012.1.00869.S
456	53.13799	−27.86825			3.17	43.1	< 0.46	91	0.154	2013.1.00884.S
463	53.14102	−27.76673			1.910	< 42.2	< 0.66	220	0.219	2012.1.00869.S
466	53.14163	−27.81656			2.78	43.2	< 1.70	393	0.566	2013.1.00884.S
470	53.14241	−27.76504			0.366	< 40.7	< 0.66	220	0.219	2012.1.00869.S
502	53.15118	−27.71608			0.968	41.9	< 0.59	220	0.198	2012.1.00869.S
503	53.15119	−27.71373			1.609	< 42.5	< 0.59	220	0.198	2012.1.00869.S
509	53.15518	−27.74074			1.10	41.9	< 2.48	393	0.828	2013.1.00884.S
522	53.15844	−27.77397			2.12	43.3	< 0.60	220	0.200	2012.1.00869.S
528	53.16150	−27.85601			2.97	43.4	< 2.31	393	0.770	2013.1.00884.S
534	53.16230	−27.71213	53.16240	−27.71222	4.379	43.5	0.44 ± 0.15	91	0.149	2013.1.00884.S
535	53.16271	−27.74426			0.679	42.4	< 0.48	220	0.162	2012.1.00869.S
574	53.17868	−27.80263			2.43	42.6	< 1.86	393	0.621	2013.1.00884.S
593	53.18583	−27.80997			2.593	43.4	< 1.88	393	0.628	2013.1.00884.S
633	53.20487	−27.91795	53.20489	−27.91800	2.30	43.4	0.94 ± 0.15	91	0.146	2013.1.00884.S
677	53.24444	−27.90757			2.41	43.4	< 1.97	393	0.658	2013.1.00884.S

Table 3.6: X-ray selected sources observed with ALMA at 870μm in COSMOS field. The columns show X-ray ID (from Marchesi et al., 2016), optical positions, ALMA positions, redshift (2 and 3 decimal places indicate photometric and spectroscopic redshifts, respectively), X-ray luminosity (rest-frame 2-10 keV), primary beam corrected ALMA fluxes, median baseline of the ALMA configuration, the RMS of the map containing the X-ray AGN and the observing ID.

X-ray ID	RA Optical (J2000)	Dec Optical (J2000)	RA ALMA (J2000)	Dec ALMA (J2000)	redshift	$\log_{10}$ ($L_{2-10keV}$/erg s^{-1})	$F_{870\mu m}$ (mJy)	Median baseline (m)	RMS (mJy)	Observing ID
cid 434	149.72072	2.34901	149.72067	2.34904	1.530	44.6	0.32 ± 0.10	91	0.095	2013.1.00884.S
cid 580	149.85469	2.60694			2.11	44.5	< 0.41	91	0.135	2013.1.00884.S
cid 1620	149.87585	2.69028			2.169	44.4	< 0.39	91	0.130	2013.1.00884.S
cid 558	149.88252	2.50513			3.10	44.8	< 0.64	91	0.214	2013.1.00884.S
cid 330	149.95583	2.02806	149.95575	2.02801	1.753	44.6	0.24 ± 0.09	91	0.090	2013.1.00884.S
cid 529	149.98158	2.31501			3.017	44.6	< 0.67	91	0.223	2013.1.00884.S
cid 474	149.99390	2.30146			1.796	44.5	< 0.27	91	0.091	2013.1.00884.S
cid 451	150.00253	2.25863	150.00258	2.25864	2.450	44.6	0.40 ± 0.13	91	0.129	2013.1.00884.S
cid 1127	150.01057	2.26939			2.390	44.1	< 0.63	91	0.211	2013.1.00884.S
cid 1205	150.01070	2.33297	150.01079	2.33300	2.255	43.9	0.35 ± 0.13	91	0.128	2013.1.00884.S
cid 706	150.01105	2.36766			2.11	43.9	< 0.41	91	0.137	2013.1.00884.S
cid 1246	150.01559	2.44216			2.89	44.0	< 0.64	91	0.214	2013.1.00884.S
cid 532	150.01985	2.34914			1.796	44.4	< 0.26	91	0.087	2013.1.00884.S
cid 1216	150.02008	2.35365			2.663	44.1	< 0.63	91	0.211	2013.1.00884.S
cid 987	150.02727	2.43472			1.860	44.0	< 0.40	91	0.132	2013.1.00884.S
cid 659	150.03290	2.45859			2.045	44.0	< 0.27	91	0.091	2013.1.00884.S
cid 1214	150.03677	2.35852	150.03680	2.35843	1.59	44.0	0.35 ± 0.09	91	0.091	2013.1.00884.S
cid 1143	150.03682	2.25778			2.454	44.0	< 0.39	91	0.132	2013.1.00884.S
cid 351	150.04262	2.06329			2.018	44.6	< 0.40	91	0.132	2013.1.00884.S
cid 708	150.05225	2.36927	150.05226	2.36935	2.548	44.0	0.70 ± 0.21	91	0.214	2013.1.00884.S
cid 352	150.05891	2.01518			2.498	44.6	< 0.39	91	0.131	2013.1.00884.S
cid 1247	150.06346	2.42192			3.09	43.9	< 0.61	91	0.202	2013.1.00884.S
cid 1215	150.06454	2.32905	150.06451	2.32912	2.450	44.1	1.33 ± 0.13	91	0.132	2013.1.00884.S
cid 459	150.06467	2.19098			2.89	44.7	< 0.64	91	0.215	2013.1.00884.S
cid 960	150.07462	2.30206	150.07455	2.30199	2.122	43.9	0.49 ± 0.12	91	0.120	2013.1.00884.S
cid 1219	150.07600	2.26429			2.946	44.1	< 0.60	91	0.200	2013.1.00884.S
cid 72	150.09154	2.39908			2.475	44.6	< 0.42	91	0.141	2013.1.00884.S
cid 85	150.09653	2.29309			1.349	43.8	< 0.27	91	0.091	2013.1.00884.S
cid 467	150.10201	2.10549	150.10194	2.10550	2.288	44.8	0.39 ± 0.13	91	0.132	2013.1.00884.S
cid 149	150.10371	2.66577			2.955	44.7	< 0.69	91	0.230	2013.1.00884.S
cid 1144	150.10477	2.24364	150.10469	2.24365	1.912	44.1	0.62 ± 0.09	91	0.090	2013.1.00884.S
cid 86	150.11958	2.29591	150.11958	2.29595	1.831	44.3	0.23 ± 0.08	91	0.084	2013.1.00884.S
cid 87	150.13304	2.30328	150.13309	2.30324	1.598	44.9	0.23 ± 0.09	91	0.090	2013.1.00884.S
cid 965	150.15218	2.30785	150.15216	2.30779	3.178	44.2	0.62 ± 0.20	91	0.197	2013.1.00884.S
cid 914	150.18001	2.23128	150.17992	2.23133	2.146	44.0	0.51 ± 0.13	91	0.127	2013.1.00884.S
cid 81	150.18655	2.45533	150.18660	2.45530	1.991	44.0	0.33 ± 0.08	91	0.085	2013.1.00884.S
cid 121	150.19180	2.54391			2.79	44.3	< 0.64	91	0.214	2013.1.00884.S
cid 917	150.19263	2.21985	150.19260	2.21983	3.090	43.9	3.58 ± 0.20	91	0.201	2013.1.00884.S
cid 124	150.20532	2.50293			3.07	44.3	< 0.63	91	0.211	2013.1.00884.S
cid 953	150.21075	2.39147			3.095	44.1	< 0.65	91	0.216	2013.1.00884.S
cid 83	150.21416	2.47502			3.075	44.5	< 0.61	91	0.202	2013.1.00884.S
cid 1085	150.21634	1.98874			2.231	44.5	< 0.43	91	0.143	2013.1.00884.S
cid 915	150.21909	2.27867			1.84	44.0	< 0.28	91	0.093	2013.1.00884.S
cid 976	150.22527	2.35122			2.478	43.9	< 0.38	91	0.128	2013.1.00884.S
cid 954	150.23180	2.36401	150.23178	2.36400	1.936	44.2	0.40 ± 0.09	91	0.086	2013.1.00884.S
cid 970	150.23550	2.36176			2.501	44.6	< 0.60	91	0.200	2013.1.00884.S
cid 75	150.24779	2.44215	150.24777	2.44216	3.029	44.7	0.51 ± 0.20	91	0.203	2013.1.00884.S
cid 31	150.27214	2.23010	150.27217	2.23009	2.611	44.8	0.64 ± 0.22	91	0.216	2013.1.00884.S
cid 90	150.28482	2.39505			1.932	44.4	< 0.29	91	0.098	2013.1.00884.S
cid 365	150.28563	2.01459			2.671	44.5	< 0.61	91	0.204	2013.1.00884.S
cid 58	150.32689	2.09415			2.798	44.5	< 0.62	91	0.205	2013.1.00884.S
cid 53	150.34372	2.14067			1.787	44.2	< 0.40	91	0.133	2013.1.00884.S
cid 581	150.35358	2.34220			1.708	44.5	< 0.26	91	0.086	2013.1.00884.S
cid 62	150.37364	2.11203	150.37366	2.11203	1.914	44.5	0.52 ± 0.09	91	0.086	2013.1.00884.S

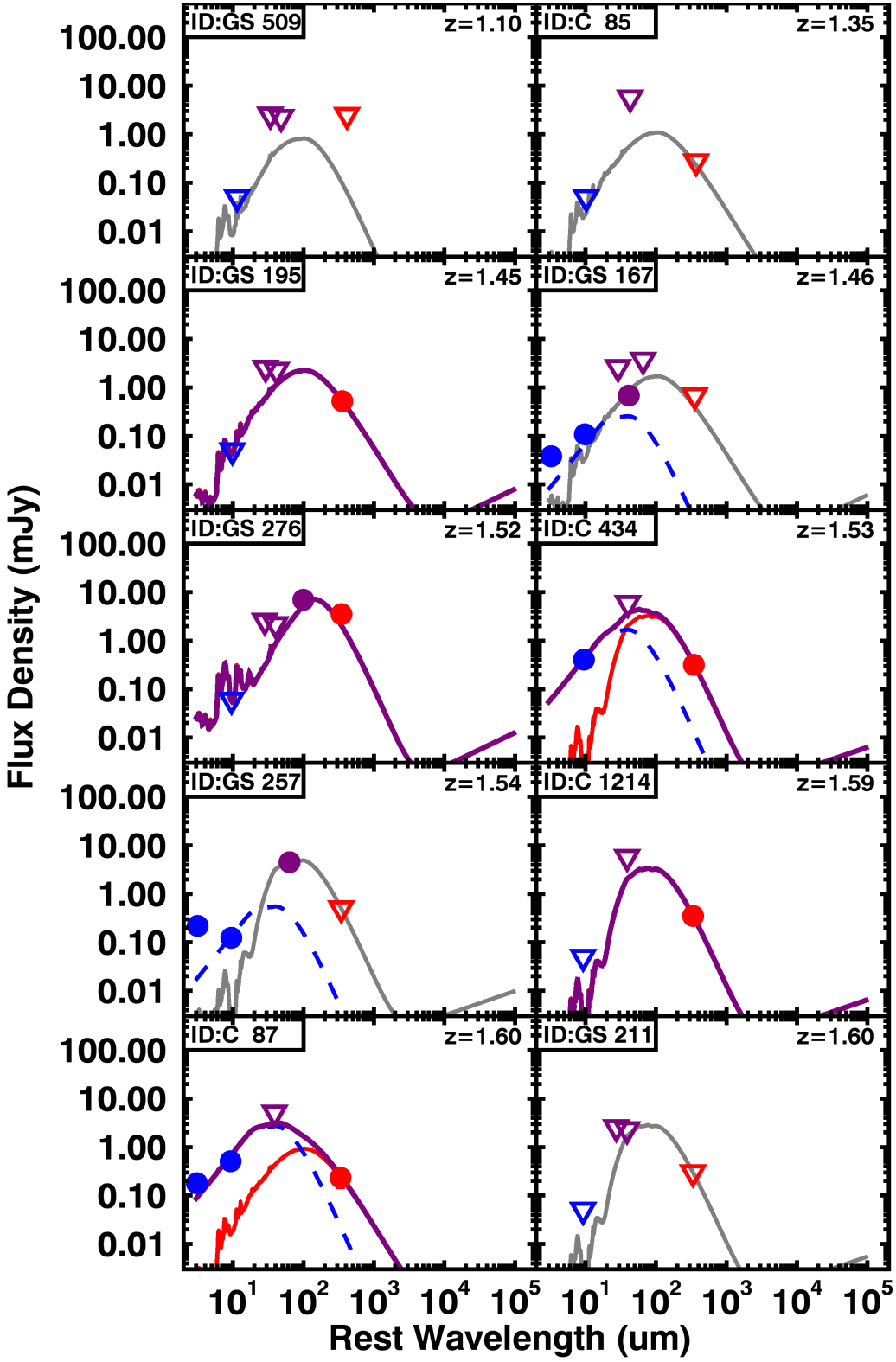

Figure 3.11: The SED fits of AGN used in our sample. The blue dashed curve is the AGN component, while the red solid curve is the star-forming component. The total combined SED is shown as a purple solid curve. The grey curves correspond to an upper limit constraint on the SF component. The photometry is colour-coded, with blue corresponding to *Spitzer*, purple to *Herschel* bands, and red to the ALMA photometry.

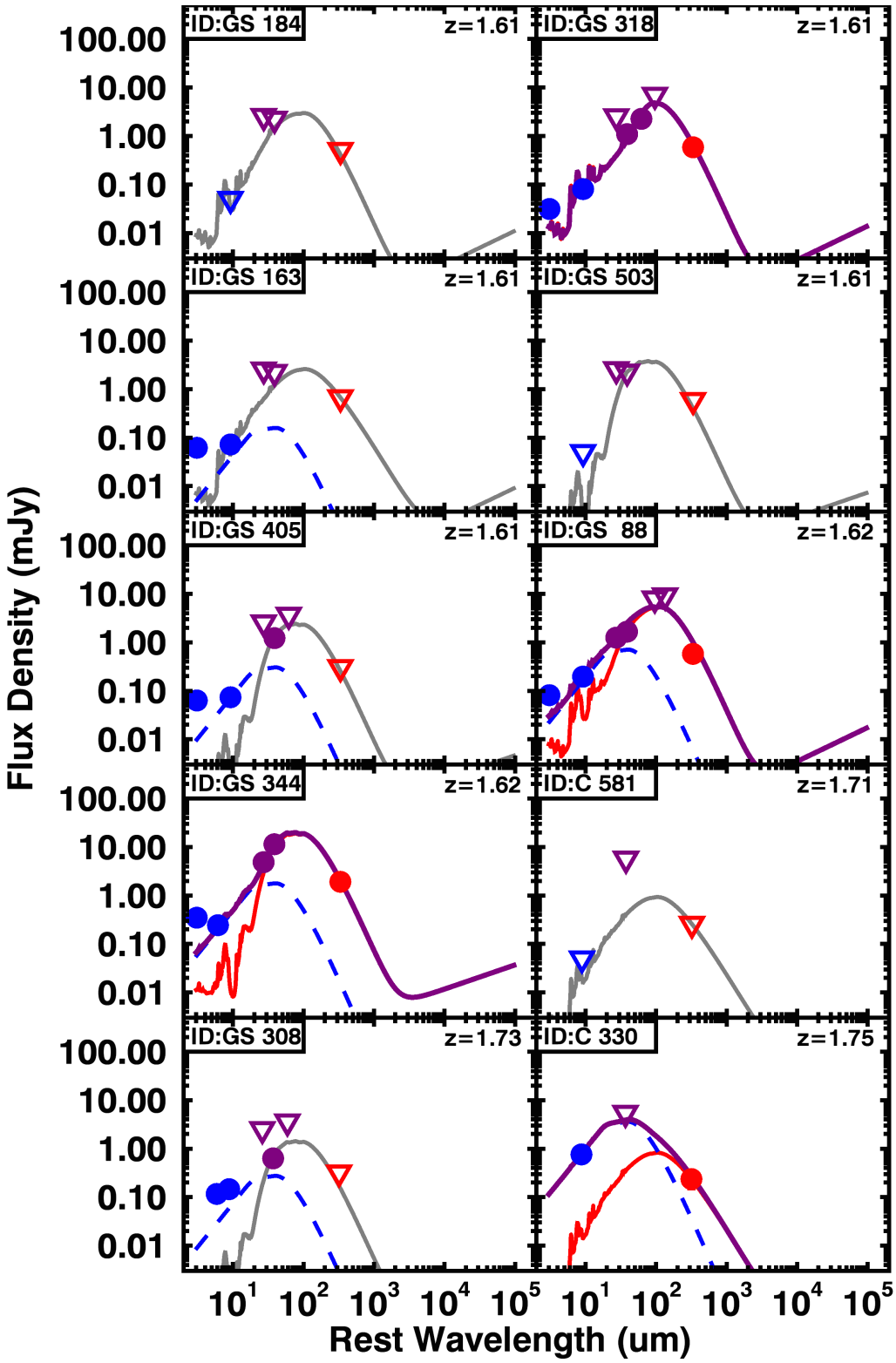

Figure 3.12: Continued

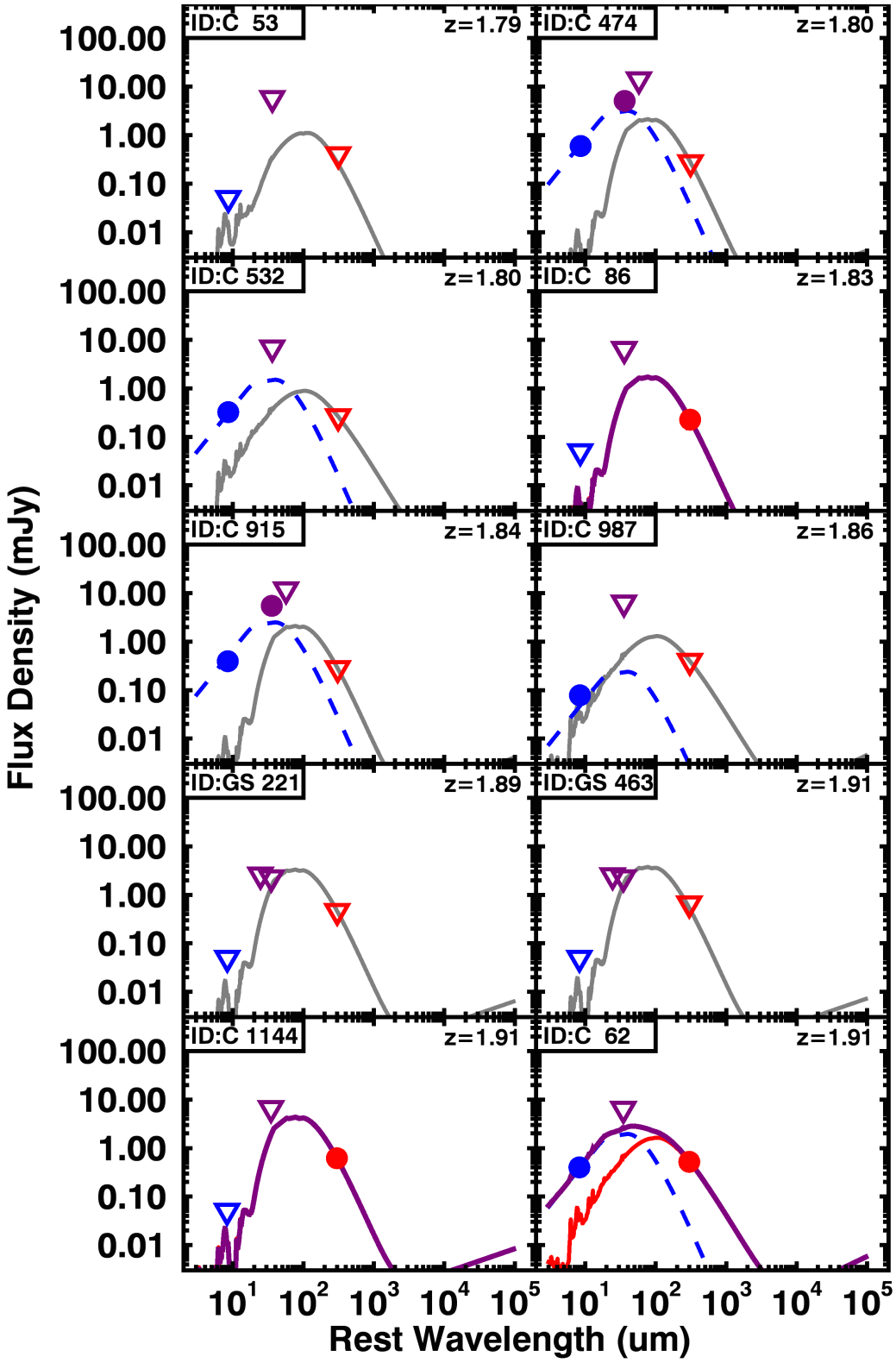

Figure 3.13: Continued

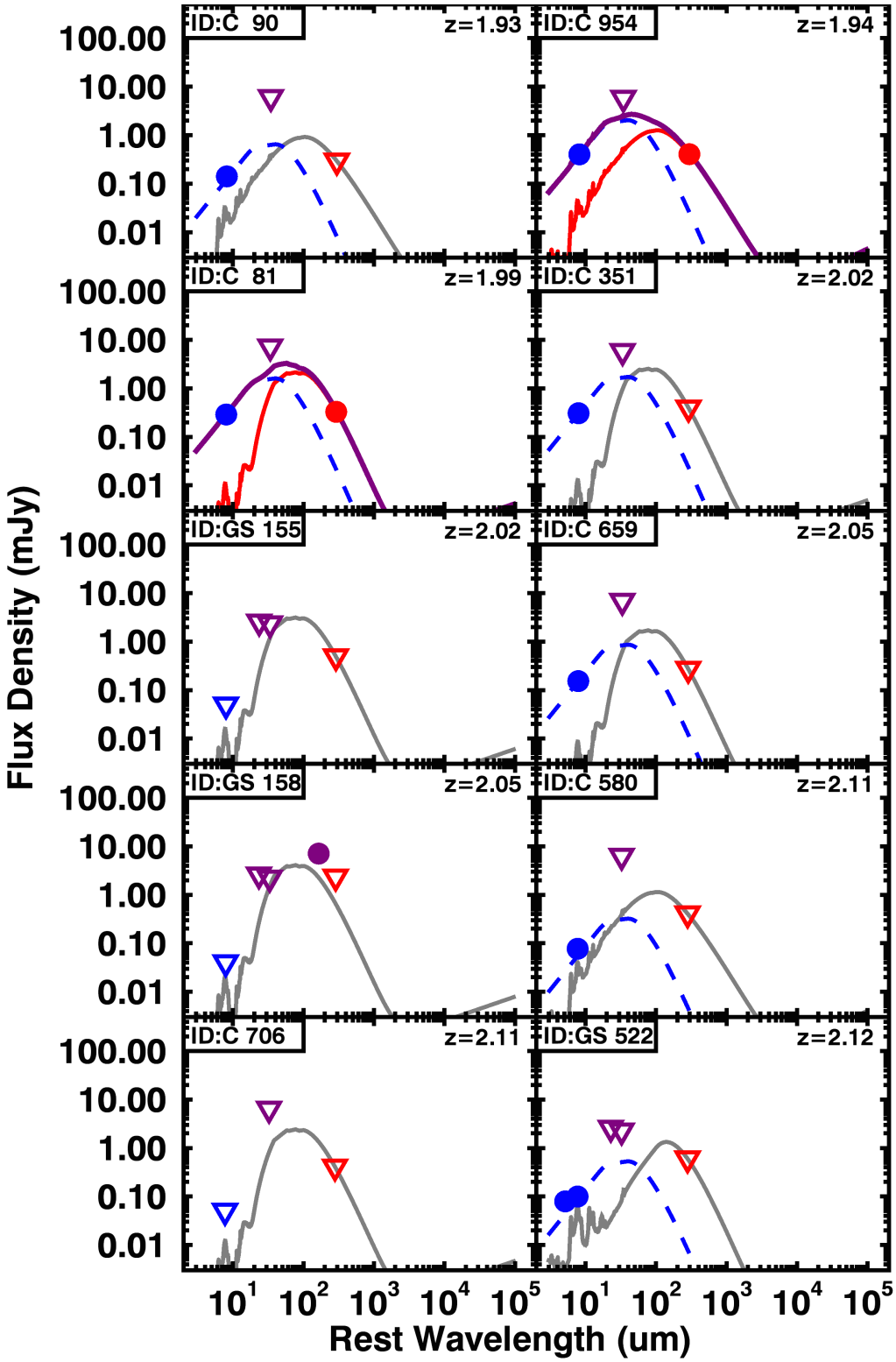

Figure 3.14: Continued

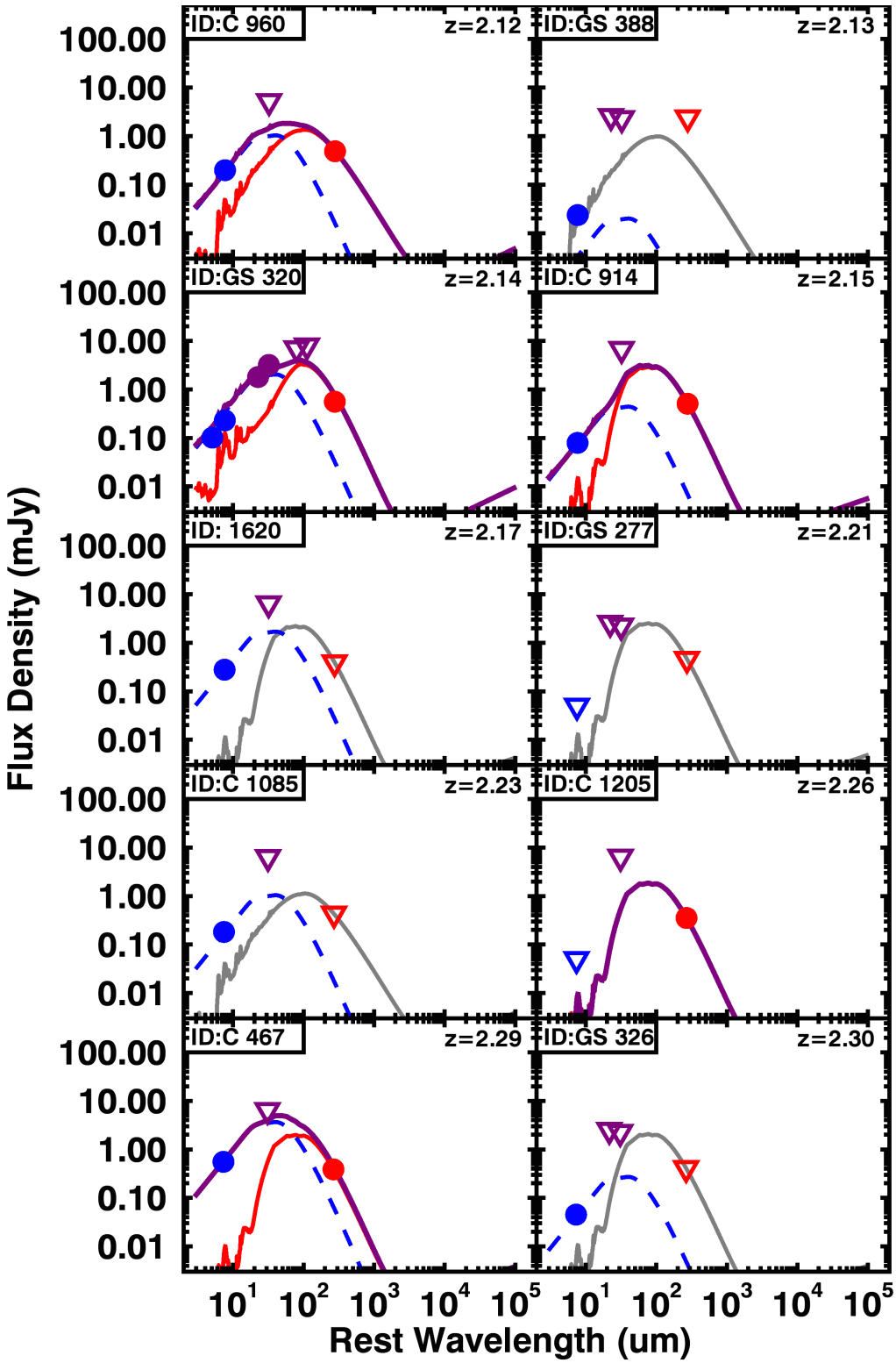

Figure 3.15: Continued

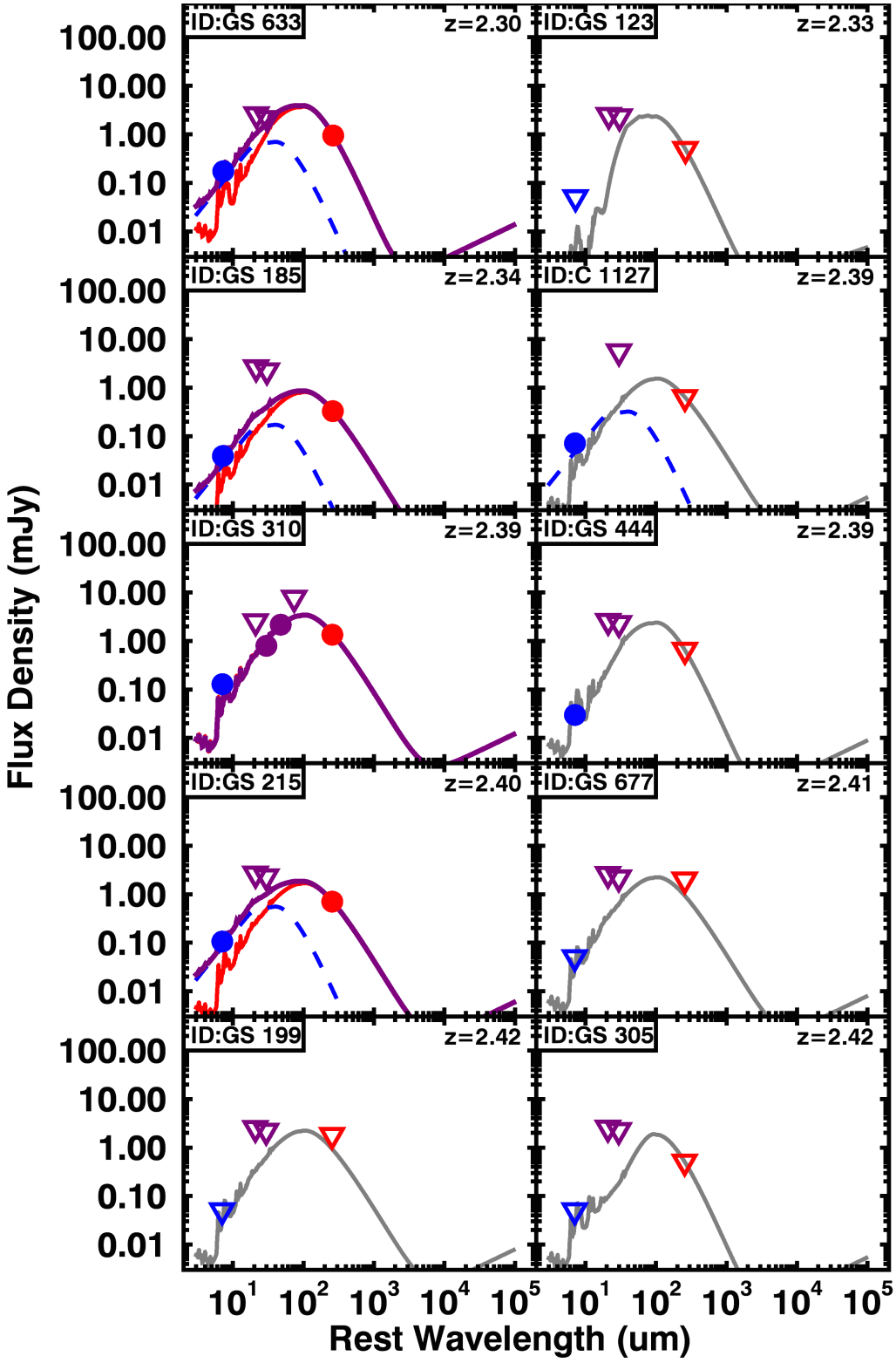

Figure 3.16: Continued

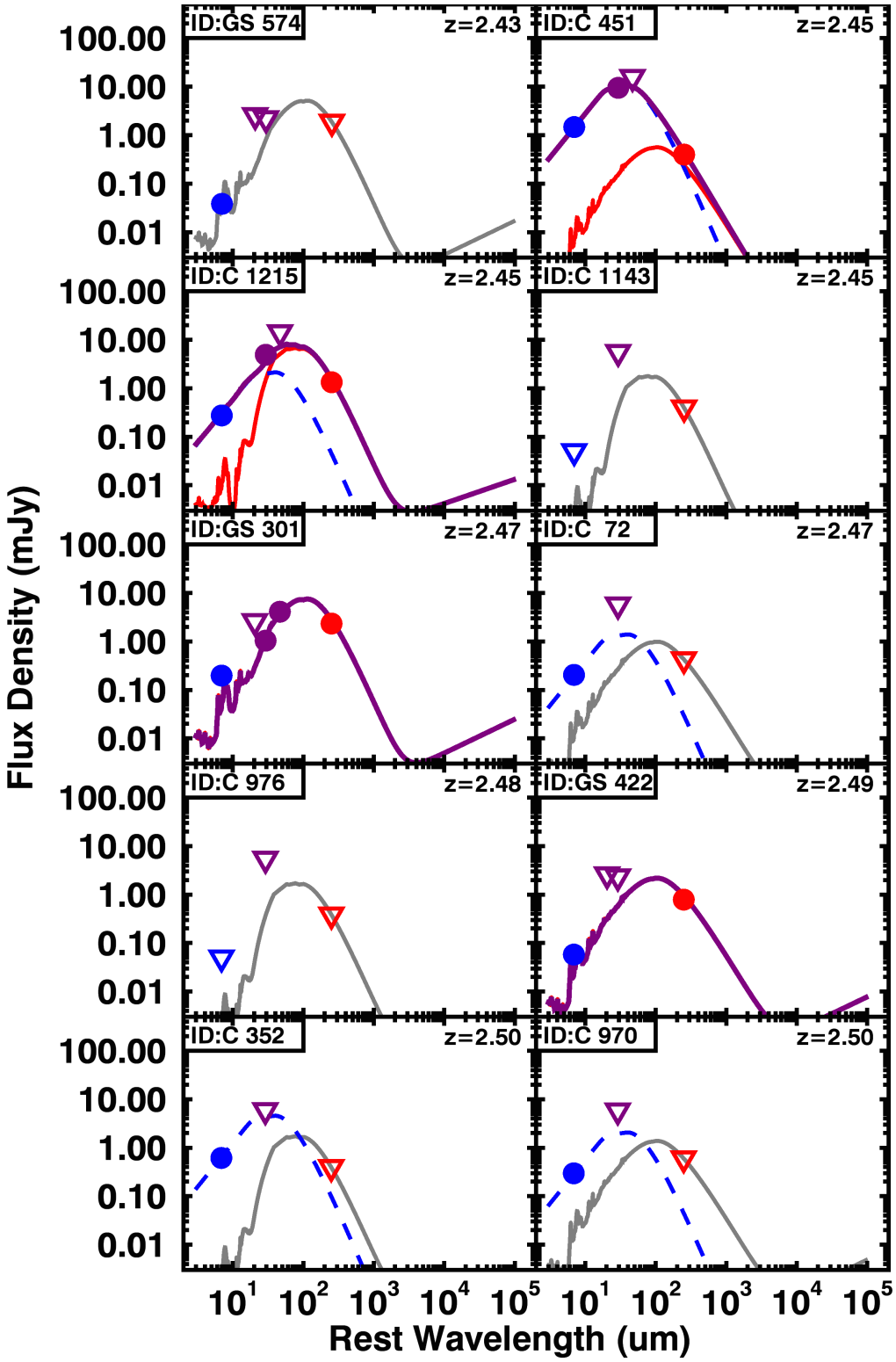

Figure 3.17: Continued

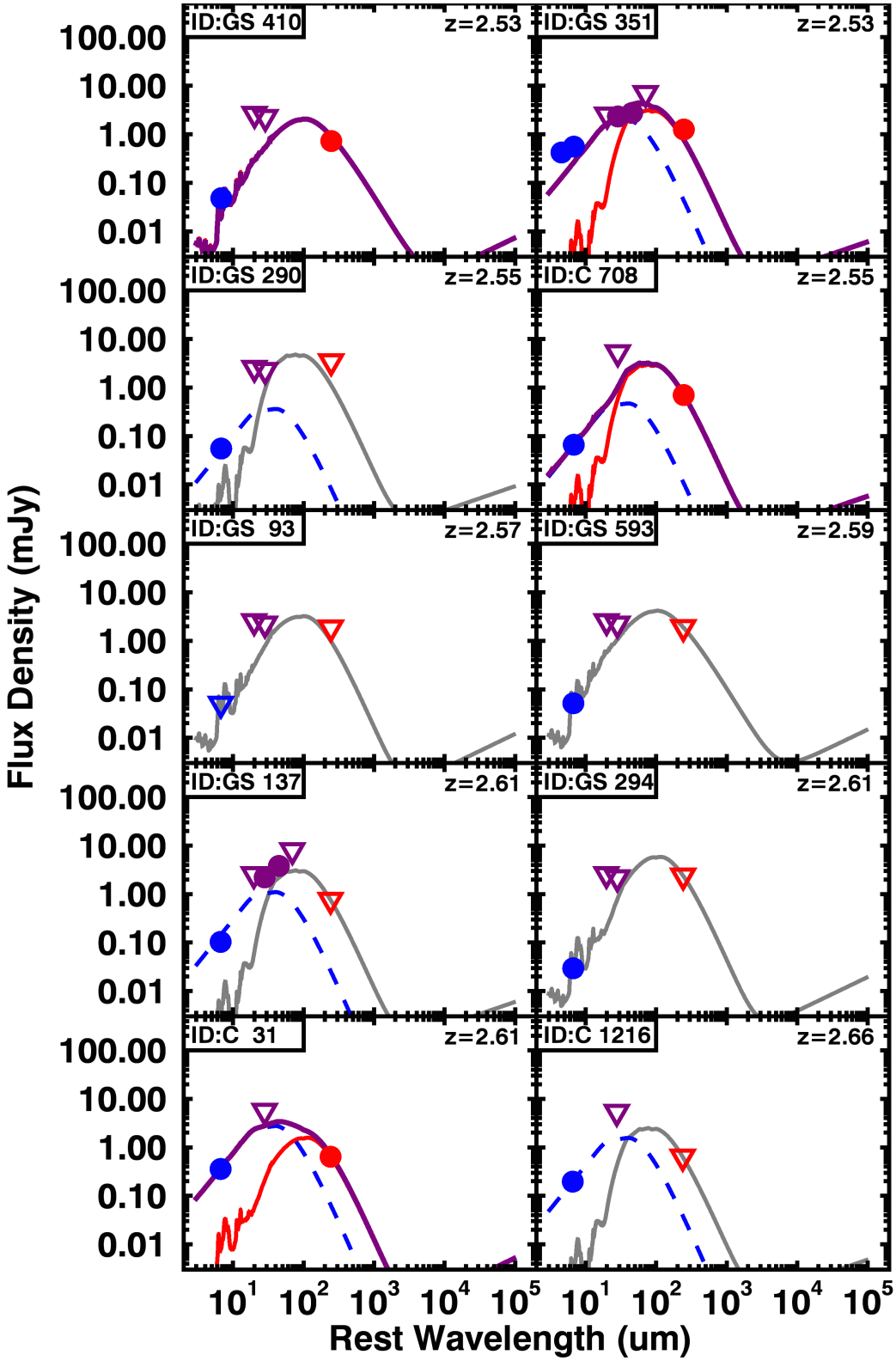

Figure 3.18: Continued

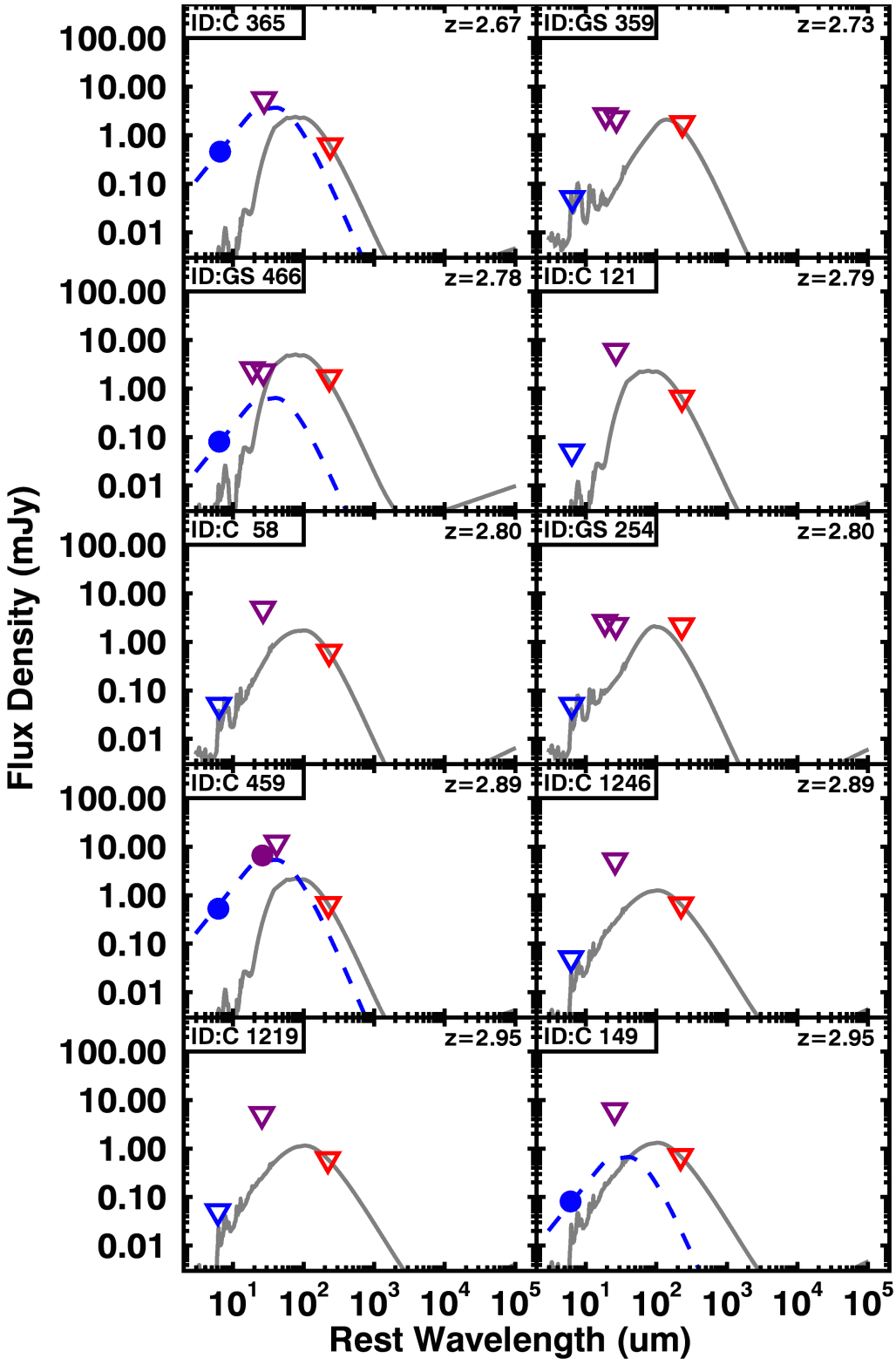

Figure 3.19: Continued

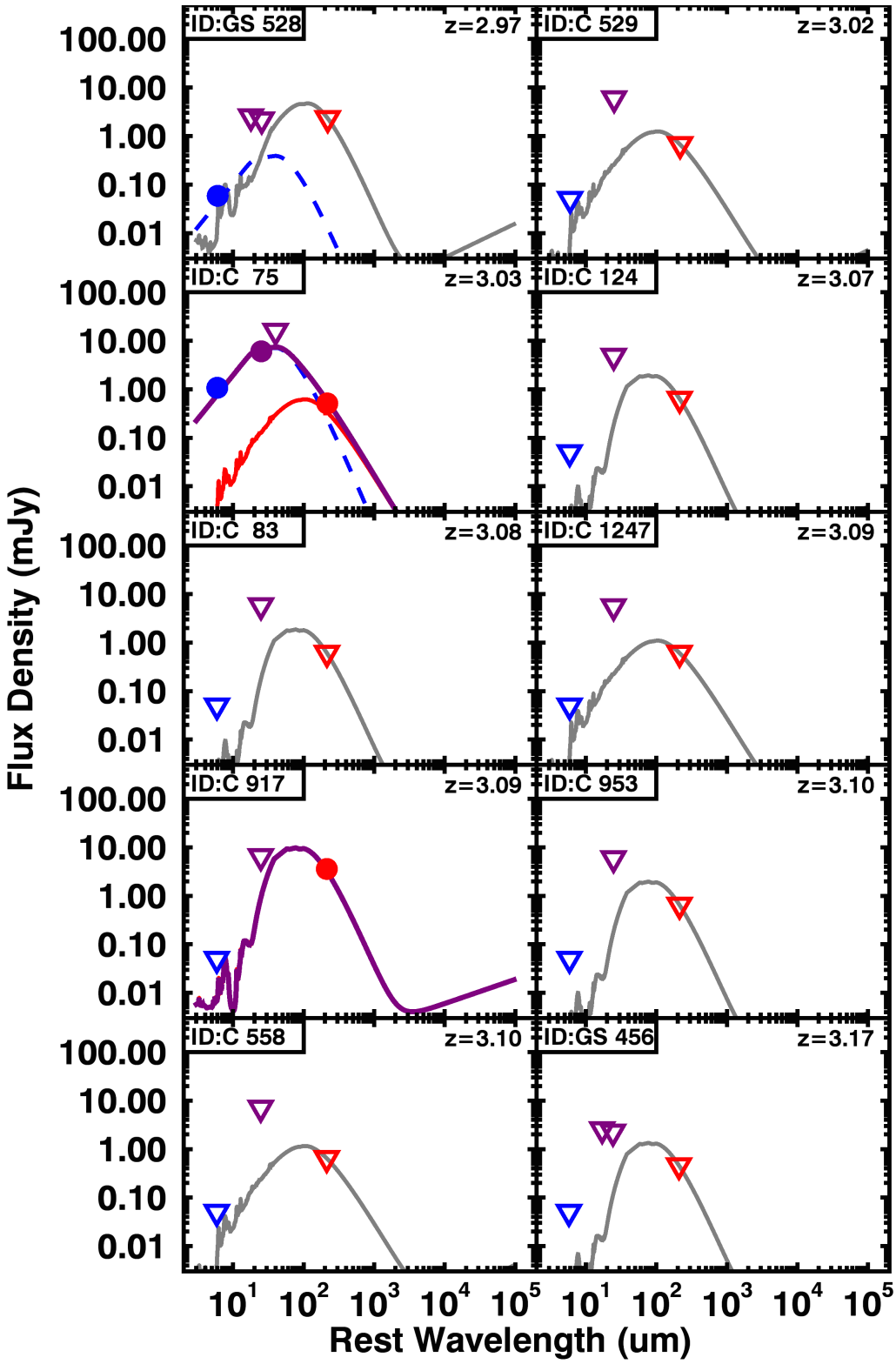

Figure 3.20: Continued

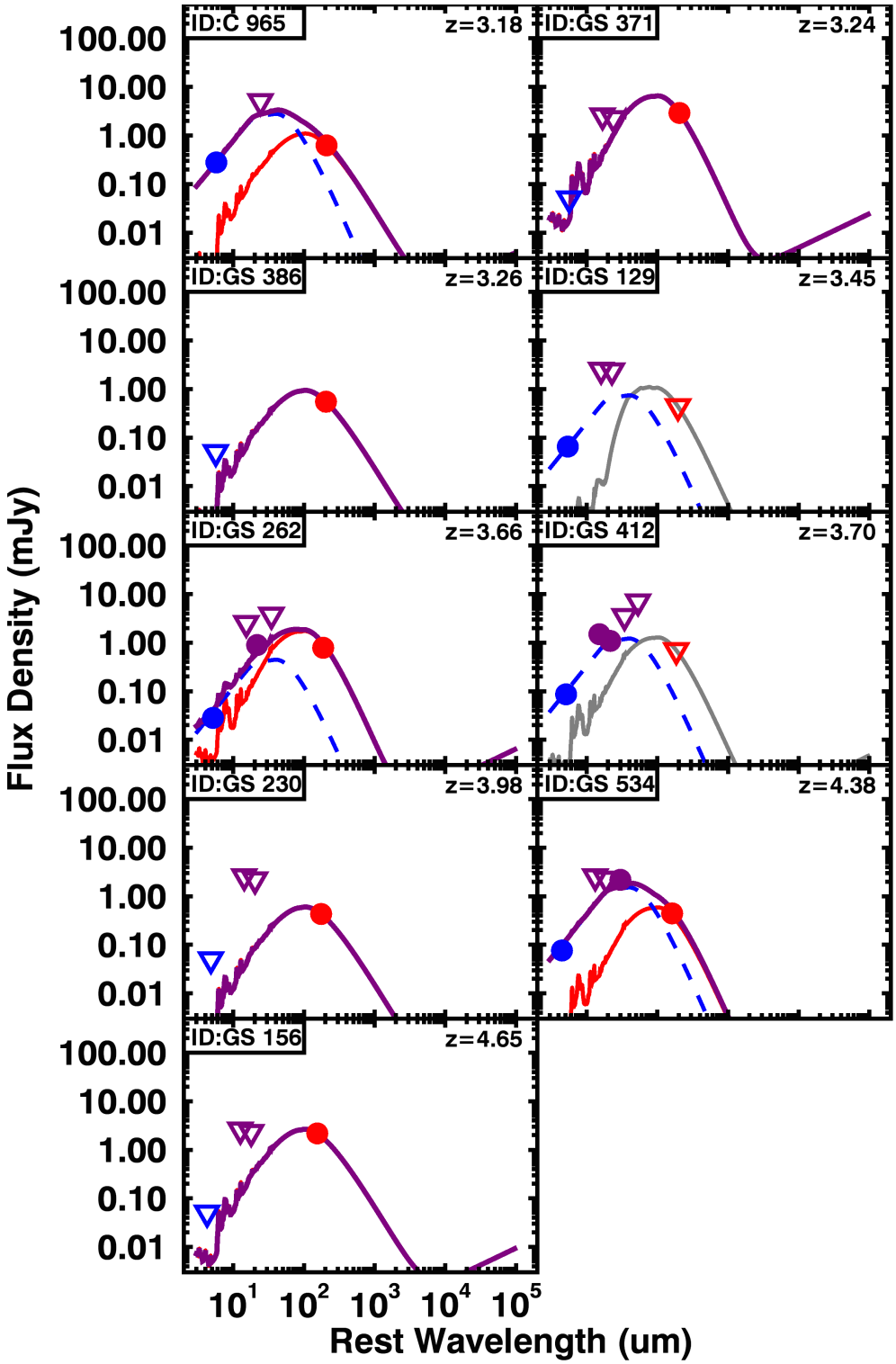

Figure 3.21: Continued

CHAPTER 4

KASHz: No evidence for ionised outflows instantaneously suppressing star-formation in moderate luminosity z=1–2.5 AGN

"It's been said that astronomy is a humbling and, I might add, a character-building experience."

–Carl Sagan, Astronomer

Abstract

As part of our KMOS AGN Survey at High-redshift (KASHz), we present spatially-resolved VLT/KMOS and VLT/SINFONI spectroscopic data and ALMA 870μm continuum imaging of eight z=1.4–2.6 moderate luminosity AGN ($L_X = 10^{42} - 10^{45}$ ergs s^{-1}). We map ionised outflows, Hα emission and rest-frame far infrared (FIR) emission to search for any spatial anti-correlation between ionised outflows and star formation, that has previously been claimed for some high-z AGN and used as evidence for negative and/or positive AGN feedback. Firstly, we conclude that Hα alone is unreliable to determine the distribution of star formation inside our AGN host galaxies based on evidence that: (i) star formation rates inferred from attenuation-corrected Hα lie below those inferred from FIR, with over an order-of-magnitude difference in one case; (ii) the FIR continuum is more compact than the Hα emission by a factor of ~ 2 on average; (iii) in half of our sample, we observe significant spatial offsets between the FIR and Hα emission, with an average offset of 1.4 ± 0.6 kpc across the sample. Secondly, for the five targets with outflows we find no evidence for a spatial anti-correlation between outflows and star

formation using either Hα or FIR as a tracer. This holds for our re-analysis of a famous z=1.6 X-ray AGN ('XID 2028') where positive and negative feedback has been previously claimed. Based on our results, any impact on star formation by ionised outflows must be subtle, either occurring on scales below our resolution, or on long timescales.

4.1 Introduction

Super massive black holes (SMBH) are known to reside at the centre of massive galaxies (Kormendy & Ho 2013). When these SMBHs grow, through accretion events, they become visible as active galactic nuclei (AGN; Soltan, 1982; Merloni et al., 2004). Current theoretical models of galaxy evolution require these AGN to inject significant energy into their host galaxies in order to replicate the basic properties of local galaxies and the intergalactic medium (IGM), such as: the black hole–spheroid relationships, the steep mass function, increased width of sSFR distributions (star formation rate normalized to stellar mass) as a function of stellar mass, galaxy sizes, AGN number densities, galaxy colour bi-modality and enrichment of the IGM by metals (e.g., Silk & Rees, 1998; Di Matteo et al., 2005; Alexander & Hickox, 2012; Vogelsberger et al., 2014; Hirschmann et al., 2014; Crain et al., 2015; Segers et al., 2016; Beckmann et al., 2017; Harrison, 2017; Choi et al., 2018; Scholtz et al., 2018). The key role of the AGN in these models is to either regulate the cooling of the interstellar medium (ISM) or intracluster medium (ICM), or to eject gas out of the galaxy through outflows. Ultimately this process, usually referred to as "AGN feedback", is believed to regulate the rate at which stars can form. However, from an observational perspective, there is still no clear consensus in the literature on the role of AGN in regulating star formation in the overall galaxy population, particularly at high redshift (e.g., Harrison, 2017; Cresci & Maiolino, 2018).

Over the past decade there have been many studies identifying and characterising multiphase outflows (see e.g., Harrison et al., 2018; Cicone et al., 2018). Indeed, there is now significant evidence that energetic ionised, atomic and molecular outflows are a common property of AGN (e.g. Veilleux et al., 2005; Morganti et al., 2005; Ganguly & Brotherton, 2008; Alexander et al., 2010; Sturm et al., 2011; Cicone et al., 2012; Harrison et al., 2012b; Mullaney et al., 2013; Cicone et al., 2014; Balmaverde & Capetti, 2015;

Carniani et al., 2015; Brusa et al., 2015; Harrison et al., 2016b; Woo et al., 2016; Leung et al., 2017; Brusa et al., 2018; Förster Schreiber et al., 2018a; Lansbury et al., 2018; Fluetsch et al., 2019; Ramos Almeida et al., 2019).

AGN-driven outflows have been identified on scales between tens of parsecs to tens of kiloparsecs (Storchi-Bergmann et al., 2010; Veilleux et al., 2013; Cresci et al., 2015a; Feruglio et al., 2015; Kakkad et al., 2016; McElroy et al., 2016; Rupke et al., 2017; Jarvis et al., 2019). However, despite observations showing that AGN outflows are common, the impact that they have on star formation is still open to debate. Although, in many of the studies, the most powerful outflows are thought to remove gas at a rate faster than it can be formed into stars, there are still considerable uncertainties in these mass outflow rate calculations due to uncertain spatial scales and the assumptions required to convert emission line luminosities into gas masses (e.g. Karouzos et al., 2016; Villar-Martín et al., 2016; Husemann et al., 2016; Rose et al., 2018; Harrison et al., 2018). Measurements are more accurate for the most nearby sources (e.g. Revalski et al., 2018; Venturi et al., 2018; Fluetsch et al., 2019); however, these samples lack the most powerful AGN which are thought to be the most important for influencing galaxy evolution.

Another approach to determine the impact of AGN-driven outflows, is to use spatially-resolved observations to map both the outflows and the star formation in or around the outflows. For example, using longslit and integral-field spectroscopy star formation has been detected *inside* outflows in local AGN host galaxies, which may be a form of 'positive' feedback (Maiolino et al., 2017; Gallagher et al., 2019). On the other hand, Cresci et al. (2015a) suggest both *suppressed* star formation at the location of an ionised outflow ('negative feedback') and *enhanced* star formation around the edges of the outflow ('positive feedback') for a z=1.6 X-ray identified AGN, commonly referred to as "XID 2028". Similar findings were presented for three z=2.5 extremely powerful (and consequently rare) quasars by Cano-Díaz et al. (2012) and Carniani et al. (2016). These latter works, studying high-redshift AGN, used high-velocity [O III]λ5007 emission-line components to map the ionised outflows and Hα emission to map the spatial distribution star formation.

Hα emission (as well as ultra-violet continuum) can be used to trace regions of ongoing star formation (e.g. Hao et al., 2011; Murphy et al., 2011). However, since this

emission is at relatively short wavelengths it is sensitive to dust obscuration. Indeed, significant levels of the star formation in high-redshift galaxies is obscured by dust (Madau et al., 1996; Casey et al., 2014; Whitaker et al., 2014) and sometimes the UV and Hα emission can be completely hidden by dust (e.g., Hodge et al. 2016; Chen et al. 2017). In these cases the UV and optical light is absorbed by the dust and re-emitted at far-infrared (8–1000 μm; TIR) wavelengths. Consequently, the FIR emission is sensitive to on-going *obscured* star formation (for reviews see Kennicutt & Evans, 2012; Calzetti, 2013). Importantly for this work, high-redshift AGN and quasar host galaxies have been shown to host significant levels of star-formation obscured by dust (e.g., Whitaker et al., 2012; Burgarella et al., 2013; Stanley et al., 2015, 2018). In this current study we investigate different possible tracers of star formation, in z=1.4–2.6 AGN host galaxies, by combining integral-field spectroscopy, to map the Hα emission, with high spatial-resolution observations of the rest-frame FIR from the Atacama Large Millimetre Array (ALMA)

A limitation of previous work, that investigates the impact of AGN outflows on star formation in distant galaxies, is that they are based on only a few targets and it is consequently unclear how common these effects are in the wider population of more typical high-redshift AGN. Therefore, in this work we make use of our large, representative parent sample of the "KMOS AGN Survey at High-z" (KASHz: Harrison et al., 2016b, Harrison et al. in prep). KASHz is a systematic integral field spectroscopy survey designed to spatially-resolve the rest-frame optical emission lines of $\approx$250 X-ray selected AGN, that are representative of the distant (z =0.6–2.6) AGN population. KASHz has the benefit of characterising the ionised gas properties of typical distant X-ray AGN and can be used to place into context other studies based on smaller numbers of targets, such as higher spatial-resolution (AO-assisted) integral field unit (IFU) observations (e.g., see Circosta et al., 2018). By combining multi-wavelength photometry from UV–submm we can characterise the star-formation rates, AGN luminosities and stellar masses of the sample, and explore the ionised gas properties, such as the prevalence of outflows, as a function of various AGN and host galaxy properties. KASHz has already demonstrated that: (1) AGN are $5--10$ times more likely to host high-velocity outflows ($>$ 600 km s^{-1}) than star-forming, non-active, galaxies; and (2) shown that the most luminous AGN ($L_X > 6 \times 10^{43}$ erg s^{-1}) are ~ 2 times more likely to host high-velocity outflows than less luminous AGN

(Harrison et al., 2016b). Importantly, the sample still contains some relatively extreme sources, both in terms of AGN luminosity and outflow properties (e.g., 'XID 2028' presented in Cresci et al., 2015a); however, we can place these objects within the context of the overall, more typical, AGN population.

In this pilot study we use sensitive high-resolution ALMA observations and IFU observations of 8 moderate luminosity AGN at redshift z=1.6-2.6. With these data we compare and contrast the FIR continuum and Hα as possible star formation tracers in our AGN host galaxies. Combining these possible star formation tracers with the observations of AGN outflows, we then investigate the impact of these outflows on the star formation. In §2 we describe the sample selection and the data used in our study, in §3 we outline the data analyses such as spectral fitting, constructing outflow maps and the analyses of the ALMA data, and in §4 we present our results and discuss them within the broader context of the impact that AGN outflows have on star formation.

In all of our analyses we adopt the cosmological parameters of $H_0 = 68\,\mathrm{km\,s^{-1}}$, $\Omega_M = 0.27$, $\Omega_\Lambda = 0.73$ and assume a Chabrier (2003) initial mass function (IMF).

4.2 Sample Selection, observations and source properties

The primary objectives of our study are to (i) compare the Hα and FIR continuum emission as tracers of the star-formation inside AGN host galaxies (at the peak of cosmic star-formation and black-hole accretion; i.e., z = 1–3; Madau & Dickinson 2014; Aird et al. 2015) and to (ii) establish if AGN-driven ionised outflows have an instantaneous impact on the star formation within these galaxies. To achieve this, we select a sample of AGN host galaxies with spatially-resolved Hα and [O III] emission from integral field spectroscopy and with ancillary rest-frame FIR data from ALMA. In § 5.2.1 we describe the selection of our sample, in § 4.2.2 and § 5.2.2 we describe the spectroscopic and ALMA observations, respectively, and in § 5.4.1 we describe our broad-band SED fitting and investigate how representative our targets are of the parent sample.

4.2.1 Sample selection

We selected our sample from the KASHz survey, which is an IFU survey of 250, z=0.6–2.6 X-ray detected AGN from the fields of CDFS, COSMOS, UDS and SSA22 (Harrison et al. 2016b). The IFU data in KASHz is predominantly from VLT/KMOS, but is also supplemented by archival VLT/SINFONI data. The survey description and the first part of the sample is described in Harrison et al. (2016b) and the full sample will be described in Harrison et al. (in prep.). Briefly, the KASHz galaxies were selected based on an X-ray detection and a known archival redshift that places the redshifted Hα and/or [O III]λ5007 within one of the YJ, H or K wavebands; 90% of the used archival redshifts were spectroscopic. Some targets were observed in only a single grating, whilst other targets were observed in two gratings to obtain data on both emission lines. Overall, 110 sources in the sample have detections in [O III] and 110 sources have detections in Hα, with 38 having detections in both emission lines.

To achieve the objectives of our study, (i,e. tracing the ionised gas kinematics using the [O III] line to map ionised outflows; the distribution of Hα emission; determining the location of the dusty star formation as traced by the rest FIR emission) we select the KASHz sources with: (1) sufficient quality IFU data to reliably map both the Hα and [O III] emission lines (i.e., both detected with SNR$>$10) and (2) significant detections (SNR$>$4) in archival ALMA images at an observed wavelength $\approx$870 or $\approx$1100 μm (i.e., ALMA Bands 6 or 7, corresponding to rest-frame wavelengths of $\approx$260–400μm; see § 5.2.2). We further required the ALMA data to have a resolution comparable to, or better than, our IFU observations (i.e., typically $\lesssim 0.7$ arcsec; see § 4.2.2). This final criterion allows us to determine the location of the FIR emission to an accuracy of $\lesssim 0.1$ arcsecond (see § 4.3.3).

Seven KASHz targets met the selection criteria described above (ID 1–7; Table 4.1). For this study we also include ALESS 75.1 (ID 8), a z=2.55 AGN from Chen et al. (2019), which is not part of KASHz, but it has existing IFU and ALMA data, matching the criteria described above. This object was identified as an AGN at mid-infrared wavelengths in previous work (Stanley et al. 2018), which we confirm here using new SED fitting (§ 5.4.1). The 12μm AGN luminosity of $10^{46.0}$ erg s^{-1} implies an intrinsic X-ray luminos-

ity of $L_{2-10\,\mathrm{keV}} = 10^{45.5}$ erg s^{-1} for this AGN (following Asmus et al. 2011).[1]

The IDs, sky positions, redshifts, X-ray IDs and X-ray luminosities for our final sample of 8 targets are presented in Table 4.1. In the table we also provide other names which have been commonly used in the literature for some of the objects. Indeed, our sample includes well-studied objects, including ID 5 which has multi-wavelength spatially-resolved observations (see a summary in Loiacono et al., 2019). In particular, ID 6 was presented in Cresci et al. (2015a) as exhibiting both suppression and enhancement of star formation, traced by Hα, by an AGN-driven outflow traced by [O III] (also see Brusa et al., 2018, for CO observations); we compare our results to the previous work on this source in § 4.4.4.

Figure 4.1 places our sources within the context of the overall KASHz sample by showing the relative distributions of X-ray luminosities and [O III] emission-line widths (W_{80}; width of the emission-line containing 80% of the flux; Harrison et al. 2016b). Our sample covers a similarly wide range of X-ray luminosities, from moderate to luminous AGN, but lacks objects with the most extreme [O III] line widths ($W_{80} > 800\,\mathrm{km\,s^{-1}}$). However, as we demonstrate in § 4.4.4, this does not mean that our targets lack outflow signatures in the [O III] emission-line profiles (§ 4.3.1 & § 4.4.4). We discuss our results in the context of the overall population in § 4.4.4.

4.2.2 IFS observations

In order to map the Hα and [O III] emission of the targets in our sample, we used data from the near-infrared integral-field spectrograph VLT/KMOS (Sharples et al., 2004, 2013) and VLT/SINFONI (Eisenhauer et al., 2003; Bonnet et al., 2004). The broad results of the KASHz survey are presented in Harrison et al. (2016b) and we give a description of the data reduction in the paragraph below. However, in Table 4.1 we give the references to the papers that provide the details of the data and reduction steps for the individual data cubes used in this work. We note that the basic methods used for reducing all of the data were fundamentally the same, and any small differences in the adopted approach in the individual papers are accounted for in our data analysis methods and therefore do no affect

[1] We note that this object is covered by, but undetected in, the E-CDFS field with relatively shallow *Chandra* X-ray coverage (Xue et al. 2016). This non-detection implies that this source is a heavily obscured AGN.

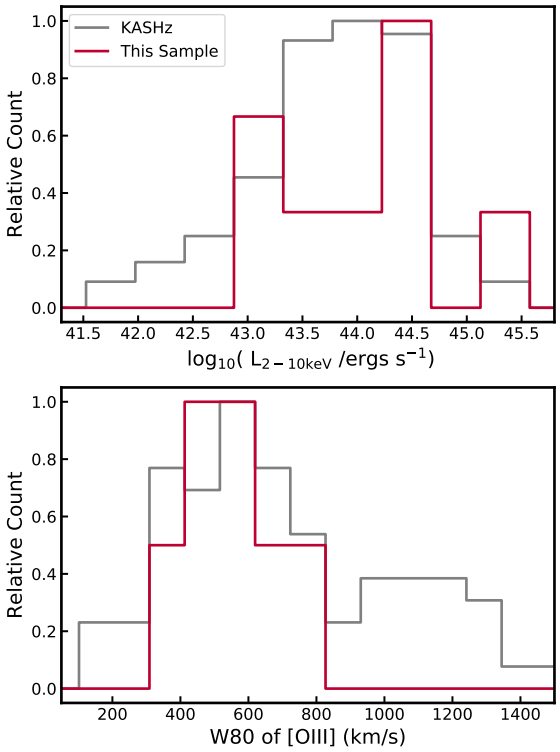

Figure 4.1: Histograms of the X-ray luminosities ($L_{2-10\mathrm{keV}}$; top panel) and W_{80} velocity width ([O III] velocity width containing 80 % of the line flux; bottom panel) for the sample in this work (red) and the parent KASHz sample (grey).

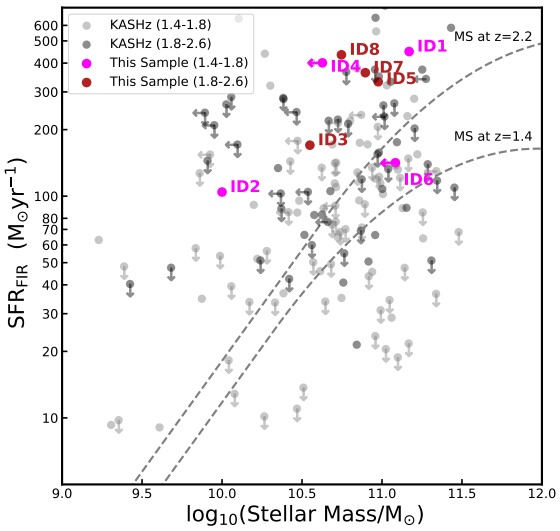

Figure 4.2: Star-formation rate (from FIR) versus stellar mass for the AGN used in this work (coloured red for z=1.8–2.6 and magenta for z=1.4–1.8) compared to the full KASHz sample (black for z=1.8–2.6 and grey for z=1.4–1.8). The lower and upper dashed curves indicate the 'main sequence' of star-forming galaxies (Schreiber et al., 2015) at z=1.4 and z=2.2, respectively. Our sample covers a broad range in star-formation rates and stellar masses but is limited to sources on, or above, the main sequence (see § 5.4.1).

Table 4.1: Basic properties of our AGN sample. (1) Object ID in this paper; (2) X-ray ID from Hsu et al. (2014); Marchesi et al. (2016); Kocevski et al. (2018); (3) other names commonly adopted in the literature; (4,5) Optical coordinates of the objects; (6) Redshift measured from the emission lines (see § 4.3.1); (7) AGN spectral type (see § 4.3.1); (8) X-ray luminosity (2-10 keV) from Hsu et al. (2014); Marchesi et al. (2016); Kocevski et al. (2018); (9) [O III] luminosity from our emission line modelling (see § 4.3.1); (10,11) Stellar mass and FIR luminosity due to star formation from our SED fitting (see § 5.4.1). The stellar mass has a 0.3 dex systematic error. (12) Reference for details of the two reduced IFU cubes for each target's [O III] and Hα emission-line data; (13) Seeing FWHM from the observed PSF stars for the cubes containing [O III]/Hα.

(1) ID	(2 X-ray ID	(3) Other names	(4) RA (optical	(5) DEC (optical)	(6) z	(7) AGN Type	(8) $\log_{10}$ (L_X /ergs s^{-1})	(9) $\log_{10}$ ($L_{[OIII]}$ /ergs s^{-1})	(10) $\log_{10}$ ($M_*/M_\odot$)	(11) $\log_{10}$ ($L_{FIR,SF}$/ergs s^{-1})	(12) IFU data reduction	(13) Hα/[OIII] Seeing (")
ID1	xuds 481	UDS 354.0 [(a)]	34.657385	-4.98064	1.41	1	44.3	42.4±0.1	11.2	$46.07^{+0.04}_{-0.04}$	(e,f)	0.98/0.85
ID2	XID 208	-	53.045467	-27.73748	1.61	1	44.3	42.5±0.1	9.0	$45.44^{+0.04}_{-0.04}$	(e,f)	0.55/0.52
ID3	XID 419	-	53.097649	-27.71527	2.14	2	43.0	42.5±0.1	10.5	$45.65^{+0.04}_{-0.04}$	(f,g)	0.61/0.45
ID4	XID 449	-	53.104855	-27.70521	1.61	1	43.8	42.6±0.1	< 10.6	$46.02^{+0.01}_{-0.01}$	(f,g)	0.55/0.85
ID5	XID 587	GS3-19791, KD20-ID5 [(b)]	53.131081	-27.77309	2.22	2	42.8	42.7±0.1	11.0	$45.94^{+0.02}_{-0.02}$	(g,g)	0.59/0.58
ID6	lid 1565	XID 2028 [(c)]	150.546996	1.61846	1.59	1	45.1	43.2±0.1	< 11.1	$45.57^{+0.21}_{-0.13}$	(e,h)	0.68/0.55
ID7	XID 614	-	53.137566	-27.70009	2.45	2	43.3	42.2±0.1	10.9	$45.98^{+0.02}_{-0.02}$	(g,g)	0.56/0.57
ID8	-	ALESS 75.1 [(d)]	52.863303	-27.93093	2.55	2	45.5[j]	43.4±0.1	10.4	$46.32^{+0.07}_{-0.06}$	(i,i)	0.59/0.58

(a) Stach et al. (2019); (b) Förster Schreiber et al. (2009); Genzel et al. (2014); Wisnioski et al. (2018); Popping et al. (2017); Talia et al. (2018); Loiacono et al. (2019); (c) Ueda et al. (2008); Cresci et al. (2015a); Brusa et al. (2018); (d) Hodge et al. (2013); Simpson et al. (2015), Chen et al 2019; (e) Harrison et al. (2016b); Stott et al. (2016); (f) Tiley et al. (2019); (g) Cirasuolo et al. in prep.; (h) This paper; (i) Chen et al. (2019); (j) Derived from mid-infrared (§ 5.2.1)

our conclusions. That is, when obtaining our measurements and their related uncertainties we take into account the spectral resolution, noise, spatial resolution and imperfect sky subtraction in each data cube (see § 4.3.1). Here we provide brief details of the universal approaches taken to obtain and reduce the data.

KMOS has 24 independent IFUs, which can be centred on targets within a 7.2 arcmin field. Each IFU has a field of view (FoV) of 2.8×2.8 arcseconds with a pixel scale of 0.2 arcseconds. Here we present the results of the YJ, H and K gratings with spectral resolutions of R≈3600, 4050 and 4200, respectively. The local spectral resolution (around the emission-lines of interest) were calculated from sky lines and the instrumental spectral broadening was subtracted off, in quadrature, from the observed emission-line widths during the fitting procedure (§ 4.3.1). Observations were carried out using an ABBA observing sequence (where A frames are on-source and B frames are on-sky), with individual exposure times of 600s (YJ-band), 300s (H-band) and 300s (K-band). The total on-source exposure times vary from 5.4–36 ks depending on the individual observing programme during which the observations were taken (see Table 4.1). The data-reduction process primarily made use of SPARK (Software Package for Astronomical Reduction with KMOS; Davies et al., 2013), implemented using ESOREX (ESO Recipe Execution Tool; Freudling et al., 2013). The SPARK recipes were used to perform dark-frame subtraction, flat-fielding, illumination correction, wavelength calibrations and construct the stacked three-dimensional data cubes. Standard star observations were carried out in the same night as the science observations, and processed in an identical manner, in order to flux calibrate the data. PSF measurements were obtained using observations of stars inside dedicated IFUs that were observed simultaneously to the targets and processed in the same manner as the science observations.

For two of the targets the IFU data were obtained using the SINFONI integral field spectrograph (ID6 and ID8). The observations presented here were all observed using the 8×8 arcsec field of view which is divided into 32 slices of width 0.25 arcsec with a pixel scale of 0.125 arcsec along the slices. SINFONI has a comparable spectral resolution to KMOS, ranging from ≈2000–4000; again, the spectral resolution was taken into account during the analyses. Our analyses of the J-band data for ID 6 were first presented in Harrison et al. (2016b) (also see Cresci et al. 2015a) and the HK-band data for ID8 were

presented in Chen et al. (2019). Here we present, for the first time, *H*-band data of ID6 which was taken under ESO Programme ID 094.B-0286(A), with 5.4 ks of on-source exposure time. For a more direct comparison to the analyses presented in Cresci et al. (2015a) for this source (see § 4.4.4) we also re-reduced the archival *HK*-band data for ID6 that was first presented in that publication.

Following Harrison et al. (2016b) and Chen et al. (2019), all SINFONI data reduction was carried out using the standard procedures within ESOREX. Centroids of individual exposures were found by creating white-light images from the datacubes. The individual data cubes where then aligned and stacked using these centroids. Solutions for flux calibration were derived using the IRAF routines STANDARD, SENSFUNC and CALIBRATE on the standard stars, which were observed on the same night as the science observations. These standard star observations were also used to estimate the PSF of the observations. Whilst this is not as reliable as the simultaneous PSF measurements we made for KMOS (see above), we note that we used the broad-line region Hα for the final constraint of the PSF for ID 6 (see § 4.3.1). Although ID 8 is type-2 source observed with SINFONI, it is very clearly extended in Hα emission (§ 4.4.3). Overall the PSF of the IFU observations range from 0.6-1.0" and are tabulated in Table 4.1.

4.2.3 ALMA observations and imaging

To map the rest-frame FIR emission for our AGN host galaxies, we make use of observations from ALMA. We queried the ALMA archive for all observations of our targets performed with Band 6 or 7 and at a resolution of $\leq$0.7 arcsec (see § 5.2.1). Here we describe the observations used in this work and how we produced the images.

ALMA observations and data reduction

The ALMA observations used in this work come from our own Cycle 1&2 programmes (Mullaney et al., 2015; Scholtz et al., 2018; Stanley et al., 2018, ID 3,4), the AS2UDS survey (Stach et al., 2019, ID 1), follow-up observations of the ALESS survey (Hodge et al., 2013; Simpson et al., 2015; Chen et al., 2019, ID 8) and other observational campaigns: (Jin et al., 2018; Santini et al., 2019, ID 2), (Talia et al., 2018, ID 5), (Brusa et al., 2018, ID 6) and (Barro et al., 2017, ID 7). Due to the archival nature of this study, the

on-source exposure times are wide ranging (between 40 and 14 000 s; where the longest observations were designed to detect CO emission lines). The individual programme IDs and central wavelengths of the observations are provided in Table 4.2.

We reduced the data by creating the calibrated measurement sets using the standard ALMA pipeline provided in the archive and the corresponding version of Common Astronomy Software Application (CASA) used during the generation of these scripts. Before creating images, we performed manual checks in CASA on the calibrated measurement sets to verify that all calibrations (such as phase calibrations) and flagging of bad antennae pairs had worked correctly during the reduction process.

Imaging the ALMA data

The calibrated ALMA measuring sets were imaged using CASA version 5.1.2. The uv-visibilities in the measuring set were Fourier transformed to create dirty images and these dirty images were subsequently cleaned using a similar technique to that described by Hodge et al. (2013), using the `tclean` command in CASA.[2] We measured the RMS in off-source regions of the dirty maps and then cleaned the maps down to a 3σ depth around the sources from the IFU data or any bright sources identified in the FOV. We verified that the spectral windows used to create the continuum images did not contain any visible emission lines ([C II], CO, etc).

We created two sets of clean images whenever possible and a summary of the resulting resolution and RMS noise of all of the maps is provided in Table 4.2. The first set of images was created to, as closely as possible, match the resolution of the IFU data containing the Hα emission line (see Table 4.1). This was done by applying a Gaussian taper[3] of an appropriate width to match the size of the resulting ALMA synthesised beam to the width of the PSF during the Hα IFU observations (i.e., $\approx$0.6–0.8 arcseconds; see Table 4.2). The ALMA maps created in this process are labelled as "IFU matched ALMA maps" (IFM). If the object was observed by ALMA at a resolution higher than the resolution of IFU

[2]Cleaning is a common technique applied to interferometric data to reduce the strength of the side lobes from bright sources to allow for the detection of faint sources.

[3]Tapering is a process during the imaging which reduces the weight of the longest baselines. This results in a reduction of the spatial resolution of the images; however, at the cost of not including all the data and consequently increasing the RMS noise in the maps.

Table 4.2: Table summarising the ALMA observations. The (IFM) and (HR) indicate IFU matched and high resolution maps (see § 4.2.3). (1) Object ID in this paper; (2) ALMA programme ID; (3) Central wavelength and ALMA Band of the observations; (4) Synthesised beam size of the IFU matched resolution maps; (5) RMS of the IFU matched resolution maps (1σ map depth); (6) Beam size of the high resolution maps; (7) RMS of the high resolution map (1σ map depth); (8) Signal-to-noise of the peak continuum measured from the IFU matched maps; (9) Flux density of the continuum measured in the uv plane (see § 4.3.2).

(1)	(2	(3)	(4)	(5)	(6)	(7)	(8)	(9)
ID	Prog	λ/Band	Beam (IFM)	RMS (IFM)	Beam (HR)	RMS (HR)	ALMA	Flux density
		μm/-	arcsecond	(mJy)	arcsecond	(mJy)	SNR	(mJy)
ID1	2015.1.01528.S	870/7	0.83x0.75	0.685	0.21x0.20	0.367	10.0	3.09 ± 0.41
ID2	2015.1.01074.S	870/7	0.61x0.50	0.344	0.19x0.16	0.268	4.3	0.74 ± 0.21
ID3	2013.1.00884.S	870/7	0.76x0.62	0.244	0.28x0.23	0.143	4.5	0.37 ± 0.11
ID4	2012.1.00869.S	870/7	0.68x0.47	0.224	0.28x0.24	0.215	23.3	1.87 ± 0.10
ID5	2015.1.01379.S	1100/6	0.66x0.56	0.031	-	-	8.1	0.68 ± 0.05
ID6	2015.1.00299.S	1100/6	0.63x0.53	0.018	-	-	12.2	0.14 ± 0.02
ID7	2015.1.00907.S	870/7	0.68x0.51	0.190	0.16x0.16	0.114	12.1	1.26 ± 0.05
ID8	2016.1.00735.S	870/7	0.57x0.54	0.323	0.17x0.12	0.110	20.1	2.61 ± 0.21

data, we also created ALMA maps without any tapering called "High Resolution ALMA maps" (HR), which have a final resolution of 0.15–0.35 arcseconds (see Table 4.2). We used these two sets of maps to assess the impact of differing spatial resolutions upon our measurements of the location of the peak emission (see § 4.3.3).

The final IFU matched ALMA maps have an RMS between 0.02 mJy and 0.69 mJy and a median RMS of 0.24 mJy. The quoted signal-to-noise measurements in Table 4.2 are derived from these maps by dividing the peak flux density by the RMS of the map. The final high resolution ALMA maps have the RMS between 0.10 mJy and 0.37 mJy (median value of 0.11 mJy). By selection (see § 5.2.1), we detected all our of our sources in the IFU-matched ALMA maps with a SNR>4 (see Table 4.2). Six of the eight targets have SNR>8, and are the most reliable for measuring the sizes of the rest-frame FIR emission (§ 4.3.2).

4.2.4 SED fitting and sample properties

We compiled multi-wavelength photometry from UV to FIR wavelengths and performed SED (spectral energy distribution) template fitting to measure the SFRs, stellar masses and the dust attenuation of our targets.

All three extragalactic survey fields that contain our sources (CDFS, COSMOS and UDS) are covered by *Herschel* and *Spitzer* imaging in the infrared waveband. We make use of public catalogues from the PEP and HERMES *Herschel* surveys for FIR fluxes over 100–500 μm (Lutz et al., 2011; Oliver et al., 2012), and catalogues from the FIDEL and SCOSMOS *Spitzer* programmes for MIPS 24 μm fluxes (available from NASA IPAC). The UV, optical, and NIR photometry are taken from public versions of the multi-wavelength catalogues available from the CANDELS, MUSYC (CDF-S), COSMOS and UKIDSS/UDS survey consortia (Guo et al., 2013; Cardamone et al., 2010; Laigle et al., 2016, and O. Almaini, priv. comm.). As a part of the processing the public photometry data, we performed the following: source matching between catalogues, adjusting small zeropoint offsets differences between catalogues, application of flags to exclude inaccurate photometry and conversion to a common flux unit.

The multi-wavelength SEDs of the targets were modelled using the Bayesian SED code `FortesFit` (Rosario, 2019). Four SED components were used in the modelling:

- a stellar component of fixed solar metallicity from the Bruzual & Charlot (2003) library, with a star-formation history modelled as a delayed exponential with a range of ages and exponential timescales. A variable screen extinction following a Milky Way law was applied.

- an AGN accretion disc with a range of spectral slopes as prescribed by the models of Slone & Netzer (2012) with a variable extinction following a Milky Way law.

- an AGN dust emission component with a range of shapes as prescribed by the empirical templates from Mullaney et al. (2011).

- dust emission heated by star-formation following the one-parameter template sequence from Dale et al. (2014).

Probabilistic priors were used to constrain the luminosity of the accretion disc and AGN dust emission components based on the X-ray luminosity. `FortesFit` generates full marginalised posterior distributions of stellar mass ($M_\star$), FIR luminosity from star formation ($L_{\rm IR,SF}$; over 8–1000μm) and stellar dust attenuation (A_V), as well as other parameters that are not used in this work. We present the individual SEDs and the resulting fits in Figure 4.3. The $L_{\rm IR,SF}$ and $M_\star$ values are provided in Table 4.1, along with their uncertainties. From the FIR luminosities, we estimate star formation rates (SFR(FIR)) using the calibration from Kennicutt & Evans (2012), and these are discussed in § 4.4.2. The dust attenuation, and the impact that this has on the observed Hα fluxes from the IFU data, is discussed in § 4.3.1.

Six objects in our sample are detected in the radio at 1.4 GHz (Simpson et al., 2006; Schinnerer et al., 2010; Miller et al., 2013). The corresponding rest-frame 1.4 GHz radio luminosities for all but one of the sample are $L_{1.4\rm GHz} \lesssim 2\times10^{24}\,{\rm W\,Hz^{-1}}$ (assuming a spectral index of $\alpha = -0.7$; defined as $f_\nu \sim \nu^\lambda$). This is consistent with these seven targets being 'radio quiet', and following Kennicutt & Evans (2012), their radio luminosities imply reasonable star formation rates of a few hundred – $1500\,{\rm M_\odot\,yr^{-1}}$, although we can not rule out low-level radio jets e.g (e.g., Jarvis et al., 2019). The one exception is ID 2 which has a luminosity of $L_{1.4\rm GHz}$=$4\times10^{25}\,{\rm W\,Hz^{-1}}$ which we discuss further below.

For this work we require that the 870μm–1100μm emission is uncontaminated by processes other than star formation (e.g., synchrotron emission from radio jets). For the

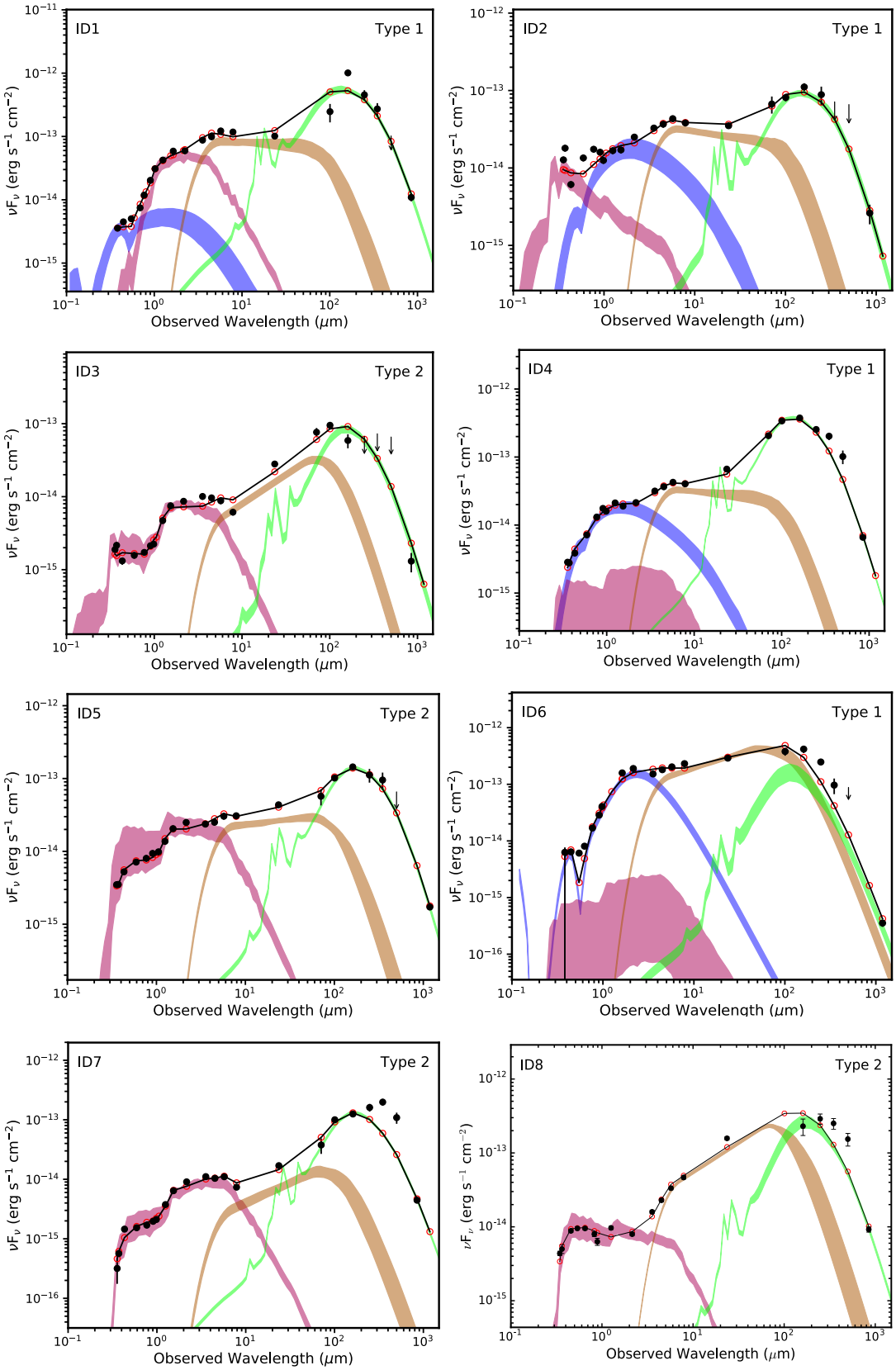

Figure 4.3: SEDs for all our objects from UV to FIR. The black and red points represent the measured and modelled photometry, respectively. The black line shows the total SED. The shaded region represents 1σ uncertainty on the fitted components. We fit the following component: AGN accretion disk (blue region), stellar component (red region), AGN torus addition (brown region) and cold dust emission from star formation (green region). The details of the SED fitting can be found in § 5.4.1.

radio-quiet sources, this is supported by the fact that the sub-mm fluxes (Table 4.2) would imply rare (highly inverted) spectral indices of $\alpha > 0.4$ if they arose from synchrotron emission. Additionally, for ID 6 the 870um/1.1 mm flux ratio is fully consistent with star-formation heated dust; see Appendix of Brusa et al. (2018). In the case of ID 2, which has a higher radio luminosity, we also consider the 2.3 GHz and 5.5 GHz data from Zinn et al. (2012) and Huynh et al. (2012), which together imply a spectral index of -0.3. Extrapolating this radio slope to ALMA band 7 suggests the ALMA emission could have a roughly equal contribution from star formation and synchrotron emission; however, we note that some contamination to the ALMA flux for this single source does not influence our main conclusions in this work. Based on these assessments and our SED results where we decomposed AGN and star formation components, we argue that the ALMA 870 and 1100 μm emission provides a good tracer of the dust obscured star formation in these sources.

In Figure 4.2 we show the SFR vs stellar mass plane for the parent KASHz sample and highlight the targets used in this work. We also show the star-forming galaxy main sequence, at two representative redshifts, as turquoise and orange dashed lines (Schreiber et al., 2015). We find that our target galaxies have SFRs which are either on, or above, the main-sequence of star-forming galaxies. The distribution to relatively high SFRs for the targets in our sample, compared to the parent sample, is due to our requirement for a strong detection in both Hα and rest-frame FIR (§ 5.2.1). We discuss the implications for this on our results in § 4.4.4.

4.3 Analyses

To achieve the goals of our study, we perform the following analyses: (1) compare galaxy-wide star-formation measurements inferred from the rest-frame FIR with those inferred from Hα; (2) map the star formation within the galaxies as inferred from maps of both Hα emission and rest-frame FIR emission and (3) compare the location of AGN-driven ionised outflows with the distribution of star formation. In this section we describe how we achieved this by extracting galaxy-wide (unresolved) and spatially-resolved emission-line measurements from the IFU data (§ 4.3.1), analysing the maps of the rest-frame FIR

emission that were created using the ALMA data (§ 4.3.2) and by measuring the offsets between the FIR and Hα emission (§ 4.3.3).

4.3.1 Emission-line properties

Each of our targets have two sets of IFU observations (see § 4.2.2), one covering the [O III] emission line (also Hβ in some cases) and one covering the Hα and [N II]6548,6583 emission lines. The emission-line profiles for each of our targets are shown in Figure 4.4. Here we describe how we used the IFU data to: (1) extract galaxy-integrated spectra from each data cube to obtain global properties (§ 4.3.1); (2) obtain constraints on the star-formation rates using Hα emission (§ 4.3.1); (3) map the distribution of the Hα emission and [O III] outflows (§ 4.3.1) and; (4) measure the sizes of the Hα emission (§ 4.3.1).

Extracting spectra and emission-line fitting procedure

We extracted galaxy-integrated spectra with the primary goals of identifying [O III] emission-line outflows (e.g., following Mullaney et al. 2013) and calculating total narrow Hα fluxes (to infer star-formation rates). To do this, we first found the peak of the continuum emission in the data cube by creating median wavelength collapsed images of our targets, excluding any spectral channels contaminated by sky-lines or the emission lines. We then fitted a single 2D Gaussian model to the wavelength collapsed continuum image to find the peak of the continuum emission. The 2D Gaussian is a sufficient model of the continuum since our seeing-limited continuum images are dominated by the point source from the central AGN (for the Type 1 AGN) or the stellar light from the galaxy which is the strongest towards the nucleus (for the Type 2 AGN).

From each data cube we extracted spectra from two different circular apertures centred on the continuum peak: (a) a nuclear aperture within 5 kpc diameter (i.e., approximately within one PSF) to characterise the emission-line profile shapes and to search for outflows (see Figure 4.4) and (b) a 'maximum' aperture to obtain total fluxes, for which the sizes were determined by extracting spectra from increasingly large apertures until maximum emission-line fluxes were obtained (see column 5 in Figure 4.5). In Table 4.3 we provide the key measured parameters from the former spectra (i.e., the emission-line flux ratios and velocity widths). The total Hα luminosities, extracted from the latter spectra, are

provided in Table 4.4.

To model the Hβ, [O III]4959, 5007$\mathring{A}$, Hα and [N II]6548, 6583$\mathring{A}$ emission-line profiles, each line was fitted with one or two Gaussian components, with the centroids, FWHM and fluxes (normalisation) as free parameters. In each case the continuum was well characterised by fitting a straight line with a normalisation and slope as a free parameter.[4] Best-fit solutions, and the uncertainties, for the free parameters were obtained using the Python `lmfit` least-square library. During the fitting procedures we masked wavelengths which were affected by strong sky-line residuals. To construct the skyline residual masks we extracted a sky spectrum by summing all of the object-free (sky only) spatial pixels in the cube and identifying the strongest skyline residuals by picking any spectral pixels outside 1σ. Visual inspection showed this method to be effective (see grey regions in Figure 4.4).

For the [O III]4959,5007Å emission-line doublet we simultaneously fit [O III]4959$\mathring{A}$ and [O III]5007$\mathring{A}$, using the respective rest-frame wavelengths of 4960.3Å and 5008.24Å. We tied the line widths and central velocities of the two lines and fixed the [O III]λ5007/ [O III]λ4959 flux ratio to be 2.99 (Dimitrijević et al., 2007). We initially fit a single Gaussian component per emission line, then, we refit with a second Gaussian component. We use the BIC to choose whether the fit needs a second broad component; for verification we also performed a visual inspection of the residual spectra after subtracting the narrow component. A 'broad' [O III] component was required to fit nuclear spectra for five of the targets (see Figure 4.4), which are consequently the targets with the strongest evidence for ionised outflows (e.g., Mullaney et al. 2013; see § 4.4.4).

For characterising the Hα emission-line profile we first identified the Type 1 sources as those with an Hα broad-line region (BLR) component in the nuclear spectrum (i.e., a broad component of FWHM$>$2000 km s^{-1} that is not seen in the [O III] or [N II] emission lines; see Figure 4.4). Reassuringly, the Type 1/Type 2 classification is consistent with the presence of a UV–optical accretion disk component identified in our broad-band SED fitting (see § 5.4.1). For both Type 1 and Type 2 AGN we treat the narrow-line emission the same. That is, we simultaneously fitted the Hα and neighbouring [N II]6548, 6583$\mathring{A}$

[4]We note that we see no significant Fe complexes in our spectra. This is likely due to the lack of very luminous Type 1 sources in our sample.

emission-line doublet, adopting the same approach as for the [O III] emission line doublet. The central velocity and line width for all three emission-line profiles of [N II]6548$\mathring{A}$, Hα, [N II]6583$\mathring{A}$ were tied, with rest-frame wavelengths of 6549.86Å, 6564.61Å and 6585.27Å, respectively. This approach, which assumes that the Hα and [N II] emission comes from the same gas, is commonly used in high-redshift observations to limit the number of free parameters (Förster Schreiber et al., 2009; Genzel et al., 2014; Harrison et al., 2016b; Förster Schreiber et al., 2018b). During the fitting the Hα and [N II]6583$\mathring{A}$ fluxes were free to vary but the [N II]6548$\mathring{A}$/[N II]6583$\mathring{A}$ flux ratio was fixed to be 3.06 (based on the atomic transition probability; Osterbrock & Ferland 2006). For the Type 1 sources an additional broad Hα component was included with a free central velocity, line width and flux.

In the unique case of the Type 2 source ID 5, an additional broad component can be identified in both the Hα and [N II] emission-line doublet (also see Genzel et al. 2014, who previously identified this as an outflow). For this case we fitted an additional Gaussian component to the Hα and [N II] doublet (with parameters coupled as above) to characterise this outflowing component. Both components were considered to be tracing the total 'narrow' Hα emission (i.e., these are not part of the broad-line region) when exploring the total Hα luminosities in § 4.4.2.

The Hβ emission line is covered by the datacubes that also contain the [O III] emission line. However, in 2 of the 8 targets the Hβ emission falls within very strong atmospheric telluric features and we can not obtain any meaningful constraints (see Figure 4.4). For the other 6 targets, we detected Hβ at $>3\sigma$ in 5 targets in the nuclear spectra. Due to the limited signal-to-noise ratio of the Hβ detections, we fitted the Hβ emission line using only a single Gaussian component and were not able to disentangle the broad-line region from the narrow-line region components.[5] Due to this limitation we only have meaningful Hβ measurements of the narrow-line regions for three targets (ID 3, ID 5 and ID 8), which we use for emission-line ratio diagnostics (§ 4.4.2) and calculating a Balmer Decrement (§ 4.3.1).

[5]We note that we do not tie the Hβ and [O III] kinematics as we often see that the Hα line (which will follow the same kinematic structure as Hβ) does not follow the kinematics of the [O III] line (see § 4.4.1).

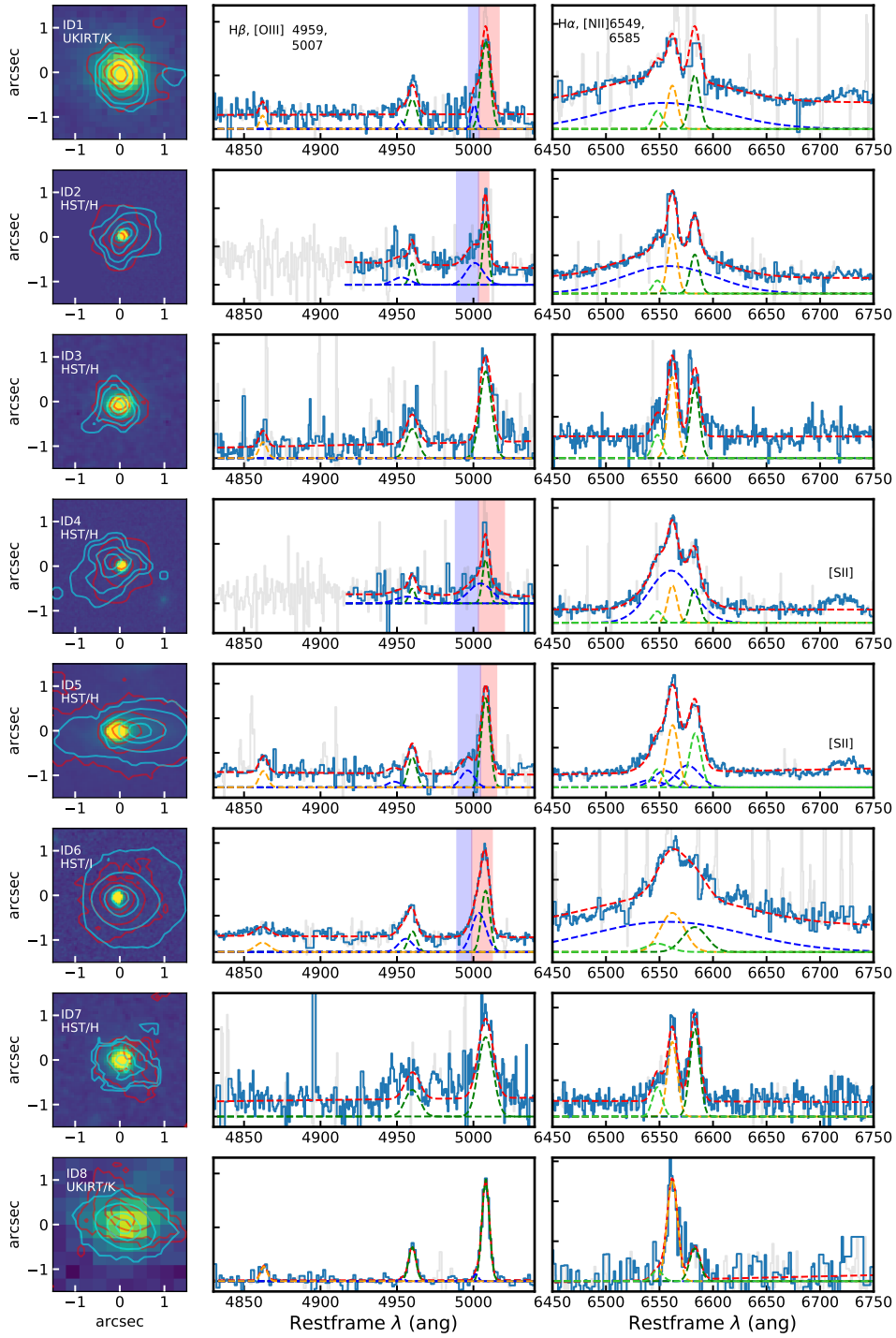

Figure 4.4: Rest-frame UV or optical images (left panel), and [O III] (centre panel) and Hα (right panel) emission-line profiles extracted from the inner 5 kpc nuclear spectra for the eight objects in our sample. As labelled, the images are from HST WFC3 *H*-band or *I*-band, when available, or UKIRT K-band images. The red and cyan contours show the narrow Hα and narrow [O III] flux maps, respectively, with levels of 90, 68, 32 and 10 % of the peak flux in the map. For the emission-line profiles the light blue curves show the data and the grey curves show the masked sky-line residuals. For the [O III] spectra the green, dark blue and red dashed curves show the narrow line, outflow components and total fits, respectively. The red and blue shaded regions indicate the wavelength slices of the non-outflowing and outflowing ionised gas, respectively, as defined in § 4.3.1. Overlaid on the Hα profiles the yellow, blue, dark green, light green and red curves show the narrow Hα, broad Hα, [N II] (6583 Å), [N II] (6548 Å) and the total fit, respectively. In the case of ID 5, the blue curve in the Hα spectrum shows the outflow components visible in both the Hα and the [N II] doublet.

Table 4.3: Table of the key emission-line properties for our sample. The spectra have been extracted from the inner 5 kpc (nuclear) region (see § 4.3.1). (1) Object ID in this paper; (2) FWHM of narrow [O III]; (3) FWHM of broad [O III]; (4) velocity offset between the narrow and broad components of the [O III]; (5) FWHM of narrow Hα; (6) FWHM of broad Hα; (7) $\log_{10}$ flux ratio of narrow Hα and Hβ used for the Balmer decrement; (8) $\log_{10}$ flux ratio of narrow [N II] and Hα ; (9) $\log_{10}$ flux ratio of total [O III] and narrow Hβ.

(1) ID	(2) [O III] Narrow FWHM (km/s)	(3) [O III] broad FWHM (km/s)	(4) [O III] Δv km/s	(5) Hα Narrow FWHM (km/s)	(6) Hα Broad FWHM (km/s)	(7) $\log_{10}$(Hα/Hβ) ratio	(8) $\log_{10}$([N II]/Hα) ratio	(9) $\log_{10}$([O III]/Hβ) ratio
ID1	339 ± 50	614 ± 70	-234 ± 30	478 ± 72	5947 ± 70	$1.16 \pm 0.1^{\star}$	0.20 ± 0.1	1.47 ± 0.1
ID2	226 ± 60	792 ± 90	-403 ± 40	363 ± 48	4622 ± 80	-	-0.06 ± 0.1	-
ID3	329 ± 50	–	-	483 ± 63	–	0.53 ± 0.1	0.06 ± 0.1	0.88 ± 0.1
ID4	429 ± 70	747 ± 70	-613 ± 60	399 ± 48	2291 ± 90	-	0.09 ± 0.1	-
ID5	316 ± 50	951 ± 90	-294 ± 40	437 ± 67	897 ± 70^{x}	0.79 ± 0.1	0.04 ± 0.1	0.97 ± 0.1
ID6	383 ± 50	647 ± 60	-262 ± 50	640 ± 138	5945 ± 90	$0.94 \pm 0.1^{\star}$	-0.16 ± 0.1	1.06 ± 0.1
ID7	724 ± 100	–	–	468 ± 80	–	> 0.91	0.20 ± 0.1	> 1.15
ID8	374 ± 60	–	–	529 ± 80	–	0.94 ± 0.1	-0.64 ± 0.1	1.02 ± 0.1

[x] velocity FWHM of the Hα outflow. ⋆ For the Type 1 AGN we do not use the Balmer Decrement to correct the Hα emission for dust obscuration (§ 4.4.2).

Dust-corrections to Hα emission and the derived star-formation rates

In § 4.4.2 we compare the star-formation rates inferred from the measured Hα luminosity (excluding the BLR; SFR(Hα)) with those inferred from the FIR (SFR(FIR)). To estimate SFR(Hα) we converted from the measured $L_{H\alpha}$ by using the calibration from Kennicutt & Evans (2012). However, it is important to also consider the dust-correction to the Hα luminosities. The preferred approach to constrain this is to measure the nebular dust attenuation ($A_{V,HII}$) using the Balmer decrement (the Hα/Hβ flux ratio; Reddy et al., 2015). For three objects (ID 3, ID 5, & ID 8), for which we have reliable narrow Hβ detections in the nuclear spectra (see § 4.3.1), we can measure the $A_{V,HII}$ directly. We assume the Calzetti et al. (2000) extinction curve and consequently correct the total Hα luminosities for dust attenuation. These correction factors are 1.5 – 18 (see Table 4.4). Unfortunately, we are unable to reliably correct for dust-obscuration for the other five sources. However, the upper limits on narrow Hβ for ID 1,6 & 7, indicate lower limits on the dust correction factors of 20–70. Although we can obtain some handle on the obscuration of stellar light from the SED fitting ($A_{V,stellar}$; § 5.4.1) we choose not to use these to correct the Hα luminosities because: (1) they are poorly constrained due to the challenges with fitting the UV–optical SEDs of AGN host galaxies (e.g. Alexander & Hickox, 2012; Hickox & Alexander, 2018); and (2) the stellar light and emission lines are often found to be obscured by different amounts, requiring a further uncertain correction factor to obtain $A_{V,HII}$ (Wild et al., 2011; Kashino et al., 2013; Price et al., 2014; Reddy et al., 2015; Puglisi et al., 2016). In § 4.4.2 & 4.4.3 we discuss the various challenges in using Hα has a star formation tracer in AGN host galaxies, considering both the dust correction and the contribution of the AGN itself (in addition to the star formation) to illuminating the gas.

Emission-line maps

To map the Hα and [O III] emission in our AGN host galaxies, we performed spaxel-by-spaxel fitting of the emission lines. We binned the spectra by averaging the nearby spaxels within radius of 0.2 arcsec. This significantly increases the SNR of the spaxels' spectra, while maintaining the seeing limited spatial resolution of ∼0.6–0.8 arcsec. We fitted the [O III] and Hα emission lines in the individual spaxels using the same overall procedure

as described in § 4.3.1.

For the spaxel-by-spaxel fitting of the Hα emission line we have taken into account the emission coming from the BLR in Type 1 AGN that will contaminate multiple pixels (due to the PSF spreading out the emission). For these targets, we fixed the central velocity and line-width of the BLR component to be the same as that obtained from the nuclear spectrum (Figure 4.4), leaving only the flux of the BLR as a free parameter. The resulting flux map of the BLR also serves as a measurement of the PSF inside these data cubes, as it is intrinsically a point source. We found reasonable agreement between the spatial profile of the BLR and the PSF stars (see § 4.3.1; see column 4 in Figure 4.5), with a median ratio of the resulting sizes of 1.1 ± 0.2 (see § 4.3.1). The maps of the narrow Hα emission (i.e., after the broad-line region emission has been subtracted) are shown in Figure 4.5, fourth column and Figure 4.6).

In case of the [O III] we were only able to fit a single component to the spaxel-by-spaxel spectra due to the low signal-to-noise ratios. This was even true for the 5 targets where we identified a second 'outflow' component in the nuclear spectra (see Figure 4.4). Therefore, we employed a different method to map the outflow for these 5 targets by creating a narrow-band image in the spectral region of the outflow. To define the velocity band to create this outflow narrow-band image, we first considered the underlying [O III] velocity map (which is dominated by the narrow component, and likely galaxy dynamics). We define the velocity range of the underling velocity structure as the maximum and minimum velocity in the map $\pm 0.5 \times$FWHM of the narrow component. These velocity ranges are shown as the red shaded region on the [O III] profiles in Figure 4.4). We then define the outflow velocity slice as any [O III] emission blue-ward of this (see blue shaded regions on the [O III] profile in Figure 4.4). Visual inspection reveals that this definition of the outflow is dominated by the broad blue-shifted components. Furthermore, we confirmed that our results on the relative location of the outflow region compared to the Hα and FIR emission (presented in § 4.4.4) are not sensitive to the exact definition of the velocity slice for the outflow. The final outflow maps are presented in § 4.4.4.

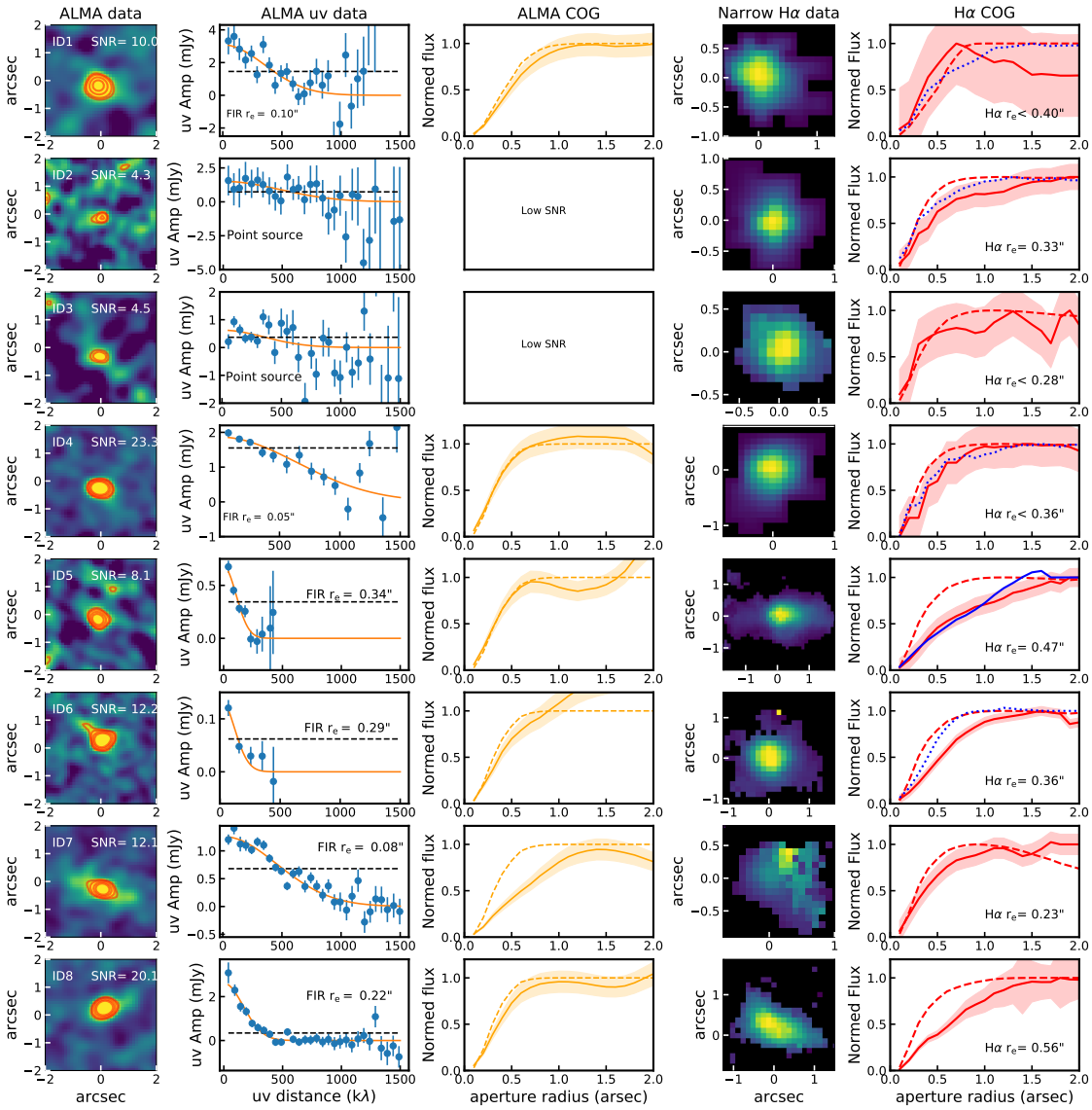

Figure 4.5: Size analyses of the ALMA and narrow Hα images. Columns from left to right: Column 1: ALMA data imaged at the resolution of the IFU data (IFU matched). The red contours indicate 2.5, 3, 4, 5 σ levels of the data. Column 2: The uv amplitude data vs the uv distance binned per 50kλ. The orange solid curves, and black dashed curves show the resolved and unresolved model fits. We show the half-light radii when measured or indicate whether it is a point source in the panel. Column 3: The curve of growth (COG) for the tapered FIR continuum (from ALMA; yellow solid curve). The yellow shaded region shows the 1 σ uncertainty on the flux density. The yellow dashed curves show the COG for the ALMA beam. We do not present the COG for objects which are detected by ALMA at SNR< 8. Column 4: The narrow Hα maps. Column 5: The COG for the Hα emission, where the solid red curve shows the COG for the narrow Hα with the shaded region indicating the 1 σ uncertainty and the red dashed curves show the COG for the PSF. The dotted blue curves indicate the COG of the broad line region (BLR) and the solid blue curve shows the COG of the Hα outflow for ID 5.

Table 4.4: Star formation properties and size measurements of our sample. (1) Object ID in this paper; (2) SFR derived from FIR luminosities; (3) Dust extinction in the V-band of the nebular lines (derived from narrow Balmer decrement, see § 4.3.1). ID 2 & 4 do not have reliable upper limits on the Hβ and therefore we were unable to determine even an upper limit on Av_{HII}; (4) Hα luminosity (narrow component) derived from the total flux; (5) SFR derived from the observed Hα luminosity; (6) SFR derived from the dust corrected Hα luminosity; (7) Half-light radii of the Hα emission (see § 4.3.1); (8) SNR of the FIR continuum; (9) The half-light radii of the FIR continuum derived using the curves of growth method (see § 4.3.1); (10) The half-light radii of the FIR continuum derived in the uv-plane (see § 4.3.2). The (P) indicates if the FIR emission is unresolved; (11) Projected physical offset between the Hα and FIR emission regions.

(1) ID	(2 SFR(FIR) ($M_\odot$ yr^{-1})	(3) Av_{HII}	(4) $\log_{10}$ ($L_{H\alpha}$/ergs s^{-1})	(5) SFR(Hα uncor) ($M_\odot$ yr^{-1})	(6) SFR(Hα cor) ($M_\odot$ yr^{-1})	(7) Hα r_e (kpc)	(8) SNR (FIR)	(9) FIR r_e (COG) (kpc)	(10) FIR r_e (uv) (kpc)	(11) Hα - FIR offset (kpc)
ID1	459^{+459}_{-230}	> 5.72	42.1±0.1	7^{+7}_{-4}	–	< 3.3	10.0	1.9±0.8	0.9±0.1	1.3±0.5
ID2	107^{+107*}_{-53}	-	42.5±0.1	15^{+15}_{-8}	–	2.7±0.8	4.3	< 2.4	(P)	1.2±0.8
ID3	174^{+174}_{-87}	0.57	42.2±0.1	9^{+9}_{-5}	14^{+14}_{-7}	< 2.2	4.5	< 2.9	(P)	0.8±0.7
ID4	409^{+409}_{-204}	-	42.3±0.1	11^{+11}_{-5}	–	< 3.0	23.3	0.3±0.8	0.5±0.1	0.8±0.6
ID5	336^{+336}_{-168}	2.71	43.0±0.1	51^{+51}_{-25}	379^{+379}_{-189}	3.8±0.8	8.1	< 2.6	2.9±0.3	1.1±0.7
ID6	145^{+145}_{-72}	> 3.93	43.0±0.1	58^{+58}_{-29}	–	2.9±0.8	12.2	1.7±0.8	2.7±0.5	1.9±0.4
ID7	369^{+369}_{-184}	> 3.63	42.5±0.1	16^{+16}_{-8}	–	1.8±0.8	12.1	4.1±0.8	0.7±0.0	2.8±0.8
ID8	806^{+806}_{-403}	3.89	43.2±0.1	83^{+83}_{-41}	1494^{+1494}_{-747}	4.4±0.8	20.1	1.6±0.8	1.8±0.1	1.5±0.8

* The FIR in this object may be contaminated by AGN radio emission (see § 5.4.1).

Hα sizes

To measure the extent of the narrow Hα emission we used a curves-of-growth (COG) method (e.g., Chen et al., 2017; Förster Schreiber et al., 2018b). We measured the total flux enclosed in a series of increasingly large circular apertures, where the apertures were centred on narrow Hα peak. For each aperture, we extracted spectra and fit the emission-line profiles following § 4.3.1. To reduce the degeneracies during the fitting procedures, for Type 1 AGN, we locked the FWHM and central velocity of the Hα BLR Gaussian component in each aperture. This is a reasonable approach for such point source emission because only the *flux* in these BLR components will vary with distance, following the PSF.

We repeated the COG process on both the science observations and the observations of the corresponding PSF stars; however, for the PSF stars we measured the *continuum* in each aperture (as opposed to the emission line flux). Figure 4.5 shows the comparison of the COG for the narrow Hα emission (solid red lines), PSF star (dashed red line), BLR Hα emission (blue dotted line, for the Type 1 AGN) and Hα outflow component (blue solid line, only applicable for ID 5). We used linear splines to interpolate between the data points and we measured the half light radii (radius containing 50 % of the total flux). We derived the objects *intrinsic* sizes (r_e) by subtracting off, in quadrature, the size of the associated PSF (see e.g., Chen et al., 2017; Förster Schreiber et al., 2018b). For the Type 1 AGN we used the BLR as the PSF measurement (because it comes from the exact same datacube) and for the Type 2 AGN we use the corresponding PSF star. We note that for the KMOS observations of the Type 1 AGN (3 objects), when we have both measurements of the PSF star, we found that the BLR sizes are 10 % larger than the PSF stars. Uncertainties on the final Hα sizes are calculated by considering the full range of possible radii for the 1σ range of fluxes at each radii (see shaded curves in Figure 4.5). We note that we obtain consistent results for the r_e of the narrow Hα emission compared to Chen et al. (2019) for ID 8, despite their use of slightly different approaches (e.g., the use of non-ciruclar apertures). The original intrinsic sizes of the narrow Hα emission, and their corresponding uncertainties, are provided in Table 4.4.

4.3.2 Flux density and size measurements from ALMA data

In this section we describe how we measured the total flux densities and sizes of the FIR emission from the ALMA data. To obtain reliable fluxes and sizes of the FIR emission, we made measurements from the data in the image plane (the images are described in § 4.2.3) as well as directly from the calibrated visibilities in the *uv* plane. As described in detail below, in Figure 4.5 we show the ALMA maps (see § 4.2.3), the COG on these images and the spatially-binned visibilities in the amplitude–*uv* distance plane (see below).

Our preferred method to obtain total flux density measurements and sizes from the ALMA data is to use the visibilities directly, as it does not rely on the choices made during the imaging process. We first phase centred our data to the objects' central coordinates using CASA's `fixvis`.[6] We then extracted the visibility amplitudes, binning across the *uv* distance in steps of 50 kλ (see Figure 4.5; second column). We modelled these binned visibility amplitudes either as a constant over *uv*-distance (describing a point source) or as Gaussian centred at 0 kλ (describing a resolved 2D Gaussian source).[7] We used the Bayesian Information Criterion (BIC) to choose the best-fit model, only accepting the Gaussian extended model if $\Delta\mathrm{BIC} \geq 15$ (see Figure 4.5). With this method we found that 6 of the 8 targets are extended in the ALMA data. We note, however, that the two sources that are consistent with being point sources, are also the two sources with the lowest signal-to-noise ratios with SNRs≈4.5, for which it has been shown that sizes can not be reliably determined (see Simpson et al. 2015 for more details). For these objects, we used the size of the beam as a conservative upper limit on the size. Reassuringly we obtain consistent result on which of the sources are extended by using CASA's `uvmodelfit` routine which directly fits to the calibrated *uv* visibilities. The intrinsic source sizes and their uncertainties, as determined from fitting the Gaussian models (shown in Figure 4.5, second column), are provided in Table 4.4.

As a further verification of our results, we measured flux densities and sizes from the ALMA data in the image plane. Because we are interested in comparing directly

[6]The objects' central coordinates were determined from the peak of the High Resolution images described in § 4.3.3

[7]In the Fourier space the large *uv* distance corresponds to a small spatial scale in the image plane. As a result, a point source has constant amplitude across all *uv* distances, while for any resolved emission the amplitude is decreases with *uv* distance (see e.g. Rohlfs & Wilson, 1996).

these sizes to the Hα sizes (see § 4.3.1) we make use of the resolution-matched ("IFU matched") ALMA maps described in § 4.2.3 (Figure 4.5, first column). To obtain the total flux density measurements we used CASA's `IMFIT` routine to fit a single elliptical Gaussian model convolved with the synthesised beam. These fits reproduced consistent flux densities (within the 1σ errors) that were obtained directly from the visibilities described above.

We then proceeded to measure the rest frame FIR sizes using a curve-of-growth method on the "IFU matched" ALMA maps, in order to be consistent with the method used to obtain Hα emission sizes (see Figure 4.5, third column). However, we do not perform the curve-of-growth analyses on the two objects which are classified as unresolved in the analysis of the visibilities above, which have low SNRs of < 8. For the other six sources, as with the Hα maps, we calculated the total flux in the ALMA maps using apertures with increasing size where the apertures were centred on the location of peak emission. The COG are normalised to the total flux densities obtained from the `IMFIT` fitting results. We note that the upturn seen in the curve-of-growth for ID5 beyond 1.5 arcseconds is caused by a faint companion seen to the North of the main sources and in ID6 there is a faint tail of emission extending to the North East (also see Brusa et al., 2018).

Following the analysis on the IFU data cubes (§ 4.3.1), we also performed the COG analysis on the synthesised beam (see Figure 4.5; third column; dashed curves) and used this measurement to de-convolve the observed size measurements to obtain intrinsic sizes.

The rest frame FIR sizes from both methods (amplitude–*uv*-distance fitting method and COG to the image place) are provided in Table 4.4. We note that we obtain consistent size measurements for both Hα and the rest-frame FIR as presented in Chen et al. (2019) for ID8. Furthermore, there are only two targets where the the two different size measurements are not consistent within their 1 σ uncertainties: ID1 and ID7. For the remainder of this work we favour the sizes from the amplitude–*uv*-distance fitting method, but highlight results from both methods in the relevant figures. The different sizes observed in Hα and rest-frame FIR for our targets are discussed in § 4.4.3.

4.3.3 Alignment of the astrometric frames and measuring spatial offsets

We aim to measure the physical offsets between the FIR emission, the Hα emission and the AGN outflows in our targets. These offsets have two main sources of uncertainty: (a) the relative astrometric calibrations of the IFU data cubes and the ALMA maps and; (b) the data quality in the images (i.e., both their resolution and sensitivity). In the following subsections we discuss how we addressed these issues by aligning the astrometric frames (§ 5.3.3) before carefully measuring the final spatial offsets and their corresponding uncertainties (§ 4.3.3).

Astrometric Alignment of the IFU and ALMA maps

The astrometric frame of ALMA observations is set during during the observations of the phase calibrators, since they are bright radio sources near the observe targets. The absolute astrometric accuracy of ALMA depends on the frequency, baseline and calibration; however, in the case of our observations it is negligible at ≈20–30 mas (ALMA Cycle 7 Technical Handbook). [8] However, the astrometric calibration of the IFU data is less accurate and requires additional calibration. Due to the limited field of view of the KMOS and SINFONI instruments (see § 4.2.2), it is not possible to calibrate the absolute astrometry by identifying known stars in the field of view with known, accurate positions. Instead, we aligned the IFU astrometry on the object itself by using supplementary high-resolution images from *HST* or UKIRT of the targets (e.g., see Fig, 4.4). To determine the central position of the AGN in the IFU date cubes we created white-light images by collapsing the data over the same wavelength range as the corresponding broad-band images. We then identified the central position of the source in the IFU data cube by fitting a 2D Gaussian model. The RA and Dec of this central position in then determined by the position of the source in the corresponding broad-band images (*HST* or UKIRT).

As with many previous studies (Miller et al., 2008; Hsu et al., 2014; Dunlop et al., 2017; Elbaz et al., 2018; Scholtz et al., 2018) we noticed a systematic offset between the optical astrometric frame (e.g., in *HST*) and the radio astrometric frame (e.g., from

[8] https://almascience.eso.org/documents-and-tools/cycle7/alma-technical-handbook

VLA or ALMA) in the CDFS field. This affects six of our eight targets in our sample which lie in this field. Previous studies typically corrected for this difference by applying a global shift to the astrometry in the optical frame. However, it has been found that this offset is not constant across the field (Elbaz et al. 2018) and for the purpose of this study we require the most precise correction possible. To accurately align the ALMA and IFU cubes we used the spatially varying second order corrections adopted in Elbaz et al. (2018) (M. Dickinson; private communication). For our six targets in this field the average correction of the optical astrometry frame is $+0.19$ and -0.23 arcseconds in RA and Dec, respectively. To calculate the final positional uncertainties we propagated the errors of the 2D Gaussian fitting, used to locate the source in the IFU data cubes, and the astrometric uncertainties on the broad-band images. Overall, we are able to constrain the astrometric positions in the IFU datacubes with 0.1 arcsec accuracy (i.e., 0.8 kpc at z$\sim$ 2).

Measuring the projected offsets

To determine the offsets between the Hα and FIR emission we first needed to find the location of the peak emission in the Hα and ALMA maps. Since we have cases where the Hα emission is extended in one direction or has a complex morphology (for example ID 7, see Figure 4.6), we cannot apply a simple 2D model to determine the peak position accurately. Instead, we determined the centre of the Hα emission by finding the brightest pixel. To find the centre of the FIR emission we used the same technique, identifying the peak pixel in the ALMA maps. In Figure 4.6 we show Hα maps with contours from the ALMA overlaid ("IFU matched" as dashed contours and "High Resolution" as solid contours); the peak positions, with 1σ error circles are shown in red and blue for Hα and rest-frame FIR, respectively. The positional uncertainties for the peak position in the ALMA maps were determined by relating the signal-to-noise ratio of the emission and the size of the PSF (or beam), following δpos = PSF/(2 $\times$ SNR) (Condon, 1997). The positions of the Hα are dominated by the 0.1 arsec systematic (see above).

We present the measured offsets in RA and Dec between the narrow Hα and FIR emission in Figure 4.7 where the final uncertainties on the offsets between the the peaks of the two emission are determined by combining the individual uncertainties on the two positions using a bootstrap method. We draw 1000 random positions from a 2D Gaus-

sian distributions, centred on the individual Hα or FIR positions and with width of the positional uncertainty. We calculated the offsets for all 1000 random positions. The final values in Figure 4.7 are the median value of the offsets. The errors are calculated as 1 σ of the offset distributions. In this figure we highlight the four sources with crosses which have significant offsets between the Hα and FIR emission (i.e., those where the positional error circles do not overlap in Figure 4.6). The final *projected* offsets range from 0.8–2.8 kpc and are provided, with their uncertainties in Table 4.4.[9] The spatial offsets between the two sources of emission are discussed in § 4.4.3.

4.4 Results and Discussion

In this section we present the results of our analyses of the IFU and ALMA observations for the eight z=1.4–2.6 AGN in our sample. Our study is motivated by previous work that has used IFU observations to map star formation, using Hα, and AGN outflows, using high-velocity components of [O III] (e.g., Cano-Díaz et al., 2012; Cresci et al., 2015a; Carniani et al., 2016). Here, in addition to Hα and [O III] constraints we also include maps of the rest-frame FIR emission of our targets to trace the obscured star formation. After giving an overview of the emission-line properties of our sample (§ 4.4.1), we present results that address our two main objectives: (1) to test Hα as a star-formation tracer (both galaxy-integrated and spatially resolved) in our high-z AGN host galaxies (see § 4.4.2 & 4.4.3), and (2) to search for evidence that AGN outflows suppress and/or enhance star formation in their host galaxies (§ 4.4.4). In § 4.4.5 we discuss the wider implications of our results for understanding the relationship between AGN outflows and star formation.

4.4.1 Overview of the emission-line properties

In Figure 4.4 we present the the Hβ, [O III], Hα and [N II] emission-line profiles for our sample (extracted from a 5 kpc diameter aperture; see § 4.3.1). Our targets have representative emission-line properties of the parent sample from which they were selected (Harrison et al., 2016b, see Figure 4.1 and § 5.2.1). For example, they have total [O III]

[9] We note that using either the "IFU-matched" and "High Resolution" ALMA maps, results in consistent results for the final projected offsets.

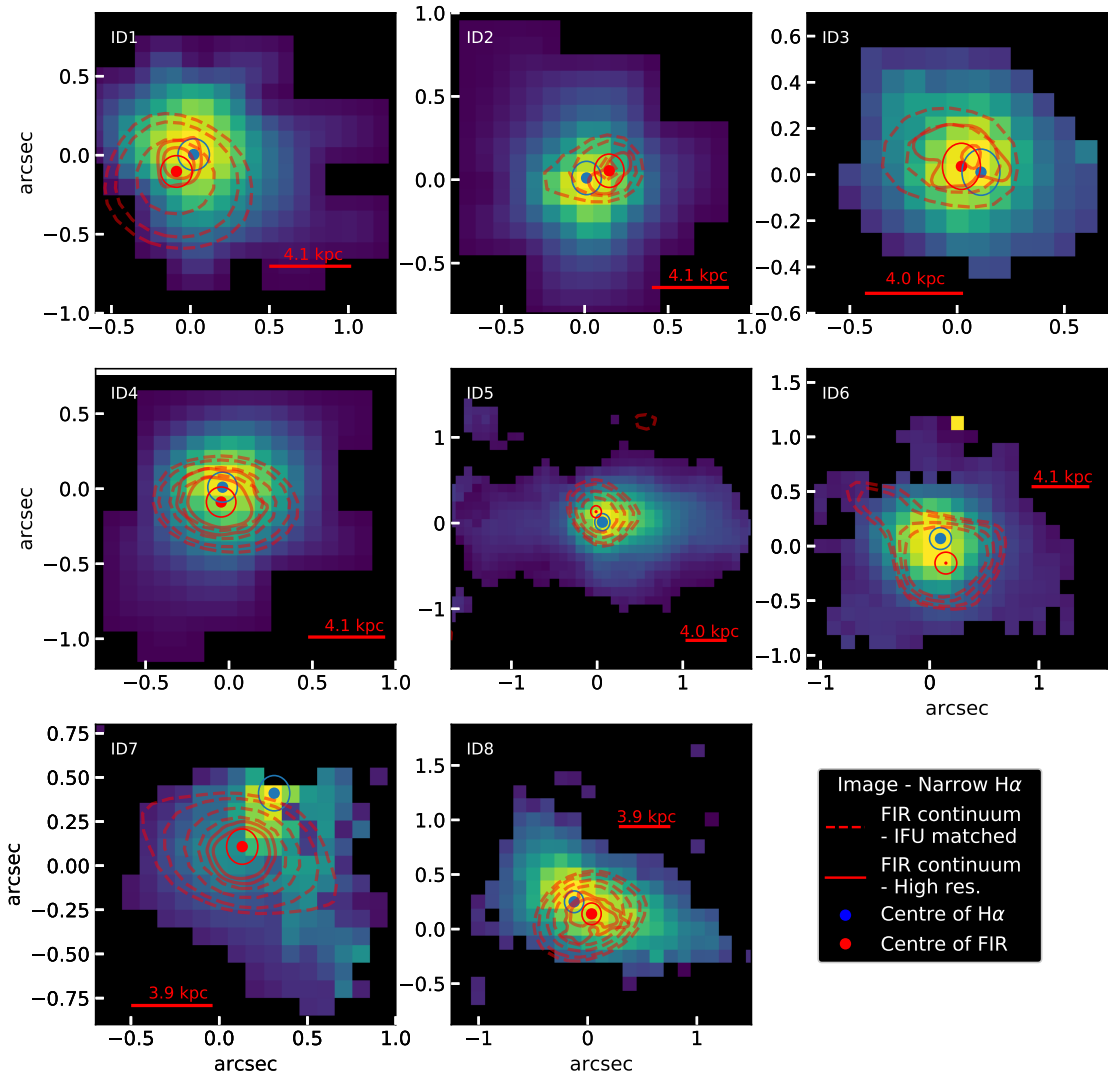

Figure 4.6: A comparison of the spatial distribution of the FIR emission and the narrow Hα emission for our AGN host galaxies. The images show the narrow Hα emission (see § 4.3.1). The red solid line represents the major-axis size of the PSF of the IFU observations, labelled with the corresponding physical scale in kiloparsec. Red contours show the FIR continuum (see § 4.2.3), where the dashed and solid contours are from the IFU-matched (comparable spatial resolution) and high-resolution ALMA maps (where applicable), respectively, with levels of 2.5, 3, 4, 5 σ. The blue and red solid circles show the centres of Hα and FIR emission, respectively. We discuss the alignment between the two sets of data in § 5.3.3. There is a range of Hα and FIR morphologies, with four targets showing significant spatial offsets between the two sources of emission (ID 5, 6, 7 and 8).

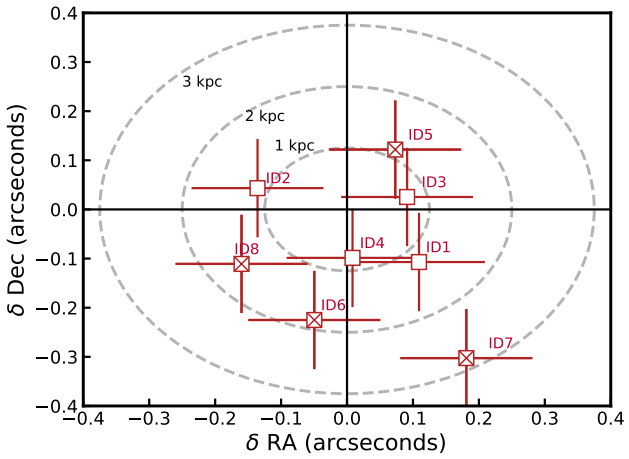

Figure 4.7: Offset between the FIR and narrow Hα emission of our AGN after correcting the astrometry (see § 5.3.3). The grey circles indicate the projected physical offset of 1, 2, and 3 kpc. The squares filled with crosses indicate the four objects with significant projected *radial* offsets between FIR and Hα emission (see § 4.4.3 and Figure 4.6).

luminosities of $\log[L_{[\mathrm{OIII}]}/\mathrm{erg\,s^{-1}}]$= 42.2–43.4, which is expected for their X-ray luminosities (see Table 4.1) based on the $L_{[\mathrm{O\,III}]}$- L_X relation of $z \approx 1$ X-ray AGN (Harrison et al., 2016b). Furthermore, they have typical [O III] emission line widths (W_{80}; Figure 4.1, bottom panel). In this respect they represent typical X-ray AGN at this redshift range; however, see § 4.4.5 for more discussion on the sample in terms of their star-formation rates. Here we describe the emission-line profiles in more detail. The key emission-line properties are summarised in the Table 4.3.

As can be seen in Figure 4.4, three of the targets have [O III] emission-line profiles characterised with single Gaussian components (ID 3, 7, 8), and five of the targets require two components (ID 1,2,4,5 and 6; see § 4.3.1). These latter five targets have second, broad components with FWHM= 600–950 $\mathrm{km\,s^{-1}}$ and are those targets which we define here as clearly having AGN-driven ionised outflows. For these targets we are able to define velocity slices in the wings which are most-likely not due to gravitational motions (§ 4.3.1; see blue shaded regions in Figure 4.4). However, we note that although ID 7 is adequately described with a single component fit, the high-velocity width of FWHM=720 $\mathrm{km\,s^{-1}}$ would strongly suggest contributions from gas motions which are non gravitational (e.g., Liu et al., 2013; Harrison et al., 2016b).

The total narrow Hα luminosities of the sample are in the range $\log(L_{\mathrm{H}\alpha}/\mathrm{erg\,s^{-1}})$=

42.1-43.2 and are discussed in § 4.4.2. The nuclear Hα kinematics from the narrow-line region (i.e., after removing broad-line region components) are typically more modest than those seen in [O III], with FWHM= 350–640 km s^{-1} (see Figure 4.4). Only in one source do we see strong evidence for an outflowing component in Hα and [N II] (ID 5; FWHM=900 km s^{-1}; see Figure 4.5; also see Genzel et al. 2014). Narrower Hα compared to [O III] has been noted before for both high-z and low-z AGN (Harrison et al., 2016b; Kang et al., 2017). Outflow components can be stronger in [O III] when compared to Hα if the outflows are co-located with the AGN ionisation cones (perpendicular to the disk) whilst the Hα is strongly dominated by star-forming disks (as has been seen in local AGN host galaxies; e.g., Venturi et al. 2018). However, we also note that the complexities and degeneracies of simultaneously fitting the [N II] doublet and Hα with broad and narrow components makes it very difficult to isolate, potentially weak, outflow components in these lines. We compare the spatial distribution of the [O III] and Hα emission for our targets in § 4.4.4.

4.4.2 Comparison of star-formation rates from FIR and Hα

In Figure 4.8 we compare the star-formation rates inferred from the Hα luminosity, SFR(Hα), to those inferred from the FIR luminosity, SFR(FIR) as calculated in § 5.4.1 and 4.3.1. By performing SED fitting on multi-wavelength photometry (UV-submm), the FIR emission used here has had the AGN contribution removed (§ 5.4.1). If we convert the observed Hα luminosities directly to star-formations rates the median ratio of the two SFR tracers is SFR(FIR)/SFR(H_α)=14.5, with a range of ≈2.5–65 (black squares in Figure 4.8). However, these ratios suffer from two important effects: (1) obscuring dust which will *lower* the observed Hα fluxes; (2) the contribution from AGN photoionisation, which will *increase* the Hα fluxes above that produced by star-formation alone.

To investigate the effect of dust attenuation, we make use of the observed Balmer decrement (i.e., the Hα/Hβ flux ratios), where possible, to calculate a single (flux-weighted average) Av_{HII} value per galaxy (§ 4.3.1). Although we detect Hβ in 5 out of 8 objects (ID 1, 3, 5, 6, and 8; Figure 4.4), it was not possible decompose the broad and narrow components in the Type 1 AGN (ID 1 & 6), therefore we only have direct Balmer decrement constraints for 3 targets (see § 4.3.1). For these targets the correction factors to the fluxes

are ≈1.5–18 (see red squares in Figure 4.8). After correcting for dust obscuration, the SFR(Hα) values of ID 5&8 are a factor 1.1–1.8 higher than the SFR(FIR).[10] Although this discrepancy is within the systematic error on the SFR calibrations, the SFR(Hα) should be considered an upper limit on the SFR, due to possible photo-ionisation from the AGN (see discussion below). Even after the dust correction, the SFR(Hα) of ID3 is a factor of 12 lower than SFR(FIR). For this source the total SFR, as inferred from FIR emission, can not be recovered from the Hα emission. Similar results have been seen for sub-mm galaxies and may be due to a different spatial distribution of obscured and unobscured star-forming regions and/or star-forming regions being completely undetected in the optical/near-infrared data due to the obscuring dust (Hodge et al. 2016; Chen et al. 2017, 2019).

Using Hα as a star-formation rate indicator in AGN host galaxies is a well known challenge, and high-redshift data typically lack the diagnostic power to carefully decompose the relative constributions to the Hα luminosity from AGN photoionisation, star formation photoionisation and shocks (Davies et al., 2014b,a; D'Agostino et al., 2019). Previous work using IFU data on AGN host galaxies presented low [N II]/Hα emission-line ratios as evidence that the Hα emission is star-formation dominated in off-nuclear regions for those specific targets (e.g., Cano-Díaz et al., 2012; Cresci et al., 2015a; Carniani et al., 2016); however, we re-assess this for one of these literature sources (our ID 6) in § 4.4.4. Based on the spectra shown in Figure 4.4 the emission-line flux ratios of $\log_{10}$ ([N II]/Hα) range between -0.64 and 0.20 (median of 0.05) for our sample. For the 5 objects with detected Hβ, the emission-line ratio of $\log_{10}$ ([O III]/Hβ) ranges between 0.97 and 1.47 (median value of 1.02). Including the non-detections of Hβ places most of our targets in the AGN-dominated region, with two possibly residing in the "composite" region of the z=0 BPT diagram (Kewley et al. 2006; see Table 4.3), although we acknowledge that characterising the emission-line ratio diagnostics for higher redshift galaxies is still a matter of on-going work (e.g., Kewley et al., 2013; Shapley et al., 2015; Kashino et al., 2019).

In summary, whilst our sample may be biased to those with particularly high levels of

[10]We note that, using independent analyses, Loiacono et al. (2019) also find SFR(Hα) is higher than SFR(FIR) for ID 5, possibly due to AGN contamination.

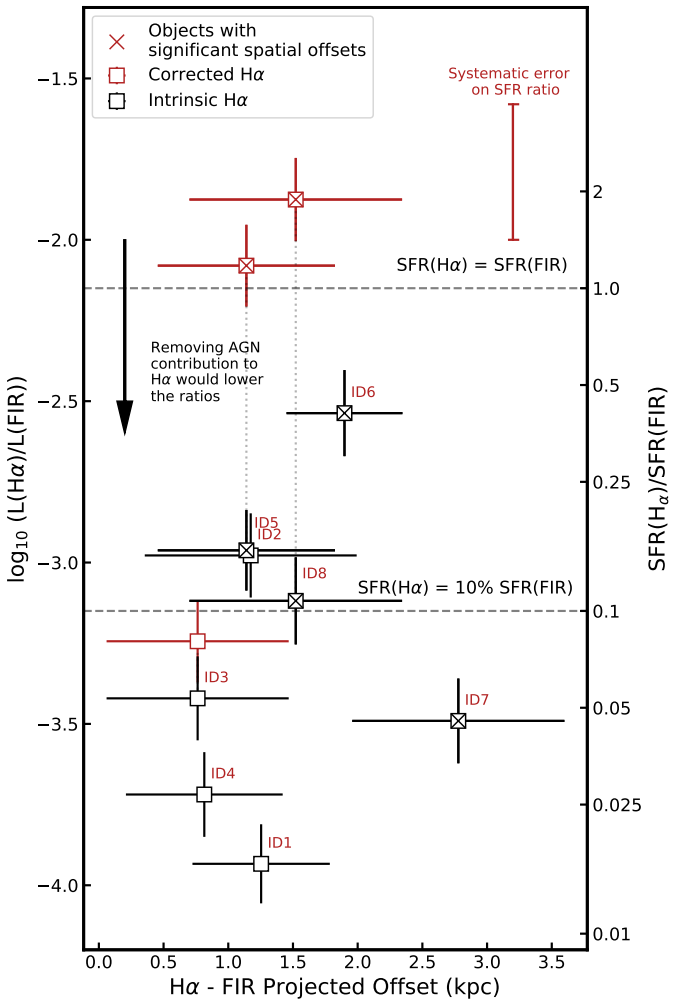

Figure 4.8: The ratio of $L_{H\alpha}$ and L_{FIR} (left axes) and, equivalently, the ratio of $SFR_{H\alpha}$ and SFR_{FIR} (right axis) as a function of projected physical offset between the Hα and FIR emission (see Figure 4.7). The black and red symbols indicate dust attenuation uncorrected and corrected Hα data, respectively (see § 4.3.1). The crosses show the objects with significant offsets between the FIR and Hα emission from Figure 4.6. The red error bar indicates the systematic error on SFR ratios due to calibrations (0.42 dex). Hα luminosities uncorrected for dust dramatically underestimate the SFRs, and in one case even after a dust-correction (ID 3). Applying a correction for a contribution from the AGN to the Hα emission would introduce a further discrepancy between the two tracers (see black arrow and § 4.4.2).

dust (due to the pre-selection of a detection in the ALMA data; § 5.2.1), we have shown the Hα luminosities uncorrected for dust could dramatically under predict the true values. Furthermore, in one target the SFR inferred from Hα is still an order of magnitude lower than that inferred from the FIR after a dust correction. On the other hand, we have shown that Hα emission is likely to have a significant ionisation contribution from the AGN which would result in the SFRs inferred from Hα being *higher* than the true values (also see black arrow in Figure 4.8). In conclusion, we find that the narrow Hα emission does not provide a reliable census of the total SFRs within our AGN host galaxies. We have shown the importance of having FIR measurements and/or emission-line ratio diagnostics to assess the true SFRs in AGN host galaxies. In the following sub-section we explore the differences between Hα and FIR further by utilising the spatially-resolved information in our data.

4.4.3 Spatially-resolved comparison of Hα and FIR emission

In Figure 4.6, we compare the spatial distribution of Hα emission (background maps) and FIR continuum (contours). The red and blue points with their respective error circles around, show the locations of peak narrow Hα and FIR emission, respectively (see § 4.3.3). Except for ID 7 we find that the Hα emission is centrally concentrated. However, we see a variety of *sizes* of the Hα emission, with ID 5 showing a particularly impressive 20 kpc wide Hα emitting region elongated in a East-West direction.[11] The FIR emission is also mostly centrally concentrated; however, for ID 6 we see a tail of rest-frame FIR emission to the North East which, as shown by Brusa et al. (2018), is extended towards a companion galaxy that is detected in the K-band LUCI+ARGOS data.

For four out of the eight targets we find a significant projected spatial offset between the peak in Hα emission and the peak in the FIR emission. That is, the positional error circles do not overlap for the two sources of emission in ID 5, 6, 7 and 8 (Figure 4.6). These conclusions are consistent if we use either the "High resolution" or "IFU matched"

[11] ID 5 has been considered a compact star-forming galaxy, progenitor of compact quiescent galaxies (Popping et al., 2017; Talia et al., 2018). Despite this, we measure the $r_{e,}$Hα to be 4 kpc and both Hα and [O III] are detected on scales up to 20 kpc. We note that these are extraordinary sizes; however, they may be due the additional photoionisation by the AGN.

ALMA maps (see § 4.2.3). In Figure 4.7 we show the positional offsets in Right Ascension and Declination between the two sources of emission. Across the full sample the projected offsets range from 1.3 kpc to 2.8 kpc, where the median offset is 1.4 ± 0.6 kpc (see Table 4.4). We could not find previous work which clearly quantifies the spatial offsets between Hα emission and FIR continuum for high-z galaxies to compare to. However, offsets between optical continuum and dust continuum have previously been reported in a qualitative way in several works (e.g., Hodge et al., 2016; Chen et al., 2017; Elbaz et al., 2018)

In Figure 4.9 we compare the half-light radii of Hα and FIR emission. These are calculated as described in § 4.3.1 and 4.3.2 and the values are provided in Table 4.4. For the five targets for which we were able to make a direct measurement we obtained Hα sizes of 1.8–4.4 kpc with an average value of 3.1 kpc. These Hα sizes for our targets are consistent with those measured by Förster Schreiber et al. (2018b), who targeted massive optically/NIR selected galaxies at z$\sim$ 2 using VLT/SINFONI and KMOS, finding Hα sizes between 1–8 kpc with a median value of 2.9 ± 1.5 kpc. For six of our targets we have a direct size measurement from the ALMA data (i.e., those with SNRs>8), and find FIR sizes of 0.5–2.9 kpc, using our preferred method of obtaining the sizes from the visibility data (see § 4.3.2), with an average value of 1.6 kpc. These FIR sizes agree well with the ≈0.6–2.5 kpc sizes previously found for X-ray AGN host galaxies (Harrison et al., 2016a) and sub–mm and star-forming galaxies (e.g. Ikarashi et al., 2015; Simpson et al., 2015; Hodge et al., 2016; Spilker et al., 2016; Tadaki et al., 2017; Fujimoto et al., 2018; Lang et al., 2019; Chen et al., 2019). In summary, the Hα and FIR sizes that we observe for our AGN host galaxies do not appear to be exceptional compared to other redshift-matched, mostly FIR bright, galaxy samples in the literature.

We find that the Hα sizes are factor of ≈2 times larger than the FIR sizes and in the four targets that we can make this comparison directly, the Hα sizes are 1.1–2.6× larger than the FIR sizes. In Figure 4.9 we compare these different size measurements of our sample to the z=1.5–2.5 sub-mm galaxies from Chen et al. (2019) (blue points) and a z=1.4 starburst galaxy from Nelson et al. (2019). These samples also exhibit Hα sizes which are ≈2× larger than the FIR sizes. Also consistent with this are other studies of high-z galaxies which have found that FIR continuum sizes to be $2-3\times$ smaller than

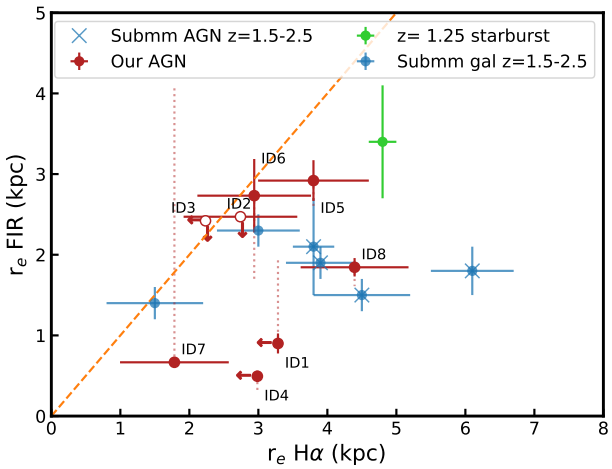

Figure 4.9: Comparison of the Hα and FIR emission sizes. The red circles represent our AGN sample (filled - FIR SNR>8, empty - FIR SNR< 8). The red dotted lines indicate the range of FIR sizes between the *uv* and COG methods (§ 4.3.2). In each case we took into account of the smearing by the beam/PSF. The blue and green points show sub-mm galaxies (Chen et al., 2019) and a starburst galaxy at z=1.5 (Nelson et al., 2019), respectively, where the blue crosses indicate sub-mm galaxies confirmed to host an AGN (X-ray or MIR). The orange dashed line indicates the one-to-one ratio between the Hα and FIR sizes. On average, the FIR emission is more compact than the Hα emission, similar to that observed in submm and starburst galaxies.

the rest-frame *optical* sizes (Hodge et al., 2016; Tadaki et al., 2017; Elbaz et al., 2018; Fujimoto et al., 2018; Lang et al., 2019), which also implies FIR sizes which are $2-3\times$ smaller than Hα, because broad-band optical and Hα sizes typically agree within ≈30% (Nelson et al., 2012; Förster Schreiber et al., 2018b).

Overall, based on the above comparison to the literature, Hα sizes that are a factor of 2–3 bigger than the FIR continuum are somewhat expected. However, what is particularly striking in Figure 4.9 is that the sub-mm galaxies which host an AGN (see crossed blue points) are those with the largest Hα sizes. Although in Chen et al. 2019 they find that the [N II]/Hα ratios are generally low, potentially indicating a low AGN contribution to ionising the gas. In our targets we are not able to rule out that AGN have a strong contribution to producing the most extended Hα emission. In the outer regions (>0.6 arsec) of the galaxies the log([N II]/Hα) ratios remain high, ranging from -0.4–0.4, which indicates AGN dominating the ionisation in the extended regions at least for some of the targets (unfortunately Hβ is too weak in the outer part of the galaxy to be realibly detected). Future work which is able to de-couple the contribution of the AGN and the star

formation components on larger samples is needed to fully understand the contribution of the overall AGN to producing the observed Hα emission sizes.

Based on (1) the discrepancy between star-formation rates inferred from Hα compared to those from FIR; (2) the different sizes and distributions of the FIR (tracing obscured star formation) compared to the Hα distribution and; (3) the challenges in decoupling the contribution of star-formation from the AGN contribution to producing the Hα emission, we conclude that Hα emission alone is not a reliable tracer of the star-formation in the AGN host galaxies in our sample. These challenges can be overcome, at least to some degree, in IFU observations of local AGN since the high spatial resolution observations can result in maps of multiple emission-line ratio diagnostics (e.g., Venturi et al., 2018; D'Agostino et al., 2019). However, with the current observational facilities this is rarely possible for high-z systems and caution, and a careful case-by-case assessment is required when using Hα emission to trace star-formation in high-z AGN host galaxies.

4.4.4 Star formation and AGN driven outflows

Despite the need for AGN feedback in cosmological simulations, we still lack a consensus on what impact AGN outflows have on star formation from observations. This is despite a lot of work in the literature that has searched for such an impact by comparing AGN-driven outflow properties with the star-formation rates and molecular gas measurements within the host galaxies. This is attempted both from a statistical point of view using large samples (e.g., Woo et al., 2016; Wylezalek & Zakamska, 2016; Lanzuisi et al., 2017; Harrison, 2017; Perna et al., 2018; Scholtz et al., 2018; Kirkpatrick et al., 2019) and from detailed, spatially-resolved observations of individual objects (e.g., Alatalo et al., 2015; Cresci et al., 2015b; Husemann et al., 2019; Shin et al., 2019). Of particular relevance for this work is the reported spatial anti-correlation between the AGN driven outflows (traced through [O III]) and the star formation (traced through Hα) in z=1.5–2.5 AGN (Cano-Díaz et al., 2012; Cresci et al., 2015a; Carniani et al., 2016). Unlike in the previous studies, we use multiple potential star formation tracers (FIR emission and Hα) to search for the impact of AGN ionised outflows on the star formation within their host galaxies of our sample, which also has representative luminosities and ionised gas kinematics of the parent AGN population (see Figure 4.1).

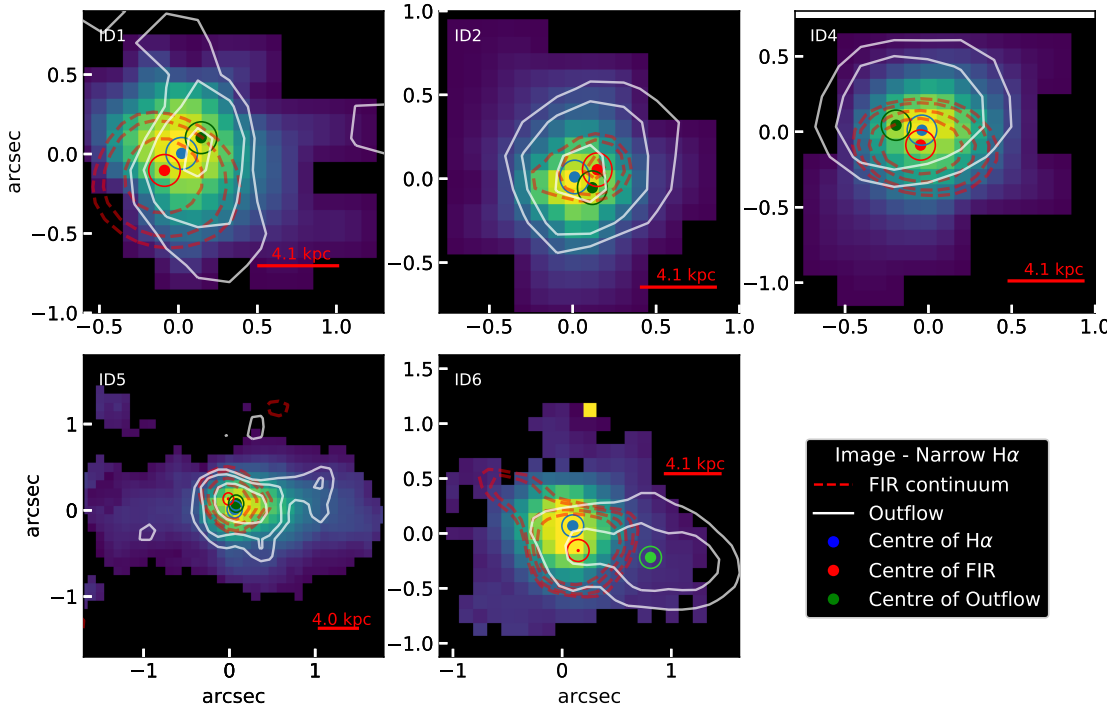

Figure 4.10: Maps to show surface brightness distribution of the narrow line Hα components, with the red-dashed contours showing the distribution of FIR emission (as described in Figure 4.6) for the five targets where we identified outflows. The red solid line represents the major axis the PSF of the IFU observations, labelled with the corresponding size in kiloparsec. The white contours show the distribution of the ionised outflow (3,4,5 σ levels), as defined by the high-velocity wings of the [O III] emission line (Figure 4.4). The blue, red and green points show the peak of the Hα, FIR and the outflow, respectively. We do not see significant anti spatial correlation between the Hα and outflows as found for a few high-z AGN (Cano-Díaz et al. 2012; Cresci et al. 2015a; Carniani et al. 2016). In Figure 4.11 we provide further insight into ID 6 which also appears in Cresci et al. 2015a. Overall, we do not see any strong evidence for the outflows instantaneously suppressing star formation in our sample.

We detected ionised gas outflows in five out of the eight objects in our sample (63 %, see Figure 4.4; § 4.4.1). In Figure 4.10 we present maps of the [O III] outflows as white contours (produced as described in § 4.3.1).[12] Three of the targets (ID1, ID5 and ID6) show significant [O III] outflows elongated beyond the central regions. In this figure, we also show maps of the Hα emission (background map) and rest-frame infrared (dashed contours). We represent the peak locations of the Hα, FIR and outflow emission as red, blue and green points, respectively. We do not see any strong evidence that the outflows suppress the star formation; i.e., either through cavities in the Hα emission at the location of the ionised outflows (cf. Cano-Díaz et al. 2012; Cresci et al. 2015a; Carniani et al. 2016) or cavities in the rest-frame FIR emission. Similarly to the offsets between Hα and FIR emission, we also measured the position of the peak of the outflow emission. Based on the positional uncertainties (see circles in Figure 4.10), in three sources (ID1, ID4 and ID6) we see significant offsets of 1.7–6.4 kpc between the outflows and the FIR emission (with a median value of $2.3^{+2.6}_{-1.3}$ kpc across the full sample). However, this could just be due to differential obscuration by the dust (i.e., [O III] is more obscured where the dust is located); unfortunately, we do not have the required signal-to-noise in the Hβ emission lines to map the Balmer decrement. Alternatively outflows may preferentially escape away from the dusty regions (e.g., Gabor & Bournaud, 2014). Only in ID 6 do we see significant offset between the peak of the Hα emission and the [O III] outflow, but this is just because the outflow is so extended beyond the centrally concentrated Hα emission. This source was originally presented with IFU observations in Cresci et al. (2015a) as showing evidence for positive and negative feedback. We do not conclude the same here, and discuss this source in detail in § 4.4.4. For three objects without any detected outflow, we do not see any systematic different star formation morphologies compared to those with detected AGN-outflow. This further indicates that the presence (or lack-there-of) of ionised outflows does not impact upon the distribution of star formation within the host galaxies in our sample.

[12] We note that, given the deep observations of ID 5, we detected outflows in both Hα and [O III] (also see Genzel et al., 2014; Loiacono et al., 2019) Comparing these two outflows, we found that they differ in both outflow kinematics (Figure 4.4) and spatial extent, with the Hα being more extended (up 4 kpc scales see Fig 4.5). However, it is not the focus of this work to characterise, in detail, the differences or origin of these two outflow components.

Overall, we do not see any strong evidence that ionised outflows are suppressing star formation (or enhancing it) in the host galaxies of our AGN host galaxies. This is in contrast to the results on three luminous z=2.5 quasars (Cano-Díaz et al., 2012; Carniani et al., 2016). These observations are quite similar to ours, in terms of using seeing-limited ground-based IFU observations to map both the Hα and [O III] emission. Although, in these works the Hα may be a more reliable tracer of star formation than for our targets (see § 4.4.3), it is worth noting that they do not include an analysis of the rest-frame FIR emission which may yet reveal dusty "obscured" star formation at the location of the observed deficit in Hα emission. It is also worth noting that these quasars represent some of the most powerful AGN in the Universe ($L_{bol} \sim 10^{47.5}$ ergs s^{-1}), which are a factor of $\sim$ 100–1000 higher than our targets. Furthermore, the [O III] FWHM of the quasars are 700–1500 kms^{-1}, representing the most extreme outflow systems (Figure 4.1). Therefore, it possible that the AGN in our sample lack the required power to rapidly impact upon the host galaxy properties, and it is only the most extreme systems where this effect can be observed. We will investigate the narrow Hα and our new ALMA band 7 continuum observations in Scholtz et al (in prep). Clearly, similar observations on a much larger sample are now warranted to establish if galactic outflows driven by powerful quasars are uniquely responsible instantaneously suppressing star formation inside their host galaxies.

No clear evidence of feedback in ID 6 - XID 2028

IFU data for target ID 6 was previously presented by Cresci et al. (2015a), where they identified a cavity in the Hα emission at the location of the AGN driven [O III] outflow, and enhanced Hα emission around the outflow edges. We do not observe similar features, instead finding that the Hα emission is spatially extended, but centrally concentrated (Figure 4.10). However, we note that in this work we present the Hα observations using the SINFONI H-band grating (ID 094.B-0286(A); not previously published), while the Cresci et al. (2015a) work used the earlier lower spectral resolution and shallower HK-grating observations (ID 383.A-0573(A)). Therefore, we repeated our analyses on the HK grating data, obtaining consistent conclusions to those seen in Figure 4.10 (discussed in more detail below). Regardless of the exact Hα morphology, there is still sufficient FIR continuum to imply significant star formation spatially-coincident with the outflow.

The difference in the results of the Hα emission between our results and those of Cresci et al. (2015a) could be the result of different analysis methods; for example, the adopted approach to account for the broad Hα emission. Therefore, we also performed similar analyses to those presented in Cresci et al. (2015a) by first fitting and subtracting the continuum and Hα broad-line region pixel-by-pixel from the cube before making a narrow-band image of the residual narrow-line component. To be fully consistent, we performed this on the *HK*-band data and the results are presented in the bottom panel of Figure 4.11. Although we do not detect Hα over the large scales measured with our original method and using the deeper *H*-band data, this analysis reveals a possible extension of the Hα emission to the West. Even-so this extension is *within* the [O III] outflow, in contrast to that presented by Cresci et al. (2015a), where the extended Hα emission is outside of the region covered by the [O III] outflow (Figure 4.6). We find that it is only when we use the same fully-reduced *HK* data cube as that used by Cresci et al. (2015a) that we are able to observe a cavity in Hα at the location of the outflow (G. Cresci, priv. communication). This implies that the differences found in this work to those in Cresci et al. (2015a) are not dominated by the adopted analyses methods but, instead, in the intermediate data reduction steps (e.g., sky subtraction or frame stacking). However, this source is scheduled for observations with *JWST*/NIRSpec, through an Early Release Science programme (Wylezalek et al., 2017),[13] which will provide sensitive and improved spatial resolution IFU observations of this source, resulting in the most definitive description of this source's Hα morphology.

We further investigate our results for ID 6 by comparing to the morphology of the rest-frame U-band emission as determined from the *HST*, *I*-band image (F814W filter) using the available 1 orbit of observations (Koekemoer et al. 2007; Figure 4.11, top panel). It can be seen that the U-band emission is slightly extended in the Western direction, within the region of the [O III] outflow. Furthermore, there is a possible slight extension of the FIR emission in this direction (in addition to the "tail" to the North East; also see Brusa et al., 2018), possibly implying star formation is located in the general direction of the outflow. Narrow Hα emission is also detected over the extent of the outflow; how-

[13] http://www.stsci.edu/jwst/observing-programs/approved-ers-programs/program-1335

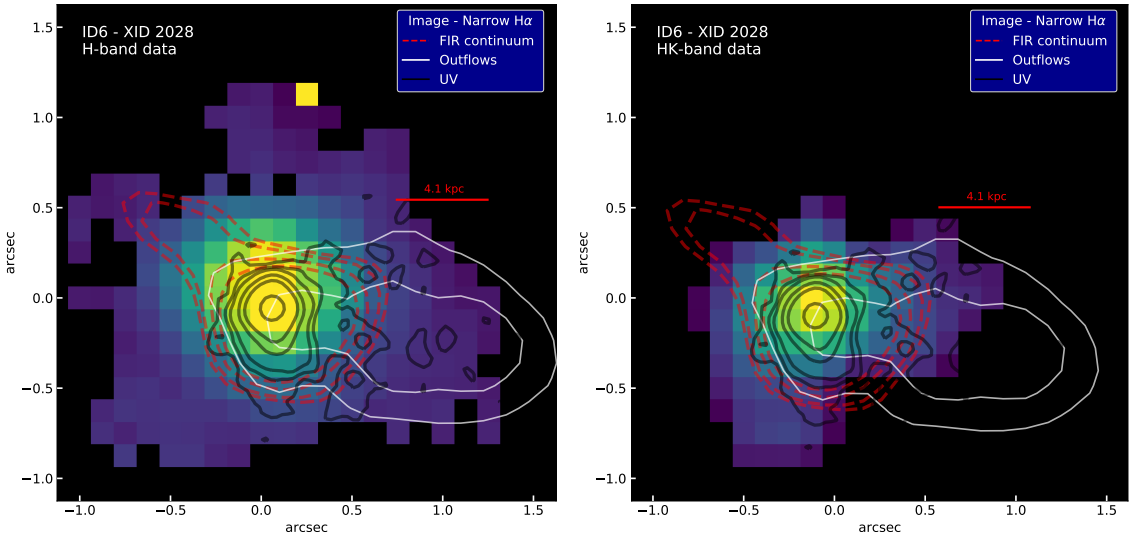

Figure 4.11: A comparison between the various emission discussed in this work for ID6 (also known as "XID 2028") from various observations. Left panel: H-band high-spectral resolution observations. Right panel: HK-band low-spectral observations. In both panels the maps show the narrow line Hα emission, the red-dashed contours show the distribution of FIR emission (2.5, 3, 5 σ levels) and the red solid line shows the size of the PSF (all as described in Figure 4.6). The white contours show the distribution of the ionised outflow (3,4,5 σ levels), as defined by high-velocity wings of the [O III] emission line (Figure 4.4). The black contours show *HST* I-band image (rest frame U-band; contour levels of 0.008, 0.015, 0.022, 0.05, 0.1, 0.5 relative to the peak). We observe marginally extended U-band emission, FIR continuum and narrow Hα emission all in the Western direction of the giant ionised outflow. We do not see evidence for suppressed star formation, instead, our results could indicate star-formation in the direction of the outflow and/or indicate the preferential direction of the ionising radiation from the AGN (§ 4.4.4).

ever, we find that the [N II]/Hα and [O III]/Hβ emission-line flux ratios are consistent photo-ionisation dominated by an AGN in this region. In summary, we find FIR emission, rest-frame U-band emission, and Hα emission all co-spatial with the [O III] outflow and consequently find no evidence for suppressed, or enhanced star formation due to the outflow in this source.

4.4.5 Implications of our results

Our work has shown that Hα emission must be used with caution as a star-formation tracer for AGN host galaxies, even when a global Balmer decrement is available to correct for dust obscuration (which is often not the case for high-z studies). Future, sensitive and high spatial-resolution IFU observations, e.g., with VLT/ERIS, *JWST*/NIRSpec or ELT/HAR-

MONI, will make it possible to map the ionisation conditions and Balmer decrements, and separate the contribution from AGN and star-formation in high-z AGN host galaxies. Except in exceptional cases of adaptive optics assisted IFU observations of lensed galaxies (Fischer et al., 2019), this is currently only possible for local galaxies (e.g., D'Agostino et al., 2019). Furthermore, for a complete census of the star formation we suggest it is necessary to also use spatially-resolved FIR observations to map the dust-obscured star formation.

Our sample is representative of typical AGN luminosities and outflow properties for $z \approx$1–2 AGN; however, it is limited to sources with existing detections in FIR and Hα emission, resulting in all of the sources lying on, or above, the 'main sequence' of star formation (Figure 4.2). We should also caution that, consequently, the systems where the star formation has rapidly shutdown may not be in our sample; however, ID 6 is a strong star-forming galaxy where suppressed star formation was previously suggested.

A key development of our study over previous work is that we focus on more common moderate luminosity AGN. However, it possible that our moderate luminosity AGN do not have sufficient power to rapidly change the star formation in their host galaxies, compared to their more powerful quasar counterparts (Cano-Díaz et al., 2012; Carniani et al., 2016). A more complete survey covering the full AGN luminosity – star-formation rate – stellar mass parameter space is now required to place more comprehensive constraints.

Useful insight to interpret our results can come from observations of nearby AGN host galaxies. Recently, Shin et al. (2019) observed both positive and negative feedback in NGC 5728, a nearby Seyfert like galaxy. The IFU and ALMA observations, showed enhanced star formation on the edges of the outflow in the very core of the galaxy as well as a lack of molecular gas in the outflow in the outskirts. However, both effects were observed on scales of $<$ 1 kpc scale. Indeed, although the samples lack the most powerful AGN, observations of local systems find that any impact by outflows and/or jets on the star formation, or molecular gas, is localised to small scales and is only affecting a small fraction of the the total star formation or gas content in the host galaxy (e.g., Alatalo et al., 2015; Cresci et al., 2015b; Rosario et al., 2019).

Based on our work, we therefore do not find any evidence that outflows from moderate luminosity AGN instantaneously influence the star formation inside their host galaxies

at least on ≈4 kpc scales. However, impact from these outflows could be occurring on spatial scales below those to which we are sensitive (i.e., <a few kiloparsec) and maybe subtle, only influencing a small region of the galaxy (e.g., Croft et al., 2006; Alatalo et al., 2015; Cresci et al., 2015b; Querejeta et al., 2016; Rosario et al., 2019; Shin et al., 2019; Husemann et al., 2019). Alternatively, the AGN outflows may have an impact over longer timescales, without an instantaneous influence on the star formation, for example, by removing low entropy gas which is later prevented from re-accreting onto the host galaxy (McCarthy et al., 2011; Gabor & Bournaud, 2014; Harrison, 2017; Scholtz et al., 2018).

4.5 Conclusions

In this work we present integral field spectroscopy (VLT/KMOS and VLT/SINFONI) and rest-frame FIR observations (ALMA) for eight z=1.4-2.6 moderate luminosity AGN ($L_X \approx 10^{42} - 10^{45}$ ergs s^{-1}). Our study is designed to build upon previous work that has claimed evidence for suppression and/or enhancement of star formation by high-z AGN by using integral field spectroscopy to spatially-resolve ionised outflows (using the [O III] line) and to map star formation (using the Hα line; Cano-Díaz et al. 2012; Cresci et al. 2015a; Carniani et al. 2016). In this work, we also used rest-frame FIR observations to map the dust-obscured star formation. We are able to assess how representative our targets are of the overall AGN population (see § 5.4.1) by utilising KASHz, an IFU survey of ≈250 AGN, as our parent sample.

We performed SED fitting on the compiled multi-wavelength photometry (UV-sub-mm) to measure the star-formation rates as traced by the FIR emission (SFR(FIR)) and confirm that the ALMA continuum traces dust-obscured star formation. We extracted galaxy-integrated Hα emission-line profiles to infer star-formation rates from Hα (SFR(Hα)). Where possible, the level of dust attenuation (A_V) was measured using Hα/Hβ ratios. Furthermore, we produced maps of the: (1) narrow component Hα emission; (2) rest-frame FIR emission and; (3) [O III]-identified ionised outflows. On the basis of our analyses we obtained the following results:

1. For all of our targets, the total SFR inferred from the observed Hα luminosities is

lower than that inferred from the FIR, by a factor of 2.5–65, with a median factor of 14.5. After applying a correction to the Hα luminosities for dust attenuation (possible for three targets), the SFR(Hα corr) is still a factor of 12 lower than SFR(FIR) for one target. Furthermore, accounting for the AGN photo-ionisation contribution to the narrow Hα emission causes further uncertainty in using this as a reliable star-formation tracer in our targets (see § 4.4.2; Figure 4.8).

2. We found that the projected spatial extent of the Hα emission is typically larger than that of the FIR continuum, by an average factor of ≈2. This is similar to that observed in sub-mm galaxies, particularly those hosting AGN, and is possibly due to dust-obscured star formation generally being more compact than unobscured star formation and/or additional photo-ionisation by the AGN to the Hα emission (§ 4.4.3; Figure 4.9). Additionally, in half of our sample we observe significant, ≈1–3 kpc, projected offsets between the peak of the FIR emission and the peak of the narrow Hα emission. The average projected offsets across the full sample of eight targets is 1.4 ± 0.6 kpc (see § 4.4.3; Figure 4.6; Figure 4.7).

3. We detected ionised outflows in five out of the eight AGN in our sample, traced by broad [O III] emission-line components (FWHM=610–950 km s^{-1}; Figure 4.4). Based on the spatial distribution of star formation and ionised outflows we see no strong evidence that the AGN outflows are rapidly suppressing or enhancing star formation in the host galaxies. The same conclusion for a lack of impact on star formation is found whether considering either the FIR or Hα emission as possible star-formation tracers; i.e., we see no "cavities" in the star formation at the location of the outflows. In three targets the [O III] outflows are offset from the peak of the FIR emission; however, this could be due to differential dust obscuration or the outflows preferentially escaping away from the dusty regions (see § 4.4.4; Figure 4.10).

4. One of AGN in our sample, ID 6, is a well studied z=1.6 X-ray AGN where a spatial anti-correlation of Hα emission and the [O III] outflow has previously been claimed as evidence for positive and negative feedback ('XID 2028' from Cresci et al., 2015a). We are able to reproduce the observations of a spectacular ≈10 kpc outflow

in this source; however, based on a re-analyses of the Hα data, including new high spectral resolution IFU observations, we do not observe any spatial anti-correlation between the outflow and Hα. We find significant star-formation (traced through FIR continuum) coincident with the outflow. Furthermore, the Hα emission, rest-frame U-band, and AGN outflow are all roughly co-spatial in the Western regions, consistent with an ionisation cone, or star formation located within the outflow (see § 4.4.4; Figure 4.11)

Overall, we have highlighted the challenges in using Hα to map the star formation in typical z=1.4–2.6 AGN host galaxies. We advocate using multiple possible tracers of star formation for a complete consensus such as FIR continuum. Within our sample we see no evidence that ionised outflows from moderate luminosity AGN are instantaneously having an impact upon the star formation inside their host galaxies. However, impact from these outflows could be occurring on spatial scales below those to which we are sensitive (<a few kiloparsec). Alternatively, the outflows may have an impact over longer timescales, for example by removing low entropy gas, without an instantaneous impact on the current rate of star formation.

CHAPTER 5

No evidence for rapid suppression of star formation by quasar driven winds at z∼2.5 revealed by ALMA and VLT/SINFONI

"Scientists normally like to do experiments. You know, they like to mix this with that and see what happens. They like to take this thing and poke it and see how it reacts. In astronomy, we can't do that. The stars, the planets, the galaxies, are so far away that we just look at them, and we have to learn things by looking at them. "

–Heidi Hammel, Astronomer

Abstract

We present new high-resolution ALMA band 7 continuum observations (rest-frame $\lambda \sim 250\mu$m) of three z∼2.5 QSOs. These targets have previously been reported as showing evidence for suppressed star formation based on cavities in the narrow Hα emission at the location of the quasar-driven outflows. Here we combine the ALMA observations with a re-analysis of the VLT/SINFONI data to map the star formation (obscured and unobscured) in these systems and to re-assess the evidence for cavities in the Hα emission. All three QSOs are significantly detected by ALMA (SNR>25) and, on the basis of a suite of analyses, we show that the ALMA data trace the dust-obscured star formation in two systems; in the third (radio bright) QSO the ALMA data is dominated by synchrotron emission. The dust-obscured star formation traced by ALMA is extended and is found at the locations of the reported Hα cavities, indicating that the star formation is not significantly suppressed in these systems. On the basis of several different approaches to map the narrow Hα emission and account for the QSO broad Hα emission we also do not find clear evidence for cavities in the Hα emission for any of the three QSOs. We verified

this result by extracting spectra around the Hα emission line from multiple regions across each QSO host galaxy, identifying the presence of a narrow Hα component in the regions. On the basis of these results we conclude that there is no clear evidence that (even powerful) AGN-driven outflows instantaneously suppress star formation. We therefore suggest that any suppression of star formation from AGN-driven outflows must occur over smaller spatial scales (<4 kpc) and/or on timescales longer than the duration of an AGN episode.

5.1 Introduction

In this chapter, I continue to explore whether AGN outflows are able to suppress star formation on large scales by investigating the spatial distribution of star formation at the location of outflows of three luminous quasars at z∼2.5.

In the previous chapter, I found no evidence that AGN driven outflows instantly suppress star formation in the moderate luminosity AGN. Furthermore, careful re-analyses of the data of XID 2028, a flagship example of negative AGN feedback in the literature, and additional rest-frame FIR observations showed no evidence of suppressed star formation in the region of the outflow.

However, it is possible that the moderate luminosity AGN do not have sufficient power to instantly alter the star formation in their host galaxy. For this reason, it is necessary to investigate the connections between AGN driven outflows and star formation in quasar (QSO) host galaxies. QSOs are AGN at a phase of a rapid SMBH growth ($M_{SMBH} = 10^9$ $M_\odot$), with bolometric luminosities of up to 10^{48} ergs s^{-1}. This massive energy output results in increased photo-ionisation of the ISM, as well as increased outflow velocity and mass outflow rates (Carniani et al., 2015; Bischetti et al., 2017).

Overall, two papers have looked at the effect of AGN driven outflow on star formation in high luminosity QSOs on a spatially resolved scale at high z> 1.5 (Cano-Díaz et al., 2012; Carniani et al., 2016). These studies observed both Hα emission and [O III] of three QSOs, tracing unobscured star formation and AGN driven outflows, respectively. In both studies, the narrow Hα emission showed cavities in the location of the AGN driven outflows. This result led to the interpretation that the AGN driven outflows instantaneously suppress star formation.

As I reported in the last chapter, it is necessary to use multiple star formation tracers to map both obscured and unobscured star formation. Therefore, it is possible that these narrow Hα cavities in the location of the AGN outflows are heavily obscured by dust, similar to the Hα cavities reported in Chen et al. (2017, 2019). Furthermore, my analyses of Hα observations of XID 2028 are in disagreement with the original study that presented the data (Cresci et al., 2015a).

Based on these facts, we deemed necessary to re-analyse the IFU data of these three QSOs from the literature, which show cavities in the narrow Hα emission with additional ALMA observations of rest-frame FIR emission. We put these QSOs in the context of the overall AGN population and we assess the contamination of the ALMA FIR observation by the AGN. In §2 we describe our targets, and the observations used in our study, in §3 describes the data analyses of the ALMA and IFU observations, including spectral fitting and constructing FIR, narrow Hα emission maps, in §4 we present our results, in §5 we draw our conclusions. In all of our analyses we adopt the cosmological parameters of $H_0 = 71$ km s^{-1}, $\Omega_M = 0.27$, $\Omega_\Lambda = 0.73$ and assume a Chabrier (2003) initial mass function (IMF).

5.2 Target description and Data

The primary objective of our study is to present new ALMA band 7 observations of objects claiming that AGN driven outflows suppress star formation in quasar host galaxies and compare the ALMA data to the narrow Hα emission from archival VLT/SINFONI observations. In §5.2.1 we describe the selection of our sample, in §5.2.2 and §5.2.3 we describe the ALMA and IFU data we used in the analyses.

5.2.1 Target description

We selected object 2QZJ002830.4-2817 from Cano-Díaz et al. (2012), LBQS0109+0213 and HB89 0329-385 from Carniani et al. (2016) and we will refer to these objects in this work as 2QZJ, LBQS and HB89. Originally, 2QZJ, LBQS and HB89 sources were selected as sources with large [O III] equivalent widths ($>$ 10Å in the rest frame) and bright in H-band ($<$ 16.5 mag) from a sample of QSOs from Netzer et al. (2004) and

Shemmer et al. (2004) (for more information see Carniani et al. 2015). The object's names, sky positions, redshifts, bolometric luminosities and W80 of the [O III] line (width containing 80% of the total line flux) are summarised in Table 5.1.

These objects were also part of ALMA CO(3-2) follow up (Carniani et al., 2017) using the Band 3 observations (3 mm) to detect emission lines from the molecular gas. We use the continuum photometry from their work in §5.4.1 to help identify sources with ALMA band 7 continuum emission contaminated by the QSO.

Figure 5.1 places our sources within the context of the overall AGN and QSOs population. In the top panel we compare the [O III] luminosity ($L_{[O\ III]}$) as a function of AGN bolometric luminosity for the three QSOs, moderate luminosity AGN from (Harrison et al., 2016b, and Harrison et al in prep.) and QSO population from Shemmer et al. (2004) and Netzer et al. (2004). The three QSOs in our sample have a bolometric luminosity $\sim 2 \times 10^{47}$ ergs/s, a factor of $\sim$ 100 larger than a typical AGN population at z = 1–2.5, as in Chapter 4. The QSOs have a similar $L_{[OIII]}$ and L_{Bol} ratio as moderate luminosity AGN (Panessa et al., 2006; Harrison et al., 2016b). Although these relationships are between $L_{[OIII]}$/X-ray luminosity, we converted the X-ray luminosity to bolometric luminosity assuming a nominal radiative efficiency of ε = 10%. In the bottom panel of Figure 5.1 we investigate the W80 of the [O III] line as a function of [O III] luminosity. The three QSOs lie in the high [O III] luminosity and high [O III] line width part of the plot, making them some of the most extreme [O III] emitters in the QSO population.

5.2.2 ALMA observations and imaging

To map the rest-frame FIR emission for our QSO host galaxies, we use yet unpublished ALMA band 7 data (870 μm, PI: Harrison, programme ID 2017.1.00112.S) with a resolution of $\sim$ 0.4 arcseconds, with a maximum recoverable scales of $\sim$4.3 arcseconds. The observations were performed using 45–49 antennae with a baselines range of 15–800 m. The ALMA band 7 continuum observations trace rest frame emission of $\approx$ 250 μm. We discuss the origin of this ALMA emission in §5.4.1.

We calibrated all the data and created the measuring sets using standard ALMA scripts for PI using a version of Common Astronomy Software Application (CASA) for the Cycle of the observations (Cycle 5; CASA v5.1.0). We performed additional checks to see if all

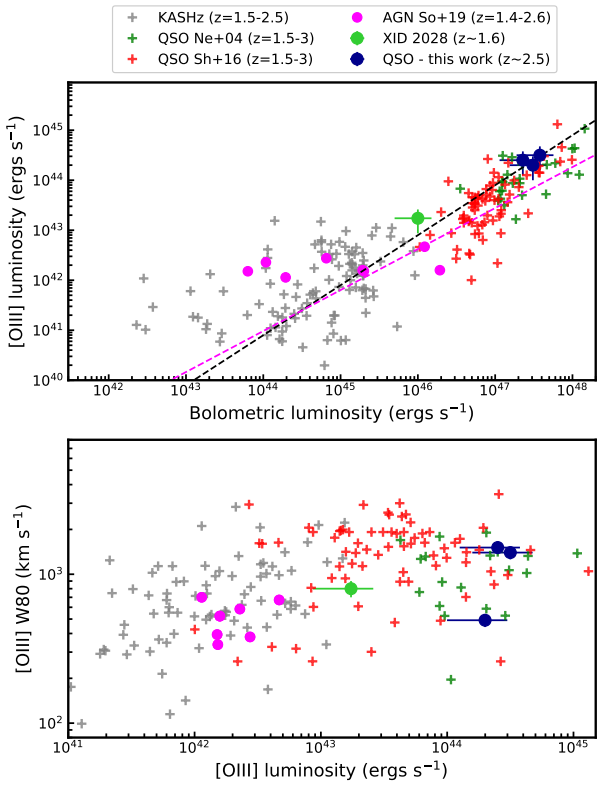

Figure 5.1: Top panel: [OIII] luminosity vs AGN bolometric luminosity. The QSOs from this work are represented as blue points. To put our sources into the context of the AGN and QSO population, we show AGN from the KASHz survey (Harrison et al., 2016b, z=1.2-2.5), AGN from Chapter 4 (z∼1.4–2.6) and QSO from Shemmer et al. (2004) and Netzer et al. (2004) (the original parent sample for these studies) as red, magenta and dark green points, respectively. We also show XID 2028, another high luminosity AGN which previously showed evidence of AGN outflows suppressing star formation (Cresci et al., 2015a). The black and magenta lines show the relationship between [O III] and AGN X-ray luminosity from Harrison et al. 2016b (z= 0.8–1.5) and Panessa et al. 2006 (z∼ 0.1), respectively. Bottom Panel: [O III] W80 (velocity width containing 80% of the total flux) vs the [O III] luminosity. The objects and symbols are the same as plotted in the top panel. The quasars studied here are some of the most extreme in terms of bolometric power and [O III] velocities.

Table 5.1: The table of the basic properties of our QSO sample. (1) Object ID in this paper; (2) Object ID from Cano-Díaz et al. (2012); Carniani et al. (2015); (3,4) Optical coordinates of the objects; (5) Redshift measured from the emission lines (see §5.3.2); (6) Bolometric luminosity from Shemmer et al. (2004); (7) W80 of the [O III] from Netzer et al. (2004); (8) Original paper analysing the SINFONI IFU data; (9) On-source exposure time in the IFU K-band (Hα) observations.

(1) ID	(2) Full name	(3) RA (optical)	(4) DEC (optical)	(5) z	(6) $\log_{10}$ $L_{Bol}/ergss^{-1}$	(7) [OIII] total W80 (kms^{-1})	(8) Original work	(9) IFU exposure time (ks)
HB89	HB89 0329-385	52.776542	-38.401389	2.445	47.5	1512	(b)	14.4
LBQS	LBQS0109+0213	18.070417	2.496389	2.352	47.5	419	(b)	14.4
2QZJ	2QZJ002830.4-281706	7.126833	-28.284667	2.401	47.3	1400	(a)	2.4

(a) Cano-Díaz et al. (2012); (b) Carniani et al. (2016)

calibrations and the pipeline flagging of bad antennae pairs worked correctly and checked that none of the spectral windows used to create the continuum image contains any visible emission lines. The data were imaged using the CASA version 5.1.2.

The uv-visibilities in the measuring set were Fourier transformed to create dirty images. We imaged the data using the natural weighting and the final resolution of the images was 0.4 arcseconds. These dirty images were consequently cleaned using a similar technique to that described by Hodge et al. (2013). We estimated the RMS in the dirty maps, put cleaning boxes around our primary science targets and any visible source in the image and finally, we cleaned the maps to 3σ. The final RMS of the maps of 2QZJ, LBQS and HB89 is 0.018, 0.020 and 0.025 mJy, respectively. We show the ALMA band 7 continuum maps in Figure 5.2.

5.2.3 IFS Data

Our targets were observed by VLT/SINFONI integral field spectrograph to trace the unobscured star formation using the Hα emission line. The Hα IFU data was first published in Cano-Díaz et al. (2012) and Carniani et al. (2016). Observations of LBQS and HB89 were performed using the 8×8 arcsec field of view which is divided into 32 slices of width 0.25 arcsec with a pixel scale of 0.125 arcsec, while the observations of 2QZJ were performed using the smaller field of view of 3×3 arcsec which is divided into 32 slices of width 0.10 arcsec with a pixel scale of 0.05 arcsec. SINFONI has a spectral resolution of R=4000 in K-band; the local spectral resolution (in the vicinity of the science emission lines) were calculated from the width of the skylines and this spectral resolution was subtracted of in quadrature from the observed emission line width. The on-source exposure time varied 14.4 ks for LBQS and HB89 and 2.4 ks for 2QZJ. The short exposure for 2QZJ resulted in a low SNR spectrum.

We used the published cubes from Carniani et al. (2016) [1] for the LBQS and HB89 objects. The IFU data for 2QZJ used in this work was reduced using the same method as in §4. The IFU data reduction was carried out using the standard techniques within ESOREX (ESO Recipe Execution Tool; Freudling et al., 2013) following Harrison et al.

[1] Available to downloaded at http://vizier.u-strasbg.fr/viz-bin/VizieR?-source=J/A+A/591/A28

(2016b) and Chen et al. (2019). The individual exposures were stacked on the centroids determined from white-light images from the datacubes. The flux calibration solutions were derived using the IRAF routines STANDARD, SENSFUNC and CALIBRATE on the standard stars, which were observed on the same night as the science observations. We will primarily use the shape of the BLR (see §5.3.2) as a measure of the PSF, since it is a measure of the PSF directly from the observations. The final FWHM of the PSF measured from the BLR (see §5.4) is 0.4 arcseconds for 2QZJ and 0.6 arcseconds for the LBQS and HB89, consistent with reports by the original studies.

5.3 Analyses

5.3.1 Analysing ALMA data

In this section, we describe measuring the fluxes and sizes of the Band 7 emission. We use the ALMA band 7 continuum sizes to assist in finding the source of this emission in §5.4.1. In order to compare the locations of the narrow Hα and ALMA band 7 emission, we also determine the location of the peak of the emission in this section (see §5.4.3).

To get reliable fluxes, sizes and positions of the FIR emission traced by ALMA, we measure these quantities in both image and the uv plane. We first analysed the data in the image plane. We used the CASA's `IMFIT` routine to fit a single elliptical Gaussian convolved with the synthesised beam to the data to measure the size and total flux of the FIR continuum.

Before looking at uv visibilities we phase centred our data to our objects using the `fixvis` routine to have our object in the centre of the field. We investigated how the visibility amplitudes vary as a function of uv-distance (see Figure 5.2). A point source has constant amplitude across all uv distances, while for a resolved emission, the amplitude is decreasing with uv distance (see e.g., Rohlfs & Wilson 1996 for more details). For each target, we extracted the visibility amplitudes from the measuring sets and binned the visibilities in bins of 50kλ. We modelled the binned amplitudes as a straight line with a gradient of 0 and as a half Gaussian model centred on 0. For each fit we cal-

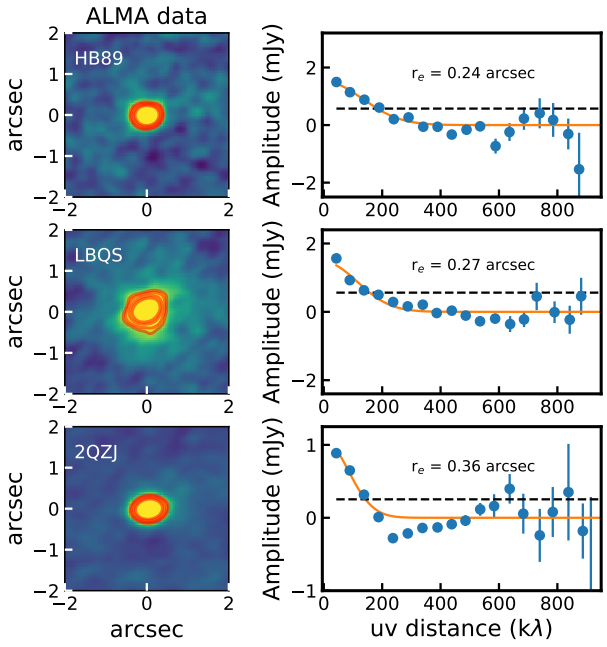

Figure 5.2: Summary of our analyses on the ALMA data. Left column: ALMA continuum images. The red contours indicate 2.5, 3, 4, 5 σ levels of the data. Right column: The uv amplitude data vs the uv distance binned per 50kλ. The orange solid curves and black dashed curves show resolved and unresolved model fits. In all cases, the ALMA band 7 continuum is resolved on 2–3 kpc scales.

culated the Bayesian Information Criterion [2] to decide which model was the better fit, and consequently to determine whether the object is resolved. We also used the CASA `uvmodelfit` routine to fit a Gaussian and a point source models to the raw uv visibilities to estimate the flux and the size of FIR continuum. We obtain consistent sizes and fluxes across all three methods used to measure these quantities. We show the ALMA band 7 continuum images and the uv visibilities amplitudes in Figure 5.2.

In order to find the centre of the FIR emission, we used the same technique as for determining the centre as for finding the centre of the Hα emission (see §5.3.2), by identifying the peak pixel of the FIR emission. We repeated these analyses on maps imaged at different pixel scales. We note that the pixel scale or resolution of the maps do not alter the location of the FIR peak emission (for more information see §4).

[2]BIC: We used the Bayesian Information Criterion Schwarz 1978), which uses $\Delta\chi^2$ but also takes into the account the number of free parameters, by penalising the fit for more free parameters. BIC is defined as BIC=$\Delta\chi^2 + k\log(N)$, where N is the number of data points and k is the number of free parameters. We accept a fit with more fits if the ΔBIC $\geq$ 15.

5.3.2 The Emission Line properties

For each of our targets, we have IFU observations covering the Hα and [N II]6548,6583 central emission lines. The integrated emission line profiles of the central 5 kpc are shown in Figure 5.3. In this section we provide information about: (a) extraction of the galaxy-integrated and spectra modelling the emission-line profiles(see §5.3.2); (b) mapping the emission-line regions (see §5.3.2); (c) curves-of-growth analyses (see §5.3.2); and (d) extraction of spectra from the grid.

Galaxy-integrated spectra emission-line modelling

We extracted the galaxy-integrated spectra with the primary goal to determine the spectrum of the QSO, necessary to subtract from the spaxel's spectrum when mapping the narrow Hα. To do this, we first determined the peak of the continuum emission in the IFU data cube, collapsing the datacube in the wavelength direction, excluding any spectral channels contaminated by the emission lines or sky-lines. We fitted a 2D Gaussian to the continuum map to find the centre of the continuum emission, the centre of the QSO host galaxy. Given that the continuum emission is dominated by the emission coming from the QSO, 2D Gaussian is a sufficient model of the continuum.

For each of the observations, we extracted two separate circular apertures centred on the continuum emission: (a) a center 5 kpc diameter (0.5 arcsec; which is roughly size of the PSF) to determine the QSO spectrum (presented in Figure); (b) 'total' aperture to determine the total emission-line flux. We also extracted a sky spectrum (i.e., object free spectrum) used to determine any spectral pixels significantly contaminated by the sky-lines residuals. We present the inner 5kpc spectra in Figure 5.3.

To model the emission line profiles observed by the IFU, each line was fitted with one or two Gaussian components (or modified Gaussian components; see below) with the centroid, FWHM and normalisation (fluxes) as a free parameter. In each case, the continuum is characterised by a linear function. In order to characterise the Hα emission-line profile we simultaneously fitted the following components: (a) broad line Hα describing emission from BLR; (b) narrow Hα; and (c) [N II]6548Å, [N II]6583Å emission line doublet. To avoid degeneracies in the fit, the central wavelength and FWHM of the narrow Hα and [N II]6548Å, [N II]6583Å doublet were tied together, with rest-frame wavelengths of

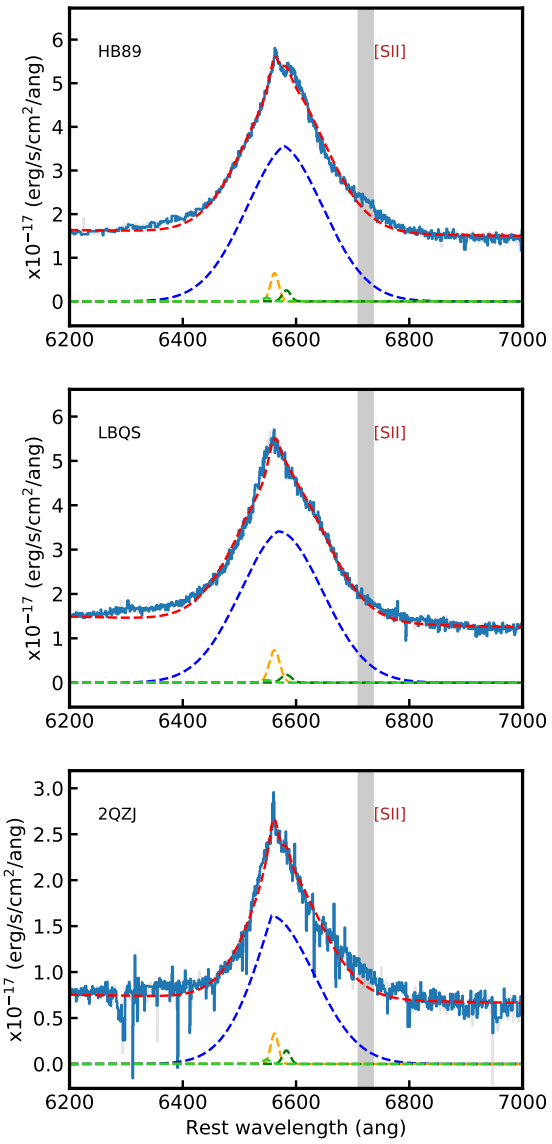

Figure 5.3: Hα emission-line profiles extracted from the inner 5 kpc nuclear spectra for the three QSOs in our sample. Light blue curves show the data and the grey curves show the masked sky-line residuals. Overlaid on the Hα profiles the yellow, blue, dark green, light green and red curves show the narrow Hα, broad line Hα, [N II] (6583 Å), [N II] (6548 Å) and the total fit, respectively. The grey shaded region shows the location of the [S II]. We investigate the excess emission in the blue wing in LBQS and the red wing in 2QZJ spectra in §5.3.2.

6549.86Å, 6564.61Å and 6585.27Å, respectively. This method assumes that the Hα and [N II] originate from the same gas and is a commonly used assumption in high redshift observations (Förster Schreiber et al., 2009; Genzel et al., 2014; Harrison et al., 2016b; Förster Schreiber et al., 2018b). During the fitting, the Hα and [N II]6583Å fluxes were free to vary but the [N II]6548Å/[N II]6583Å flux ratio was fixed to be 3.06 (based on the atomic transition probability; Osterbrock & Ferland 2006).

Following the approach by other studies, we modelled the Hα emission originating from the BLR as a Gaussian component multiplied by a broken power-law (Netzer et al., 2004; Nagao et al., 2006; Cresci et al., 2015a; Carniani et al., 2016). This model is a good fit for the asymmetrical nature of broad line emission lines in high luminosity sources such as our QSOs. We also tested the same BLR characterisation as done by the other authors, i.e., using one or two Gaussians (Cano-Díaz et al. 2012 and §4). Furthermore, we note a small residual amount of emission above our fit over wavelengths 6300–6400 Å in Figure 5.3 and is likely attributed to a blend of multiple weak emission lines over this region such as: [O I], S III and Si II. This was treated as an additional broad and weak Gaussian component "X" by Carniani et al. (2016). Including these additional components does not impact upon morphology of the narrow Hα in our analyses.

The models were fitted using the Python `lmfit` least-square library, excluding spectral channels which were affected by the skylines. To construct a skyline residual mask we extracted a sky spectrum by assuming all of the object-free (sky only) spatial pixels in the cube and identifying the strongest skyline residuals by picking any spectral pixels outside 1σ and these are shown as grey data in Figure 5.3.

Multi-component fitting of spaxel spectra

To map spatial distribution the narrow Hα and [OIII] outflows in our QSO host galaxies, we used two different methods: (i) multi-component fit performed spaxel-by-spaxel (used in Cano-Díaz et al. 2012 and see §4; (ii) subtracting the broad line and continuum component first to create a narrowband image of the emission line (Cresci et al., 2015a; Carniani et al., 2016). To increase the SNR of the spaxel's spectra, we binned the spectra by averaging the nearby spaxels within a radius of 0.2 arcseconds. This greatly enhances the SNR, while keeping the seeing limited spatial resolution of 0.4–0.7 arcseconds. We

Table 5.2: The table of the basic properties of our QSO sample. (1) Object ID in this paper; (2) velocity FWHM of the narrow Hα; (3) velocity FWHM of the broad line Hα; (4) Half-light radii of the Hα emission (see §5.3.2); (5) The half-light radii of the FIR (dust) emission derived in the uv-plane (see §5.3.1) (6) Flux density of the ALMA continuum measured in the uv plane. (7) Signal-to-noise of the peak continuum measured from the maps.

(1) ID	(2) Hα narrow FWHM kms^{-1}	(3) Hα broad FWHM (kms^{-1})	(4) Hα r_e (kpc)	(5) FIR r_e (uv) (kpc)	(6) ALMA Flux band 7 (mJy)	(7) ALMA SNR
HB89	802 ± 78	7488 ± 250	3.6	1.9 ± 0.8	1.53±0.030	28
LBQS	450 ± 65	7685 ± 150	< 2.7	2.3 ± 0.8	1.57±0.020	29
2QZJ	614 ± 80	6585 ± 200	< 1.72	3.0 ± 0.8	1.06±0.032	36

note that binning does not alter the morphology of our maps, however, it provides better SNR in when mapping the extended narrow Hα emission.

We note that regardless of the method used to create the narrow Hα map, we inspected the map of the BLR to verify that the fitting routine ran correctly. In all cases, the BLR map is well fitted with a 2D Gaussian. The FWHM of the 2D Gaussian is in agreement with the sizes of the BLR region measured from the curves-of-growth (see §5.3.2 and Figure 5.4).

The first method for producing narrow Hα maps is the multi-fit method. In this method, we fitted narrow Hα and [N II] and broad line Hα components simultaneously. We fixed the central wavelength and line-width of the BLR component (i.e. both the Gaussian component and broken power-law) to be the same as obtained from the nuclear spectrum (Figure 5.3), leaving only the flux of the BLR as a free parameter. This is a reasonable approach for such point source emission because only the *flux* in these BLR components will vary with distance, following the PSF. The maps of the narrow Hα component from the spatial fitting are shown in the left column of Figure 5.4. We compare the total narrow Hα flux in the maps compared to the flux estimated from the total aperture spectra, and we find that the fluxes are within uncertainties on the respective measurements.

Although the multi-component fit of the spatial spectra is our preferred method of creating the maps of the narrow component, we repeat the method used in Cresci et al. (2015a) and Carniani et al. (2016) to allow easier comparison between the studies. This method consists of subtracting the BLR and continuum emission from the cube first, followed by creating a narrowband image of the narrow Hα in the residual cube. We will refer to this method as QSO-sub method.

Before we fit and subtract the broad line Hα emission, we masked the spectral regions containing the narrow Hα, [N II] and [S II] doublets. This ensures that the narrow Hα and [N II] line-emission does not boost the broad line Hα fit, eventually over-subtracting the broad emission in the cube. We perform the spaxel-by-spaxel fitting, by only fitting a single Gaussian multiplied by a broken power-law component describing the Hα emitted from the BLR and a continuum model (see §5.3.2 for more details). We fix the central wavelength and line-width to same values as obtained in the inner 5 kpc spectrum. We

subtract the broad line Hα and the continuum model to create a residual cube, only containing the emission of the narrow line emission lines (narrow Hα, [N II] doublet and [S II] doublet).

In order to create a narrowband image of the narrow Hα emission, we created a galaxy integrated spectrum from the residual cube in the total aperture described in §5.3.2. We fitted this residual total spectrum with models describing the narrow emission lines. We note that the fluxes of the narrow Hα from galaxy integrated spectra using the original and QSO-subtracted cubes are consistent within 10 %. We then collapsed the cube along the spectral channels within the FWHM of the narrow Hα emission fit. We present the narrow Hα maps created by this method in the second column of Figure 5.4. The peak fluxes in the maps from the QSO-sub method are systematically 10 % lower than the peak fluxes in the maps form the multi-fit method. However, the morphology is consistent between these maps.

Modelling the Curves-of-growth of Hα emission

We used the curve-of-growth (COG) to measure the sizes of the narrow Hα emission as well as an assessment of the morphology of the narrow Hα by creating mock maps with different morphology and modelling their COG.

To measure the size of the narrow Hα emission, we used a COG method (see e.g., Chen et al., 2017, 2019, and §4). This method consists of measuring the total enclosed flux in a series of increasingly large apertures, centred on the QSO position. We fitted models describe in §5.3.2 to the aperture spectra. Similarly to the creation of the emission line maps (see §5.3.2), we lock the central wavelength and line-width of the broad line Hα component. The COG of the BLR component is used to estimate the size of the PSF of the observations.

The left column of Figure 5.4 shows the comparison of the COG for the narrow Hα emission (solid red lines) and BLR Hα emission (blue dotted lines). To interpolate between the data points, we used linear splines and we estimated the half-light radii, radius containing 50 % of the total flux. We calculated the objects *intrinsic* size emission (r_e), by subtracting off the size of the PSF (from the BLR) in quadrature. Uncertainties on the final Hα sizes are calculated by considering the full range of possible radii for the

1σ range of fluxes at each radii. The intrinsic sizes of the narrow Hα emission and their corresponding uncertainties are provided in Table 5.2. We spatially resolved narrow Hα in one object (HB89). For LBQS and 2QZJ, we estimated an upper limit on the narrow Hα size as the size of the PSF determined from the BLR.

In order to help to interpret the morphology of our narrow Hα maps in §5.4.2, we compared our COG to three theoretical COG, obtained from mock maps with different morphology. We created three mock maps: (a) a smooth 2D Gaussian profile; (b) 2D Gaussian profile with a symmetrical cavity in the middle (a doughnut); (c) 2D Gaussian profile with an extended cavity in one direction cavity (an arc). We additionally add random noise from a Gaussian distribution with a $\sigma \approx 0.05\times$peak value of the 2D Gaussian profile, which is a typical noise measured in the narrow Hα maps. In §4, we see a smooth distribution whilst for these QSOs the previous authors have claimed cavities/arcs in the narrow Hα emission. Therefore, we constructed three maps with these morphology. All three mock maps are showed in the third column of Figure 5.4. We repeated our COG analyses on these mock maps and we show these COG in the fourth column of Figure 5.4. While the COG for a smooth map is steadily rising from the centre of the QSO, the disturbed morphology maps show a flat COG in the core. The COG of the disturbed maps start to increase only once it starts to include flux from the outside of the cavity. We investigate the morphology of the narrow Hα emission further in §5.4.2.

Regional spectra of the QSO host galaxies

As a final verification of the spatial distribution on the narrow Hα maps, we extracted spectra from nine rectangular regions in the QSO host galaxies. These regions were defined as a grid of 3×3 squares with a size of 0.5×0.5 arcseconds. Therefore, the entire grid samples a region of 1.5×1.5 arcseconds, which contains most of the emission from the QSO host galaxy. We centred the grid on the QSO location.

The spectral line fitting was performed using the same models as described in §5.3.2. Similarly to the mapping of narrow Hα in §5.3.2 and creating the COG in §5.3.2, we lock the central wavelength and line-width of the broad line Hα component. This was done to avoid degeneracies in the fit, especially in the outer regions where the signal-to-noise of the spectra is lower. We present the regional spectral for each of the objects in Figures

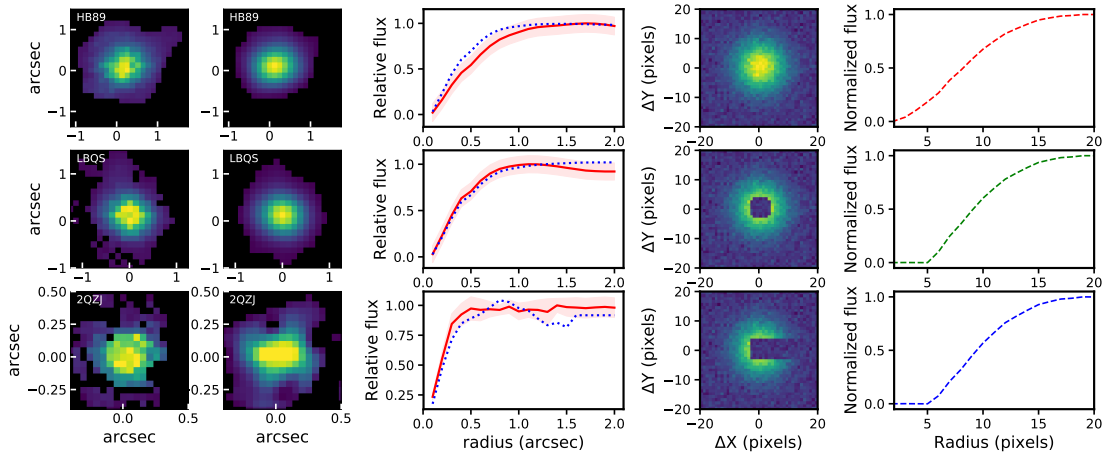

Figure 5.4: Summary of our analyses on the Hα data and modelling the COG for different narrow Hα morphologies. Columns from left to right: Column 1: The narrow Hα maps from the multi-fit method (see §5.3.2). Column 2: The narrow Hα maps from the QSO-subtraction method (see §5.3.2). Column 3: The curves of growth for the Hα emission. The solid red curve shows the COG for the narrow Hα with the shaded region indicating the 1 σ uncertainty. The dashed blue curves indicate the COG of the broad line region (BLR). Column 4: Model images illustrating a smooth spatial distribution of narrow Hα and different cavities as found in Cano-Díaz et al. (2012) and Carniani et al. (2016). Column 5: COG corresponding to the modelled image in the third column. We resolve the narrow Hα emission in HB89, but all sources are not consistent with any sort of cavity in the central regions.

5.7, 5.8 & 5.9.

5.3.3 Astrometry Alignment

The goal of this work is to compare the location of Hα, dust emission and AGN driven outflows in luminous QSOs. To perform this analysis, it is necessary to align the astrometric frame of each of the observations.

The nature of interferometric observations requires accurate astrometry of the targets to accurately calculate the phase differences from each of the antennae. The absolute astrometric accuracy of ALMA depends on the baseline and frequency of the observations. For our setup of baseline 800 m and 350 GHz, the accuracy of the astrometric frame is ≈20–30 mas (see §4).

The limited field of view of SINFONI does not allow standard astrometric calibrations used in optical and NIR astronomy, of identifying known stars within the field of view with known and accurate positions. The astrometric calibration of IFU data is described in §4, however here we modify the method to include GAIA observations to account for lack of high resolution optical/NIR imaging. To determine the central position of the QSO in the IFU cube, we collapse the cube along the spectral channels to create a white-light (continuum) image. We then proceeded with fitting a simple 2D Gaussian model to the continuum image. However, GAIA observations provide excellent astrometry positions and our sources are sufficiently bright (H-band magnitude $<$16.5) to be detected in the GAIA DR2 (Gaia Collaboration et al., 2018). The final RA and Dec of these central positions are determined from the GAIA positions.

5.4 Results

We present new ALMA band 7 continuum observations to trace the obscured star formation and a new analysis of Hα VLT/SINFONI observations of three QSOs at z∼2.5 that showed evidence that AGN driven outflows are rapidly suppressing star formation in QSO host galaxies. In §5.4.1 we investigate the potential contribution AGN heated dust and AGN synchrotron emission to the FIR emission traced by ALMA band 7 observations. In §5.4.2 we discuss the morphology of the narrow Hα maps. In §5.4.3 we compare

the location and morphology of the narrow Hα emission and FIR continuum. Finally, in §5.4.4 we discussed the implications of our results.

5.4.1 Assessing the origin of the ALMA band 7 emission

We compiled multi-wavelength photometry from MIR to radio (1.4 GHz) to assess the contamination of the ALMA band 7 observations by either AGN heated dust or the radio synchrotron emission from the AGN.

Our QSOs were selected to be brighter than 16 mag in H-band. As a result, these QSO are bright enough to be detected in all-sky surveys. We use the MIR–radio photometry from the all-sky survey such as WISE and NVSS. We used the data from the WISE all-sky survey in W1 (3.4 μm), W2 (4.6 μm), W3 (12 μm) and W4 (22 μm) bands. We queried radio sky surveys such as FIRST and NVSS to compile the radio photometry. Furthermore, these objects were targeted by ALMA band 3 observations to trace CO(3–2) emission. These observations were published in Carniani et al. (2017) and we compiled the band 3 continuum (3 mm) photometry from this work. ALMA band 3 continuum observations provide a valuable data point for assessing the contamination of the ALMA band 7 data point from the AGN radio synchrotron emission. We show the compiled photometry for each QSO as a SED normalised to WISE W4 (22μm) in Figure 5.5.

We first assess the contribution to the ALMA band 7 photometry by radio synchrotron emission. We only detect a single object in the radio band, HB89. The radio 1.4 GHz flux of HB89 is 29.8 mJy, which corresponds to radio luminosity of $\sim (7-9) \times 10^{26}$ W/Hz, assuming spectral slopes of -0.7 and -0.5. This high luminosity makes this quasar a radio loud source. In the bottom panel of Figure 5.5, we plotted a range of radio slopes (-0.5 – -0.7) as magenta region, normalised to the NVSS 1.4 GHz flux. A radio slope -0.7 is capable of predicting both ALMA band 3 and band 7 photometry. We conclude, that the ALMA band 7 photometry is heavily contaminated by the radio synchrotron emission and it is no longer reliably tracing cold dust emission heated by star formation.

In objects 2QZJ and LBQS, we only have an upper limit on radio NVSS photometry. A range of radio SED with different radio slopes (-0.5 – -0.7) normalised to the radio upper limit is capable of explaining the ALMA band 3 flux, however, it cannot predict the ALMA band 7 flux at the same time. As a result, we conclude that the ALMA band 7

observations are not contaminated by the AGN radio emission for these two objects.

To assess the contamination of the ALMA band 7 continuum photometry from the AGN hot dust emission, we calculated the WISE colours as [W3]-[W4] and [W1]-[W2] with average values of 2.15 and 0.9, respectively. Based on the results from Mateos et al. (2012), these colours indicate at least 80 % AGN contribution to rest-frame 1–10μm emission. Since our objects are luminous QSOs, we use the QSO template from Mor & Netzer (2012) and three templates from Lyu & Rieke (2018), called the normal QSO, hot dust deficient (HDD) and warm dust deficient (WDD) templates. We normalise these AGN templates to the WISE W4 band (rest-frame 6μm) which is dominated by the AGN emission shown above. We show these normalised templates as red, blue, orange and yellow curves in Figure 5.5. The AGN templates are a good fit for the WISE photometry in all three objects. However, these AGN templates under-predict the ALMA band 7 & 3 fluxes. To explain the ALMA band 7 flux in objects 2QZJ and LBQS, we normalised two star formation templates from Mullaney et al. (2011) to the ALMA band 7 fluxes. In 2QZJ and LBQS, the normalised star formation templates are a good fit to the ALMA band 3 photometry, indicating that in 2QZJ and LBQS the ALMA band 7 photometry is dominated by the emission from star formation heated dust.

To further strengthen the argument that the ALMA band 7 observations trace star formation heated dust in 2QZJ and LBQS, we investigate the 22μm – 870μm colours of our targets in Figure 5.6. Following Stanley et al. (2018), we plot 870μm/22μm (ALMA band 7/WISE [W4]) flux ratio as a function redshift for 2QZJ and LBQS objects as green points. We also plotted this ratio for pure star forming templates from Mullaney et al. (2011) and for the AGN templates from Mor & Netzer (2012) and Lyu & Rieke (2018) as shaded regions. As indicated by the black arrow in Figure 5.6, the increasing 870μm/22μm flux ratio indicates an increasing contribution of star formation towards the ALMA band 7 continuum photometry. This plot indicates that the FIR emission has a significant star formation contribution.

Furthermore, as shown in Figure 5.2, the ALMA band 7 continuum is well resolved and the uv amplitudes fall to 0 at large baselines. This shows that there isn't any underlying unresolved point source in the continuum data, that would correspond to the AGN heated dust surrounding the AGN.

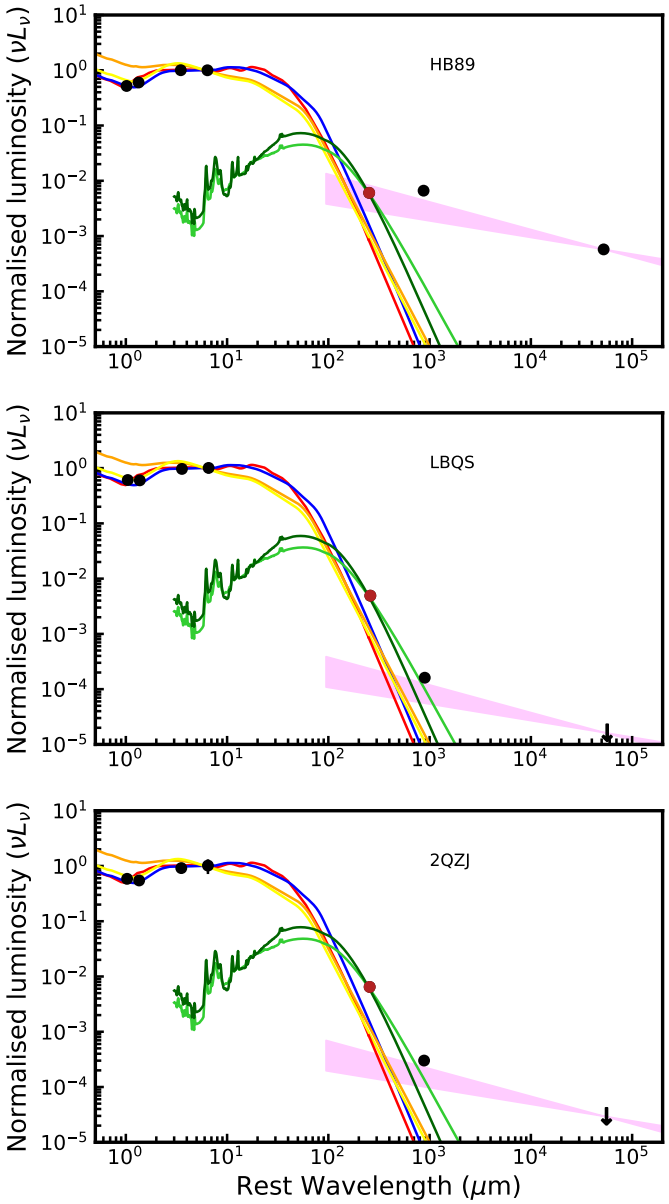

Figure 5.5: Photometry from mid infra-red to radio wavebands normalised to the 22μm photometry point (WISE W4 band). The black points indicate the observed photometry from WISE, ALMA band 3 and NVSS. We highlight the ALMA band 7 observations as a dark red point. The errors on the photometry are smaller than the size of the photometry points. The red solid curve shows an AGN template from Mor & Netzer (2012), while the blue, orange and yellow curves show the normal, hot dust deficient and warm dust deficient AGN templates from Lyu & Rieke (2018), normalised to 22 μm flux. It can be seen the AGN templates fail to explain the emission at 870μm (ALMA Band 7). The light and green curves show two star formation templates normalised to the ALMA band 7 photometry point from Mullaney et al. (2011). The magenta shaded region shows radio emission with slopes between -0.5 and -0.7. In HB89 the ALMA band 7 is heavily contaminated by the radio emission from the AGN. In the other two sources, the 3 mm emission may be contaminated by synchrotron emission, but the Band 7 emission is contaminated at $<\sim$1% level.

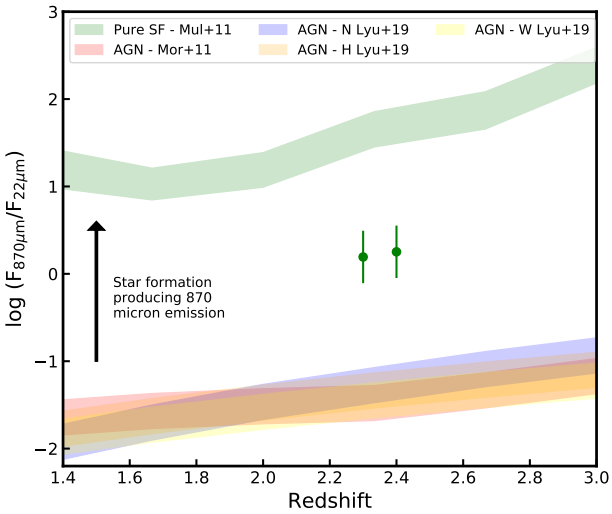

Figure 5.6: $F_{870\mu m}/F_{22\mu m}$ ratio as a function of redshift for 2QZJ and LBQS (green points). The red region shows the ratio for pure star formation templates from Mullaney et al. (2011). The red, blue, orange and yellow regions show AGN template from Mor & Netzer (2012), normal QSO (N), hot dust deficient QSO (H) and warm dust deficient QSO (W) templates from Lyu & Rieke (2018), respectively. The black arrow indicates an increasing contribution from star formation to the 870μm emission. The 870/22μm colour can not be explain by pure AGN emission and the 870μm traces dust-heated star formation (also see Figure 5.5).

Overall, we conclude that the ALMA band 7 emission is likely to be severely contaminated by the radio synchrotron emission in the HB89 object. For 2QZJ and LBQS objects, based on the observational evidence that: (1) the radio emission cannot explain both ALMA band 3 & 7 fluxes; (2) The AGN templates normalised to WISE [W4] cannot explain the ALMA band 7 flux; (3) 870μm/22μm indicates a strong star formation contribution; and (4) The lack of evidence of a point source in the ALMA uv-data; we conclude that in these objects the ALMA band 7 observations traces dust heated by star formation and it is not severely contaminated by AGN emission.

5.4.2 Morphology of the narrow Hα emission

Previous works that study our objects showed cavities in the Hα emission in the locations of the AGN driven outflows. This led to interpretations that outflows rapidly suppress star formation in QSO host galaxies (Cano-Díaz et al., 2012; Carniani et al., 2016).

We describe the COG of narrow Hα and the size estimates in §5.3.2 and we present them in Figure 5.4. We spatially resolve the narrow Hα in HB89 with a size of 1.9 ±

0.8 kpc, while the other two objects were unresolved. We also modelled three mock narrow Hα representing a smooth spatial distribution, a cavity in the centre and an arc. By comparing the COG from the data to the COG from the mock maps, we show that the narrow Hα in all three objects follow a smooth spatial distribution without any cavities.

We created narrow Hα maps in § 5.3.2, using two different methods: (a) simultaneous fitting of all the spectral components to spaxel's spectra (multi-fit method); and (b) subtracting the QSO broad line and continuum emission from the spaxel's spectra to create a narrowband image of the narrow Hα emission (QSO-sub method). We present the narrow Hα maps created by these two separate methods in left columns of part 1 of Figures 5.7, 5.8 & 5.9. In both sets of maps, we show the ALMA band 7 continuum observations as red dashed contours, the PSF determined from the BLR as red shaded regions and the white regions from which we extracted spectra on the right as white squares. We present regional spectra extracted from the nine regions in the QSO host galaxies in right panels of Figures 5.7, 5.8 & 5.9. We defined these regions and extracted these spectra in §5.3.2.

Furthermore, in part 2 of each of these Figures, we also include the Hα spectrum (left panel) and a narrow Hα map (right panel), from the original study that presented the K-band IFU data for easy comparison between our results and results from Cano-Díaz et al. (2012) & Carniani et al. (2016). In the next two sections, we look in detail at maps and regional spectra for each of the objects and we compare our results to the original studies presenting this IFU data.

HB89 & LBQS

The SINFONI observations of HB89 and LBQS were first presented in Carniani et al. (2016). In Figures 5.7 & 5.8, we present our results for these two objects. In both cases, we observed a smooth Gaussian like distribution of the narrow Hα emission without any cavities or arcs in the emission. We detect narrow Hα emission on scales up to 20 kpc, however, LBQS is not resolved using the COG method (see §5.4). We show the spectra extracted from the 9 regions (indicated on the maps as white squares) in the right panels of Figures 5.7 & 5.8. The regional Hα spectra indicates, that there is a strong narrow Hα emission in the centre. Calculating the fluxes in these regions confirms the brightest narrow Hα emission is in the central regions.

We show the narrow Hα maps, regional maps and their results for HB89 object in Figure 5.7. The regional spectra show a strong narrow Hα component in the centre and East region of the QSO, in disagreement with the map presented by Carniani et al. (2016) (see bottom right panel of Figure 5.7). However, the QSO spectrum extracted by Carniani et al. (2016) from the central 2×2 pixels around the QSO, as shown in bottom left panel of Figure 5.7, shows a strong narrow Hα component (labelled B on their spectrum). This is in disagreement with their own map, which shows a negative flux in the central region of the QSO. Overall both our and their Hα spectra indicate a bright narrow Hα component in the centre of the QSO, in agreement with our analyses.

We present our results for LBQS object in Figure 5.8. The spectra extracted from the nine regions of the QSO narrow Hα map (show on the right) are in good agreement with both our maps (see in the left column). In contrast with the narrow Hα map from Carniani et al. (2016), we detect strong narrow Hα component in both central, West and South-West region. However, as is the case in HB89 object, the Hα spectrum extracted from the central 2×2 pixels around the QSO by Carniani et al. (2016) (bottom left panel of Figure 5.8) also exhibits a strong narrow Hα component (labelled as B). This is in a disagreement with their own narrow Hα map (bottom right panel), which shows negative narrow Hα flux in the centre region. This further indicates that there is a strong narrow Hα emission in the centre of the QSO host galaxy, in agreement with the morphology of our maps, regional spectra and COG modelling from Figure 5.4.

2QZJ

The results of our analyses and that from Cano-Díaz et al. (2012) for 2QZJ are presented in Figure 5.9. The SNR of the narrow Hα component in the inner 5kpc spectrum (see §5.3.2) is only 5.5, which is insufficient to spatially map the narrow Hα component. This is shown by the unresolved emission determined from the COG analysis and we detect narrow Hα only in the region corresponding to the seeing FWHM surrounding the QSO with no extended emission. We note that whether the broad line Hα is modelled by a Gaussian with a broken power law (as we did in §5.3.2) or with a two independent broad Gaussian components (as did Cano-Díaz et al. 2012; see G and H component in bottom left panel of Figure 5.9), the flux of the narrow Hα or morphology of the narrow Hα map,

(1)

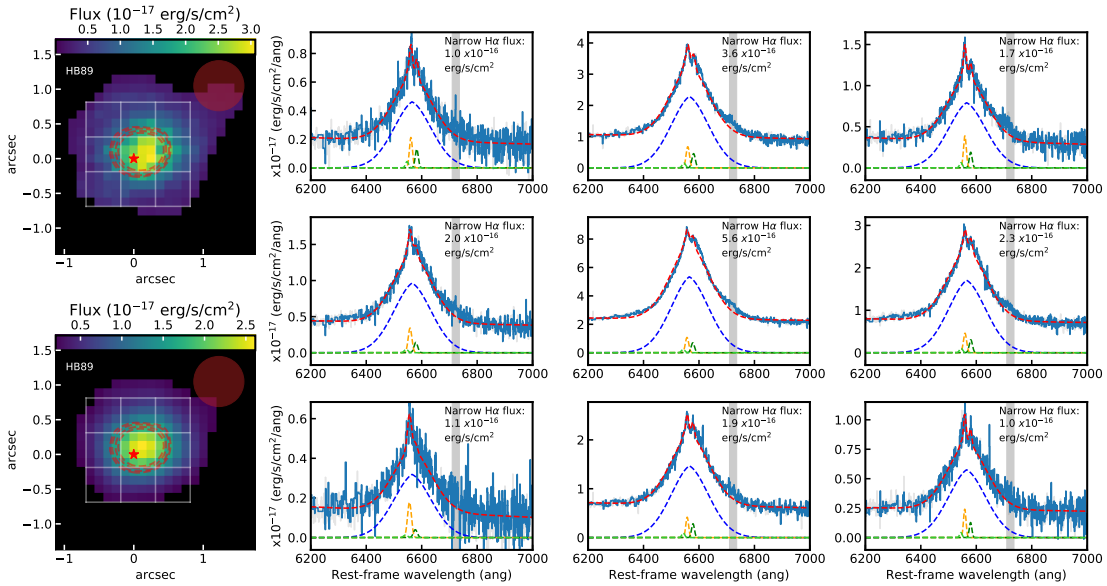

(2)

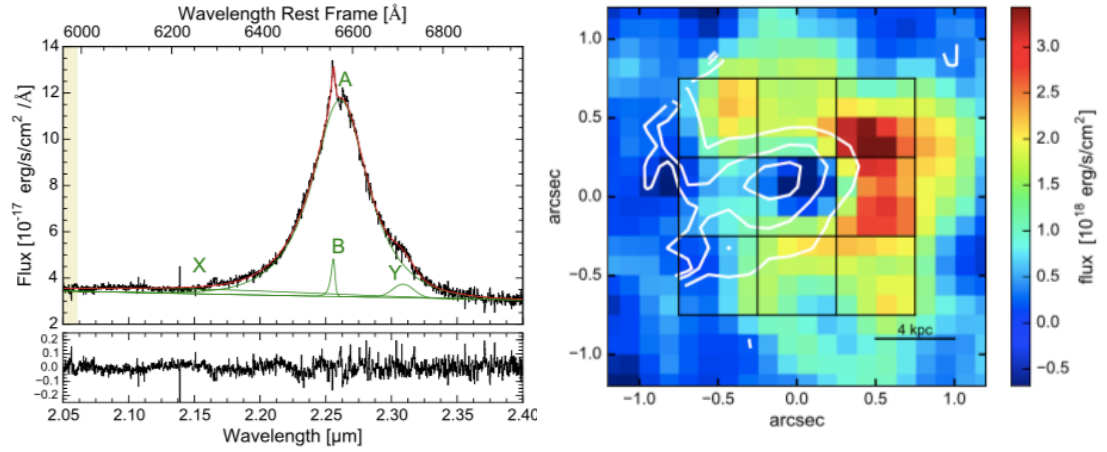

Figure 5.7: Part (1) Narrow Hα maps and region spectra for HB89 from our work. Top left image: Narrow Hα image created by simultaneously modelling all the spaxel's spectrum components. Bottom left image: narrowband image of the narrow Hα image created after subtracting the broad line Hα (see §5.3.2. In both of these images, the red circle indicates the PSF of the observations determined from the BLR, while the white squares show regions from which we extracted spectra on the right. The ALMA band 7 continuum data is displayed as red contours (2.5, 3, 4, 5 σ levels). Spectra on the right: Hα and [N II] spectra extracted from the regions corresponding to the white squares in the images on the left. We show the narrow Hα flux in each subplot to allow comparison between the maps and the spectra. For the emission-line profiles, the curves refer the same components as in Figure 5.3. The grey shaded area shows the location of the [S II]. Part (2) Narrow Hα maps and region spectra for HB89 from Carniani et al. (2016). Left panel: The Hα spectrum from the central 2×2 pixel around the QSO. Right panel: Image showing the narrow Hα map with the white contours indicating the location of the AGN-driven outflow. Our maps show narrow Hα emission in the central region, i.e., at the location of the outflow. Also the spectra presented in Carniani et al. (2016) is inconsistent with there being negative narrow Hα flux in the central regions.

(1)

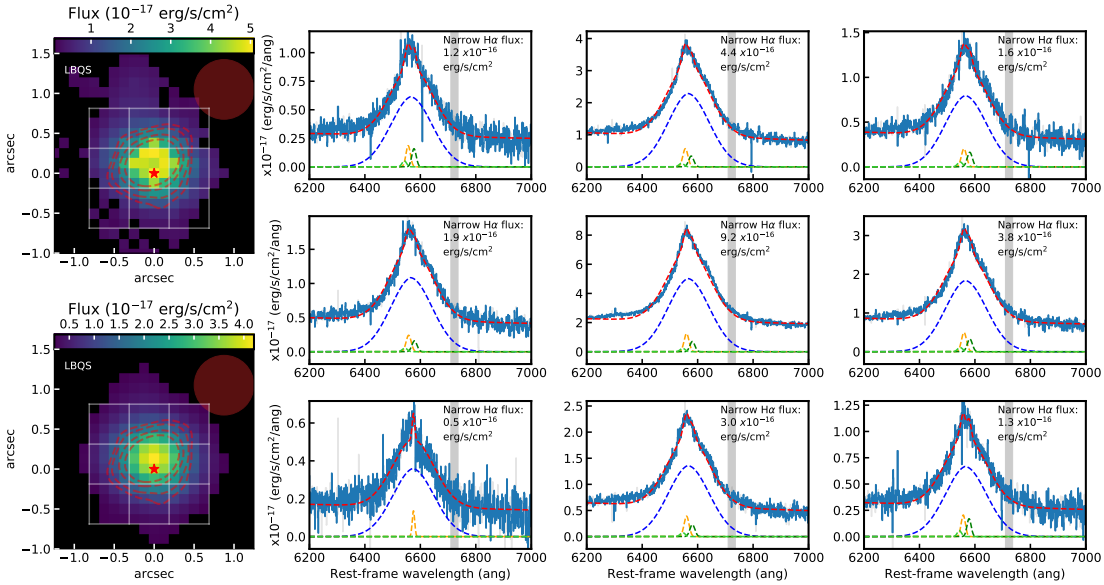

(2)

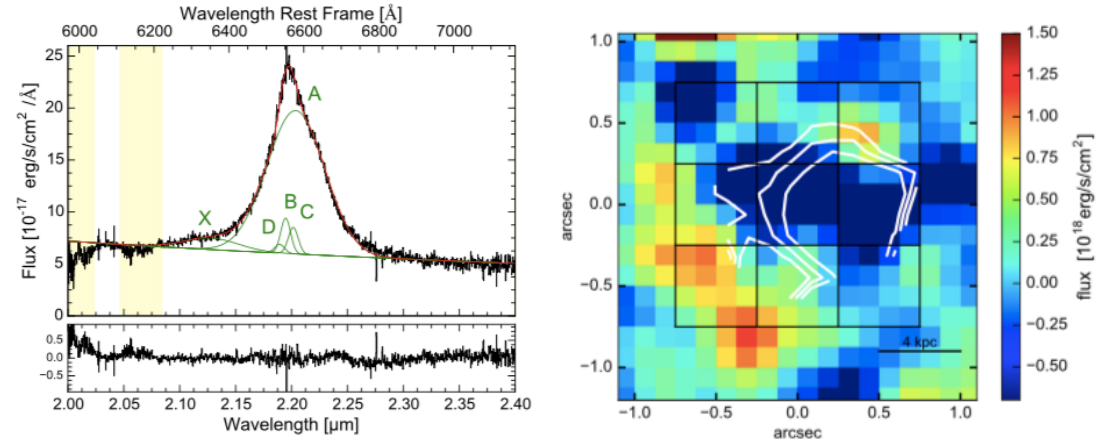

Figure 5.8: Part (1) Narrow Hα maps and region spectra for LBQS from our analyses. Top left image: Narrow Hα image created by simultaneously modelling all the spaxel's spectrum components. Bottom left image: narrowband image of the narrow Hα image created after subtracting the broad line Hα (see §5.3.2. In both of these images, the red circle indicates the PSF of the observations determined from the BLR, while the white squares show regions from which we extracted spectra on the right. The ALMA band 7 continuum data is displayed as red contours (2.5, 3, 4, 5 σ levels). Spectra on the right: Hα and [N II] spectra extracted from the regions corresponding to the white squares in the images on the left. We show the narrow Hα flux in each subplot to allow comparison between the maps and the spectra. For the emission-line profiles, the curves refer the same components as in Figure 5.3. The grey shaded area shows the location of the [S II]. Part (2) Narrow Hα maps and region spectra for LBQS from Carniani et al. (2016). Left panel: The Hα spectrum from the central 2×2 pixel around the QSO. Right panel: Image showing the narrow Hα map with the white contours indicating the location of the AGN-driven outflow. Our maps show narrow Hα emission in the central region, i.e., at the location of the outflow. The spectra presented in Carniani et al. (2016) is inconsistent with there being negative narrow Hα flux in the central regions. Furthermore, the ALMA band 7 continuum observations indicate strong obscured star formation in the centre.

(1)

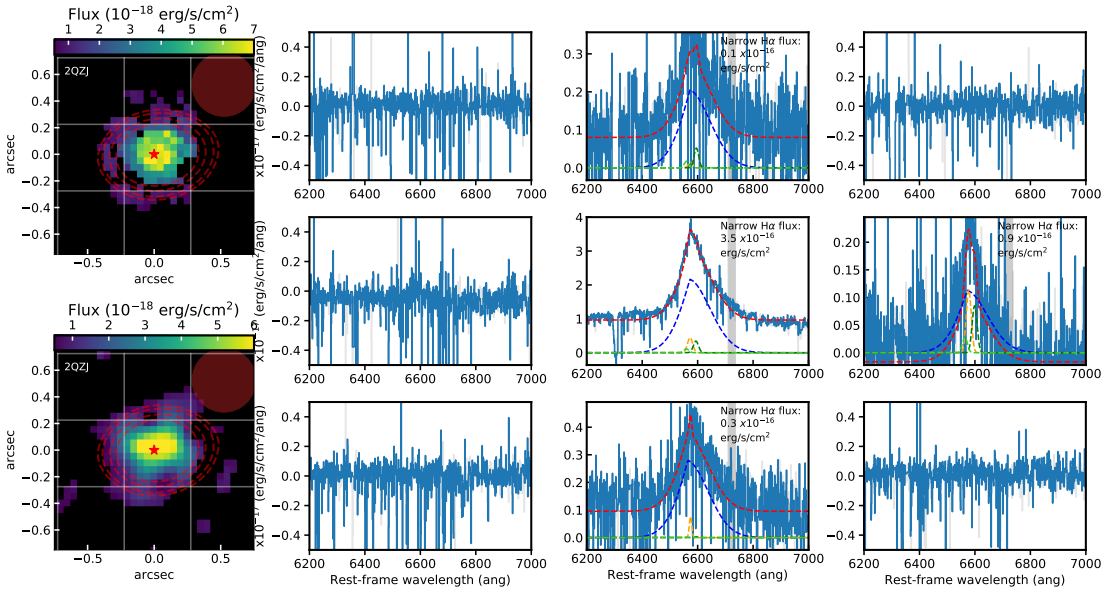

(2)

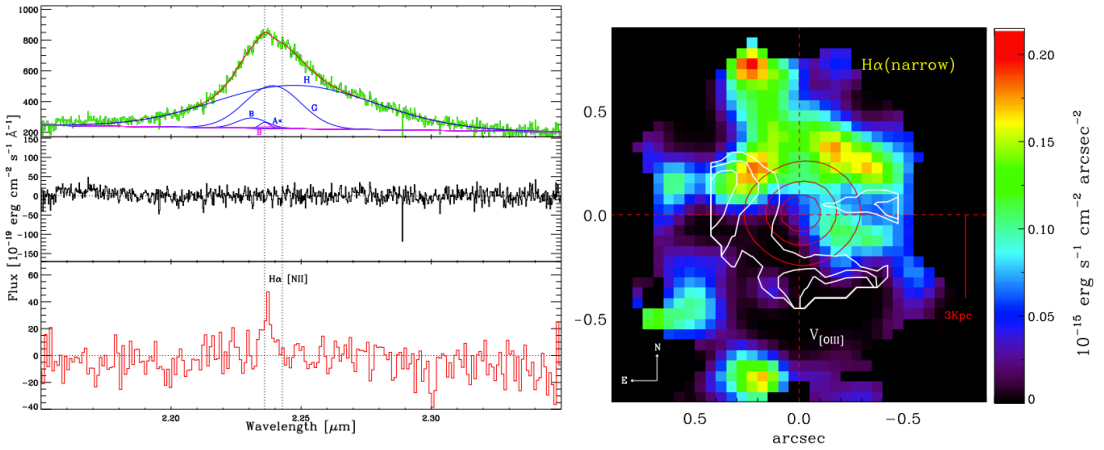

Figure 5.9: Part (1) Narrow Hα maps and region spectra for 2QZJ from our work. Top left image: Narrow Hα image created by simultaneously modelling all the spaxel's spectrum components. Bottom left image: narrowband image of the narrow Hα image created after subtracting the broad line Hα (see §5.3.2. In both of these images, the red circle indicates the PSF of the observations determined from the BLR, while the white squares show regions from which we extracted spectra on the right. The ALMA band 7 continuum data is displayed as red contours (2.5, 3, 4, 5 σ levels). Spectra on the right: Hα and [N II] spectra extracted from the regions corresponding to the white squares in the images on the left. We show the narrow Hα flux in each subplot to allow comparison between the maps and the spectra. For the emission-line profiles, the curves refer the same components as in Figure 5.3. The grey shaded area shows the location of the [S II]. Part (2) Narrow Hα maps and region spectra for 2QZJ from Cano-Díaz et al. (2012). Left panel: (top) The QSO integrated spectrum with aperture size of 1"×1". (middle) Residual spectra from modelling the QSO spectrum. (bottom) Difference between the spectra in the top and bottom regions. Right panel: Image shows the narrow Hα map. The white and red contours show the AGN-driven outflow and continuum, respectively. The ALMA band 7 continuum observations indicate strong obscured star formation in the centre.

does not change. The Hα spectra extracted from the nine regions of the QSO host galaxy do not show any evidence for a suppressed narrow Hα emission south of the QSO.

5.4.3 Comparison of the Hα and FIR continuum

In the previous section, we described the narrow Hα maps, potentially tracing the unobscured star formation. However, in §4 I showed that Hα is not a reliable tracer of star formation on its own, and it is necessary to also use a star formation tracer mapping obscured star formation such as FIR continuum. In §5.4.1 we show that the ALMA band 7 emission is tracing the cold dust emission heated by the star formation in 2QZJ and LBQS objects, while in HB89 this observation is contaminated by radio synchrotron from the AGN. We still compare the location of ALMA band 7 observations in HB89, but we stress that ALMA band 7 continuum maps the location of the radio emission such as jets, rather than cold dust heated by star formation. We imaged the ALMA band 7 continuum data in §5.2.2 and we align the IFU and ALMA astrometry frames in §5.3.3.

In Figure 5.10 we compare the spatial distribution of the narrow Hα emission (background map), created using the multi-fit method and FIR continuum, shown as red contours. The red and blue points show the location of the peak of Hα and FIR emission, while the red star indicates the location of the QSO. The FIR emission is centrally concentrated around the QSO, the peaks of the Hα and FIR emission are co-spatial in all three QSOs. The FIR emission is located in the same region of the QSOs as the narrow Hα emission cavities observed in Cano-Díaz et al. (2012); Carniani et al. (2016). Based on the morphology of the narrow Hα, the location of the FIR continuum we see no evidence of suppressed star formation anywhere in the QSO host galaxies.

5.4.4 Implications of our results

In this work, we presented new ALMA band 7 continuum observations, that traces dust obscured star formation in two out of three objects in our objects. With a careful reanalysis of the IFU observations of the Hα emission, we see no evidence of suppressed star formation in these QSO host galaxies.

Given that we did not observe any evidence of decreased star formation emission,

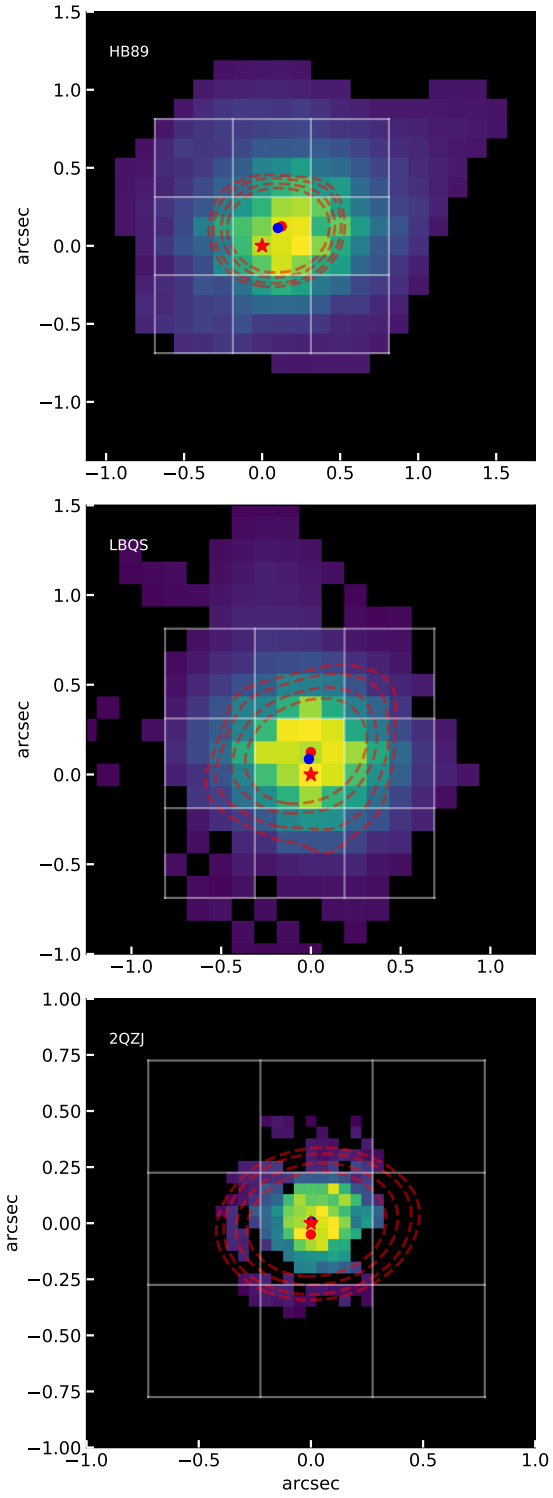

Figure 5.10: A comparison of the spatial distribution of the FIR emission and the narrow Hα emission for our QSO host galaxies. The images show the narrow Hα emission (from the simultaneous fitting see §5.3.2). Red contours show the FIR continuum (see §5.2.2), with levels of 2.5, 3, 4, 5σ. The white boxes indicate the location of the spectra we extracted in Figures 5.7, 5.8 & 5.9. Both Hα and the FIR continuum is centrally concentrated on the QSO. In LBQS and 2QZJ, the FIR is attributed to star formation (see §5.4.1).

traced by narrow Hα and FIR continuum, in any part of their host galaxy, even in the location of the AGN outflows observed by Cano-Díaz et al. (2012) and Carniani et al. (2016), we see no evidence that AGN driven outflows rapidly suppress star formation in QSO host galaxies. This result is in agreement with my results in §4, where I did not observe any evidence for this effect in moderate luminosity AGN at z= 1.4–2.6. However, using VLT/MUSE and ALMA, studies focusing on the effect of AGN feedback in local galaxies observed both positive and negative feedback on a scale of $<$ 1 kpc scale (e.g., Alatalo et al., 2015; Cresci et al., 2015b; Rosario et al., 2019; Shin et al., 2019).

However, with seeing limited nature of the IFU observations, with a spatial resolution of $\sim$ 5 kpc at z$\sim$2.5, we are unable to observe a subtle impact of AGN driven outflow on star formation on a small spatial scale. To improve upon current observations of these objects, it is necessary to use future high-resolution IFU facilities such as with VLT/ERIS, *JWST*/NIRSpec and ELT/HARMONI, which will allow observations at a similar spatial resolution as is currently possible for low redshift AGN host galaxies (Cresci et al., 2015b; Venturi et al., 2018; Husemann et al., 2019; Shin et al., 2019).

Based on our results in this work, the results from §4 and local AGN studies, we see no evidence that AGN instantaneously influence star formation inside their host galaxies on scales of at least 4 kpc, contrary to previous claims. It is possible that AGN influence star formation on much smaller scale scales (as has been see in some nearby AGN, e.g., Croft et al., 2006; Alatalo et al., 2015; Cresci et al., 2015b; Querejeta et al., 2016; Rosario et al., 2019; Shin et al., 2019; Husemann et al., 2019) or the AGN outflows have an impact over long timescales (McCarthy et al., 2011; Gabor & Bournaud, 2014; Harrison, 2017; Scholtz et al., 2018).

5.5 Conclusions

We presented new high-resolution ALMA band 7 continuum observations (rest-frame $\lambda \sim 250\mu$m) of three QSOs at $z \sim$2.5 that had previously been presented as showing evidence for suppressed star formation based on cavities in the narrow Hα emission at the location of the quasar-driven outflows. All three QSOs are significantly detected by ALMA (SNR$>$25) and we exploited these observations to trace the dust-obscured star

formation. Furthermore, we re-analysed the Hα IFU data using multiple approaches to reassess the evidence for cavities in the narrow Hα emission. On the basis of our analyses we find:

1. **ALMA traces the dust-obscured star formation in two of the three QSOs.** This result is based on three different analyses: (a) the MIR–radio photometry requires a star-forming template (see §5.4.1 and Figure 5.5); (b) 870μm/22μm colour ratio indicates a strong star forming contribution (see Figure 5.6); (c) ALMA band 7 observations are spatially extended (see Figure 5.2). Therefore, we conclude that we can use the spatially-resolved maps to trace the star formation in these targets. In the third QSO (HB89), the ALMA band 7 observation is dominated by synchrotron emission.

2. **Dust-obscured star formation in the two QSOs is found at the location of the claimed narrow Hα cavities.** We compared the locations of the narrow Hα and ALMA band 7 continuum in Figure 5.10. The ALMA band 7 continuum is located in the centre of the QSO host galaxies, on top of the peak of the narrow Hα emission, and is in the same location as the cavities in the narrow Hα reported by Cano-Díaz et al. (2012) and Carniani et al. (2016). This indicates that dust-obscured star formation is present at the location of the claimed narrow Hα cavities.

3. **No significant evidence for cavities in the Hα emission for all three QSOs.** We based our conclusion on three analyses of the Hα IFU data: (a) We created narrow Hα maps using two separate methods in §5.3.2 and we present these maps in Figures 5.7, 5.8 & 5.9; (b) We modelled the curve-of-growth of the narrow Hα component in §5.3.2 and Figure 5.4. By modelling mock maps, we determined that the narrow Hα has a smooth spatial distribution; (c) We extracted spectra from nine regions in the QSOs (see §5.4.2 and Figures 5.7, 5.8 & 5.9). Our spectra showed that these objects have a strong narrow Hα emission in the centre of these QSOs in agreement with our narrow Hα maps and spectra presented by (Carniani et al., 2016). Based on the results from the narrow Hα maps, curves-of-growths and the spectra extracted from nine regions of the QSO host galaxy, we concluded that the narrow Hα is centrally concentrated and there is no evidence for any cavities or ”holes” in the central

regions as reported by Cano-Díaz et al. (2012) and Carniani et al. (2016). Based on the location of the ALMA band 7 observations and the smooth morphology of the narrow Hα emission, we see no evidence that star formation is suppressed in these QSO host galaxies.

Within our sample, we see no evidence that ionised outflows rapidly suppress star formation even in these extreme quasars (based on luminosity and/or outflows; see Figure 5.1) on ~ 4 kpc scales, despite previous claims in the literature. Based on this study, any instantaneous impact by these quasars and their ionised outflows must be subtle, occurring on spatial scales lower than the resolution of these observations (< 4 kpc) or on larger timescales, by removing the gas from the galaxy or heating it up. It is now necessary to re-observe these targets with adaptive optics, to probe smaller spatial scales at which AGN feedback has been observed in local galaxies.

CHAPTER 6

Conclusions and future work

"The history of astronomy is a history of receding horizons."
– Edwin Powell Hubble, Astronomer

This thesis presents scientific experiments to investigate the role of AGN feedback in galaxy evolution at redshift 1–3. Using deep ALMA observations combined with either the EAGLE hydrodynamical simulations or IFU observations, I have put constraints on the effect of AGN feedback on star formation. In this chapter, I summarise the main results presented in this work and also discuss ongoing and future projects to address many outstanding questions in the field.

6.1 Summary of main results

As discussed in Chapter 1, there have been many observational findings supporting the theory that the evolution of SMBHs and their host galaxies are linked. This co-evolution is expected to be driven by two broad processes in galaxy evolution: AGN activity and star formation. To constrain the effect of AGN on star formation, I have investigated star formation in the host galaxies of AGN and its connection to AGN-driven outflows, exploiting the observational techniques of interferometry and integral field spectroscopy; see Chapter 2. In the following section, I summarise the results of the three experiments performed in this thesis, which were described in detail in Chapters 3–5.

6.1.1 Identifying the subtle signatures of feedback from distant AGN using ALMA observations and the EAGLE hydrodynamical simulations

In Chapter 3, I made use of the largest sample of X-ray AGN (114 in total) observed with ALMA at high redshift. Using the available ALMA band 7 ($\sim 870\mu$m) data I was able to construct a sample of 81 X-ray AGN ($L_X = 10^{43} - 10^{45}$ ergs s^{-1}) over the redshift range z=1.5-3.2 and with stellar mass $> 2 \times 10^{10}$ $M_\odot$. I combined the ALMA data with other archival photometry (UV–FIR) of our sample to estimate the SFRs and stellar masses via the technique of SED fitting and calculated specific star formation rates (sSFR). Since the ALMA observations improve the detection rates at FIR from 10% to $\sim$ 38%, I used a Bayesian hierarchical fitting code to estimate the mode (most common value) and the width of the sSFR distributions, assuming that the shape of the distribution is a log-normal (Gaussian distribution in logarithmic space). To help interpret our results, I utilised two "flavours" of the EAGLE cosmological hydrodynamical simulation: a simulation run with AGN feedback, and a simulation run with the same parameters but without AGN feedback implemented.

I found no strong evidence that the sSFR distributions change with X-ray luminosity. This is in agreement with the predictions from the standard EAGLE simulations when I mass match the X-ray AGN sample with the sample from the EAGLE simulation. The lack of a dependence of X-ray luminosity on the sSFR distributions rules out a simple model of AGN feedback where high-luminosity AGN instantaneously suppress star formation.

By comparing the sSFR distributions of galaxies in the EAGLE simulations with and without AGN feedback, I identified a subtle signature of AGN feedback on star forming properties of AGN host galaxies. The sSFR distributions of galaxies above $M_* > 2 \times 10^{10}$ $M_\odot$ in the EAGLE simulation with AGN feedback is broader by a factor of $\sim$2 than in EAGLE without AGN feedback. The measured sSFR distributions from our ALMA observations are in good agreement with the simulation with AGN feedback, irrespective of whether the simulated galaxies currently host AGN or not.

Overall I have shown that the signature of AGN feedback is present in both inac-

tive and AGN host galaxies. The lack of evolution in the sSFR distribution with AGN luminosity rules out a model whereby AGN feedback rapidly quenches star formation, but advocates a more subtle cumulative feedback scenario, where the suppression of star formation occurs over multiple AGN episodes.

6.1.2 KASHz: No clear evidence for ionised outflows instantaneously suppressing star-formation in moderate luminosity AGN z=1–2.5

In Chapter 4, I tested claims that AGN-driven outflows instantaneously suppress star formation in high-redshift AGN host galaxies, as reported by Cano-Díaz et al. (2012),Cresci et al. (2015a) and Carniani et al. (2016). I used ALMA observations and IFU spectroscopy to investigate the FIR and Hα emission as possible star-formation tracers as well as the AGN-driven outflows of 8 moderate luminosity AGN ($L_X = 10^{43} - 10^{45.5}$ ergs s^{-1}). I selected my AGN sample from the KASHz survey (KMOS AGNs at High-z), taking systems with high signal-to-noise observations of the Hα and [O III] emission lines and ALMA continuum observations. With this set of observations, I traced the unobscured star formation, AGN-driven outflows and obscured star formation in 8 sources at z=1.2–2.5.

Using SED template fitting on the UV to ALMA band 6/7 photometry, I measured the SFR(FIR) and stellar masses of my AGN. I extracted the galaxy-integrated Hα emission-line profiles to estimate the SFR(Hα) and corrected the SFR(Hα) for dust obscuration for three targets with Hβ emission line constraints using the Balmer decrement. Furthermore, I created maps of the narrow Hα emission, rest-frame FIR emission, and the [OIII] emission used to trace ionised outflows.

Using these data I found that Hα underestimates SFRs by a median factor of 20 when uncorrected and by a factor 0.5–12 when corrected. Furthermore, accounting for the AGN photo-ionisation contribution to the narrow Hα emission would increase the discrepancy further between the two tracers. I determined that the Hα emission is $\sim 2\times$ larger than the FIR emission in these AGN host galaxies. This is similar to that observed in sub-mm galaxies, particularly those hosting AGN, and is possibly due to dusty star formation

generally being more compact than unobscured star formation and/or additional photo-ionisation by the AGN to the Hα emission. In half of the sample I found significant, 1–3 kpc, projected offsets between the peak of the FIR emission and the peak of the narrow Hα emission. The average offsets between the emission regions across the full sample of eight targets are 1.4 ± 0.6 kpc. Based on these results I concluded that it is necessary to use the FIR continuum in addition to Hα when tracing the star formation in a AGN host galaxy.

I also included in my sample a famous object (XID 2028) from Cresci et al. (2015a) which has been proposed as showing evidence for both positive and negative feedback. By combining the star formation tracers with the mapped AGN-driven outflows, I did not find any evidence that AGN-driven outflows instantaneously suppress or enhance star formation in the host galaxy of this AGN. The lack of any clear impact on the star formation is also found when considering both the FIR and Hα emission as star-formation tracers; i.e., there is no absence of star formation at the location of the outflow. I was able to confirm the identification of a spectacular ≈13 kpc outflow in XID 2028; however, based on a re-analysis of the Hα data, including new high spectral resolution IFU observations, I did not find evidence of their claimed spatial anti-correlation between the outflow and the Hα emission.

Overall, I concluded that it is necessary to use tracers sensitive to both obscured and unobscured star formation to map all of the star formation in high-redshift galaxies. Furthermore, I did not find any evidence that AGN-driven outflows rapidly suppress star formation. It is important to consider that the seeing-limited observations are not probing sufficiently small spatial scales to observe any feedback on $<$ 4kpc scales. This further strengthens the conclusions of Chapter 3, which showed no evidence that AGN *rapidly* suppress star formation based on the sSFR distributions.

6.1.3 No evidence of rapid suppression of star formation by quasar driven winds

Building on my previous study in Chapter 4, I presented new ALMA band 7 continuum observations of three z∼2.5 QSOs, which showed evidence of suppressed star formation

by AGN driven outflows (Cano-Díaz et al., 2012; Carniani et al., 2016). I additionally re-analyzed the IFU observations of the Hα emission line to create comprehensive maps of star formation in these three QSO host galaxies. Utilising MIR–radio photometry from the all-sky survey as well as ALMA band 3 observations from Carniani et al. (2017), I was able to show that the ALMA band 7 continuum observations are tracing star formation in two out of three objects (LBQS and 2QZJ), while in the third object (HB89) these observations are severally contaminated by AGN radio synchrotron emission.

I created the narrow Hα maps using two separate methods: (1) by fitting all components of the spectral regions to the spaxel's spectra; and (2) fitting and subtracting the Hα from the broad line region first to create a narrowband image of the narrow Hα image. Although these maps were in agreement, I performed multiple additional tests to verify the map's morphology. I extracted spectra from 9 separate regions in QSO host galaxies to confirm that the narrow Hα emission is centrally concentrated and it is decreasing symmetrically from the QSO. I created three mock narrow Hα images with different morphology, representing a smooth Gaussian spatial distribution and two with various cavities. By modelling the curves-of-growth (COG) of both the data and the mock maps, I reached the conclusion that the COG from the data is consistent with a smooth spatial distribution.

Overall, in all three objects, our results and tests are consistent with a smooth spatial distribution, without any cavities in the narrow Hα maps. Furthermore, the Hα spectra extracted from the location of the cavities reported by Carniani et al. (2016) show strong narrow Hα component in both my and their work. We compared the location of the narrow Hα and the FIR emission from the ALMA band 7 continuum observations. The FIR emission is located in the centres of the QSO host galaxies, in the location of the narrow Hα cavities reported by the original studies. Based on the analyses of the Hα emission and the location of the FIR continuum, we see no evidence that the star formation is suppressed anywhere in these QSO host galaxies on a spatial scale of > 5 kpc. Given these observations, we are unable to reach the same conclusions that AGN-driven outflows are rapidly suppressing star formation in these QSO host galaxies. This further indicates that both moderate and high luminosity AGN or their outflows do not instantly suppress star formation in AGN host galaxies.

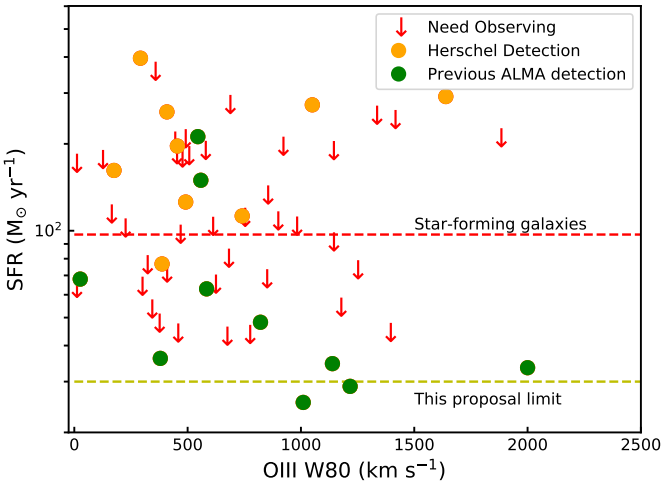

Figure 6.1: Figure from my successful ALMA proposal. SFR from the FIR SED fitting as a function of velocity widths for the [O III] doublet. Currently, we have sufficient SFR constraints for 40% of our sample. The red points indicate the sample that is scheduled for observations by ALMA, the orange and green points indicate *Herschel* and ALMA detection, respectively. The yellow dashed line indicates the SFR upper limit that we will achieve given the depth of the ALMA data.

6.2 Ongoing and future work

The work in this thesis has constrained the effect of AGN feedback on the star formation in the host galaxies of AGN and has resulted in a number of follow-up projects. In the next few subsections, I describe ongoing and future projects designed to further progress our understanding of AGN feedback and its effect on the evolution of galaxies.

6.2.1 Statistical study of a connection between AGN outflow and star formation

In Chapters 4–5 I showed that AGN outflows do not rapidly suppress star formation on the scales of >4 kpc. However, due to the need for high-quality IFU and ALMA data to perform these analyses, the sample size currently available with this data is very small. In the past few years, two studies Woo et al. (2016); Wylezalek & Zakamska (2016) have investigated the SFR and sSFR as a function of outflow properties at low redshift ($z < 1$). However, they found contradictory results between outflow and star-formation properties. While Woo et al. (2016) found that sSFRs are higher for AGN with outflows, Wylezalek & Zakamska (2016) found a decrease in sSFRs with the outflow velocity.

I am the PI of a successful ALMA band 6/7 proposal of 60 *Herschel* undetected AGN, with [O III] emission detected in the KASHz survey. With an additional 20 targets with *Herschel* detections, I have a sample of 80 X-ray AGN at z=1.2–2.5 ($L_X = 10^{42} - 10^{45}$ erg s^{-1}) with excellent constraints on their outflow and star-formation properties. I show the current constraints on the SFR against the [O III] line-width in Figure 6.1. Using the multi-wavelength photometry (UV–FIR) available in the deep fields, I will measure the stellar masses and star formation rates of these AGN to estimate the sSFR of this sample. Using the Bayesian code described in Chapter 3, I will constrain the sSFR distributions. With this data I plan to:

- Measure the sSFR distribution properties as a function of the AGN-outflow property (e.g., emission-line width; spatial extent; outflow energetics) to compare with the overall sSFR distribution. This analysis will enable me to identify deviations in the sSFR distributions and hence provide insight on what AGN-outflow property has the greatest impact on the star formation, if any. On the basis of my previous results we predict that the deeper ALMA data will allow us to measure the sSFR distribution properties for different subsamples (with 30 objects in each subsample) to the same degree of accuracy as in our previous ALMA programs. Even the lack of significant differences will place unique constraints on the immediate impact of outflows (e.g., the timescale of the suppression) on the star formation across the host galaxy.

- Explore whether there is a systematic difference in the AGN outflow properties between the systems with the lowest levels of star formation (i.e., the most suppressed systems) and those undergoing significant star formation. This analysis extends those above by using the star formation as the key quantity, rather than the outflow property, and will provide complementary constraints on what drives the suppression of star formation.

6.2.2 Mapping obscured and unobscured star formation in star forming galaxies

In Chapter 4, I showed that there are significant offsets between the locations of obscured and unobscured star formation in high redshift AGN host galaxies, and the difference in the sizes of these star forming regions. Even though there are studies looking at the properties of the FIR emission and stellar light, or stellar light and Hα emission (Simpson et al., 2015; Hodge et al., 2016; Harrison et al., 2017; Tadaki et al., 2017; Förster Schreiber et al., 2018a; Chen et al., 2019; Lang et al., 2019; Nelson et al., 2019) , we currently lack studies directly explaining the obscured and unobscured star formation of galaxies at high redshift on the star-forming main sequence on spatially resolved scales of > 4 kpc. Such study is important to test our results in Chapter 4, since Hα will be a more reliable tracer in the inactive galaxies because it will not have the complication of a contribution from AGN photoionisation.

The GTO programmes with VLT/KMOS, like KMOS3D, KGES and KROSS, built a sample of 1600 star forming galaxies between z=0.6-2.5 in the deep fields such as CDF-S, COSMOS and UDS with spatially-resolved Hα measurements. ALMA is now finishing the sixth year of observations and consequently, there is a significant amount of data in the ALMA archive, especially in the deep fields. As a result, there are now at least 100 star forming galaxies with both Hα emission-line and FIR continuum observations (ALMA band 6/7 continuum). Compiling this data with deep HST imaging from the deep fields will allow me to compare the FIR, Hα and UV continuum as star formation tracers.

With this sample I will perform the following analyses:

- Measure and compare the SFRs from Hα, FIR, and rest-frame UV data, to constrain the amount of obscured and unobscured star formation. I will also be able to constrain the dust obscuration using the SED fitting and compare it dust obscuration from Balmer decrement, when available.

- Determine the location and sizes of the emission from each of the three star formation tracers and whether obscured and unobscured star formation is preferentially centrally located or extended or whether it has a clumpy structure.

These experiments will constrain the nature of obscured and unobscured star formation in high redshift galaxies. I will compare my results to those of submm galaxies from Chen et al. (2019) and the AGN from Chapter 4. Furthermore, this study will enhance our understanding of tracing star formation in high redshift galaxies, which is an essential tool for future studies studying the connection between AGN and star formation.

6.2.3 sSFR distributions of Quasars with ALMA

In Chapter 3, I constrained the sSFR distributions of moderate X-ray luminosity AGN at z=1.5–3.2 and I did not find any evolution in the sSFR distribution with AGN luminosity over the AGN luminosity range. However, my study did not include the highest luminosity systems such as quasars. Recently, Schulze et al. (2019) used ALMA observations to constrain the SFR distributions of 20 optically selected QSOs at z$\sim$2 and found that the mode of the SFR distribution increases with the bolometric luminosity of AGN, similarly to the study of quasars from Stanley et al. (2017), which is explained by the increasing stellar mass. I am a co-I on a successful ALMA proposal which has observed an additional 90 high redshift QSO from the SDSS survey in band 6/7, tracing the dust continuum emission.

With the addition of the X-ray AGN from Scholtz et al. (2018), the QSOs from Schulze et al. (2019) and data from the proposed project described in §6.2.1, I will have a sample of 270 AGN, spanning the broad AGN bolometric luminosity of 10^{44}–10^{48} ergs s^{-1} at z=1.2–3.2. With these new observations, I will estimate the SFR and stellar masses (using the SMBH mass estimates) to calculate the sSFR of the QSO sample using available MIR and FIR photometry, UV–FIR photometry for the AGN, and the SED fitting code `FORTES`, as exploited in Chapters 3–4. With this large sample of AGN, I will constrain the mode and the width of (s)SFR distribution across a broad range of AGN bolometric luminosity. This will allow me to robustly determine whether QSO host galaxies have different star formation properties to the more common AGN.

6.3 Final remarks

In the past 20 years, AGN feedback has received a significant amount of attention in the literature due to its predicted effect on the evolution of galaxies. Both theoretical and observational studies have investigated the mechanics of AGN feedback and the effect on galaxies. As a result, AGN are now thought to be a crucial part in the evolution of massive galaxies. Theoretical models predict that AGN are capable of ejecting large amounts of energy into the ISM and CGM and hence regulate the amount of cold gas in the galaxy and therefore the amount of star formation. Although there is increasing evidence of powerful AGN outflows such as ionised and molecular outflows and radio jets expelling and heating up the gas in galaxies, we still lack the direct "smoking gun" signature of AGN feedback regulating star formation. We are currently in the era of several large IFU surveys both at high and low redshifts such as KMOS-3D, KROSS, KGES, KASHz, SUPER, S7, SAMI and MaNGA. These surveys target statistically significant samples which will help progress our understanding of galaxy evolution. However, future facilities such as the Large Synoptic Survey Telescope, James Webb Space Telescope, Square Kilometer Array, European-Extremely Large Telescope, ATHENA and many others will enable us to study high redshift galaxies across different phases at a spatial resolution equivalent to local objects. With these state of art observations as well as the next generation of cosmological simulations, we will be able to find the prove that AGN feedback influences star formation and constrains its mechanisms.

And to reward you for getting all the way to the end of this thesis, here is a XKCD comic:

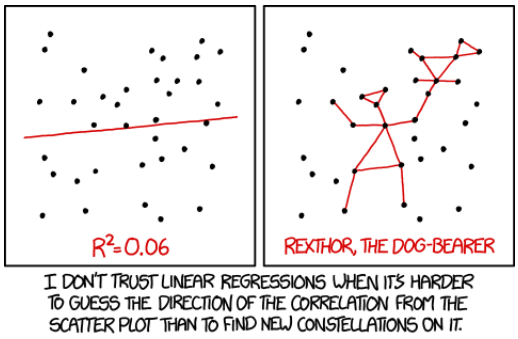

Figure 6.2: 95 % confidence interval suggets that the Rexthor's dog could also be a cat, or possibly a tea pot. Image credit: https://xkcd.com/1725/

Bibliography

Aird, J., Nandra, K., Laird, E. S., et al. 2010, MNRAS, 401, 2531

Aird, J., Alexander, D. M., Ballantyne, D. R., et al. 2015, ApJ, 815, 66

Alam, S., Albareti, F. D., Allende Prieto, C., et al. 2015, APJS, 219, 12

Alatalo, K., Blitz, L., Young, L. M., et al. 2011, ApJ, 735, 88

Alatalo, K., Lacy, M., Lanz, L., et al. 2015, ApJ, 798, 31

Alexander, D. M., & Hickox, R. C. 2012, , 56, 93

Alexander, D. M., Swinbank, A. M., Smail, I., McDermid, R., & Nesvadba, N. P. H. 2010, MNRAS, 402, 2211

Asmus, D., Gandhi, P., Smette, A., Hönig, S. F., & Duschl, W. J. 2011, A&A, 536, A36

Azadi, M., Aird, J., Coil, A. L., et al. 2015, ApJ, 806, 187

Balmaverde, B., & Capetti, A. 2015, A&A, 581, A76

Balmaverde, B., Marconi, A., Brusa, M., et al. 2016, A&A, 585, A148

Barro, G., Faber, S. M., Koo, D. C., et al. 2017, ApJ, 840, 47

Beckmann, R. S., Devriendt, J., Slyz, A., et al. 2017, ArXiv e-prints

Bennert, N., Falcke, H., Schulz, H., Wilson, A. S., & Wills, B. J. 2002, ApJL, 574, L105

Benson, A. J., Bower, R. G., Frenk, C. S., et al. 2003, ApJ, 599, 38

Bernhard, E., Grimmett, L. P., Mullaney, J. R., et al. 2019, MNRAS, 483, L52

Berta, S., Magnelli, B., Nordon, R., et al. 2011, A&A, 532, A49

Bertin, E., & Arnouts, S. 1996, AAPS, 117, 393

Bianchi, S., Maiolino, R., & Risaliti, G. 2012, Advances in Astronomy, 2012

Bischetti, M., Piconcelli, E., Vietri, G., et al. 2017, A&A, 598, A122

Blustin, A. J., Branduardi-Raymont, G., Behar, E., et al. 2003, A&A, 403, 481

Bonnet, H., Conzelmann, R., Delabre, B., et al. 2004, in Society of Photo-Optical Instrumentation Engineers (SPIE) Conference Series, Vol. 5490, Advancements in Adaptive Optics, ed. D. Bonaccini Calia, B. L. Ellerbroek, & R. Ragazzoni, 130–138

Booth, C. M., & Schaye, J. 2009, MNRAS, 398, 53

Boroson, T. 2005, AJ, 130, 381

Boroson, T. A., & Green, R. F. 1992, APJS, 80, 109

Boroson, T. A., Persson, S. E., & Oke, J. B. 1985, ApJ, 293, 120

Bower, R. G., Benson, A. J., Malbon, R., et al. 2006, MNRAS, 370, 645

Bower, R. G., Schaye, J., Frenk, C. S., et al. 2017, MNRAS, 465, 32

Bradshaw, E. J., Almaini, O., Hartley, W. G., et al. 2013, MNRAS, 433, 194

Brandt, W. N., & Alexander, D. M. 2015, , 23, 1

Brusa, M., Bongiorno, A., Cresci, G., et al. 2015, MNRAS, 446, 2394

Brusa, M., Cresci, G., Daddi, E., et al. 2018, A&A, 612, A29

Bruzual, G., & Charlot, S. 2003, MNRAS, 344, 1000

Burgarella, D., Buat, V., & Iglesias-Páramo, J. 2005, MNRAS, 360, 1413

Burgarella, D., Buat, V., Gruppioni, C., et al. 2013, A&A, 554, A70

Calzetti, D. 2013, Star Formation Rate Indicators, ed. J. Falcón-Barroso & J. H. Knapen, 419

Calzetti, D., Armus, L., Bohlin, R. C., et al. 2000, ApJ, 533, 682

Cano-Díaz, M., Maiolino, R., Marconi, A., et al. 2012, A&A, 537, L8

Cardamone, C. N., van Dokkum, P. G., Urry, C. M., et al. 2010, APJS, 189, 270

Carniani, S., Marconi, A., Maiolino, R., et al. 2015, A&A, 580, A102

—. 2016, A&A, 591, A28

—. 2017, A&A, 605, A105

Casey, C. M., Narayanan, D., & Cooray, A. 2014, , 541, 45

Chabrier, G. 2003, PASP, 115, 763

Charlot, S., & Fall, S. M. 2000, ApJ, 539, 718

Chen, C.-C., Hodge, J. A., Smail, I., et al. 2017, ApJ, 846, 108

Chen, C.-C., Harrison, C., Smail, I., et al. 2019, , 846, 108

Chen, C.-T. J., Hickox, R. C., Alberts, S., et al. 2013, ApJ, 773, 3

Choi, E., Somerville, R. S., Ostriker, J. P., Naab, T., & Hirschmann, M. 2018, ApJ, 866, 91

Cicone, C., Brusa, M., Ramos Almeida, C., et al. 2018, Nature Astronomy, 2, 176

Cicone, C., Feruglio, C., Maiolino, R., et al. 2012, A&A, 543, A99

Cicone, C., Maiolino, R., Sturm, E., et al. 2014, A&A, 562, A21

Ciesla, L., Charmandaris, V., Georgakakis, A., et al. 2015, A&A, 576, A10

Circosta, C., Mainieri, V., Padovani, P., et al. 2018, A&A, 620, A82

Civano, F., Marchesi, S., Comastri, A., et al. 2016, ApJ, 819, 62

Civano, F. M., Elvis, M., Brusa, M., & Chandra COSMOS Team. 2009, 41, 422

Colina, L., Arribas, S., & Borne, K. D. 1999, ApJL, 527, L13

Collet, C., Nesvadba, N. P. H., De Breuck, C., et al. 2015, A&A, 579, A89

Condon, J. J. 1997, PASP, 109, 166

Cowley, M. J., Spitler, L. R., Tran, K.-V. H., et al. 2016, MNRAS, 457, 629

Crain, R. A., Schaye, J., Bower, R. G., et al. 2015, MNRAS, 450, 1937

Crenshaw, D. M., Kraemer, S. B., Gabel, J. R., et al. 2003, ApJ, 594, 116

Cresci, G., & Maiolino, R. 2018, Nature Astronomy, 2, 179

Cresci, G., Mainieri, V., Brusa, M., et al. 2015a, ApJ, 799, 82

Cresci, G., Marconi, A., Zibetti, S., et al. 2015b, A&A, 582, A63

Croft, S., van Breugel, W., de Vries, W., et al. 2006, ApJ, 647, 1040

Croton, D. J., Springel, V., White, S. D. M., et al. 2006, MNRAS, 365, 11

D'Agostino, J. J., Kewley, L. J., Groves, B. A., et al. 2019, MNRAS, 487, 4153

Dale, D. A., Helou, G., Magdis, G., et al. 2014, in American Astronomical Society Meeting Abstracts, Vol. 223, American Astronomical Society Meeting Abstracts #223, 453.01

Dalla Vecchia, C., & Schaye, J. 2008, MNRAS, 387, 1431

Damen, M., Labbé, I., van Dokkum, P. G., et al. 2011, ApJ, 727, 1

Davies, R. I., Agudo Berbel, A., Wiezorrek, E., et al. 2013, A&A, 558, A56

Davies, R. L., Kewley, L. J., Ho, I. T., & Dopita, M. A. 2014a, MNRAS, 444, 3961

Davies, R. L., Rich, J. A., Kewley, L. J., & Dopita, M. A. 2014b, MNRAS, 439, 3835

Debuhr, J., Quataert, E., & Ma, C.-P. 2012, MNRAS, 420, 2221

Del Moro, A., Alexander, D. M., Mullaney, J. R., et al. 2013, A&A, 549, A59

Di Matteo, T., Springel, V., & Hernquist, L. 2005, Nature, 433, 604

Dimitrijević, M. S., Popović, L. Č., Kovačević, J., Dačić, M., & Ilić, D. 2007, MNRAS, 374, 1181

Dole, H., Lagache, G., Puget, J. L., et al. 2006, A&A, 451, 417

Done, C., Davis, S. W., Jin, C., Blaes, O., & Ward, M. 2012, MNRAS, 420, 1848

Dunlop, J. S., McLure, R. J., Biggs, A. D., et al. 2017, MNRAS, 466, 861

Eisenhauer, F., Abuter, R., Bickert, K., et al. 2003, in Society of Photo-Optical Instrumentation Engineers (SPIE) Conference Series, Vol. 4841, Instrument Design and Performance for Optical/Infrared Ground-based Telescopes, ed. M. Iye & A. F. M. Moorwood, 1548–1561

Elbaz, D., Dickinson, M., Hwang, H. S., et al. 2011, A&A, 533, A119

Elbaz, D., Leiton, R., Nagar, N., et al. 2018, A&A, 616, A110

Elvis, M. 2012, Journal of Physics Conference Series, 372, 012032

Elvis, M., Wilkes, B. J., McDowell, J. C., et al. 1994, APJS, 95, 1

Elvis, M., Civano, F., Vignali, C., et al. 2009, APJS, 184, 158

Event Horizon Telescope Collaboration, Akiyama, K., Alberdi, A., et al. 2019, ApJL, 875, L1

Fabian, A. C. 2012, ARAA, 50, 455

Fath, E. A. 1909, Lick Observatory Bulletin, 5, 71

Faucher-Giguère, C.-A., & Quataert, E. 2012, MNRAS, 425, 605

Feldman, F. R., Weedman, D. W., Balzano, V. A., & Ramsey, L. W. 1982, ApJ, 256, 427

Feruglio, C., Fiore, F., Carniani, S., et al. 2015, A&A, 583, A99

Fischer, T. C., Rigby, J. R., Mahler, G., et al. 2019, ApJ, 875, 102

Fixsen, D. J., Dwek, E., Mather, J. C., Bennett, C. L., & Shafer, R. A. 1998, ApJ, 508, 123

Fluetsch, A., Maiolino, R., Carniani, S., et al. 2019, MNRAS, 483, 4586

Förster Schreiber, N. M., Genzel, R., Bouché, N., et al. 2009, ApJ, 706, 1364

Förster Schreiber, N. M., Genzel, R., Newman, S. F., et al. 2014, ApJ, 787, 38

Förster Schreiber, N. M., Übler, H., Davies, R. L., et al. 2018a, arXiv e-prints

Förster Schreiber, N. M., Renzini, A., Mancini, C., et al. 2018b, APJS, 238, 21

Freudling, W., Romaniello, M., Bramich, D. M., et al. 2013, A&A, 559, A96

Fritz, J., Franceschini, A., & Hatziminaoglou, E. 2006, MNRAS, 366, 767

Fu, H., & Stockton, A. 2009, ApJ, 690, 953

Fujimoto, S., Ouchi, M., Kohno, K., et al. 2018, ApJ, 861, 7

Furlong, M., Bower, R. G., Theuns, T., et al. 2015, MNRAS, 450, 4486

Gabor, J. M., & Bournaud, F. 2014, MNRAS, 441, 1615

Gaia Collaboration, Brown, A. G. A., Vallenari, A., et al. 2018, A&A, 616, A1

Gallagher, R., Maiolino, R., Belfiore, F., et al. 2019, MNRAS, 485, 3409

Ganguly, R., & Brotherton, M. S. 2008, ApJ, 672, 102

Genzel, R., Eisenhauer, F., & Gillessen, S. 2010, Reviews of Modern Physics, 82, 3121

Genzel, R., Newman, S., Jones, T., et al. 2011, ApJ, 733, 101

Genzel, R., Förster Schreiber, N. M., Rosario, D., et al. 2014, ApJ, 796, 7

George, I. M., & Fabian, A. C. 1991, MNRAS, 249, 352

Gibson, R. R., Brandt, W. N., Gallagher, S. C., & Schneider, D. P. 2009, ApJ, 696, 924

Gofford, J., Reeves, J. N., Turner, T. J., et al. 2011, MNRAS, 414, 3307

Greene, J. E., Ho, L. C., & Barth, A. J. 2008, ApJ, 688, 159

Greene, J. E., Zakamska, N. L., Ho, L. C., & Barth, A. J. 2011, ApJ, 732, 9

Greene, J. E., Peng, C. Y., Kim, M., et al. 2010, ApJ, 721, 26

Greenstein, J. L., M. T. A. 1963, Nature, 197, 1041

Griffin, M. J., Abergel, A., Abreu, A., et al. 2010, A&A, 518, L3

Grogin, N. A., Kocevski, D. D., Faber, S. M., et al. 2011, APJS, 197, 35

Guo, Y., Ferguson, H. C., Giavalisco, M., et al. 2013, APJS, 207, 24

Hao, C.-N., Kennicutt, R. C., Johnson, B. D., et al. 2011, ApJ, 741, 124

Harrison, C. M. 2017, Nature Astronomy, 1, 0165

Harrison, C. M., Alexander, D. M., Mullaney, J. R., & Swinbank, A. M. 2014, MNRAS, 441, 3306

Harrison, C. M., Costa, T., Tadhunter, C. N., et al. 2018, Nature Astronomy, 2, 198

Harrison, C. M., Alexander, D. M., Swinbank, A. M., et al. 2012a, MNRAS, 426, 1073

Harrison, C. M., Alexander, D. M., Mullaney, J. R., et al. 2012b, ApJL, 760, L15

Harrison, C. M., Simpson, J. M., Stanley, F., et al. 2016a, MNRAS, 457, L122

Harrison, C. M., Alexander, D. M., Mullaney, J. R., et al. 2016b, MNRAS, 456, 1195

Harrison, C. M., Johnson, H. L., Swinbank, A. M., et al. 2017, MNRAS, 467, 1965

Heckman, T., & Best, P. 2014, arXiv:1403.4620

Heckman, T. M., Armus, L., & Miley, G. K. 1990, APJS, 74, 833

Heckman, T. M., Miley, G. K., & Green, R. F. 1984, ApJ, 281, 525

Heckman, T. M., Miley, G. K., van Breugel, W. J. M., & Butcher, H. R. 1981, ApJ, 247, 403

Herschel, W. 1786, Royal Society of London Philosophical Transactions Series I, 76, 457

Hickox, R. C., & Alexander, D. M. 2018, ARAA, 56, 625

Hickox, R. C., Mullaney, J. R., Alexander, D. M., et al. 2014, ApJ, 782, 9

Hirschmann, M., Dolag, K., Saro, A., et al. 2014, MNRAS, 442, 2304

Ho, L. C. 2008, ARAA, 46, 475

Hodge, J. A., Karim, A., Smail, I., et al. 2013, ApJ, 768, 91

Hodge, J. A., Swinbank, A. M., Simpson, J. M., et al. 2016, ApJ, 833, 103

Högbom, J. A. 1974, AAPS, 15, 417

Holt, J., Tadhunter, C. N., & Morganti, R. 2008, MNRAS, 387, 639

Hönig, S. F., Beckert, T., Ohnaka, K., & Weigelt, G. 2006, A&A, 452, 459

Hopkins, P. F., Cox, T. J., Hernquist, L., et al. 2013a, MNRAS, 430, 1901

Hopkins, P. F., & Hernquist, L. 2006, APJS, 166, 1

Hopkins, P. F., Hernquist, L., Martini, P., et al. 2005, ApJL, 625, L71

Hopkins, P. F., Kereš, D., Murray, N., et al. 2013b, MNRAS, 433, 78

Hsu, L.-T., Salvato, M., Nandra, K., et al. 2014, ApJ, 796, 60

Hubble, E. 1929, Proceedings of the National Academy of Science, 15, 168

Hubble, E. P. 1926, ApJ, 64, 321

Huggins, W., & Miller, W. A. 1864, Royal Society of London Philosophical Transactions Series I, 154, 437

Hughes, D. H., Serjeant, S., Dunlop, J., et al. 1998, Nature, 394, 241

Humphrey, A., Villar-Martín, M., Sánchez, S. F., et al. 2010, MNRAS, 408, L1

Husemann, B., Scharwächter, J., Bennert, V. N., et al. 2016, A&A, 594, A44

Husemann, B., Wisotzki, L., Sánchez, S. F., & Jahnke, K. 2013, A&A, 549, A43

Husemann, B., Scharwächter, J., Davis, T. A., et al. 2019, A&A, 627, A53

Huynh, M. T., Hopkins, A. M., Lenc, E., et al. 2012, Monthly Notices of the Royal Astronomical Society, 426, 2342

Ikarashi, S., Ivison, R. J., Caputi, K. I., et al. 2015, ApJ, 810, 133

Jarvis, M. E., Harrison, C. M., Thomson, A. P., et al. 2019, MNRAS, 485, 2710

Jin, S., Daddi, E., Liu, D., et al. 2018, ApJ, 864, 56

Jogee, S. 2006, The Fueling and Evolution of AGN: Internal and External Triggers, ed. D. Alloin, Vol. 693, 143

Kakkad, D., Mainieri, V., Padovani, P., et al. 2016, A&A, 592, A148

Kang, D., Woo, J.-H., & Bae, H.-J. 2017, ApJ, 845, 131

Karouzos, M., Woo, J.-H., & Bae, H.-J. 2016, ApJ, 819, 148

Kashino, D., Silverman, J. D., Rodighiero, G., et al. 2013, ApJ, 777, L8

Kashino, D., Silverman, J. D., Sanders, D., et al. 2019, APJS, 241, 10

Kellermann, K. I., Sramek, R., Schmidt, M., Shaffer, D. B., & Green, R. 1989, AJ, 98, 1195

Kennicutt, R. C., & Evans, N. J. 2012, ARAA, 50, 531

Kennicutt, Jr., R. C. 1998, ARAA, 36, 189

Kewley, L. J., Groves, B., Kauffmann, G., & Heckman, T. 2006, MNRAS, 372, 961

Kewley, L. J., Maier, C., Yabe, K., et al. 2013, ApJL, 774, L10

Khachikian, E. E., & Weedman, D. W. 1971, Astrofizika, 7, 389

King, A. 2005, ApJL, 635, L121

King, A., & Nixon, C. 2015, MNRAS, 453, L46

Kirkpatrick, A., Sharon, C., Keller, E., & Pope, A. 2019, ApJ, 879, 41

Kocevski, D. D., Hasinger, G., Brightman, M., et al. 2018, APJS, 236, 48

Koekemoer, A. M., Aussel, H., Calzetti, D., et al. 2007, APJS, 172, 196

Koekemoer, A. M., Faber, S. M., Ferguson, H. C., et al. 2011, APJS, 197, 36

Komossa, S., Xu, D., Zhou, H., Storchi-Bergmann, T., & Binette, L. 2008, ApJ, 680, 926

Kormendy, J., Bender, R., & Cornell, M. E. 2011, Nature, 469, 374

Kormendy, J., & Ho, L. C. 2013, ARAA, 51, 511

Lacey, C. G., Baugh, C. M., Frenk, C. S., et al. 2016, MNRAS, 462, 3854

Lagache, G., Puget, J.-L., & Gispert, R. 1999, APSS, 269, 263

Laigle, C., McCracken, H. J., Ilbert, O., et al. 2016, APJS, 224, 24

Lang, P., Schinnerer, E., Smail, I., et al. 2019, ApJ, 879, 54

Lansbury, G. B., Jarvis, M. E., Harrison, C. M., et al. 2018, ApJL, 856, L1

Lanzuisi, G., Delvecchio, I., Berta, S., et al. 2017, A&A, 602, A123

Laor, A., & Behar, E. 2008, MNRAS, 390, 847

Le Floc'h, E., Aussel, H., Ilbert, O., et al. 2009, ApJ, 703, 222

Leavitt, H. S. 1908, Annals of Harvard College Observatory, 60, 87

Lehnert, M. D., & Heckman, T. M. 1996, ApJ, 462, 651

Leung, G. C. K., Coil, A., Azadi, M., et al. 2017, ArXiv e-prints

Lipari, S., Sanchez, S. F., Bergmann, M., et al. 2009, MNRAS, 392, 1295

Lípari, S., Bergmann, M., Sanchez, S. F., et al. 2009, MNRAS, 398, 658

Liu, G., Zakamska, N. L., Greene, J. E., Nesvadba, N. P. H., & Liu, X. 2013, MNRAS, 436, 2576

Loiacono, F., Talia, M., Fraternali, F., et al. 2019, MNRAS, 2095

Lutz, D. 2014, ARAA, 52, 373

Lutz, D., Mainieri, V., Rafferty, D., et al. 2010, ApJ, 712, 1287

Lutz, D., Poglitsch, A., Altieri, B., et al. 2011, A&A, 532, A90

Lynden-Bell, D. 1969, Nature, 223, 690

Lyu, J., & Rieke, G. H. 2018, The Astrophysical Journal, 866, 92

Madau, P., & Dickinson, M. 2014, ARAA, 52, 415

Madau, P., Ferguson, H. C., Dickinson, M. E., et al. 1996, MNRAS, 283, 1388

Magnelli, B., Popesso, P., Berta, S., et al. 2013, A&A, 553, A132

Magorrian, J., Tremaine, S., Richstone, D., et al. 1998, AJ, 115, 2285

Maiolino, R., Russell, H. R., Fabian, A. C., et al. 2017, Nature, 544, 202

Marchesi, S., Civano, F., Elvis, M., et al. 2016, ApJ, 817, 34

Mateos, S., Alonso-Herrero, A., Carrera, F. J., et al. 2012, Monthly Notices of the Royal Astronomical Society, 426, 3271

Matthews, T. A., & Sandage, A. R. 1963, ApJ, 138, 30

McAlpine, S., Bower, R. G., Harrison, C. M., et al. 2017, MNRAS, 468, 3395

McAlpine, S., Helly, J. C., Schaller, M., et al. 2016, Astronomy and Computing, 15, 72

McCarthy, I. G., Schaye, J., Bower, R. G., et al. 2011, MNRAS, 412, 1965

McCarthy, P. J., Baum, S. A., & Spinrad, H. 1996, APJS, 106, 281

McElroy, R. E., Husemann, B., Croom, S. M., et al. 2016, A&A, 593, L8

McNamara, B. R., & Nulsen, P. E. J. 2012, New Journal of Physics, 14, 055023

Merloni, A., Rudnick, G., & Di Matteo, T. 2004, MNRAS, 354, L37

Messier, C. 1781, Catalogue des Nébuleuses & des amas d'Étoiles (Catalog of Nebulae and Star Clusters), Tech. rep.

Miller, N. A., Fomalont, E. B., Kellermann, K. I., et al. 2008, APJS, 179, 114

Miller, N. A., Bonzini, M., Fomalont, E. B., et al. 2013, The Astrophysical Journal Supplement Series, 205, 13

Mor, R., & Netzer, H. 2012, MNRAS, 420, 526

Morganti, R., Tadhunter, C. N., & Oosterloo, T. A. 2005, A&A, 444, L9

Mullaney, J. R., Alexander, D. M., Fine, S., et al. 2013, MNRAS, 433, 622

Mullaney, J. R., Alexander, D. M., Goulding, A. D., & Hickox, R. C. 2011, MNRAS, 414, 1082

Mullaney, J. R., Pannella, M., Daddi, E., et al. 2012a, MNRAS, 419, 95

—. 2012b, MNRAS, 419, 95

Mullaney, J. R., Alexander, D. M., Aird, J., et al. 2015, MNRAS, 453, L83

Murphy, E. J., Chary, R. R., Dickinson, M., et al. 2011, ApJ, 732, 126

Nagao, T., Marconi, A., & Maiolino, R. 2006, A&A, 447, 157

Nelson, C. H., & Whittle, M. 1996, ApJ, 465, 96

Nelson, E. J., van Dokkum, P. G., Brammer, G., et al. 2012, ApJL, 747, L28

Nelson, E. J., Tadaki, K.-i., Tacconi, L. J., et al. 2019, ApJ, 870, 130

Nenkova, M., Sirocky, M. M., Ivezić, Ž., & Elitzur, M. 2008, ApJ, 685, 147

Nesvadba, N. P. H., Lehnert, M. D., De Breuck, C., Gilbert, A. M., & van Breugel, W. 2008, A&A, 491, 407

Nesvadba, N. P. H., Lehnert, M. D., Eisenhauer, F., et al. 2006, ApJ, 650, 693

Netzer, H. 2015, ARAA, 53, 365

Netzer, H., Shemmer, O., Maiolino, R., et al. 2004, ApJ, 614, 558

Netzer, H., Lutz, D., Schweitzer, M., et al. 2007, ApJ, 666, 806

Newman, S. F., Genzel, R., Förster-Schreiber, N. M., et al. 2012, ApJ, 761, 43

Noeske, K. G., Weiner, B. J., Faber, S. M., et al. 2007, ApJL, 660, L43

Oliver, S. J., Bock, J., Altieri, B., et al. 2012, MNRAS, 424, 1614

Osterbrock, D. E. 1989, Astrophysics of gaseous nebulae and active galactic nuclei, ed. Osterbrock, D. E.

Osterbrock, D. E., & Ferland, G. J. 2006, Astrophysics of gaseous nebulae and active galactic nuclei

Page, M. J., Carrera, F. J., Stevens, J. A., Ebrero, J., & Blustin, A. J. 2011, MNRAS, 416, 2792

Page, M. J., Symeonidis, M., Vieira, J. D., et al. 2012, Nature, 485, 213

Panessa, F., Bassani, L., Cappi, M., et al. 2006, A&A, 455, 173

Perna, M., Sargent, M. T., Brusa, M., et al. 2018, A&A, 619, A90

Pier, E. A., & Krolik, J. H. 1992, ApJ, 401, 99

Poglitsch, A., Waelkens, C., Geis, N., et al. 2010, A&A, 518, L2

Polletta, M., Courvoisier, T. J.-L., Hooper, E. J., & Wilkes, B. J. 2000, A&A, 362, 75

Popping, G., Decarli, R., Man, A. W. S., et al. 2017, A&A, 602, A11

Price, S. H., Kriek, M., Brammer, G. B., et al. 2014, ApJ, 788, 86

Puget, J. L., Abergel, A., Bernard, J. P., et al. 1996, A&A, 308, L5

Puglisi, A., Rodighiero, G., Franceschini, A., et al. 2016, A&A, 586, A83

Querejeta, M., Schinnerer, E., García-Burillo, S., et al. 2016, A&A, 593, A118

Ramasawmy, J., Stevens, J., Martin, G., & Geach, J. E. 2019, MNRAS, 486, 4320

Ramos Almeida, C., Acosta-Pulido, J. A., Tadhunter, C. N., et al. 2019, MNRAS, 487, L18

Ranalli, P., Comastri, A., & Setti, G. 2003, A&A, 399, 39

Reddy, N. A., Kriek, M., Shapley, A. E., et al. 2015, ApJ, 806, 259

Rees, M. J. 1984, ARAA, 22, 471

Reeves, J. N., O'Brien, P. T., & Ward, M. J. 2003, ApJL, 593, L65

Revalski, M., Dashtamirova, D., Crenshaw, D. M., et al. 2018, ApJ, 867, 88

Richards, G. T., Lacy, M., Storrie-Lombardi, L. J., et al. 2006, APJS, 166, 470

Roberts, T. P., Middleton, M. J., Sutton, A. D., et al. 2016, Astronomische Nachrichten, 337, 534

Rohlfs, K., & Wilson, T. L. 1996, Tools of Radio Astronomy, 127

Rosario, D. J. 2019, FortesFit: Flexible spectral energy distribution modelling with a Bayesian backbone

Rosario, D. J., Togi, A., Burtscher, L., et al. 2019, ApJL, 875, L8

Rosario, D. J., Santini, P., Lutz, D., et al. 2012, A&A, 545, A45

—. 2013, ApJ, 771, 63

Rosas-Guevara, Y. M., Bower, R. G., Schaye, J., et al. 2015, MNRAS, 454, 1038

Rose, M., Tadhunter, C., Ramos Almeida, C., et al. 2018, MNRAS, 474, 128

Rovilos, E., Comastri, A., Gilli, R., et al. 2012, A&A, 546, A58

Rowan-Robinson, M. 1995, MNRAS, 272, 737

Rupke, D. S. N., Gültekin, K., & Veilleux, S. 2017, ApJ, 850, 40

Rupke, D. S. N., & Veilleux, S. 2011, ApJL, 729, L27

—. 2013, ApJ, 768, 75

Salpeter, E. E. 1964, ApJ, 140, 796

Sanders, D. B., Salvato, M., Aussel, H., et al. 2007, APJS, 172, 86

Santini, P., Rosario, D. J., Shao, L., et al. 2012, A&A, 540, A109

Santini, P., Merlin, E., Fontana, A., et al. 2019, MNRAS, 486, 560

Schawinski, K., Koss, M., Berney, S., & Sartori, L. F. 2015, MNRAS, 451, 2517

Schaye, J., Crain, R. A., Bower, R. G., et al. 2015, MNRAS, 446, 521

Scheiner, J. 1899, ApJ, 9, 149

Schinnerer, E., Sargent, M. T., Bondi, M., et al. 2010, The Astrophysical Journal Supplement Series, 188, 384

Schmidt, M. 1963, Nature, 197, 1040

Scholtz, J., Alexander, D. M., Harrison, C. M., et al. 2018, MNRAS, 475, 1288

Schreiber, C., Pannella, M., Elbaz, D., et al. 2015, A&A, 575, A74

Schulze, A., Silverman, J. D., Daddi, E., et al. 2019, MNRAS, 1696

Schwarz, G. 1978, Ann. Statist., 6, 461

Segers, M. C., Schaye, J., Bower, R. G., et al. 2016, MNRAS, 461, L102

Seyfert, C. K. 1943, ApJ, 97, 28

Shakura, N. I., & Sunyaev, R. A. 1973, A&A, 24, 337

Shao, L., Lutz, D., Nordon, R., et al. 2010, A&A, 518, L26

Shapley, A. E., Reddy, N. A., Kriek, M., et al. 2015, ApJ, 801, 88

Sharples, R., Bender, R., Agudo Berbel, A., et al. 2013, The Messenger, 151, 21

Sharples, R. M., Bender, R., Lehnert, M. D., et al. 2004, in Society of Photo-Optical Instrumentation Engineers (SPIE) Conference Series, Vol. 5492, Ground-based Instrumentation for Astronomy, ed. A. F. M. Moorwood & M. Iye, 1179–1186

Shemmer, O., Netzer, H., Maiolino, R., et al. 2004, ApJ, 614, 547

Shin, J., Woo, J.-H., Chung, A., et al. 2019, arXiv e-prints, arXiv:1907.00982

Silk, J., & Rees, M. J. 1998, A&A, 331, L1

Silva, L., Granato, G. L., Bressan, A., & Danese, L. 1998, ApJ, 509, 103

Simpson, C., Martínez-Sansigre, A., Rawlings, S., et al. 2006, Monthly Notices of the Royal Astronomical Society, 372, 741

Simpson, J. M., Smail, I., Swinbank, A. M., et al. 2015, ApJ, 807, 128

Slipher, V. M. 1915, Popular Astronomy, 23, 21

—. 1917a, Proceedings of the American Philosophical Society, 56, 403

—. 1917b, Lowell Observatory Bulletin, 3, 59

Slone, O., & Netzer, H. 2012, MNRAS, 426, 656

Smith, H. E., Lonsdale, C. J., & Lonsdale, C. J. 1998, ApJ, 492, 137

Soltan, A. 1982, MNRAS, 200, 115

Somerville, R. S., Hopkins, P. F., Cox, T. J., Robertson, B. E., & Hernquist, L. 2008, MNRAS, 391, 481

Speagle, J. S., Steinhardt, C. L., Capak, P. L., & Silverman, J. D. 2014, APJS, 214, 15

Spilker, J. S., Marrone, D. P., Aravena, M., et al. 2016, ApJ, 826, 112

Springel, V. 2005, MNRAS, 364, 1105

Springel, V., Di Matteo, T., & Hernquist, L. 2005, ApJL, 620, L79

Stach, S. M., Dudzevičiūtė, U., Smail, I., et al. 2019, arXiv e-prints

Stanley, F. 2016, PhD thesis, Durham University

Stanley, F., Harrison, C. M., Alexander, D. M., et al. 2018, MNRAS, 478, 3721

—. 2015, MNRAS, 453, 591

Stanley, F., Alexander, D. M., Harrison, C. M., et al. 2017, MNRAS, 472, 2221

Stockton, A. 1976, ApJL, 205, L113

Stockton, A., & MacKenty, J. W. 1987, ApJ, 316, 584

Storchi-Bergmann, T., Lopes, R. D. S., McGregor, P. J., et al. 2010, MNRAS, 402, 819

Stott, J. P., Swinbank, A. M., Johnson, H. L., et al. 2016, MNRAS, 457, 1888

Sturm, E., González-Alfonso, E., Veilleux, S., et al. 2011, ApJL, 733, L16

Swinbank, A. M., Webb, T. M., Richard, J., et al. 2009, MNRAS, 400, 1121

Swinbank, A. M., Simpson, J. M., Smail, I., et al. 2014, MNRAS, 438, 1267

Swinbank, A. M., Harrison, C. M., Tiley, A. L., et al. 2019, MNRAS, 487, 381

Tadaki, K.-i., Genzel, R., Kodama, T., et al. 2017, ApJ, 834, 135

Tadhunter, C., & Tsvetanov, Z. 1989, Nature, 341, 422

Tadhunter, C., Wills, K., Morganti, R., Oosterloo, T., & Dickson, R. 2001, MNRAS, 327, 227

Talia, M., Pozzi, F., Vallini, L., et al. 2018, MNRAS, 476, 3956

Teplitz, H. I., Chary, R., Elbaz, D., et al. 2011, AJ, 141, 1

Tiley, A. L., Swinbank, A. M., Harrison, C. M., et al. 2019, MNRAS, 485, 934

Tombesi, F., Cappi, M., Reeves, J. N., & Braito, V. 2012, MNRAS, 422, L1

Tombesi, F., Cappi, M., Reeves, J. N., et al. 2010, A&A, 521, A57

Trayford, J. W., Theuns, T., Bower, R. G., et al. 2016, MNRAS, 460, 3925

Trayford, J. W., Camps, P., Theuns, T., et al. 2017, ArXiv e-prints

Trump, J. R., Hall, P. B., Reichard, T. A., et al. 2006, APJS, 165, 1

Ueda, Y., Watson, M. G., Stewart, I. M., et al. 2008, APJS, 179, 124

Urry, C. M., & Padovani, P. 1995, PASP, 107, 803

Vanden Berk, D. E., Richards, G. T., Bauer, A., et al. 2001, AJ, 122, 549

Veilleux, S. 1991, APJS, 75, 383

Veilleux, S., Cecil, G., & Bland-Hawthorn, J. 2005, ARAA, 43, 769

Veilleux, S., Kim, D.-C., Sanders, D. B., Mazzarella, J. M., & Soifer, B. T. 1995, APJS, 98, 171

Veilleux, S., Meléndez, M., Sturm, E., et al. 2013, ApJ, 776, 27

Venturi, G., Nardini, E., Marconi, A., et al. 2018, A&A, 619, A74

Veron, M. P. 1981, A&A, 100, 12

Villar-Martín, M., Arribas, S., Emonts, B., et al. 2016, MNRAS, 460, 130

Villar-Martín, M., Fosbury, R. A. E., Binette, L., Tadhunter, C. N., & Rocca-Volmerange, B. 1999, A&A, 351, 47

Vito, F., Maiolino, R., Santini, P., et al. 2014, MNRAS, 441, 1059

Vogelsberger, M., Genel, S., Springel, V., et al. 2014, MNRAS, 444, 1518

Vrtilek, J. M. 1985, ApJ, 294, 121

Walker, M. F. 1968, ApJ, 151, 71

Wampler, E. J., Burbidge, E. M., Baldwin, J. A., & Robinson, L. B. 1975, ApJL, 198, L49

Wang, J., Mao, Y. F., & Wei, J. Y. 2011, ApJ, 741, 50

Weedman, D. W. 1970, ApJ, 159, 405

—. 1977, ARAA, 15, 69

Westmoquette, M. S., Clements, D. L., Bendo, G. J., & Khan, S. A. 2012, MNRAS, 424, 416

Whitaker, K. E., van Dokkum, P. G., Brammer, G., & Franx, M. 2012, ApJL, 754, L29

Whitaker, K. E., Franx, M., Leja, J., et al. 2014, ApJ, 795, 104

Whittle, M. 1985, MNRAS, 213, 1

Whittle, M., Pedlar, A., Meurs, E. J. A., et al. 1988, ApJ, 326, 125

Wild, V., Charlot, S., Brinchmann, J., et al. 2011, MNRAS, 417, 1760

Wilson, A. S., & Heckman, T. M. 1985, in Astrophysics of Active Galaxies and Quasi-Stellar Objects, ed. J. S. Miller, 39–109

Wisnioski, E., Mendel, J. T., Förster Schreiber, N. M., et al. 2018, ApJ, 855, 97

Woo, J.-H., Bae, H.-J., Son, D., & Karouzos, M. 2016, ApJ, 817, 108

Wylezalek, D., Veilleux, S., Zakamska, N., et al. 2017, Q-3D: Imaging Spectroscopy of Quasar Hosts with JWST Analyzed with a Powerful New PSF Decomposition and Spectral Analysis Package, JWST Proposal ID 1335. Cycle 0 Early Release Scienc

Wylezalek, D., & Zakamska, N. L. 2016, MNRAS, 461, 3724

Xue, Y. Q., Luo, B., Brandt, W. N., et al. 2016, APJS, 224, 15

—. 2011, APJS, 195, 10

York, D. G., Adelman, J., Anderson, Jr., J. E., et al. 2000, AJ, 120, 1579

Zakamska, N. L., & Greene, J. E. 2014, MNRAS, 442, 784

Zeldovich, Y. B., & Novikov, I. D. 1964, Dokl. Acad. Nauk. SSSR, 158, 811

Zhang, K., Dong, X.-B., Wang, T.-G., & Gaskell, C. M. 2011, ApJ, 737, 71

Zinn, P. C., Middelberg, E., Norris, R. P., et al. 2012, Astronomy and Astrophysics, 544, A38

Zubovas, K., & King, A. 2014, arXiv:1401.0392

Appendix A

Acronyms

2QZ	The 2dF QSO Redshift Survey
ACS	Advanced Camera for Surveys
AGN	Active Galactic Nuclei
ALMA	Atacama Large Millimeter/submillimeter Array
BH	Black Hole
BLR	Broad Line Region
BPT	Baldwin-Phillips-Terlevich
C-COSMOS	Chandra COSMOS
CDF-S	Chandra Deep Field-South
COSMOS	COSMOlogical evolution Survey
EAGLE	Evolution of GaLaxies and their Environment
E-CFDS	Extended-Chandra Deep Field South
ESA	European Space Agency
ESO	European Southern Observatory
FIR	Far Infrared
FIRST	Faint Images of the Radio Sky
FWHM	Full Width at Half Maximum
GOODS	Great Observatories Origins Deep Survey
GOODS-S	GOODS-South
GRASIL	GRAphite and SILicate
GTO	Guaranteed Time Observations
HerMES	Herschel Multi-tiered Extragalactic Survey
HST	Hubble Space Telescope

IFS	Integral Field Spectroscopy
IFU	Integral Field Unit
IGM	InterGalactic Medium
IMF	Initial Mass Function
IR	Infra Red
IRAF	Image Reduction and Analysis Facility
IRAM	Institut de Radioastronomie Millimetrique
IRAS	InfraRed Astronomical Satellite
ISM	InterStellar Medium
JVLA	(Karl G.) Jansky Very Large Array
JWST	James Webb Space Telescope
KMOS	K-band Multi-Object Spectrograph
LINER	Low-Ionization Nuclear Emission-line Region
LIRG	Luminous InfraRed Galaxy
MIR	Mid Infrared
MS	Main Sequence
NIR	Near InfraRed
NLR	Narrow Line Region
NRAO	National Radio Astronomy Observatory
NVSS	NRAO VLA Sky Survey
PACS	Photodetector Array Camera and Spectrometer
PdBI	Plateau de Bure Interferometer
PSF	Point Spread Function
QSO	Quasi-Stellar Object
SDSS	Sloan Digital Sky Survey
SED	Spectral Energy Distribution
SF	Star Formation
SFR	Star Formation Rate
sSFR	Specific Star Formation Rate
SINFONI	Spectrograph for Integral Field Observations in the Near Infrared
SKA	Square Kilometre Array

SFMS	Star Forming Main Sequence
SMBH	Super Massive Black Hole
SMG	SubMillimetre Galaxy
SPIRE	Spectral and Photometric Imaging REceiver
UDS	Ultra Deep Survey
ULIRG	Ultra-Luminous Infrared Galaxy
VLA	Very Large Array
VLT	Very Large Telescope
WFC3	Wide Field Camera 3
WISE	Wide-field Infrared Survey Explorer
XMM	X-ray Multi-Mirror Mission